# Durham E-Theses

## *Controlling Terahertz Radiation - Novel Fabrication Methods and Materials for Terahertz Components*

### ANDREAS KURT KLEIN

**How to cite:**

**Use policy**

# Controlling Terahertz Radiation

## Novel Fabrication Methods and Materials for Terahertz Components

# Andreas Kurt Klein

A thesis presented for the degree of

Doctor of Philosophy
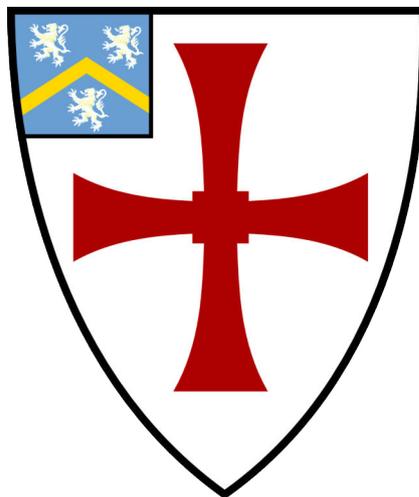
Department of Engineering

University of Durham

United Kingdom

September 2019

## Abstract

The interaction between light and matter has been a field of research for centuries, from the days of Sir Isaac Newton in the $17^{\text{th}}$ century up to today, where new effects, such as plasmonics open up new applications or the extension of the accessible electromagnetic spectrum, are still engaging scientists and engineers in this field of research. The understanding of the interaction between light, or more general: electromagnetic radiation and matter is a crucial step in the development of components which give the necessary control to gain access to the desired part of the electromagnetic spectrum. One of the less developed parts of the electromagnetic spectrum is terahertz (THz) radiation. THz radiation promises many applications, from spectroscopy for material and medical applications to communication technology. But, so far, most applications have not managed to overcome the experimental status, mostly because of missing materials and manufacturing methods suitable for the required length scales and material properties in the terahertz regime. This thesis focuses on structures for the control of THz radiation. To do so, and to overcome the natural limitations of many materials in the THz region, new materials and modern fabrication techniques are used to find new ways to overcome the shortage of readily available components for this part of the electromagnetic spectrum. As such, ceramics and polymers are used for various components, from lenses to spoof plasmonic waveguides, fabricated with a variety of techniques, including 3D printing and micro-milling. Finite-Difference Time-Domain simulations are used for the design of all structures. The ultimate goal is to demonstrate low-cost methods to produce THz components for future industrial implementation.

# Acknowledgements

Also, greetings to my parents to which I am grateful for the continuing support. You can now stop asking when I will finish my PhD.

Finally, I would like to thank Polly again for her loving assistance through those last few months.

*"Of course a certain number of scientists have to go mad, just to keep the tradition alive."*

— Matt Ruff

# Contents

# Declaration

The work in this thesis is based on research carried out at the Department of Engineering, University of Durham, England. No part of this thesis has been submitted elsewhere for any other degree or qualification, and it is the sole work of the author unless referenced to the contrary in the text.

Some of the work presented in this thesis has been published in journals and conference proceedings - the relevant publications are listed on the next pages.

# Publications

Corresponding author marked by *

## Journal Publications

1 "Scattering of spoof surface plasmon polaritons in defect-rich THz waveguide", Andreas K. Klein*; Alastair Basden; Deli Geng; Luke Tyas; Michael Cooke; Jonathan Hammler; Claudio Balocco; Dagou Zeze; John M. Girkin; Andrew Gallant, Scientific Reports 9, 6288, 2019.

2 "Machinable ceramic for high performance and compact THz optical components," Andreas K. Klein*; Jonathan M. Hammler; Claudio Balocco; Andrew Gallant, Optical Materials Express 8(7): 1968-1975, 2018.

## Conference Abstracts

3 "Whispering-Gallery Resonators for Highly Integrated Plasmonic THz Circuits", Andreas K. Klein*,Polina Stefanova, Michael Cooke, Claudio Balocco, and Andrew Gallant; 44th International Conference on Infrared, Millimeter, and Terahertz waves (IRMMW-THz), 2019.

4 "THz Spatial Modulation In The Fourier Plane", Polina Stefanova*, Andreas K. Klein, Claudio Balocco, and Andrew Gallant; 44th International Conference on Infrared, Millimeter, and Terahertz waves (IRMMW-THz), 2019.

5 "Rotational Cuvette Measurements for Refractive Index Testing using a THz Vector Network Analyser", Rhiannon Lees*, Andreas K. Klein, Michael Cooke,

Claudio Balocco, and Andrew Gallant; 44th International Conference on Infrared, Millimeter, and Terahertz waves (IRMMW-THz), 2019.

6 "THz Metasurfaces for Spatial Beam Modulation and Chemical Identification," Polina Stefanova, Rhiannon Lees, Andreas K. Klein, Michael D. Cooke, Andrew J. Gallant, and Claudio Balocco*, META 2019, 2019.

7 "The Grazing Angle Performance on Thin Polyurethane Film," Adrian Boland-Thoms*, Andreas Klein, Polina Stefanova, Mohammad Nordin, Nick Zakhleniuk, Andrew Gallant and Anthony Vickers, Optical Terahertz Science and Technology 2019.

8 "Material Characterization with Frequency Domain THz Ellipsometry," Andreas K. Klein*, Polina S. Stefanova, Andrew Gallant, Claudio Balocco, 43st International Conference on Infrared, Millimeter, and Terahertz waves (IRMMW-THz), 2018.

9 "Porous Polymers as a Substrate for Terahertz Spectroscopy," Anwen Smith, Andreas K. Klein*, Claudio Balocco, and Natasha Shirshova, 43st International Conference on Infrared, Millimeter, and Terahertz waves (IRMMW-THz), 2018.

10 "Ultra-low-cost THz wave plates based on high-contrast gratings," Andreas K. Klein*, Jonathan M. Hammler, Claudio Balocco, Andrew Gallant, 43st International Conference on Infrared, Millimeter, and Terahertz waves (IRMMW-THz), 2018.

11 "Low-loss, low-cost, high refractive index machinable ceramic for THz optical components", Andreas K. Klein* ; Jonathan M. Hammler ; Dagou Zeze ; Claudio Balocco ; Andrew Gallant, 42st International Conference on Infrared, Millimeter, and Terahertz waves (IRMMW-THz), 2017.

12 "Photonic-crystal based enhancement of terahertz spectroscopy in microfluidic cells", Andreas K. Klein* ; Jonathan M. Hammler ; Dagou Zeze ; Claudio Balocco ; Andrew Gallant, 41st International Conference on Infrared, Millimeter, and Terahertz waves (IRMMW-THz), 2016.

13 "Switchable spoof surface plasmon polariton slow light structures", Andreas K. Klein*; Dagou Zeze; Claudio Balocco; Andrew Gallant, Lasers and Electro-Optics (CLEO), 2016.

14 "High quality filter for high traffic load short range high bandwidth future communication networks at THz frequencies", Andreas Klein*, IET Radio Propagation and Technologies for 5G Conference, 2016.

15 "Micro fabricated spoof surface plasmon polariton structures for THz applications", Andreas K. Klein*; Yi Pan; Claudio Balocco; Dagou Zeze; Andrew J. Gallant, 40th International Conference on Infrared Millimeter, and Terahertz waves (IRMMW-THz), 2015.

16 "Polymer-based micro-golay cells for THz detection", Polina S. Stefanova; Jonathan M. Hammler; Andreas K. Klein*; Andrew J. Gallant; Claudio Balocco, 41st International Conference on Infrared, Millimeter, and Terahertz waves (IRMMW-THz), 2016.

17 "Effect of Wood's anomalies on the THz transmission spectra of free-standing metallic hole arrays", Carlo K. A. Hill*; Andreas K. Klein; Claudio Balocco; David Wood; Andrew J. Gallant,40th International Conference on Infrared, Millimeter, and Terahertz waves (IRMMW-THz), 2015.

18 "Quality Factor Comparison of Terahertz Cavities Formed by Photonic Crystal Slabs".A. K. Klein*, D. Zeze, C. Balocco, A. J. Gallant; Nanostructures for Photonics NSP-2016.

19 "Stacked Metamaterials as Bragg Reflectors for THz Frequencies", Andreas K. Klein*, International Meeting on Materials for Electronic Applications IMMEA-2015.

20 "Microfabricated plasmonic THz structures", Andreas K.Klein*, Rank Prize Funds Symposium on New Terahertz Sources and Emerging Applications 2016.

21 "Vector Network Analyser Based Angular Resolved Measurements at THz Frequencies", Andreas K. Klein*, Jonathan M. Hammler, Dagou Zeze, Claudio Balocco, and Andrew Gallant; Optical Terahertz Science and Technology 2017.

# List of Figures

# List of Tables

# Nomenclature

**AlN** aluminium-nitride

**ATR** Attenuated Total Reflection

**BWO** backward wave oscillator

**CFL** Courant-Friedrichs-Lewis

**CNC** Computer Numerical Control

**DBR** distributed Bragg reflector

**EOS** electro-optic sampling

**FDM** Frequency-Division multiplexing

**FDTD** finite-difference time-domain

**FFT** fast Fourier transformation

**HCG** high-contrast grating

**HRFZ-Si** high resistivity float zone

**LC** liquid crystal

**OPL** optical path length

**PCA** photoconductive antenna

**PEC** perfect electric conductor

**PPWG** parallel-plate waveguides

**PSD** power spectral density

**RTD** resonant tunneling diode

**SEM** scanning electron microscope

**SEW** surface electromagnetic waves

**SOLT** Short-Open-Load-Through

**SPP** surface plasmon polariton

**SSIM** structural similarity index

**THz** Terahertz

**TE** transverse electric

**TM** transverse magnetic

**VNA** vector network analyzer

**WG** whispering gallery

# Introduction

In this chapter, first the Terahertz (THz) spectrum is introduced and why its special properties make it a challenging field with unique opportunities. Following this, a quick summary of why THz components and devices are not as readily available as for other parts of the electromagnetic spectrum is presented. The chapter closes with a brief overview of the structure of this thesis.

## 1.1 The THz spectrum

Terahertz radiation is the region of the electromagnetic spectrum between millimetre waves and infrared light. While THz simply describes a unit with its prefix (THz=$10^{12}$Hz), the term usually refers to what is still today called the THz gap, a frequency sub-domain of 0.3 to 10 THz, even if this gap is continuously closing [1–4]. THz radiation is still a quite young field of research, compared to other parts of the electromagnetic spectrum which have been investigated for decades, if not centuries. The reason for this is not the lack of interest but rather the challenges associated with coherently generating and detecting this kind of radiation. The wavelengths at a frequency of 1 THz is $300\,\mu m$ which corresponds to a photon energy of 4.1 meV, which is six times smaller than the thermal energy at room temperature ($\sim$26 meV). Such small energy quanta cannot be realised in traditional semiconductor laser or sensor concepts which rely on interband transitions

of charge carriers. Instead, complex intraband transitions have to be employed and cooling to liquid nitrogen or helium temperatures is necessary [5].
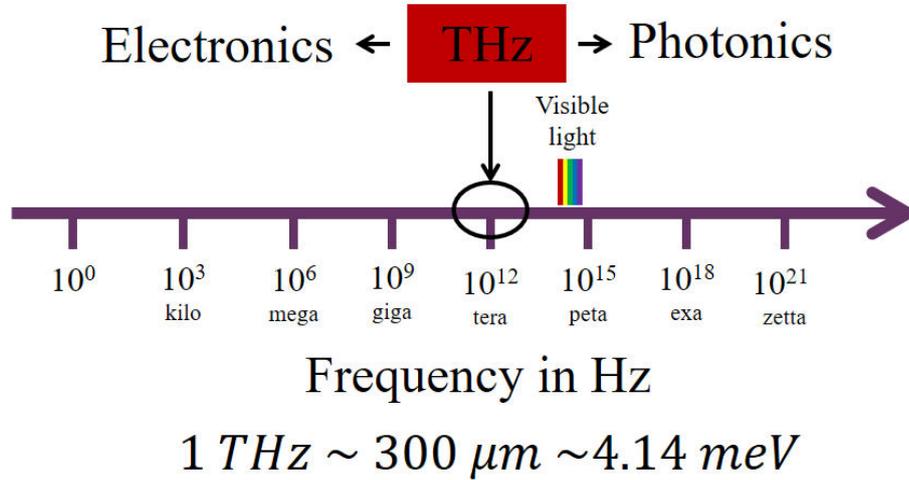


Figure 1.1: Electromagnetic spectrum with corresponding wavelength and energy for 1 THz. Radiation below THz frequencies are generated with electronic sources, frequencies above are commonly generated with photonic sources. For the THz region in between, both electronic and photonic sources are used.

Despite these challenges, THz technology has experienced considerable progress in the past decade. The reason for the increased efforts in the field of THz science is not simply the scientific desire to extend the available spectrum, but the applications enabled by it. There are applications such as THz communications, which have great commercial potential. But they fundamentally rely on the same physical principle as wireless communications at other frequencies, just with a higher frequency and therefore data rate [6, 7]. The largest advantage of THz radiation is based on the fact that most molecules have their resonant frequencies in the THz range. Therefore their absorption spectrum, so-called 'fingerprints' or signatures, are unique for a given material and therefore do allow for identification via THz spectroscopy [8]. Therefore, initially THz science attracted considerable attention for security applications, e.g. the identification of illicit drugs [9] or explosives [8]. But due to the challenging measurement environment of realistic measurement scenarios, there have been few real applications. A different set of applications with equally great potential but better controllable measurement environments lay in

the biomedical field. For example the identification of cancerous tissue [10] due to a change in the absorption and cancer biomarkers due to their spectral fingerprint [11]. In summary, there is the potential for many applications enabled by THz technology. Many of them unique to this part of the electromagnetic spectrum. however, the technology overall has to mature to achieve the required availability and sensitivity.

## 1.2 Fabrication and Material Challenges for THz components

However, THz technology is not only challenging in the field of generating and detecting radiation at the desired frequencies but also in auxiliary components, such as optics and waveguides. Therefore, many standard components and technologies are not readily available at THz frequencies, which has brought about the combination of long wavelength and material properties in this frequency domain. A good example of the complications caused by the long wavelength are epitaxially grown components. For example distributed feedback lasers [12], which is a standard technology for components in the optical and infrared spectrum. As the layer thickness increases proportional to the wavelength, the required layers are either too thick to be grown for technical reasons, such as stress in the crystal lattice due to lattice mismatch, or simply too expensive to be suitable for mass manufacturing. Inversely, the wavelength of THz frequencies causes an issue for fabrication techniques used at microwave frequencies, where often centimetre-sized resonators are machined with traditional milling and drilling. Machining the small length scales as required for THz components is challenging. The relevant tool dimension, which in most cases will be the diameter, is commonly a magnitude of order smaller than the feature size, which reaches the limits of technical capability and makes the assembly of such components extremely costly. Therefore, THz components often lay in a region between the fabrication methods designed for the nanometre length

scale utilised by the semiconductor industry and the mm sized fabrication method of traditional machining. This means, depending on the target frequency and component, semiconductor or traditional machining might be preferable as there are trade-offs in surface quality and feature size between different techniques.

Another explanation of why THz components are lagging in performance to other parts of the electromagnetic spectrum is the intrinsic material absorption. Many materials have higher absorption at THz frequencies. For example 3D printable polymers such as Acrylonitrile butadiene styrene (ABS) whose attenuation coefficient increases tenfold from 0.2 to 1 THz [13]. A similar effect can even be seen for high resistivity float zone silicon , as seen in Figure 1.2, which shows the attenuation per wavelength travelled, i.e. specific attenuation. This metric is useful for photonic components, such as photonic crystals, as their functionality is commonly based on interference effects and therefore scale with the wavelength. The attenuation at infrared frequencies is at least two orders of magnitude lower than at THz frequencies, making it far superior in performance at these frequencies. This is remarkable, given that HRFZ-Si is usually considered one of the best materials for THz components.

The higher absorption by materials and challenging feature sizes are inherent features of THz components. The influence of bulk components is apparent, as fewer suitable materials are available they either suffer from losses, an inconvenient form factor due to the low refractive index or are simply expensive and hard to machine. For waveguides, the impact is similar, albeit it depends on the waveguide type if material properties limit the performance, which is the case for optical fibres or photonic crystals. For rectangular waveguides, the machining precision poses the largest issue with increasing frequencies and the integration of active components in such waveguides with micrometre precision is tedious work resulting in high cost and long assembly times.

Other traditional waveguides, such as strip line, suffer from both the small dimensions and more substantial material losses and are therefore seldom found in THz
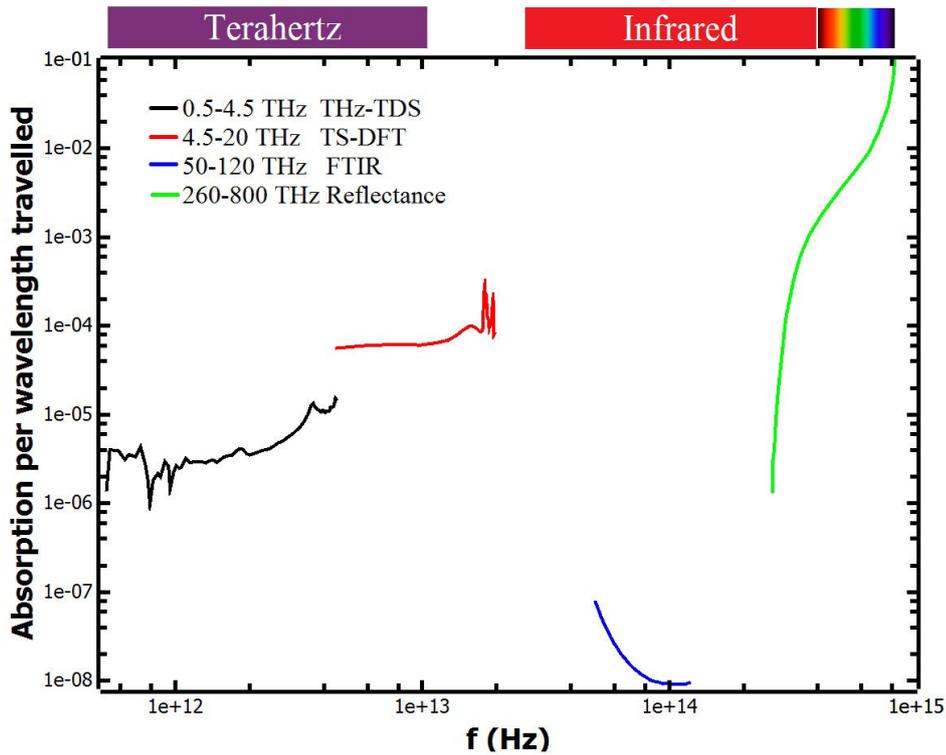
Figure 1.2: The absorption per wavelength travelled in silicon for different frequencies. Data recorded with various techniques from: THz Time-Domain Spectroscopy (THz-TDS) [14], Time stretch dispersive Fourier transform spectroscopy (TS-DFT)[15], Fourier-transform infrared spectroscopy (FTIR) [16] and reflectance measurements [17].The discontinuity between the THz-TDS and TS-DFT is most likely caused by the different techniques, as different techniques, and even different instruments based on identical techniques, are known to deliver different attenuation coefficient for low absorption materials in the high frequency region [18**?** , 19].

devices.

Hence, this thesis addresses new materials and fabrication methods that overcome the stated shortcomings of THz components. New ceramic materials, which are unstudied at THz frequencies to date, are used as a material for optics. The use of longer wavelength opens up the possibility to 3D print optical components and waveguides, which would have a too poor surface quality for components at shorter wavelengths. Interesting new physical properties arising from the surface quality are studied and compared to established fabrication techniques, such as photolithography.

## 1.3 Structure of Thesis

Chapter 2 presents the fabrication methods and measurement instruments used in the thesis, including a small comparison between techniques. As the different components presented here do require experimental techniques unique to this type of structure, these techniques are explained in the respective chapter. The second chapter also introduces finite-difference time-domain (FDTD) simulation as the dominant design method used in this thesis.

The third chapter is about THz optical components made out of ceramics and polymers, produced with subtractive and additive manufacturing, respectively. The ceramic materials are first tested on their optical properties at THz frequencies and subsequently machined into optical components. High-contrast gratings are fabricated from the polymers as the geometrical simplicity and short optical path length of this type of structure are suitable for the shaping limitations of the laser cutter and high absorption of the 3D printer used.

This is followed by cavity design with photonic crystal and their application for microfluidic analysis in chapter 4. Initially, the general influence of geometric constraints for the length scales required for a THz photonic crystal cavity are discussed. The gained insights are then applied to a microfluidic device in a photonic crystal to increase the sensitivity to chemicals in the fluidic channel.

In chapter 5 THz ellipsometry is discussed, as the ellipsometer was constructed as a byproduct of the angular-resolved measurement setup, which was required for the characterisation of some of the spoof plasmonic waveguides presented in the following chapter. The system development is discussed and the performance of the THz ellipsometer is evaluated by characterising multiple materials and comparing the measured optical constants to literature and other measurement techniques. The advantage of the reflection configuration is demonstrated with in-situ thickness measurements of a wafer during etching.

Chapter 6 is the final results chapter and discusses spoof plasmonic waveguides.

Multiple components for integrated photonic circuits, such as filters and splitters, based on spoof plasmonic waveguides are discussed. This is followed by a section on 3D printed waveguides with high defect concentrations. The defect density gives rise to new physical effects, such as the unassisted free-space coupling of radiation, and the scattering is discussed in light of the Mie theory and compared to FDTD simulation.

# Methods and Instruments

This chapter discusses the fabrication techniques, followed by the measurement instruments used and concludes with an introduction and validation of FDTD simulation for the design of THz components.

## 2.1 Fabrication Techniques

Three different fabrication techniques have been employed during this thesis: Photolithography, micro-machining and 3D printing. Photolithography is a parallel fabrication technique which writes the structures of a single layer all at once as opposed to micro-machining and 3D printing, which are both serial techniques that write the individual features of a structure sequentially – much like writing with a pen on a piece of paper. The classic advantage of a parallel technique is the quick fabrication of several samples and, in this case, it also provides a smaller minimal feature-size than the other techniques. Photolithography is the standard technique in semiconductor technology and ideal for situations where the same structure has to be repeatedly produced with high reliability, but every structure needs a separate mask which makes it an inflexible technique and expensive for situations where only a few copies of a structure are required. The major advantage of serial techniques is quick prototyping, adjustable structure and, in case of micro-machining and 3D printing, the control in an additional dimension. While photolithography

only allows lateral structuring of a uniform film, micro-machining and 3D printing also allow variable features in the third dimension. The "rapid prototyping" capability of serial techniques makes them attractive for research purposes where the effects of small changes in structures are to be explored.

## 2.1.1 Photolithography

Photolithography is a microfabrication process which transfers patterns from a master, a photomask, to a thin film. A schematic of a photolithography process can be seen in Figure 2.1. The patterns are transferred via a layer of light-sensitive
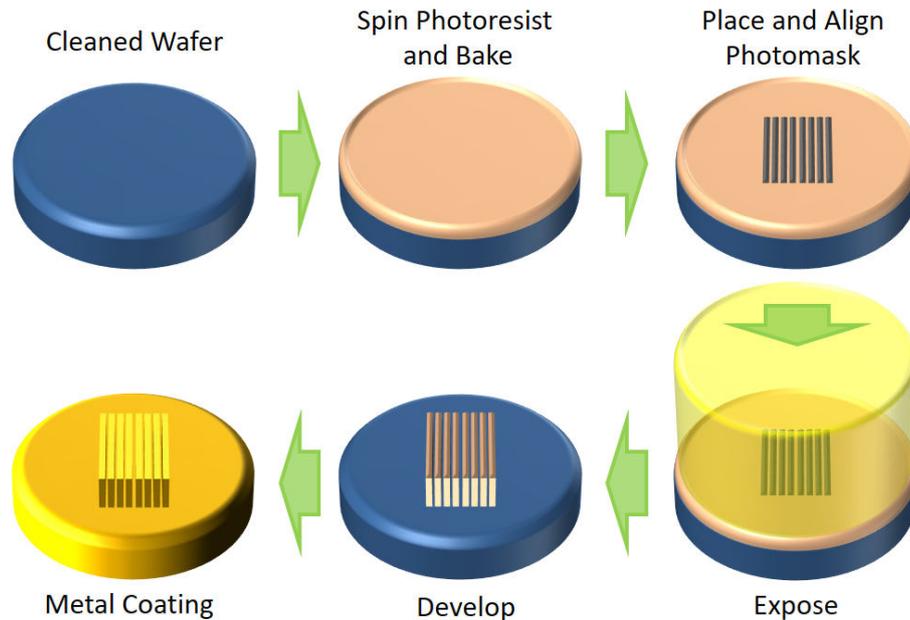
Figure 2.1: Schematic of the photolithography process used for the production of spoof surface plasmon polariton (SPP) structures. Photoresist is spun on a cleaned wafer and baked. It follows the alignment of the photomask and exposure. The non-exposed parts of the photoresist are removed during the developing step. The structures are subsequently coated with metal.

polymers called photoresist. The photoresist is exposed to UV light. Some parts are shadowed by the pattern on the photomask and therefore not exposed. The light triggers a chemical process in the exposed parts of the film, which changes the chemical structure that causes it to behave differently from the inexposed part

of the film in the subsequent chemical treatment. The chemical treatment, called development, removes the inexposed part of the film, creating a negative of the original structure on the photomask. Consequently, this type of photoresist is called negative photoresist. The schematic process in Figure 2.1 uses a negative resist. Positive photoresist, which removes the exposed part of the photoresist and creates a positive copy of the photomask also exist but is not used in this thesis.

The main photoresist employed during this thesis is SU-8 2000. SU-8 2000 is a high contrast, epoxy-based photoresist [20]. It is designed for the fabrication of thick layers in the order of tens to a few hundred micrometres in a single coating process. The exposed, and subsequently thermally cross-linked portions of the film are highly stable from a chemical, thermal and mechanical perspective. The cross-linking proceeds in two steps. First, a strong acid is formed during exposure. Second, the acid serves as a catalyst for the thermally-driven epoxy-cross linking during the post exposure bake. The fabrication process used is close to the datasheet [20] and shown in Figure 2.2.

The geometric properties are stated for each sample. The geometric parameters
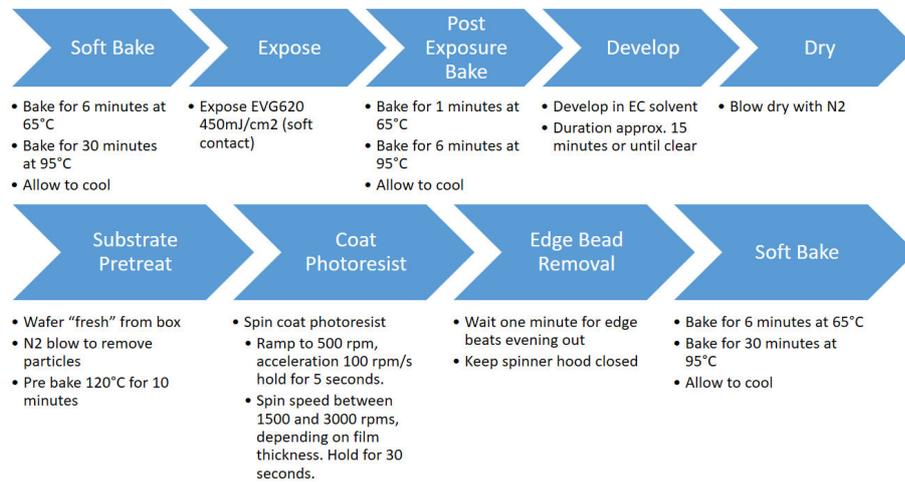


Figure 2.2: Process flow chart for a photolithographic process with SU8 photoresist.

are measured with optical microscopy for the horizontal dimension and a shearing microscope for the lateral dimensions.

## 2.1.2 CNC Micro-Machining

Computer Numerical Control (CNC) machining is a well-established fabrication method in the manufacturing industry, especially for materials that cannot be cast or where complex shapes that cannot be extruded. It is the automated version of traditional machining, such as milling or drilling, controlled by a computer. The efforts of recent years have increased the precision, with tool sizes down to the tens of micrometres. Hence it is common to talk about micro-machining, despite this term being also used for the etching of semiconductors, especially by the micro-electromechanical systems (MEMS) community. However, feature sizes required for THz components such as waveguides do push the limits of what is currently possible which makes both fabrication and the often required following assembly an elaborate and expensive procedure.

The CNC machine used for the micro-machining here is a bespoke piece of equipment of the THz lab in Durham under ongoing development. The machine consists of three linear motorised translation stages (Thorlabs MT S50-Z8) with an air motor spindle (Nakanishi SMS401) and is controlled with a regular Linux computer.

## 2.1.3 3D printing

3D printing is a technique where the material is solidified in a computer-controlled process. Various processes can cause the solidification, such as the cooling of previously melted material or a photoactivated process, such as curing of a resin. Only the latter technique is described as it is used in this thesis. This technique, usually referred to as stereolithography (SLA), uses an ultraviolet laser to induce photopolymerization in a resin. 3D printing is conducted in a layer by layer process. The laser is focused on parts of the layer to solidify them. It, therefore "writes" the structure. Afterwards, another layer of resin is added, and the writing is repeated. In this way, a three-dimensional object is created layer by layer. One of the main advantages of the technique is the freedom of shaping the workpiece to one's de-

sire, which is the most considerable advantage of additive fabrication techniques, such as 3D printing, over subtractive techniques, such as micro-machining. There are virtually no limits to the shape within the constraints of a minimum feature size. Even cavities or enclosures can be incorporated, which is impossible with subtractive techniques where the tool cannot access the inside of a closed shape. An example of the complexity of 3D printed structures can be seen in Figure 2.3.

With a resolution in the order of tens to hundreds of micrometres, the feature
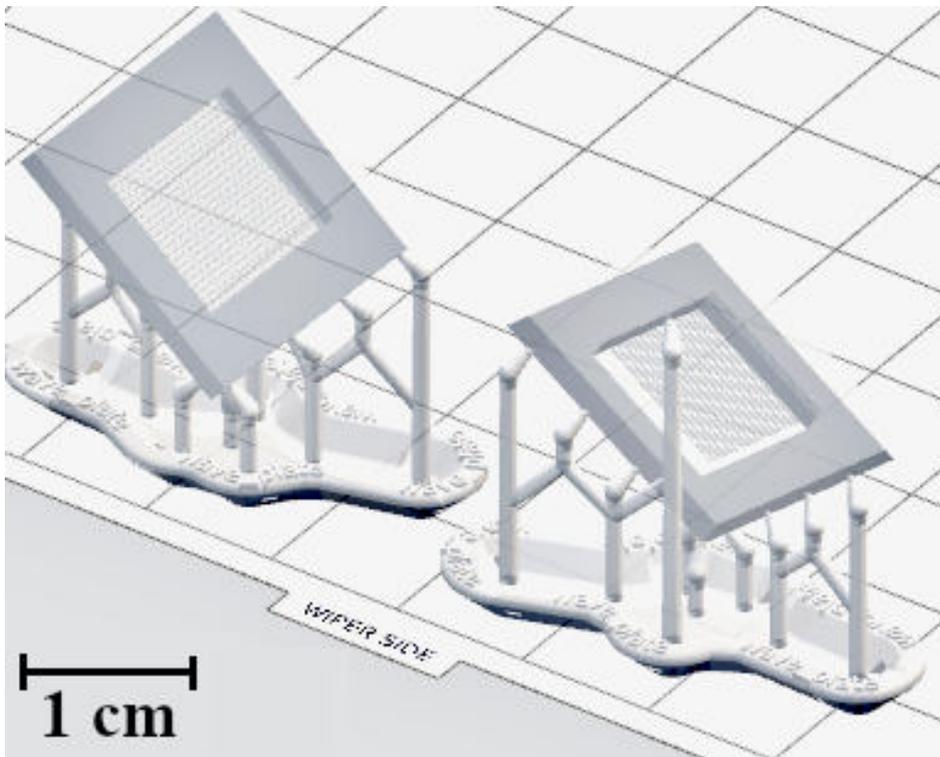


Figure 2.3: Screenshot from the design software of 3D printed high contrast gratings used as THz waveplates on their support structures. The support structures are needed to release the structures afterwards.

sizes that high-end 3D printer can achieve are suitable for THz optical components and photonics. To fabricate dielectric components, the optical properties of the 3D printed materials employed, especially the attenuation coefficient, have to be suitable as well. Many materials used for thermally-induced 3D printing are already known in literature [13].

However, the optical properties for the THz region of the resins used by the Form-

labs Form 2 printer, which has been used to produce the components in this thesis, are not present in literature and therefore have to be tested to evaluate the suitability for its use for dielectric THz components. The resins tested are the clear resin, Clear Resin v2 (GPCL02), and a green resin, referred to as tough resin by the manufacturer. The exact composition of the resins is not available. Figure 2.4 shows the transmission for the two available resins.
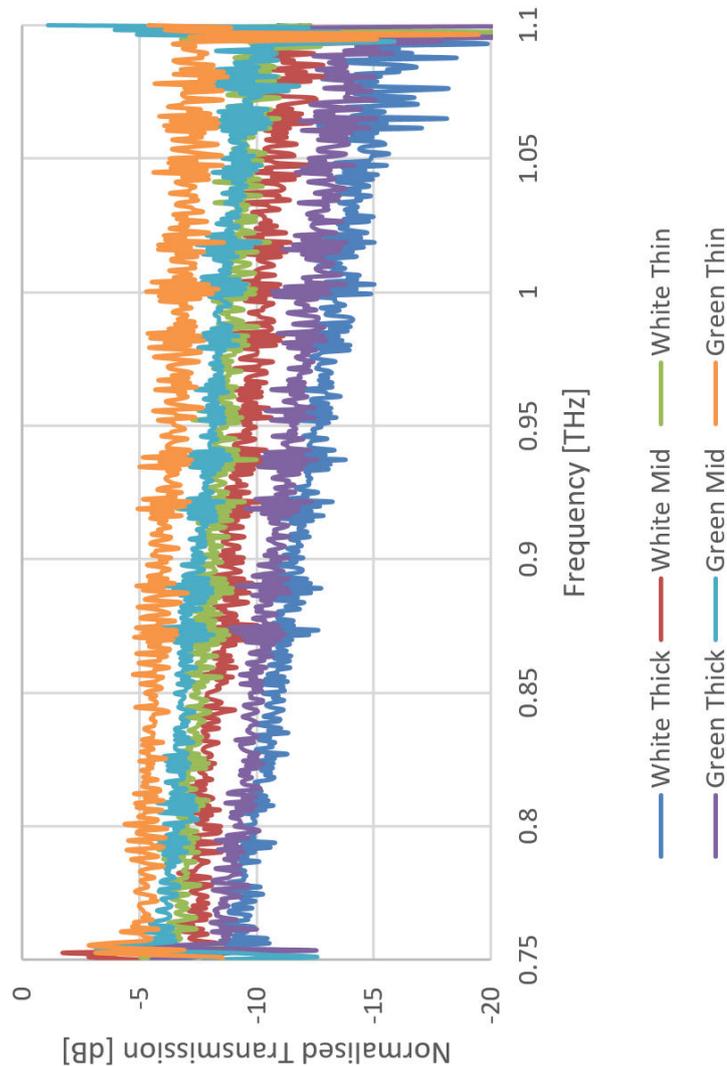


Figure 2.4: The transmission of the white resin is consistently lower than the absorption of the green resin at equal thickness. This makes the white resin less desirable than the green resin as a material for refractive optics. Thicknesses for thick, medium and thin are 1.1, 0.7, 0.5 mm respectively. Normalisation to empty beam path.

The absorption of the green material is consistently lower than the absorption of the white resin. This makes the green resin more suitable for THz optical components, albeit it is worth mentioning that the white resin achieves better surface finishes, hence it is more suitable for smaller features. With the three different thicknesses, a crude fit, shown in Figure 2.5, can be used to estimate the attenuation coefficient $\alpha$ of the green resin to $11.8\pm1.1\,\text{cm}^{-1}$.

Such a high absorption makes the material unsuitable for bulk THz compon-
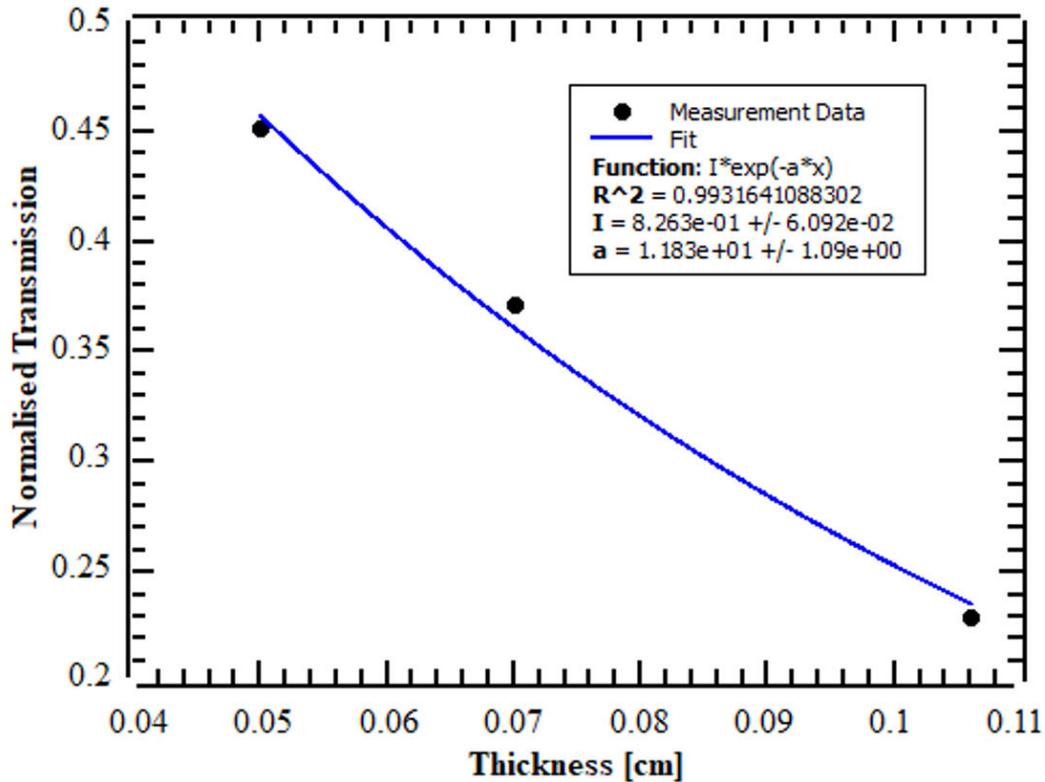


Figure 2.5: Plotting the transmission data of the three different thicknesses of the green resin at 1 THz allows for a simple fit to estimate the absorption coefficient.

ents such as lenses and prisms which preferably are made from materials with $\alpha < 1\,\text{cm}^{-1}$, but still could be suitable for flat components such as Fresnel-Lenses or high-contrast gratings, as these components usually have thicknesses of only a few wavelengths along the optical axis.

3D printing is also used to fabricate spoof plasmonic components, where the attenuation of the material is irrelevant as they are subsequently coated with metal.

### 2.1.4 Laser Cutter

An HPC LS6840 PRO laser cutter is used. The machine uses a water-cooled $CO_2$ gas tube with 50 W power. Stepper motors are used for the positioning in x, y and z with a location precision of <0.01 mm. The machine is designed to cut a wide range of softer materials, such as plastics, fabrics and wood. The maximum resolution is $\sim 150$ $\mu m$, but is considerably larger for samples thicker than paper. Additionally, heat dissipation becomes an issue for materials, such as polymers, and melting occurs if the feature size is too small.

### 2.1.5 Metallic coating

The SPP structures in this thesis were produced with photolithography and 3D printing are metal coated. Neither the photoresist used in photolithography nor the resin used in 3D printing are metallic. Therefore, after fabrication, the structures are subsequently coated with metal. The metal is deposited through sputtering. As sputtering produces different coating thicknesses on flanks and flats, the thickness of the metal coating is above 300 nm to be thicker than the skin-depth at THz frequencies (<100 nm) in all places.

## 2.2 Measurement instruments

This section discusses the measurement instruments. It focuses on the THz instruments available in the Durham University THz lab. The other instruments, such as the scanning electron microscope (SEM), are only used in a qualitative way for visualisation. With other instruments, such as the surface profiler, it is an external service, and others conduct the measurements. Therefore, these instruments are just briefly discussed.

At the start some general remarks about THz characterisation techniques and cur-

rent issues in the community can be found, followed by the introduction of the THz vector network analyzer (VNA) and the THz TDS.

## 2.2.1 THz metrology

Even well after two decades, THz science still struggles with standardisation, sometimes resulting in vast differences in optical properties for the same material, especially regarding the attenuation coefficient, as seen in Figure 2.6. While a relative attenuation is usually sufficient for applications such as material identification, absolute attenuation is essential, e.g. for the development of photonic components and comparability of results, which helps the field of THz technology and science to mature.

The recent efforts to compare different systems and methods and the ongoing
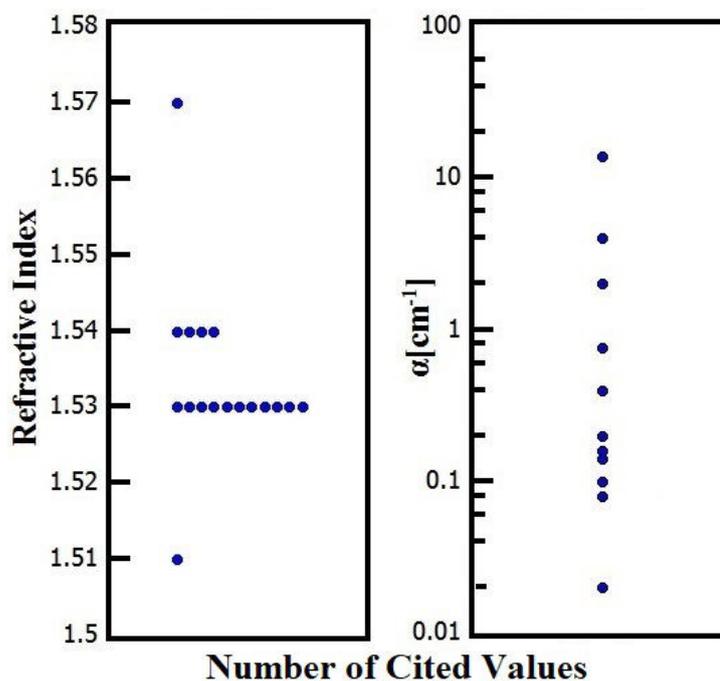


Figure 2.6: Comparison of literature values of the optical constants of HDPE at THz frequencies. While the values for the refractive index do agree reasonably well with each other with a spread of <3% (left), the values for the attenuation coefficient from the same publications deviate by three orders of magnitude (right). Literature values extracted from [13, 21–23].

attempts to develop new methods to extract the optical constants all face one

common problem: How to validate the results if another instrument or technique delivers different results for identical samples [18, 19, 21, 24]. The characterisation of materials at THz frequencies with THz time-domain spectroscopy is challenging. While the technique is a powerful and versatile tool and probably the most used characterisation technique at THz frequencies, it is also strongly dependant on the configuration, setup and alignment, which can lead to significant deviations in measurements conducted on identical samples [21, 25–29]. These factors are of lesser importance when diode-based frequency domain systems are used, such as the VNA, which are less susceptible to alignment and post-processing errors and are increasingly available at higher frequencies. The downside of such systems is the narrow frequency range, e.g. 0.75-1.1 THz which is the frequency range of the instrument used in this thesis, when compared to the broadband THz-TDS, which usually covers at least the frequency range from 0.3-2.5 THz.

The necessity of standardisation for THz measurements especially in regard of the attenuation coefficient becomes apparent in Figure 2.6, which shows a large spread of over two order of magnitudes for the attenuation coefficient for HDPE, one of the most commonly used polymers in THz science, while showing only little deviation in the refractive index.

Therefore, developing components which are highly susceptible to attenuation, such as resonators, with literature values only, has more uncertainties in the THz regime than, for example at optical frequencies. This often makes the characterisation of material before using it for components a necessity.

## 2.2.2 THz Vector Network Analyser

The THz VNA consists of a network analyser model N5224A from Agilent Technologies in combination with two full-band multipliers of the type WR-1.0 from Virginia Diodes to extend the original frequency region from 10 MHz to 43.5 GHz of the Agilent network analyser to 0.75 to 1.1 THz.

The specification of the WR-1.0 extender heads can be seen in Table 2.1 and Fig-

Table 2.1: Specification of the frequency range extender VNAX WR-1/0 (WM250). From [30]

| Standard Frequency Coverage ($GHz$) | 750-1000 |
|---|---|
| Dynamic Range ($bandwidth = 10\,Hz, dB, typical$) | 65 |
| Dynamic Range ($bandwidth = 10\,Hz, dB, minimum$) | 45 |
| Magnitude Stability ($\pm dB$) | 0.5 |
| Phase Stability ($\pm^\circ$) | 6 |
| Test Port Power( $dBm\ typ.\ power$) | -30 |
| Directivity ($dB$) | 30 |

ure 2.7.

In many aspects, the VNA is complementary to THz-TDS. While TDS works in
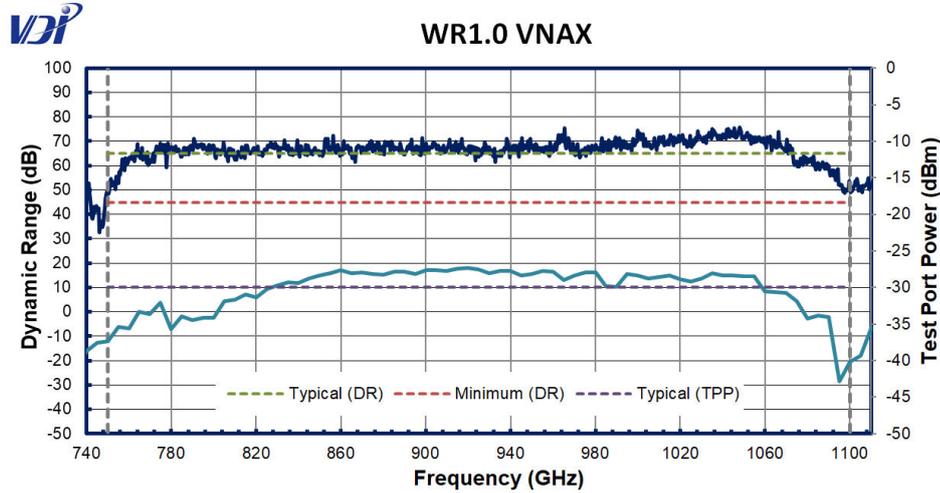


Figure 2.7: Dynamic range and test port power of the VNA frequency extenders. DR: Dynamic Range, TPP: Test Port Power. From [30].

the time domain, the VNA works in the frequency domain. The TDS is a pulsed system, the VNA operates in continuous wave; the TDS has a broad frequency range (approx.. 0.5-4.5 THz) but takes 20-30 minutes for a single scan with the bespoke Durham system, the VNA has around a tenth of the frequency range, but can complete a full scan of this span within seconds. The frequency resolution of a TDS is ultimately limited by the duration of the sampled time-domain waveform. The 150 mm delay line used in the Durham system allows for a theoretical maximum resolution of $\sim 0.5$ GHz[31], but as scans are commonly considerably shorter a resolution of a few GHz is achieved. In contrast, the frequency resolution of the

VNA depends on the stability of the local oscillator and resolutions in the order of kHz are easily possible.

The many differences make the VNA a good complement to the THz-TDS, even if the limited frequency range can be challenging. The VNA's near to real-time response is advantageous and a necessity for the realisation of experimental setups where an exact adjustment is crucial. This is the case for the knife-edge scattering technique as described in Section 6.1.3, or in setups when a complete characterisation would otherwise take days with the TDS like the angle-resolved measurements as discussed in Chapter 5. Additionally, the VNA records S-parameters, which means it can measure reflection (S11, S22) and transmission (S12, S21) without a change of setup and in both directions thourgh the sample.

In general, electronic sources are a quickly maturing field for the THz spectrum. While frequency multiplying at such high frequencies has been available for a few decades already, these components were part of costly instruments with highly specialised purposes, such as the Herschel Space Observatory [32], which only work at very low temperatures that only can be reached with liquid nitrogen or even liquid helium cooling. Therefore these components were not readily available for lab use until recently, but these issues have been addressed by clever circuit design enabling room temperature functionality [33, 34]. The used VNA Range Extenders are the first to reach a frequency of 1 THz and only have been commercially available since 2011 and are therefore a fairly new characterisation method for the THz community [35]. Additional information on the VNA can be found in the appendix.

### 2.2.2.1 Calibration

One of the advantages of the frequency extenders over other THz systems, such as the TDS, is that calibration kits for full s-parameter calibration are readily available and calibration for waveguides is well established through the microwave community. For the frequency range used, a Short-Open-Load-Through (SOLT) calibration is used to determine the 2-port 12-term error coefficients which are com-

monly used [36]. It consists of one-port measurements of each of the ports using three known reflection standards (shorted termination, open termination and load termination) and one transmission standard (1" through). For waveguides, the shorts are offset by a quarter-wave as an open waveguide acts comparable to a load due to radiation. The quarter-wave adds a total of $180°$ to the wave reflected by the short, which is the desired phase differences between open and short. Therefore, the 'open' is actually a flush short, i.e. the short without offset. This produces the same phase difference to the offset short as an open has to a short for calibration standards with other connectors like coaxial cables.

One issue of the calibration is that it only is applied up to the test ports, i.e. the waveguides without antenna and free-space in between. Therefore, free-space measurements with a THz VNA are not using fully calibrated instruments. Known calibration methods for free-space at microwave frequencies are commonly based on changing either the distance between antennas and a reflective surface or dielectric materials with exactly known thicknesses [37, 38]. This becomes increasingly difficult with higher frequencies, as the precision of the calibration depends on the phase delay which is proportional to the change in distance or optical path length $L$ over the wavelength $L/\lambda$. Therefore, for the frequency range used, placement within micrometres would be required.

## 2.2.3 THz Time-Domain Spectroscopy

As part of this thesis, a new THz-TDS has been developed. The TDS is most likely still the most commonly used technique for THz characterisation. The main advantage is the broad frequency range when compared to other THz sources. The Durham University system has a frequency range of approx. 0.5-5 THz, but systems with significantly higher maximum frequencies above 15 THz are known [39]. While there are different ways to generate the THz radiation for a TDS, such as electro-optical rectification, the thesis will focus on photoconductive antennas photoconductive antenna (PCA), as these are used in the system. For the same

reason, only electro-optic sampling will be discussed for detection.

### 2.2.3.1 Photoconductive Antennas

For the generation of THz radiation with a PCA, a mode-locked femtosecond laser pulse is shone onto a photoconductive switch, which consists of two biased metal contacts separated by a (semi-)insulating semiconductor, as seen in Figure 2.8. The
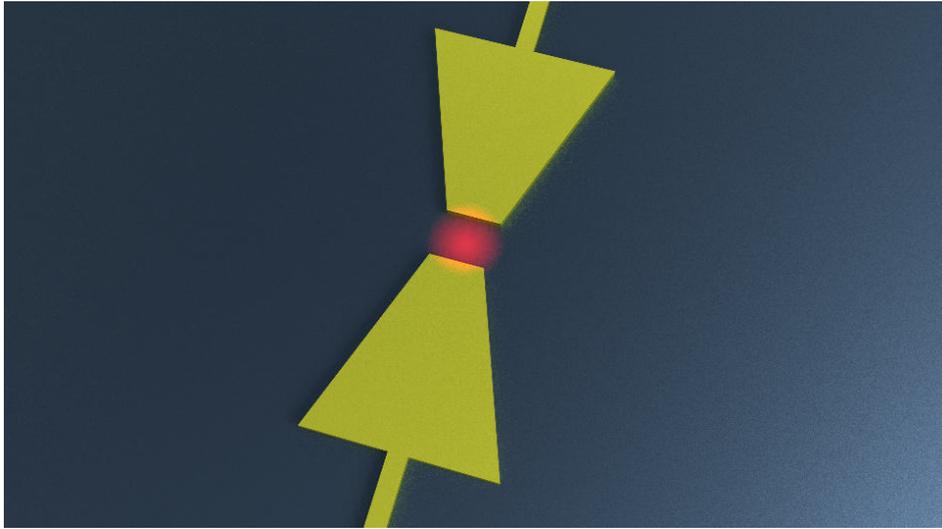


Figure 2.8: Illustration of a photoconductive antenna. A femtosecond laser illuminates the gap between the two biased electrodes of a bow-tie antenna, which causes a rapid transient current that generates the THz radiation.

photoconductive switch, also called the Auston switch, functions as an optically gated antenna, where the pulse causes a rapid transient of the conductivity due to photoexcitation, as illustrated in Figure 2.9. The sudden surge in current generates electromagnetic radiation, which is in the THz frequency range when the laser pulse duration is sub-picosecond.

This principle can also be used to detect THz radiation in a 'reverse' of the emission process where the laser pulse creates charge carriers, but the antenna is unbiased so that only the incident THz radiation accelerates the carriers, producing a current which is recorded by a detector circuit. The frequency and bandwidth of the generated radiation depend on the pulse length of the photocurrent, which means that not only the optical pulse length must be as short as possible, but also
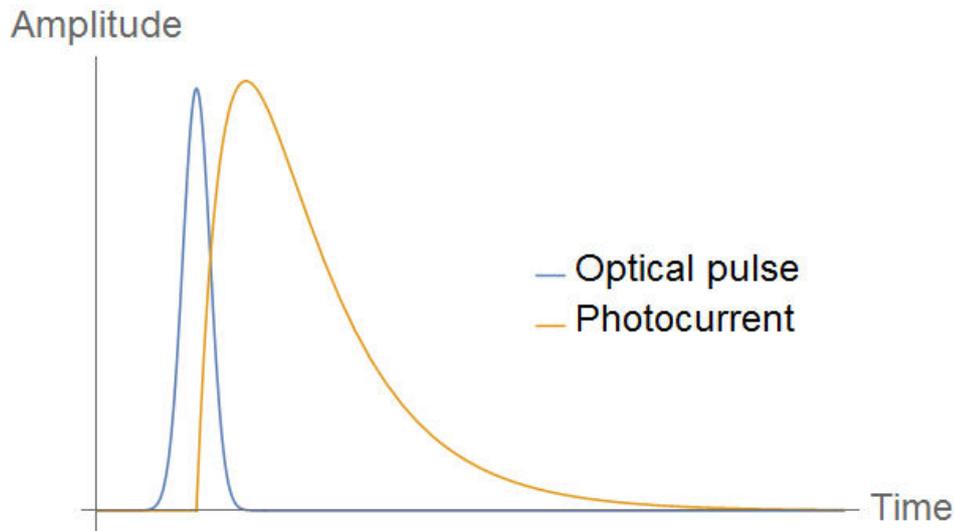
Figure 2.9: Illustration for the time-domain response of an optically gated photo-conductive antenna. As the photocurrent has a longer duration than the optical pulse that caused it, femtosecond lasers are required for the generation of pico-second THz pulses. From [40].

the generated electrical pulse must fulfil this precondition. Hence, direct bandgap semiconductors are used which exhibit both, fast generation and recombination, leading to a short charge carrier lifetime, which results in picosecond switching [41]. To produce a current, the energy of the photons in the laser pulse must exceed the bandgap energy of the semiconductor. For the most commonly used direct semiconductor, GaAs, this means an energy gap of 1.39 eV has to be bridged, therefore light with a wavelength shorter than $\sim 892\,\mathrm{nm}$ must be used. Hence, the usage of Ti: Sapphire lasers is required, but it is worth mentioning that the development of fibre-based lasers using $1.55\,\mu\mathrm{m}$ wavelength in combination with more complex semiconductor structures is progressing as well [42], decreasing the costs and therefore increasing the availability of THz-TDS systems.

The antenna itself consists of two metallic (Au/Ti) contacts on the semiconductor surface, fabricated with photolithography. The geometry of the antenna can take different forms and influences the shape of the emitted spectrum as well as the polarisation [43]. One of the most common design uses bow-tie antennas to increase the electric field in the gap. In general, electromagnetic radiation generated by

a change in velocity of charged particles is proportional to the derivative of the current change. In the case of a photoconductive antenna, the simplified case of a Hertzian dipole [44], the generated electric $E_{THz}$ field is given by

$$E_{THz} \propto \frac{\partial j}{\partial t},$$

(2.1)

where $j$ is the current density and $t$ the time. The current density in a semiconductor is linearly dependent on the charge carrier concentration $n_{charge}$ and the carrier drift velocity $v$, which leads to

$$\frac{\partial j}{\partial t} \propto ev \frac{\partial n_{charge}}{\partial t} + en \frac{\partial v}{\partial t},$$

(2.2)

where $e$ is the charge of an electron and only considers majority charge carriers. $v$ is the relative speed between electrons and holes. As seen in the second term of Equation (2.2), the change in current is dependent on the temporal changes in charge carrier density, which is induced by the laser pulse and therefore depends on the incident optical power. This part of the term is much larger than the contribution of the charge carrier acceleration and dominates the equation. Nevertheless, as this dominating term part linearly depends on the carrier drift velocity, there is also a proportionality to the applied bias between the antennas.

## 2.2.3.2   Detection of THz Radiation with Electro-Optic Sampling

While many commercial systems, especially 1.55 $\mu$m fibre-based ones, use PCAs for detection, electro-optic sampling (EOS) via a birefringent crystal is still a popular detection method for self-built systems. EOS offers a few advantages over photoconductive detection, such as higher bandwidth or a flatter frequency response, since the birefringence is reasonably constant over the relevant frequency range. From an experimentalist's point of view in a lab that produces its own PCAs, electro-optic sampling is the more robust method. Small changes in characteristics between different PCAs are unavoidable, given the small volume batch process which is used for self-made antennas. Finally, the smaller active area in the order

of tens or hundreds of micrometres compared to the millimetre-sized birefringent crystal makes PCAs more amenable to be influenced by the environmental conditions which cause the laser beam to drift. Therefore, the Durham University uses electro-optic sampling.

Electro-optic sampling exploits the Pockels effect to change the birefringence of a crystal-induced by the incident THz radiation. The Pockels effect describes a change in refractive index of a medium in linear proportion to the strength of an applied optic field. The effect only occurs in noncentrosymmetric crystals [45]. The thus obtained change in refractive index can be approximated by

$$n(E) \approx n - \frac{1}{2}n^3 r_{Pockels}E^2,$$ (2.3)

where $r_{Pockels}$ is the Pockels Coefficient [46]. ZnTe is the preferred traditional material for the birefringent crystal because of its high signal to noise ratios [47]. The complete backend for the electro-optic detection consists of the birefringent ZnTe crystal, a quarter wave plate, a Wollaston prism and two balanced photodiodes, as illustrated in Figure 2.10. The linearly polarised probe beam passes through the ZnTe crystal, which changes the polarisation to elliptical. The probe beam then passes the quarter-wave plate and the Wollaston prism, where it gets split up into two beams with horizontal and vertical components, as such is the nature of a Wollaston prism, and each beam hits one photodiode. The quarter-wave plate is used to compensate so that the photodiodes are balanced when no THz radiation is present. During a measurement, the incident THz radiation changes the birefringence of the ZnTe crystal and therefore the polarisation of the probe beam, resulting in unequal intensities for the horizontal and vertical polarised split beams, which throws the photodiodes out of balance, causing a change in current. The difference in photocurrents is sent to a transimpedance amplifier, which produces an output voltage proportional to that difference.
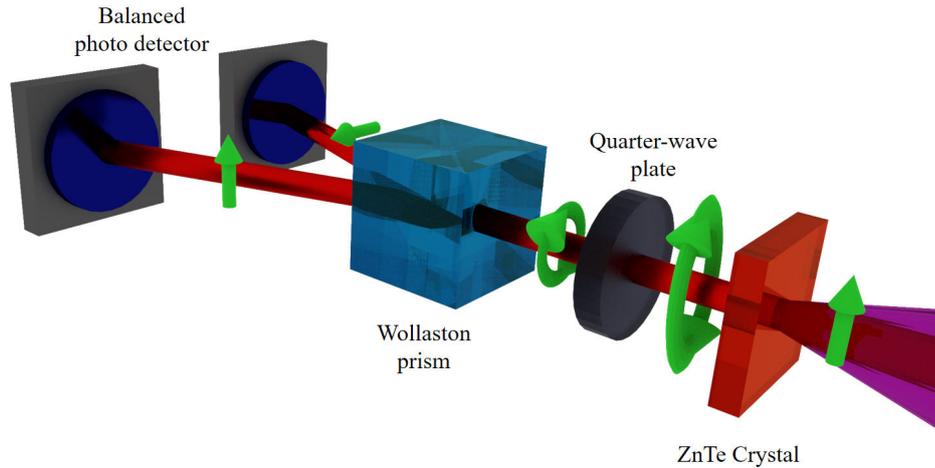
Figure 2.10: Illustration of electro-optic sampling as used in the Durham THz-TDS system. The incident THz beam (purple) is focused on the ZnTe crystal (orange). The coaxial propagating laser beam (red) is changed in polarisation by the THz beam. The quarter-wave plate (grey) is used to balance the intensity between p- and s-polarisation. The Wollaston prism (blue cube) splits the elliptical polarised laser into p- and s-polarisation.

### 2.2.3.3   THz-TDS Setup

The previous subchapters contain all information about how to generate and detect THz radiation. Therefore this section explains how the complete setup, as seen in Figure 2.11, operates and how the THz pulse is reconstructed in the time domain.

After exiting the laser, the beam is split into two; the probe beam for detection and a pump beam which is used to generate the THz radiation. Only a small fraction of the laser power is required for detection, as the sensitivity of the balanced photodetectors are high. Additionally, it is desirable to maximise the amount of power for the THz generation as shown in Section 2.2.3.1. Therefore a 90/10 beam splitter is used, leaving 90% of the optical power to be used for THz generation. The probe beam is directed towards the optical delay line, which is a motorised stage with two mirrors on it. By changing the position of the mirror pair, it increases the optical path length and therefore delays the laser pulse. The delay line stage is 15 cm long and thus provides a delay of 30 cm in the optical path which corresponds to a time delay of 1 ns. The positioning has micrometre precision which
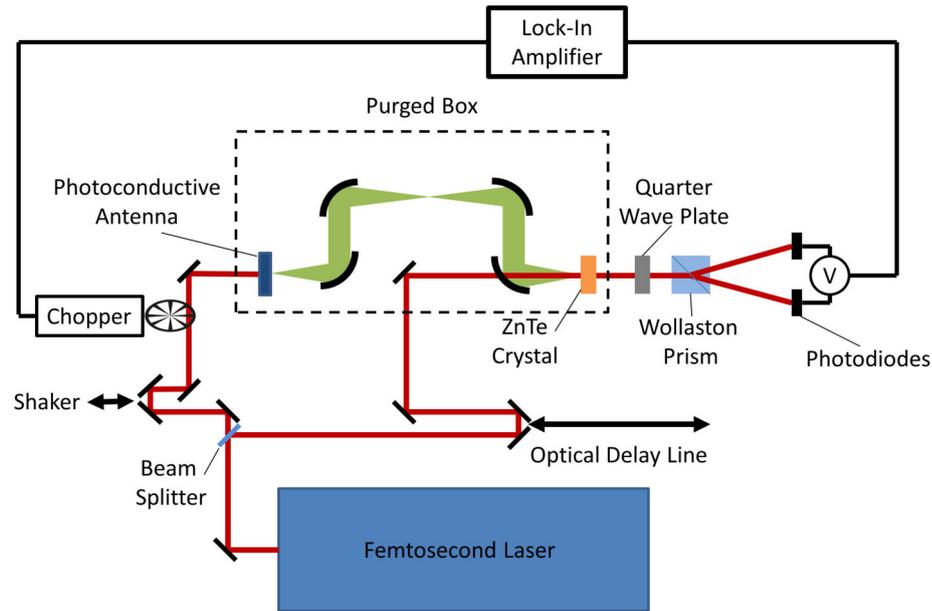
Figure 2.11: Schematic of the Durham Engineering THz-TDS system.

results in subpicosecond temporal resolution since 1 picosecond corresponds to 300 micrometres. Subsequently, the laser beam is directed towards the ZnTe crystal for the detection via electro-optic sampling.

After the beam splitter, the pump beam is directed to the shaker (APE scanDelay 50). A shaker is an opto-mechanical device which introduces an optical delay, just as the delay line does, but with periodic movement and a much smaller deflection, commonly less in the order of one centimetre or less. In case of the used shaker, the maximum scan range is $\pm 3.75$ mm. Commonly a deflection of $600\,\mu$m with a frequency of $1\,Hz$, the lowest available frequency, is used. This small change in optical path length is very useful during the necessary daily alignment of the system. However, the positioning of the shaker is imprecise, only few points can be acquired, and the small deflection only allows visualisation of the main pulse. Therefore, the shaker scan is not useful for full-fledged spectroscopy as the spectral information following the main pulse is not recorded. Nevertheless, the reconstructed signal can be used to extract the electric field amplitude. This can be used for THz imaging, and the maximisation of the amplitude is part of the necessary daily alignment, making the shaker a handy tool for daily maintenance of the system; the changes

are displayed within seconds, in contrast to minute long scans with the optical delay line. The next component in the beam's path is the optical chopper, which provides the necessary reference signal for the lock-in amplifier. Afterwards, the laser beam is focused on the PCA's gap and the THz radiation is generated. The THz radiation is then directed by parabolic mirrors. The samples can either be placed in a parallel section of the beam, between mirrors 1 and 2 or 3 and 4, or in the focal spot of the THz beam, between mirrors 2 and 3. The THz beam is then overlapped with the optical probe beam at the ZnTe crystal for the electro-optical sampling. The part of the setup where THz radiation is present is in a nitrogen purged box to avoid the absorption of water vapour [48].

The THz measurement itself works as follows: The optical delay line changes its position and therefore delays the pulse in time. At each step, the readout of the lock-in amplifier is recorded as a function of the delay line's position, and since the position in space corresponds to a delay in time, the data is recorded in the time domain. When the optical path length of the probe beam and the THz radiation beam are equal, the THz pulse and probe pulse overlap in time. Since the probe pulse is several magnitudes of order shorter than the THz pulse, the induced change in refractive index in the ZnTe crystal by the THz radiation can be seen as static for the probe pulse. By stepping multiple times the complete THz pulse can be reconstructed. Since the change in refractive index is linearly dependent on the incident THz radiation, the obtained signal is a direct measurement of the complex electric field of the THz pulse.

## 2.2.4 Optical Profilometer

A Talysurf CLI 2000 3D optical profilometer is used. The Talysurf is a scanning surface topography instrument where the workpiece is moved under a stationary chromatic length aberration gauge head. White light is directed through a chromatic aberration lens onto the surface. Due to the chromatic properties, only a certain wavelength will be in focus at any point, depending on the distance between

lens and workpiece. The light is reflected from the surface to a pin hole which only allows the wavelength in focus to pass through. A spectrometer grating deflects the light onto a CCD sensor to interpolate the spatial position of the data point. By changing the focal distance to the workpiece, different wavelengths are addressed. The vertical and lateral resolution are $10\,\text{nm}$ and $10\,\mu\text{m}$ respectively.

## 2.3   Finite-difference time-domain Simulation

Finite-difference time-domain (FDTD) is a numerical analysis technique, which is based on finding approximate solutions to Maxwell's equations. The most common algorithm [49] replaces the derivatives in Maxwell's equations with finite differences. Space and time are discretised so that a staggered grid results both in time and space. The electric and magnetic fields are calculated in alternating turns. The resulting differences are updated every time step so that the simulation ideally converges to a solution.

From the description of the algorithm, it is obvious, that it is an intrinsic property
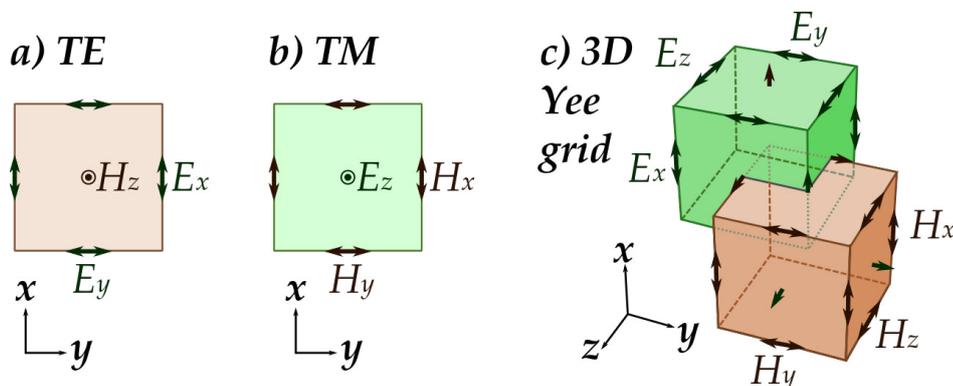


Figure 2.12: Illustration of the Cartesian Yee cell used in most FDTD solvers. The cubic voxels for the electric (orange)) and magnetic (green,) with their field components which form the edges of the cubes, which also form the normals to the faces of the respectively other cube (a/b). c) The staggered arrangement of the two cubes which form the 3D Yee grid. From [50].

of the method that the simulation can demand a large amount of computational resources since the information of every mesh point at every time step have to be saved and updated with time. This also explains while the method became increasingly popular since the 90s, given the exponential rise in computational power available. However, there are also advantages coming with the technique, the major one being that the method can be applied to all kinds of structures and has virtually no limitations or requirements to the shape of the simulated objects. This is in stark contrast to other popular methods, such as Eigenmode expansion, which

is very efficient when periodic structures are simulated that only possess a small number of Eigenmodes due to periodicity or symmetry, but usually are less efficient to find a solution for structures without or broken symmetry. This advantage of the FDTD method is utilised in this work because even if periodic structures are investigated, such as photonic crystals, the limitations of the available fabrications methods result in so-called photonic crystal slabs. These are periodic structures which deviate from the theoretical model of an infinitely extended structure in at least one dimension, by limiting its extension to the order of a few wavelengths and therefore breaking the symmetry that would benefit other electromagnetic solver methods. However, it has to be mentioned that periodic structures, or more generally resonators, are not the traditional strong suit of FDTD simulations since a common approach to set the simulation time is to observe the stored energy in the simulation region and wait until the majority of it has dissipated, meaning that the simulation converges towards a result. An additional advantage of the FDTD model is that it works in the time-domain, as in contrast to the frequency domain of other methods, which provides the possibility to compare the results directly with the measurements of the THz Time-Domain Spectroscopy system and, also as a result of using the time domain, the simulated response is a broadband result, covering a frequency range matching with the available experimental characterisation methods in a single simulation.

A commercial simulation software called Lumerical FDTD is used in the version 2019b R6. The fundamentals on how to set up FDTD simulation in general, and Lumerical FDTD specifically, can be found in the appendix. Here the validation of the results is in focus, to show that the commercial FDTD software is a suitable tool to design THz components.

## 2.3.1 Validation of FDTD simulation for THz application

The validation of simulation results can be achieved in different manners with different levels of strength of the validation. One possibility to validate a simulation is to compare it to the results of a different simulation method, which would be a weak validation as long as this simulation method is not proven to produce accurate results with other validation methods. A stronger validation method is to compare the results to theory based on fundamental equations, but this has the downside that often only simple cases which wouldn't necessarily need simulation can be validated in this manner in the first place. Another possibility is the validation with experiments. As long as the experiments allow to measure the same quantity that is simulated, the validation is straightforward.

Here the results of the FDTD simulation are validated at the example of the dielectric materials based photonic crystals.

While a comprehensive theory for photonic crystals exists[51], some photonic crystals designed in this thesis are based on already existing photonic crystal waveguides [52], so the results can be compared to measurements existing in literature. Additionally, one of the photonic crystal waveguide cavity has also been produced by collaborators in Osaka University, therefore allowing for a direct comparison with experimental results.

Figure 2.13 shows the comparison of a simulated and a measured photonic crystal WG. The measured and simulated lower cut-off of the waveguide at 0.315 THz are in excellent agreement; the higher cut-off is outside the frequency range of the instrument. Both curves are in good agreement at the low-loss region at 0.32 THz, which has been identified as the preferred region for waveguiding [52]. The curves deviate for frequencies above 0.33 THz, but this can be explained by the short length of the waveguide that has been characterised. Additionally, the measurement suffers from standing waves which can influence the spectrum.

The comparison of measurement and FDTD simulation for a photonic crystal cavity is shown in Figure 2.14. The centre frequency and full width at half max-
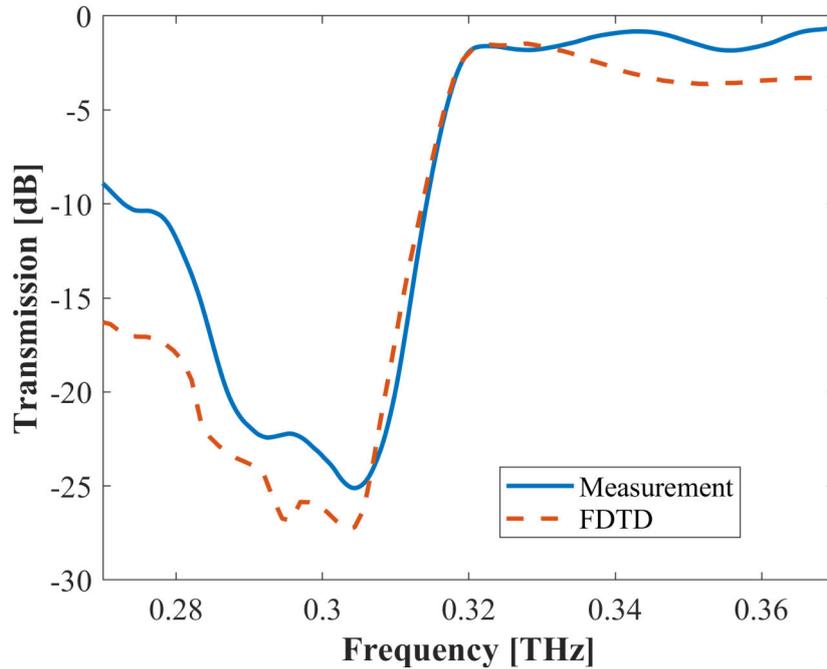
Figure 2.13: Comparison between the measurement and FDTD simulation of the lower cut-off of a photonic crystal waveguide. The cut-off frequency of measurement and simulation are in excellent agreement. Above the fundamental waveguide mode at 0.32 THz, the curves deviate slightly, probably due to standing waves in the measurement setup.

imum (FWHM) for the measured and simulated data are 336 GHz and 3.8 GHz and 336 GHz and 4.6 GHz respectively. This excellent agreement shows that the FDTD simulation can be used to design resonant dielectric THz components. The discrepancy in FWHM can be explained by the limited time of the simulation, as the simulation automatically stops when the majority of the energy is dissipated , hence not all intensity is captured for high quality factor resonators.
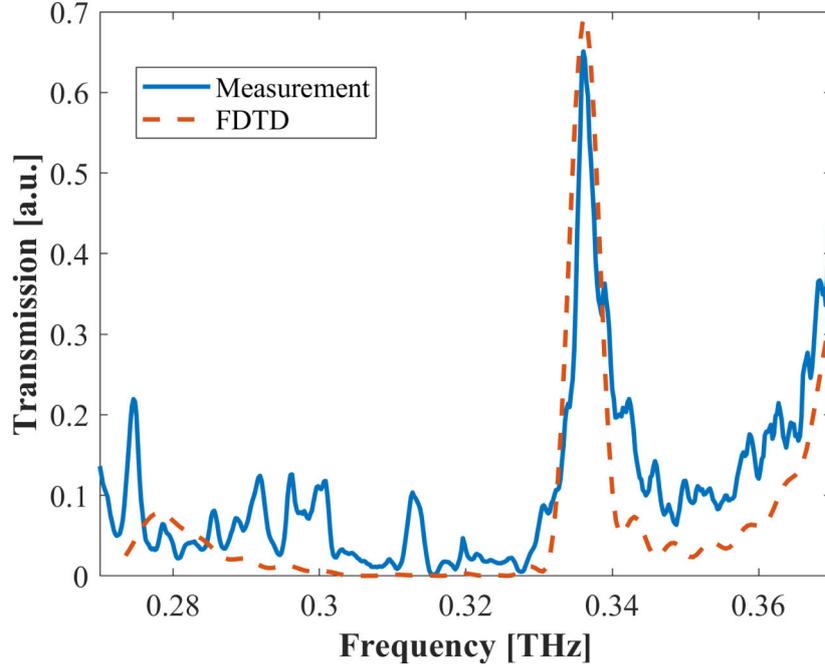
Figure 2.14: Comparison between the measurement and FDTD simulation of a photonic crystal waveguide cavity. The resonant frequency of both measurement and simulation is at 336 GHz, and the FWHM is in close agreement as well with 3.8 GHz and 4.8 GHz, respectively.

## 2.4 Summary

All relevant fabrication, characterisation and design techniques used in this thesis were discussed. The precision of the four fabrication methods (photolitography, CNC Micro-Machining, 3D printing, and laser cutting) are addressed. While photolitography offers excellent lateral precision, it also offers the lowest flexibility for medial variations and is the most elaborate and costly of the presented methods. CNC Micro-Machining offers significantly more freedom in 3D forming of surfaces than photolitography, but the required feature sizes in the order of tens of micrometres do push the limits of possible tool sizes, making the technique less desirable with increasing frequency, as feature size decreases with frequencies. While 3D printing offers the highest flexibility in 3D fabrication of the four techniques, it is shown that commonly used resins for SLA printers are unsuitable dielectric mater-

ials for THz components due to the large attenuation. But 3D printed components can be metal coated to produce metallic THz components. Laser cutting allows only lateral structuring, similar to photolitography, of polymers. These polymer can be chosen to have a sufficiently low absorption to be suitable as dielectric THz components, but melting of plastic limits the minimum feature size which again makes it difficult to produce components for higher frequencies towards 1 THz. Details of the experiments and particularities of the simulation of certain components are discussed in the respective chapters itself for clarity. FDTD simulations as the main design tool in this thesis have been introduced and the suitability for the simulation of THz components has been validated with the comparison between simulated and experimentally characterised photonic crystals. The comparison has shown good agreement between the simulated and experimentally determined low-loss waveguiding region of a photonic crystal and excellent agreement with a deviation of $\ll 1\%$ in the centre frequency of a photonic crystal resonance and approximately 20% difference in FWHM.

# Terahertz Optical Components

While THz photonic structures are necessary to enable integrated systems, there is still a need for traditional optical components. THz optical components have applications in the coupling and manipulation of radiation, and beamforming. While the number of commercial suppliers of THz components is ever-increasing, many components, such as bespoke lenses, prisms or wave plates for phase retardation are not readily available. These components can be only purchased with extremely high prices compared to optics for other parts of the electromagnetic spectrum and they often have long lead times.

Therefore, for research purposes, it is convenient to find means to produce components in-house or demonstrate alternatives that can be easily adapted in the industry in the future to reduce component prices and increase availability. In this chapter, multiple alternatives to currently commercially available components with innovative materials and manufacturing techniques are presented. First optical components made out of a machinable ceramic are discussed and its capabilities by producing a microstructured optical component, a Fresnel lens, and a bulk component, a prism, are discussed. Afterwards, low-cost wave plates produced with 3D printing and laser cutting are presented.

## 3.1 Machinable ceramic for high performance and compact THz optical components

Currently used THz optics can be classified as either high performance, such as high-resistivity float-zone silicon or low cost, such as HDPE, ltra-high-molecular-weight polyethylene (UHMWPE), and wax polymers. While HRFZ-Si has very low absorption and a high refractive index [53], it is also expensive, brittle and requires elaborate and expensive techniques to produce complex shapes [54]. Therefore, whilst silicon lenses are commonly used, for example in THz Time-Domain Spectroscopy systems (THz-TDS) [55], the limited shaping capabilities usually require some adjustment to the components,such as using a stack of wafers as spacer [56] or many processing steps if semiconductor manufacturing is used [57]. Conversely, the low-cost materials that can be readily shaped using traditional subtractive manufacturing techniques, in addition to 3D-printing, also have a low refractive index ($n \approx 1.2-1.8$ [58]) which results in less compact optical components. Such materials are also not very resilient to being scratched or exposed to large temperature ranges, making them less suitable for some real-world applications. Wax materials have only been successfully used in laboratory environments [59] with, bulky high dynamic range measurement systems, e.g. THz-TDS, which can overcome significant losses within the optical components. Similarly, the use of more exotic components, e.g. based on oil, which has good optical properties at THz frequencies, will probably remain limited to laboratory environments due to practicality issues [60].

Here an alternative material option is presented, an aluminium-nitride (AlN) based ceramic, tradename Shapal Hi-M Soft, which is shown to have a relatively high refractive index ($n = 2.65$) within the THz region, reasonably low losses ($\alpha < 1\,cm^{-1}$), and is compatible with standard subtractive manufacturing technologies, making it suitable for high performance, compact optics. Additionally, the low absorption and high refractive index make Shapal an interesting altern-
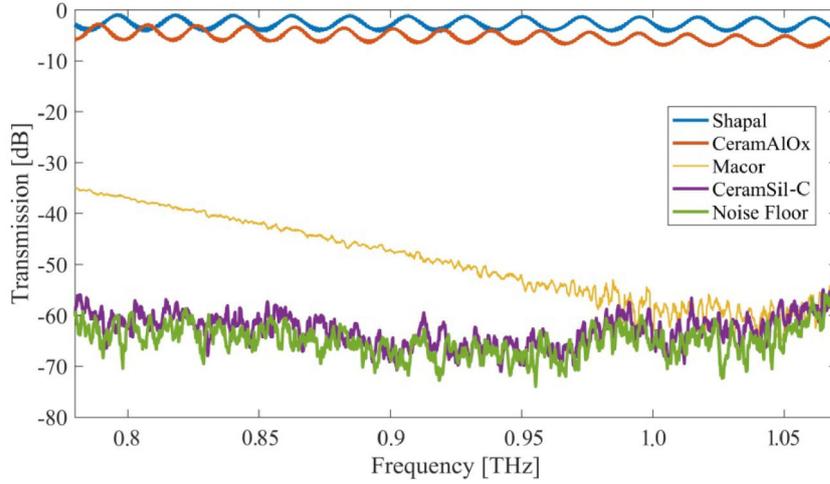
Figure 3.1: THz transmission spectra of the ceramics listed in Table 1, measured with the THz VNA. Both Macor and CeramSil exhibit very high losses in this region, and there is no measurable transmission through silicon carbide Shapal and CeramAlOx both exhibit low absorption in the frequency range around 1 THz. Sample thickness for all materials was 2.54 mm.

ative material for traditional components, where even fundamental components like prisms made of HRFZ-Si often cost thousands of USD could be offered for a fraction of the price when made from a ceramic alternative. The ceramic will be compared to commonly used materials for THz optics, such as HRFZ-Si and polymers, and other ceramics with regards to the refractive index, optical losses and shaping capabilities. As for the shaping capabilities, this work focuses on machinability using general purpose tools and machinery, as this is the most commonly available method of fabrication. Furthermore, avoiding highly specialised manufacturing techniques is most likely necessary for a material to have commercial success. A range of commercial available ceramic materials is tested which can be found in Table 3.1.

All measurements were taken in an environment maintained at standard temperature and pressure conditions: 21°C, 7% relative humidity. Samples were placed in an oven at 100°C for one day at reduced pressure (<0.1 Bar) to remove any humidity within and measured directly afterwards. A second measurement after storing the samples at the previously mentioned ambient conditions for several days did
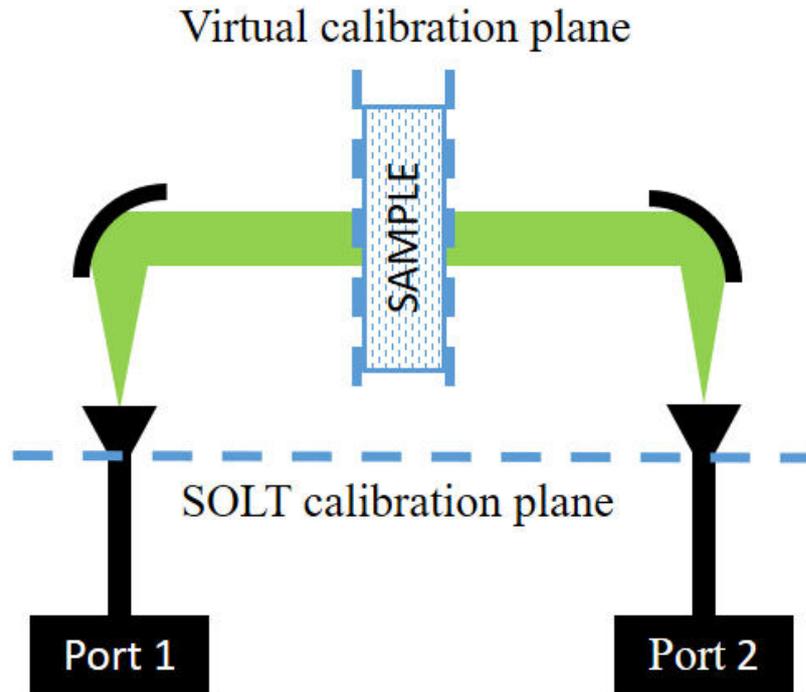
Figure 3.2: Schematic of the measurement setup. The system is calibrated up to the waveguides with the SOLT calibration kit. The free-space part of the system is calibrated with a numerical de-embedding process up to the virtual calibration planes. This method allows an improved precision by a factor of almost 50 when compared to a closed-form extraction technique.

not show any differences in transmission, and thus, despite being hydrophilic like most ceramics, the water content absorbed in the material appears to be negligible. The Durham Engineering THz-TDS system was used for an initial broadband characterization to give an impression of the material performance at higher frequencies, but as THz-TDS has a larger uncertainty for low attenuation coefficients [21, 61] the full characterization was only conducted with the THz VNA.

Table 3.1: Composition and material properties of the ceramic materials under test and other ceramics and THz optical materials from literature.

| (Trade) Name | Composition | Machinable | Refractive Index (n) | Loss Coefficient (@1 THz) $[cm^{-1}]$ |
|---|---|---|---|---|
| Shapal | $71-74\% AlN$, 26% BN, various impurities [62] | Yes | ~2.65 | ~0.4 |
| Macor | $46\% SiO_2, 17\% MgO, 16\% Al_2O_3$, 10% $K_2O, 7\% B_2O_3, 4\% F$ [63] | Yes | NA | >30 |
| CeramSil-C | $SiC$ | No | NA | >20 |
| CeramAlOx | $Al_2O_3$ | No | ~3.1 | ~1.8 |
| Alumina from [64] | See reference | No | ~3 | ~1 |
| Boron Nitride from [65] | Various, see reference | No | ~1.97-2.15 | 1-3 |
| Aluminium Nitride [65] | See reference | No | ~2.92 | ~0.5 |
| Low-loss polymers from [66] | See reference | Yes | ~1.45-1.6 | ~0.5-2 |
| HRFZ silicon from [53] | See reference | No/limited | ~3.42 | <0.05 |

The refractive indices for the tested materials, as shown in Table 3.1, have been determined with the method described by Hammler et al. [67] and briefly introduced here. The s-parameters are recorded with the setup shown in Figure 3.2. First, the s-parameters are measured in the absence of the sample to move the measurement plane to the sample surfaces computationally. This de-embedding process does not require exact knowledge of the systems geometric lengths. An iterative method is used to determine sample thickness and electric permittivity simultaneously.

The attenuation coefficient, $\alpha$, was determined by measuring the transmission dependence upon material thickness, as can be seen in Figure 3.3. Unprocessed samples, with flat and smooth parallel faces, were pressed into stacks after having been individually cleaned. An exponential fit (all with $R^2 > 0.95$) at each individual frequency leads to $\alpha$ for the corresponding frequency. Fabry-Perot resonances are addressed by only using the transmission maxima and interpolating between them in the valleys caused by the resonances. In theory, this could result in the loss of information, for example feature like sharp absorption peaks, but as the spacing between resonances is approximately 15 GHz, as can be seen in fig. 3.1, and the resonances occur at different frequencies for each thickness, this possibility can be neglected. $\alpha$ is found to be 0.40±0.04 cm$^{-1}$ for Shapal at frequencies of 1 THz, which is consistent with the previously reported values for AlN and BN individually [65]. The attenuation of CeramAlOx is determined in the same way to be ~ 1.80±0.18 cm$^{-1}$, which is consistent with the values for alumina [64].

### 3.1.1 Micromachining of Optical Components

Initial starting points for machining parameters for larger features (>1 mm) for Shapal can be obtained from the datasheets of the material [62, 63] and tooling, but no information is available about machining with tools in the order of tens or hundreds of microns, as is required for THz optics and photonic applications. Micro-milling can be used to realise micro-structured components such as Fresnel lenses. Due to the higher refractive index, the components can be thinner than
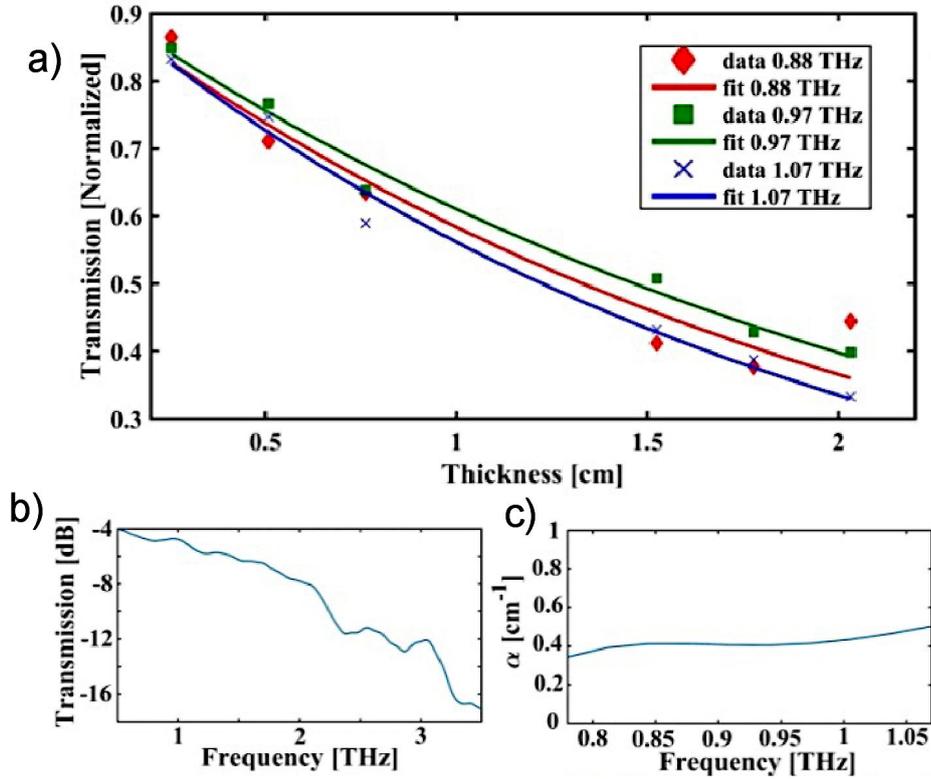
Figure 3.3: a) Signal attenuation at three different frequencies, plotted against material thickness allows extraction of the attenuation coefficient, shown in b), from exponential fit lines. c) The broadband THz-Time-Domain Spectroscopy scan shows little attenuation to well beyond 1 THz.

comparable ones made from plastic.

To demonstrate the shaping capabilities of Shapal, a continuous Fresnel lens is machined with a nominal diameter of 11.2 mm on top of a 12.7 mm thick slab that focuses the incident THz radiation to the bottom face of the slab. Finite-difference time-domain simulations using the measured material properties show a -3 dB focal spot of around 190 $\mu$m width in the design. The lens was designed using the lensmaker equation for a hemispherical lens and a modulus was used to introduce a step size of 198, $\mu$m [68]. The simulations were conducted as a 2D simulation because a 3D simulation of the full-scale component requires significant computational resources. To account for the effect of polarization, the polarisation of the incident radiation was rotated by 180° in 1° steps and the electric field summed up. Perfectly matched layers were used as boundaries.

First, a pocket was created in a sacrificial bed on the CNC micro-milling machine,
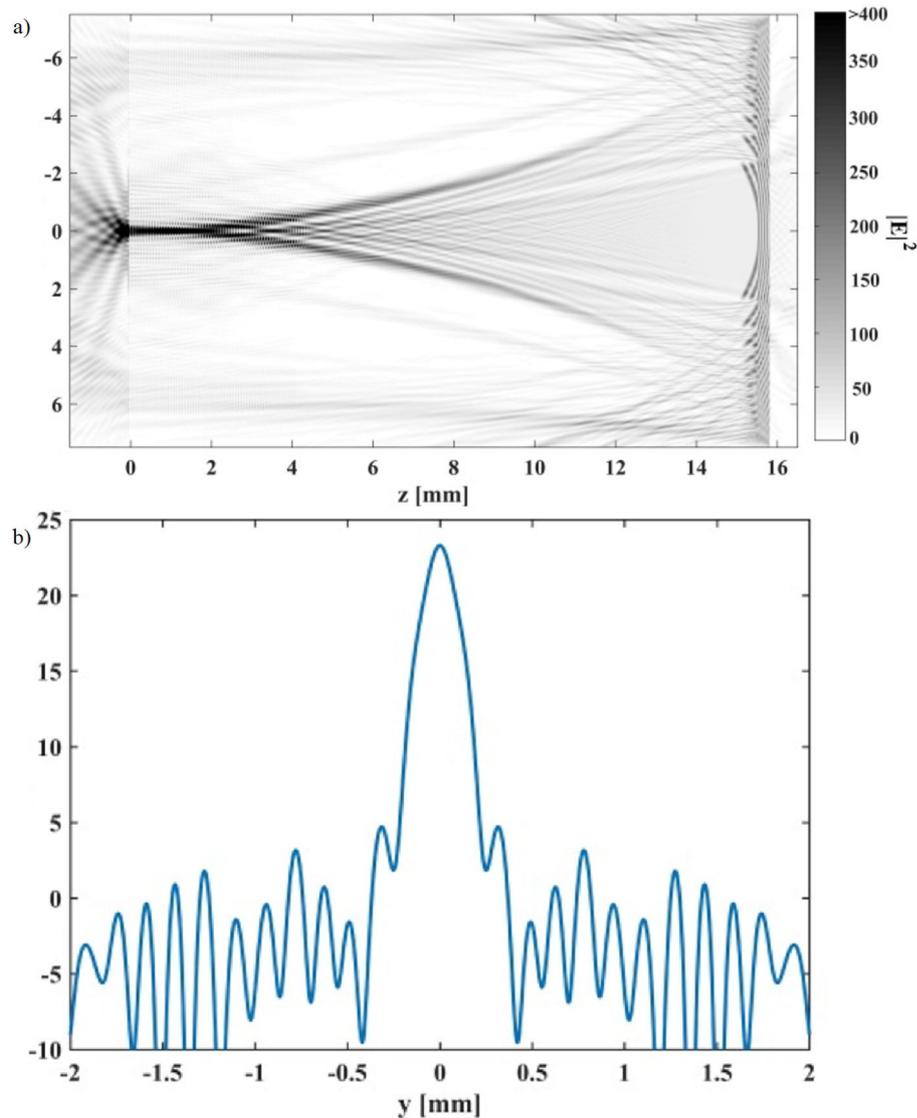


Figure 3.4: a) FDTD simulation shows that the THz radiation, coming from the right, propagates along the z-axis and is focused at the bottom of the structure on the left. b) A planar slice of the electric field intensity $50\,\mu$m below the surface shows a -3 dB focal spot width of $190\,\mu$m.

to which the stock material was firmly attached. A coordinate system was established and the operations in Table 3.2 were performed.

All operations used a $12°$ spiral lead-in, where appropriate, to reduce thrust forces during plunges and prevent tool breakage. The spindle speed was fixed at 40,000 RPM, with a feed rate of 30 mm/min. All tools used were endmills, due to the unavailab-

Table 3.2: Machining operations for Fresnel lens prototyping. The machine uses a spindle speed of 40,000 RPM, a feed rate of 30 mm/min and has a compressed air/low viscosity mineral oil/WD-40 mist as coolant.

| Step | Description | Tool Diameter (mm) | # Tools Used | Axial Depth of Cut Increment (mm) | Stepover |
|---|---|---|---|---|---|
| 0 | Bed pocket | 3.0000 | 1 | — | — |
| 1 | Roughing horizontal raster | 0.2032 | 2 | 0.300 | 0.9D = 0.183 mm |
| 2 | Roughing vertical raster | 0.2032 | 2 | 0.300 | 0.9D = 0.183 mm |
| 3 | Roughing waterline | 0.0760 | 1 | 0.050 | 0.6D = 0.046 mm |
| 4 | Finishing waterline | 0.0300 | 3 | 0.015 | 0.45D = 0.014 mm |

ility of economical ballnose/bullnose cutters, at the detriment of the surface finish of the lens. Finishing toolpaths were machined with Zecha 596.030.0003 endmills. A micrograph of the finished component is in Figure 3.5. Surface finish and uniformity of the finished lens structure would be improved by being performed on a machining centre equipped with a rotary axis to tilt the tool and another to spin the lens, however it serves as a demonstration of a realisable prototype manufactured with a general-purpose machine.

Addtionally, the fixed speed air spindle in the bespoke Durham system has a rotational speed which is around an order of magnitude too high for the tool sizes required for THz components with 40000 rpm. Therefore, the surface quality of the manufactured components is relatively poor and rough edges and tool marks are clearly visible. Therefore, components with features in the order of tens of micrometres, such as THz spoof plasmonic structures, could not be manufactured at all.

The Fresnel lens was then cleaned with compressed air and acetone. Afterwards, the lens was characterised using the THz vector network analyser in the following configuration: the radiation from the transmitting antenna is collimated with an off-axis parabolic mirror and directed towards the lens. The receiver is mounted on an xyz stage assembly and scans the planes perpendicular to the beam direction. The receiver's horn antenna has a 3 dB half angle of 10° and a beam waist

Figure 3.5: Scanning electron micrograph of a prototype Shapal Hi-M Soft Fresnel lens.

radius of 0.66 mm, therefore the effective minimum detector size is ∼1.3 mm. A scan of the xy plane at the front face of the lens serves as a reference. To find the focal spot, multiple xy scans were taken with a z-step of 300 $\mu$m, starting at the bottom face of the lens. The focal spot is determined by measuring the extrapolated average diameter of the 3 dB attenuation contour line. Figure 3.6 shows the intensity in the focal plane. The smallest measured focal spot was captured with an xy step size of 300 $\mu$m at a distance of 1.2 mm from the sample surface. Nevertheless, the focal spot is measured to have a diameter around 200 $\mu$m which is in good agreement with the simulations, with the only discrepancy being that the focal spot was found at a distance of 1.2 mm from the surface rather than directly below the surface, which can be attributed to an incomplete removal of material as the tools have a finite diameter and therefore cannot produce the sharp discontinuities which occur at the steps where the modulus is applied. Each valley theoretically tapers to zero width at the root of a ring, however, the tool occupies a finite width. As the attenuation of the 12.7 mm thick block of Shapal is 5 dB and the measured intensity is approx. -2 dB in the focal spot corresponding to a net gain of almost 3 dB in intensity. The most challenging machining conducted was the drilling of 100 $\mu$m diameter holes to a depth of 1.3 mm, which can be used for structures like THz photonic crystals. The drilling operations required many pecking cycles, to facilitate chip removal at the extreme aspect ratio of 13. As seen in the micrographs in Figure 3.7, the machining produces a good finish with no
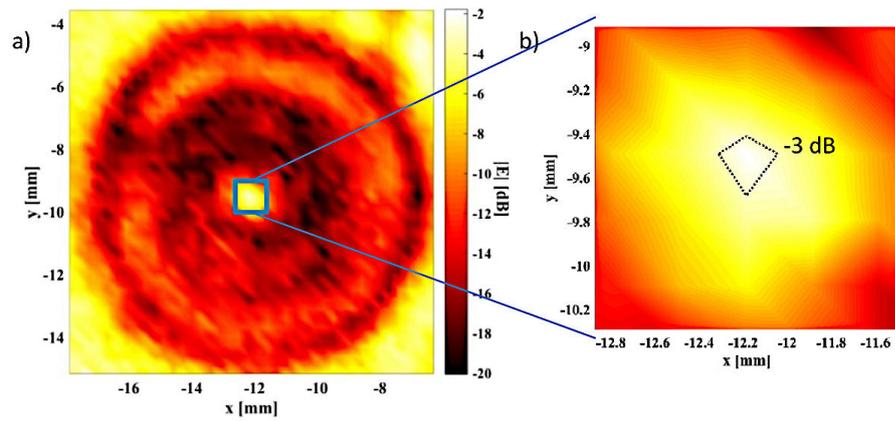
Figure 3.6: a) The measured intensity in the xy-plane, $1.2\,\mathrm{mm}$ below the lens' back face. b) Zoom into the centre shows a -3 dB focal spot size of around $200\,\mu m$ in width.

cracks, permitting the placement of holes with the high packing density required for photonic crystals. Thin walls of just $25\,\mu$m separate the holes. As can be seen in the higher resolution micrograph (Figure 3.7, Right) the sidewalls of the holes are smooth with the visible roughness originating from the grains of the ceramic material. This is, therefore, the best achievable surface finish. Since the grain size, measured in SEM micrographs, is less than 1% of the wavelength at 1 THz this will have no influence on the performance of the components.
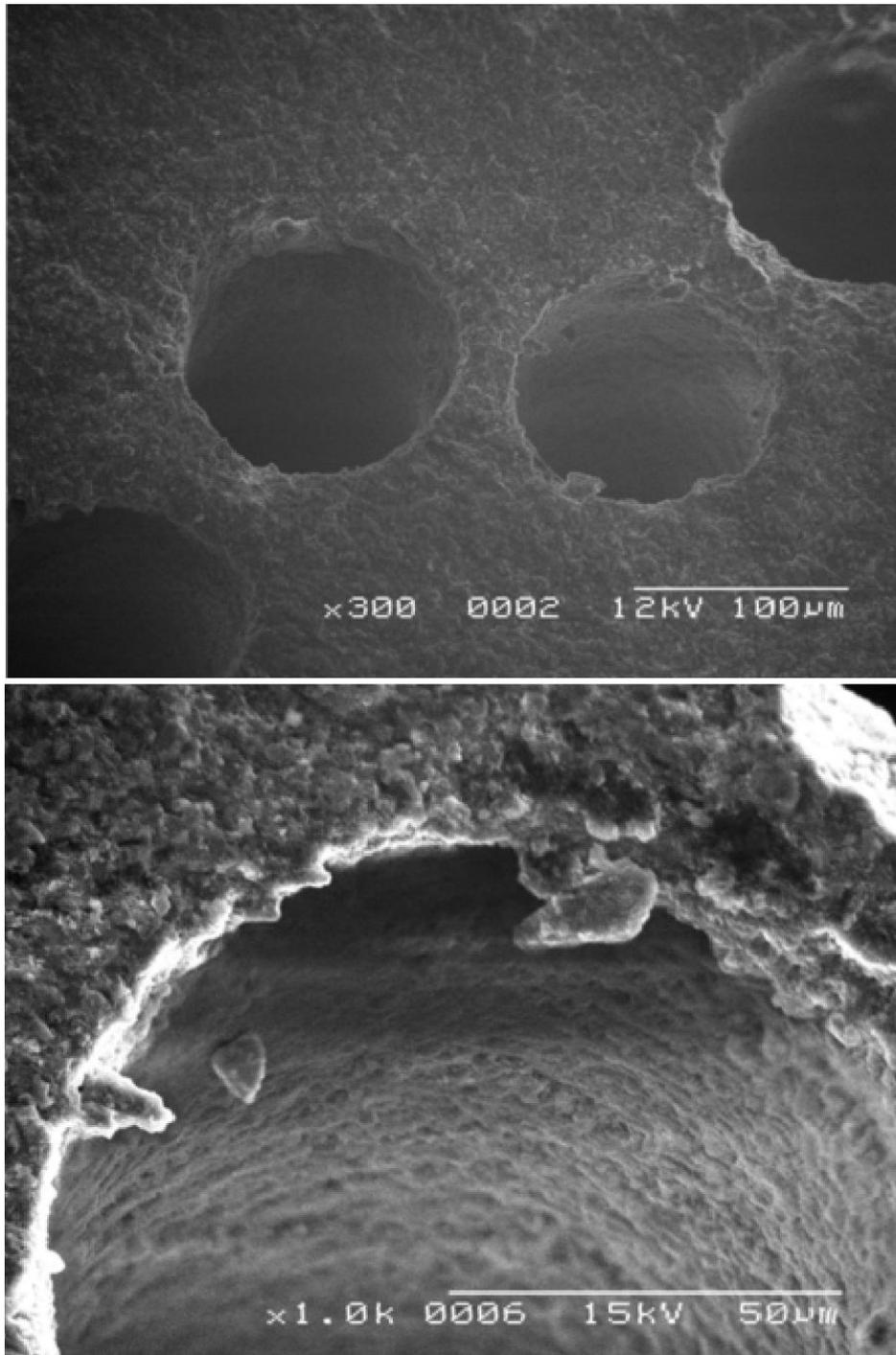
Figure 3.7: Top: Micrograph from an array of holes on a hexagonal lattice suitable for use as a THz photonic crystal. The thin sidewalls with no cracks on the surface show the high packing density required for photonic crystals, is possible. Bottom: Zoomed micrograph on the second hole from the right. The smooth sidewalls show the grain structure of the material and no machining marks are visible, proving the surface finish is of suitable quality for THz photonic components.

## 3.1.2   Traditional bulk components: Ceramic prism

For many optical components, such as lenses, the absorption of a material does not have a great impact on the performance of components as the optical path length (OPL) is only a few mm. This changes for bulk components, such as prisms, that often require an OPL in the order of cm. This means that the performance of the components is heavily impacted by material losses which is one of the reasons why standard optical components are still not as readily available for THz frequencies as they are for other parts of the spectrum. While prisms made from polymers such as PTFE do have a low enough absorption coefficient, their low refractive index results in a small operational range of angles and makes them less suitable for certain applications, such as prism coupling to plasmonic devices. The isosceles prism used here has a base length of 25 mm and a vertex angle of 90°. This prism is intended for Attenuated Total Reflection (ATR) measurements and, therefore, the incoming beam reflects from the base at most incident angles, thus most standard prism characterisation methods, e.g. measuring the minimum deviation angle, are impossible. As the requirements for a prism, such as size and shape, and, therefore, the optical path length, are highly dependent on the application, here the dispersion is demonstrated to show the function of the prism. The measurements have been conducted with the THz VNA in an angular setup, where the incident beam is kept at a fixed angle and the exit angle is scanned in $0.1°$ steps to find the maximum transmission for the respective frequency as shown in fig. 3.8.

The incident, collimated beam has a diameter of 5 mm and a slot aperture with a width of $\sim 2\,mm$ is used on the receiving side to increase the angular resolution. Figure 3.9 shows that over a range of 0.78–1.07 THz there is only an angular difference of $1.3°$, which reflects the low dispersion of the material.

While the calculation of the Abbe number, a measure for the dispersion of a material, is standardised in the optical region [69], there is no standardisation available at THz frequencies. However, it is possible to calculate the Abbe number in a similar way. As the ratio in wavelengths of the used Fraunhofer lines in the optical re-
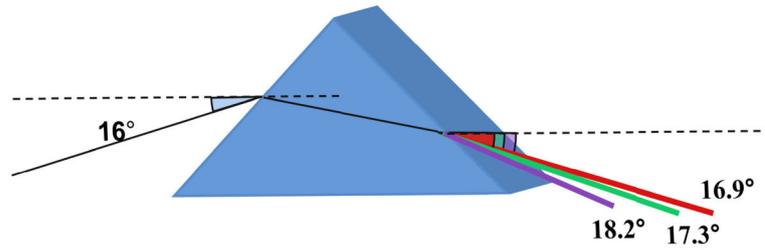
Figure 3.8: Schematic of the measured dispersion of the prism with the different refraction angles for 0.78 THz (red), 0.92 THz (green) and 1.07 THz (purple) indicated. The overall measured deflection through dispersion in the frequency range is very low with only 1.3° difference.
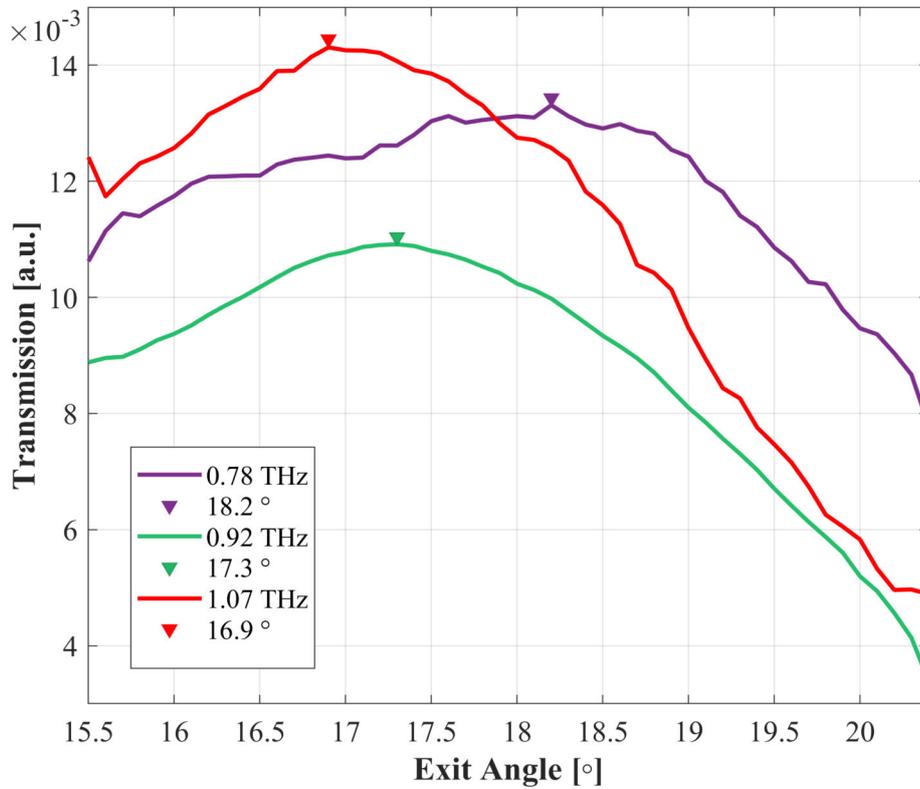


Figure 3.9: Angular resolved measurement of the ceramic prism at an incident angle of 16°. 2 mm slit apertures are used to increase angular resolution.

gion ($480\,nm/648.1\,nm \approx 0.74$) is similar to ratio of the wavelength available with the VNA ($280\,\mu m/384\,\mu m \approx 0.73$), the resulting Abbe number can be directly compared to those of prisms in the optical region as the span the same relative frequency range. To calculate the Abbe number, the refractive indices at the same frequencies for which the angles were measured are used as the long wavelength

(lowest frequency, 0.78 THz), centre wavelength (centre frequency, 0.925 THz), and short wavelength (highest frequency, 1.07 THz). The refractive is determined in the same manner as before, but this time using a 26.25 GHz window (which corresponds to 151 points of the 2001 measurement points for the whole instrument range) instead of the whole frequency range, and the equation for the Abbe number is

$$V_{e,THz} = \frac{n_{centre} - 1}{n_{long} - n_{short}} = \frac{2.64 - 1}{2.66 - 2.62} \approx 41. \tag{3.1}$$

With an Abbe number of 41, the material would be classified as flint glass, which is arbitrary defined for values up to 50 or 55, depending on the definition, and means that Shapal would be placed in the category of materials with a higher dispersion. However, it is worth mentioning that this classification is for materials in the optical region, which all have refractive indices below 2, and that there is a general tendency for the Abbe number to decrease with increasing refractive index, i.e. materials become more dispersive as their refractive index increases. As such, no crown glass (Abbe Number above 50 or 55) with a refractive index above 1.8 is available within the range of common optical materials and glasses with a similar Abbe number as Shapal, such as Lanthanum Dense Flint (LaSF31), have refractive indices of less than 1.9. Therefore, Shapal has a comparatively low dispersion for its high refractive index.

In summary, the low attenuation coefficient, high refractive index and low dispersion for its refractive index makes Shapal interesting for bulk components for coupling or spectroscopic experiments, where the used material of the optical components is intended to have as little influence on the experiment as possible.

## 3.2 THz Wave Plates

In this subsection, THz wave plates are discussed, which are optical devices that can alter the state of polarisation. An illustration of the principle of operation can be seen in Figure 3.10. After discussing the general principles of wave plates, the concept of high-contrast grating (HCG) is introduced as a possibility to realise broadband THz wave plates. This is followed by simulation and experimental results.

As with many standard optical components, wave plates for THz frequencies have limited availability. While there are commercial suppliers available that offer crystal-based broadband wave plates, they are made to order with long waiting times and are expensive. Therefore, finding a way to produce wave plates for the desired frequency range is desirable.

Waveplates are used to transform the polarisation state of radiation. They are optical components that introduce different retardation along one of their axes, the axes are therefore called the fast and slow axes, with the slow axis introducing larger retardation than the fast axis. Both axes are usually orthogonal to each other, and both axes are orthogonal to the direction of propagation as depicted in Figure 3.10. The two most common wave plates are quarter and half-wave plates. As the name suggests, a quarter-wave plate introduces retardation of a quarter of a wavelength on its slow axis while the half-wave plate introduces a half wavelength retardation. This means, quarter-wave plates can be used to change the polarisation from linear to circular and vice versa while a half-wave plate is used to rotate a linear polarisation by $90°$, changing it from p- to s-polarisation (and vice versa). The retardation itself can be introduced by different means. Non-symmetrical crystals can exhibit different refractive indexes along their different axes. If the thickness of the crystal is chosen carefully, this can introduce the desired difference in optical path length for the slow axis. As one can imagine, the difference in path length can only be achieved for a narrow frequency window. Therefore simple
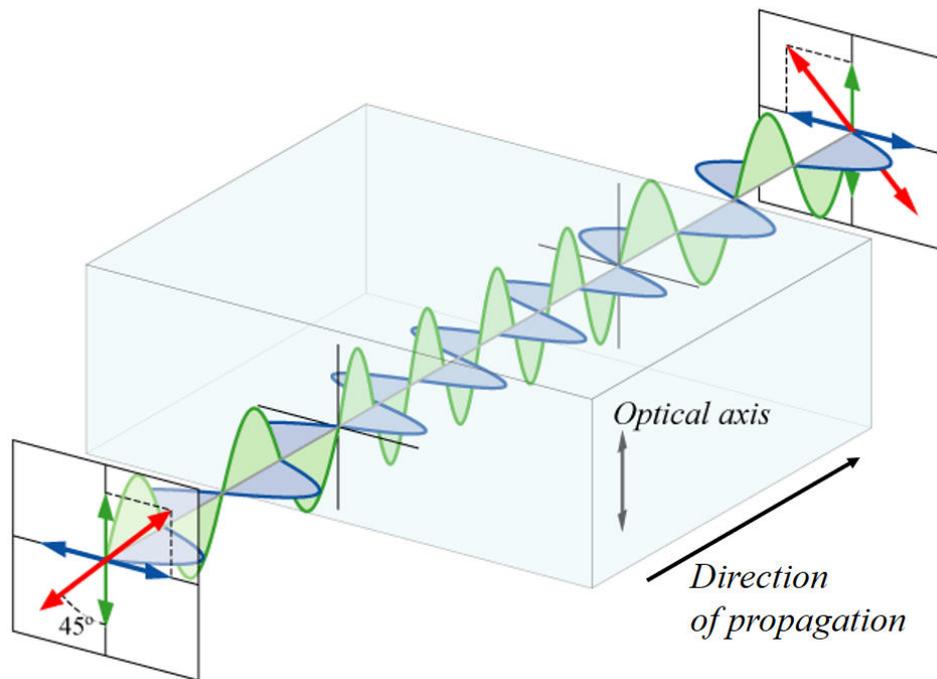
Figure 3.10: Illustration of the principle function of a wave plate. The incoming light is polarised at 45°when entering the crystal. As the light parallel to the optical axis propagates slightly slower through the crystal, the polarisation changes so that the polarisation is rotated by 90°when the light exits the crystal at its far side.From [70].

crystal wave plates have a single operating frequency specified. By using dispersive crystals, the frequency range can be extended, and broadband waveplates are made out of carefully matched stacks of different crystals so that uniform retardation is introduced over a broad frequency range [71]. An alternative and relatively new concept are HCGs [72]. While crystal plates have been available for decades and are used in classical optical experiments, HCGs are developed for integrated opto-electronics and can be as thin as 15% of the operation wavelength [72]. Gratings are very common optical components, but usually, gratings with a grating period either much larger than the wavelength or much smaller than the wavelength are used. HCGs operate in the regime in between, where the period lies between the wavelength in the material and the wavelength of the surrounding material. This fairly unexplored regime has been shown to produce compact components with high reflectance [73], selective transmission [74] or the possibility to produce waveplates

which depend on the geometry instead of the material properties [75] . Metamaterials have also been demonstrated as wave plates [76, 77]. However, by nature, metamaterials only operate in a narrow frequency range, making HCGs an attractive option for THz wave plates.

## 3.2.1 Physical Background

Optical gratings are well understood in the diffracting regime, where the wavelength is smaller than the grating period [78, 79] and the deep-subwavelength regime, where the wavelength is much larger than the grating period [80]. For near-wavelength gratings, the common approximations such as ignoring the electromagnetic field profile inside the grating cannot be used as for the previously mentioned regimes. A rigorous formulism exists for these gratings [81–83], and so do simpler analytic solutions for specific cases [84–86]. Demonstrated devices in literature are commonly simulated. Here, FDTD simulation are used for the design, therefore the behaviour is described phenomenologically, but a complete analytical formulation can be found in [72]. The main difference of THz HCGs to those demonstrated for significantly shorter NIR and optical wavelengths is that free standing, self supporting gratings can be fabricated. Therefore, the material contrast is between air and whichever material the grating consists of , making even lower refractive index materials like polymers suitable.

Figure 3.11 shows a schematic of an HCG. The structure is polarisation sensitive due to the one-dimensional periodicity. Incident light propagating in the z-direction with E-field polarisation along the grating bars are referred to as transverse electric (TE) and transverse magnetic (TM) if the field is polarised perpendicular to the bars. Only normal incidence is considered here for simplicity.

The bars of the grating can be considered as a periodic waveguide array along the z-direction. If a plane wave is incident waveguide modes are excited, which depend on the geometry and refractive index of the material. The near-wavelength dimensions and high index contrast cause only two of the modes ($TE_0$ and $TE_2$ and
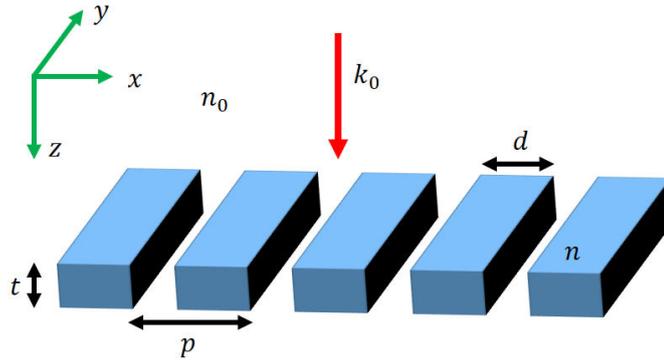
Figure 3.11: Schematic of an High Contrast Grating. A wave propagating in the z-direction is incident on top of the HCG. The grating extends quasi-infinitely into the y-direction and has a quasi-infinite number of periods in x-direction. The grating has a period between bars, $p$, the bars have a width, $d$, and a thickness, $t$. The contrast is between refractive indices of the surrounded air $n_0 = 1$ and the bar material, $n$.

$TM_0$ and $TM_2$, respectively) to have real propagation constants in the direction of propagation. The operational bandwidth is equal to this dual-mode region where the two modes overlap, as seen in Figure 3.12, and, as the refractive index contrast increases the spacing between modes, increases with the material contrast. The two modes will be reflected from the bottom face of the grating. The higher-order modes are below the cut-off when the grating is correctly designed and, therefore, will have the form of evanescent surface-bound waves. The modes obtain a phase difference while travelling through the grating which is dependent on the thickness of the HCG, making it one of the most important design parameters which also determines if an HCG acts as quarter- or half-wave plate. Due to the strong mismatch between the two guided waves, the reflections at the bottom surface do not only reflect back into themselves but also couple to each other. The same will occur with the reflection at the incident plane. Following the mode through a round trip leads to the solution of the reflectivity. At both surfaces, the modes also transmit out of the HCG, however, due to the subwavelength period only the zeroth diffraction order carries energy, which are plane waves. This purely zeroth-order behaviour is a significant factor that dominates the properties of the HCG.

To maximise reflection, the thickness of the HCG is chosen so that destructive

interferences occur at the exit plane, therefore cancelling transmission. For maximum transmission, the thickness is chosen so that the incident wave and reflected wave are in phase. A matched interference leads to spatial overlap of the waveguide mode with the incoming wave which is a complete impedance match, thus no reflection occurs. For high-Q resonators, the thickness is chosen such that constructive interference is obtained at both input and exit planes. In this case, the modes are strongly coupled to each other and a wave will propagate back and forth many times, resulting in a high-Q resonator. As for wave plates, the phase mismatch between the TE and TM modes has to be brought to the desired value while maximising transmission of both TE and TM modes. Since this is not a clear case of choosing the parameters to fulfil the required boundary conditions as for the components with maximum transmission or reflection, being a trade-off between the transmission for TE and TM modes while also maintaining the phase difference between the two, simulations are a more suitable approach for the design of such components rather than trying to find analytical solutions.
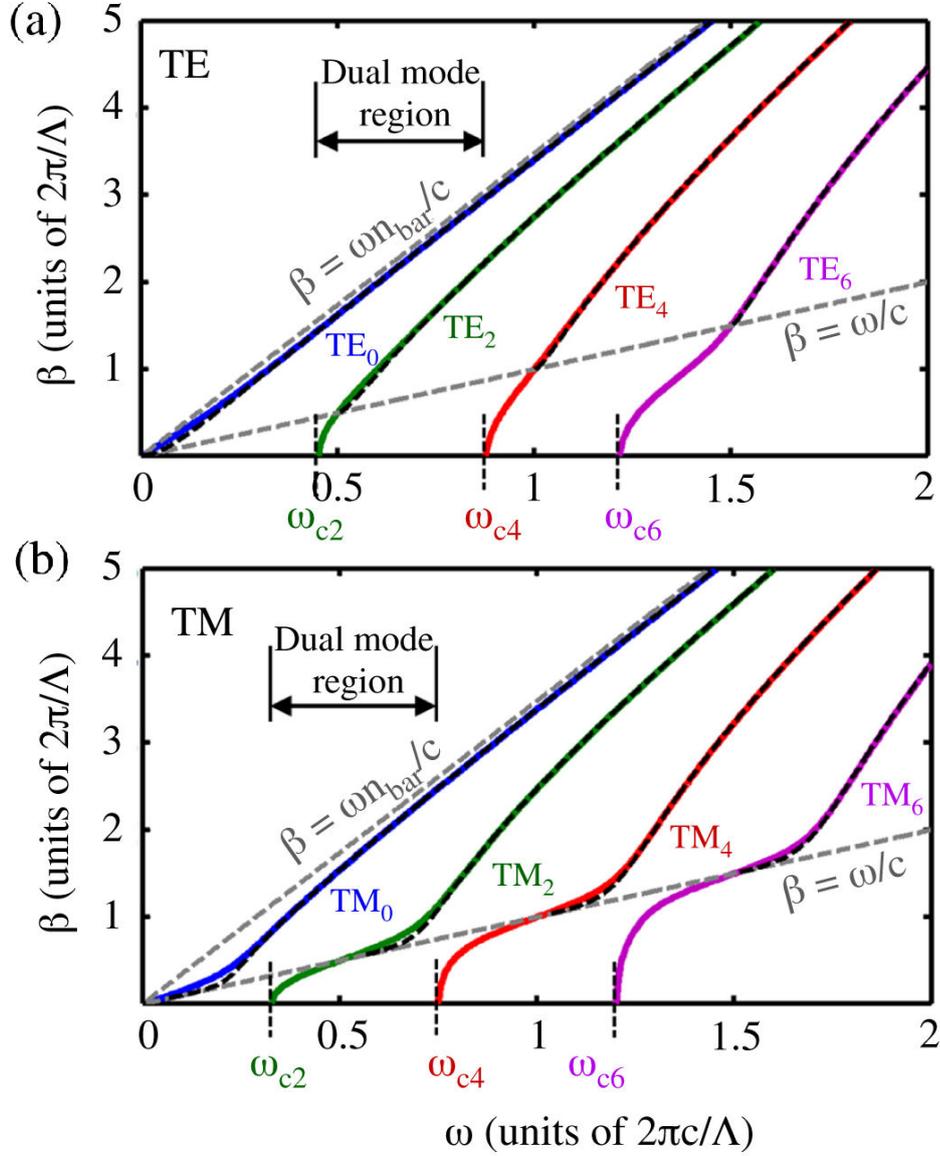
Figure 3.12: Dispersion curves of a single slab waveguide (dashed) and waveguide array modes (solid), for the same bar width d and index $nr$, $\beta$ being the z wavenumbers. Between the two light lines, the dispersion curves of the waveguide array modes are nearly identical to those of the single slab waveguide [87]. Below the air light line ($> \omega/c$) there is a discrete set of modes due to subwavelength grating periodicity. $\omega_{c2}$ and $\omega_{c4}$ are the cut-offs of the $TE_2/TM_2$ and the $TE_4/TM_4$ modes, respectively, and between them, the grating operates at a dual-mode regime. For HCG with surface-normal incidence, only the even modes need to be considered. The TE condition is plotted in (a), and TM in (b). In this calculation, $d/p = 0.6$, $n = 3.48$. From [72].

### 3.2.2 FDTD design process

For the fabrication, two different manufacturing techniques, 3D printing and laser cutting, are used and, hence, two different design algorithms are employed. 3D printing theoretically offers complete freedom in the design with no limitations on thickness, bar width and pitch. As the theoretical feature size of the 3D printer is $> 10\,\mu$m, this is an order of magnitude smaller than the feature size required to create sub-wavelength gratings which are meant to have width on the order of the wavelength within the material $\lambda/n < 300\,\mu$m. Therefore, the goal of the design process is to obtain as large as possible bandwidth while keeping the thickness as small as possible to reduce material losses. To do this, the pitch, $p$, and bar width, $d$, are swept over a range of values while keeping the thickness constant. The results are plotted to identify suitable candidate designs which show the desired 90 $^\circ$ phase shift. Results of such a sweep for the d parameter for a given thickness and pitch can be seen in Figure 3.13.

The design process is similar for the laser cut samples, but the geometrical re-
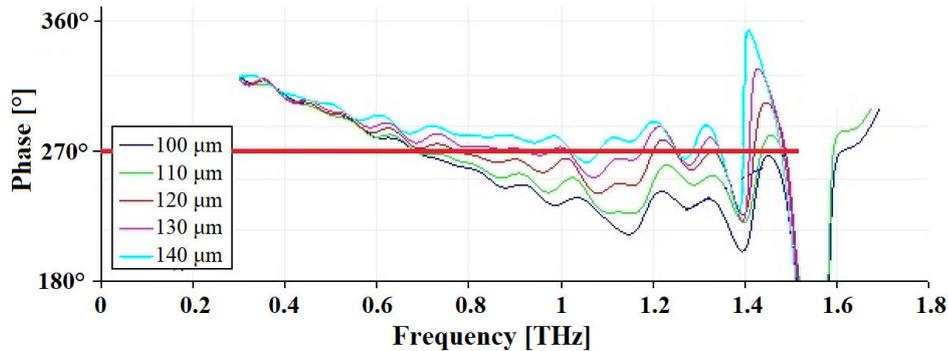


Figure 3.13: FDTD simulation showing the phase difference between TE and TM polarisation for a 3D printed structure with a thickness of $t = 700\,\mu$m, a pitch of $p = 220\,\mu$m and varying bar widths. The red line indicates a 90° phase difference. The graph shows that a component with a bar width of $d = 130\,\mu$m has the desired phase shift between ~0.8 THz and ~ 1 THz, meaning it has an operational bandwidth of around 200 GHz.

strictions of the manufacturing method have to be accommodated. The restrictions arise from the material thickness of the available substrate (1 mm), the minimum

cut-width of the laser ($125\,\mu$m) and the minimum required pitch as melting occurs during manufacturing.

### 3.2.3 Results

First the results of the 3D printed structures, shown in Figure 3.14, are discussed, followed by the results of the laser-cut samples. At the end the operational bandwidth of both structures is compared with a simulated silicon structure which provides a higher material contrast.



Figure 3.14: 3D printed HCG samples with their support structures.

Figure 3.15 shows the phase shift produced by a 3D printed structure with the geometric parameters $p = 220\,\mu$m, $d = 90\,\mu$m, $t = 300\,\mu$m. An operational bandwidth of $200\,$GHz centred at $900\,$GHz is expected from simulation. It is apparent that the operational bandwidth with the desired phase shift of $90° \pm 10°$ is considerably smaller at approximately $50\,$GHz.

This is caused by residual resin in between the bars. Due to the surface tension of the resin and the small gaps between the bars, the resin cannot be entirely removed. The residual resin effectively shortens the length of the waveguides, hence changing the phase difference between the TE and TM polarisation. Additionally, through the shortening, the phase does not show the desired plateau. Different attempts were undertaken to remove the resin, e.g. by blasting with a nitrogen gun or the removal in an ultrasonic bath with isopropanol, but ultimately remained unsuccessful. Increasing the pitch to increase the gap size was also attempted up to a pitch of $400\,\mu$m, but did not improve the removal of excess resin. A further
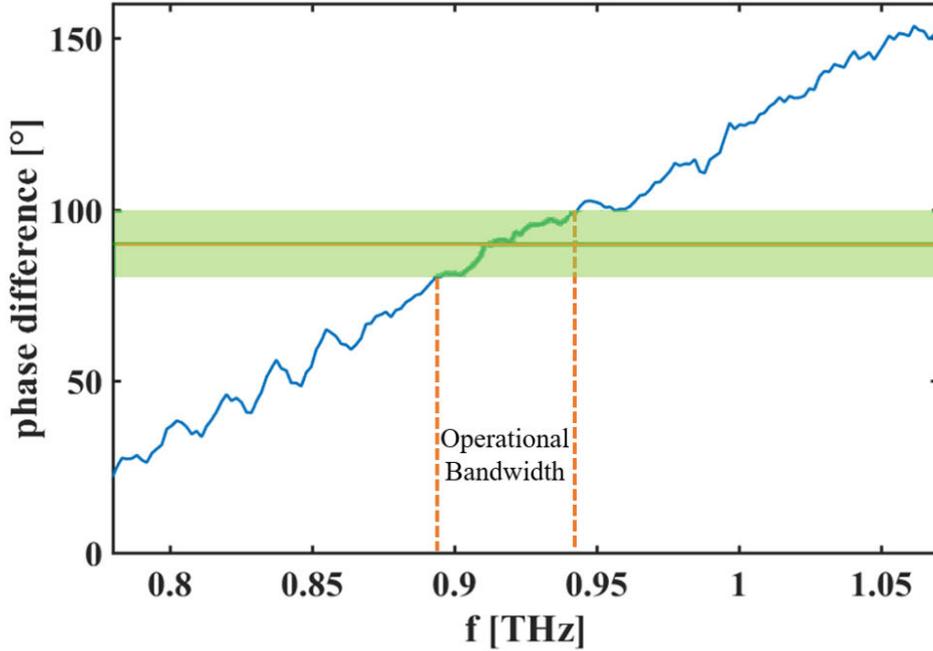
Figure 3.15: The phase difference between the TE and TM polarisation of a 3D printed sample with the geometric values ($p = 220\,\mu m$, $d = 90\,\mu m$, $t = 300\,\mu m$). The green area highlights the $\pm 10°$ tolarance for the operational bandwidth.

increase of the pitch would deteriorate the operational bandwidth to a similar value to the components with residual resin and was therefore not pursued.

As mentioned before, one of the challenges for laser machining PTFE, or any polymer for that matter, is heat dissipation. As the bars of the grid are made of thin "wires" of PTFE, melting turned out to be a significant challenge during the fabrication and ultimately limited the minimum feature size. An example of this can be seen in Figure 3.16.

This limited the pitch, $p$, to a minimum value of $400\,\mu m$, and the bar width, therefore, being $p$ minus the minimum cut width of $125\,\mu m$ to $d = 275\,\mu m$. With this geometrical parameters, the cut-off of the desired dual-mode region is lower than the target frequency range. This means the component operates in the less desirable multi-mode region, as opposed to the dual mode frequency range, where the plateaus for the phase are harder to achieve, which reduces the operational bandwidth. Therefore, a single grating could not achieve the desired phase shift of $90°$, but this issue can be simply circumvented by stacking the grids. The phase

Figure 3.16: Photo of two laser-cut PTFE HCG wave plates. While the left wave plate has straight bars, the right one shows considerable warping of the bars which are melted together at some spots.

difference between the fast and slow axis of such a stacked of three grids is shown in Figure 3.17.

It can be seen, that overall the spectrum is considerably flatter than that of the
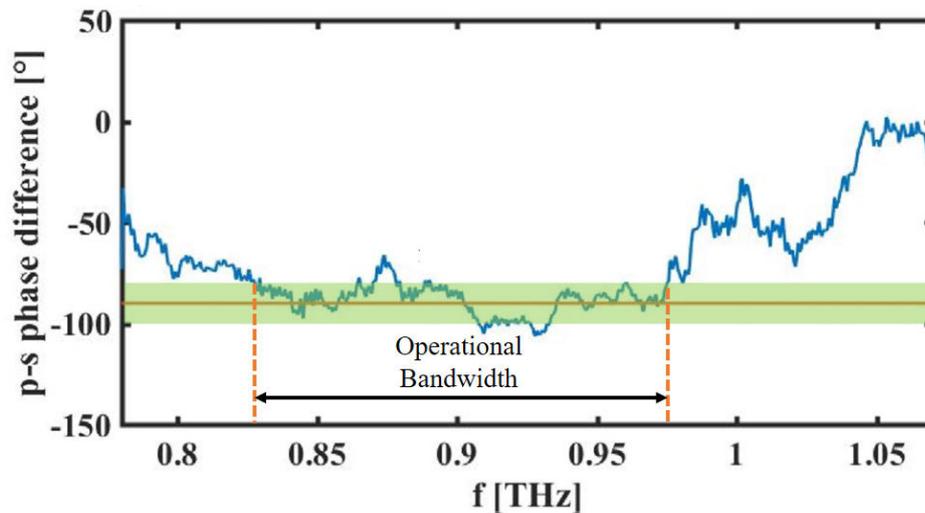


Figure 3.17: Measured phase difference of a stack of laser-cut PTFE wave plates with the geometric parameters ($p = 400\,\mu$m, $d = 275\,\mu$m, $t = 3000\,\mu$m). The wave plate has an overall larger operational bandwidth of almost $0.25\,THz$ between $\approx$ $0.83\,$THz and $\approx 0.98\,$THz, albeit with some small dips where the phase difference exceeds the $\pm 10°$ desired accuracy.

3D printed component and a large part of it lies in the region of the desired region of $90° \pm 10°$. Neglecting the few dips that exceed the desired $\pm 10°$ tolerance, the component has an operational bandwidth of approximately $150\,$GHz. This is a

threefold improvement compared to the 3D printed devices. Despite being more than 4 times thicker than the 3D printed HCG, due to the significantly lower attenuation in PTFE, the absorption of the PTFE stack is still comparable to that of the 3D printed wave plate with both showing values of less than 3 dB. When comparing the measurements of the laser-cut HCG stack in Figure 3.17 with a simulation of a single wavep late with identical thickness, as shown in Figure 3.18, it can be seen that the operational bandwidth and centre frequency are in good agreement, but there are some additional features. The most striking difference beeing the peak at 1.05 THz. These differences can be explained with misalignment of the stack layers ant potential effects of the interfaces.

Overall, it can be summarised that both fabrication techniques reach their limit-
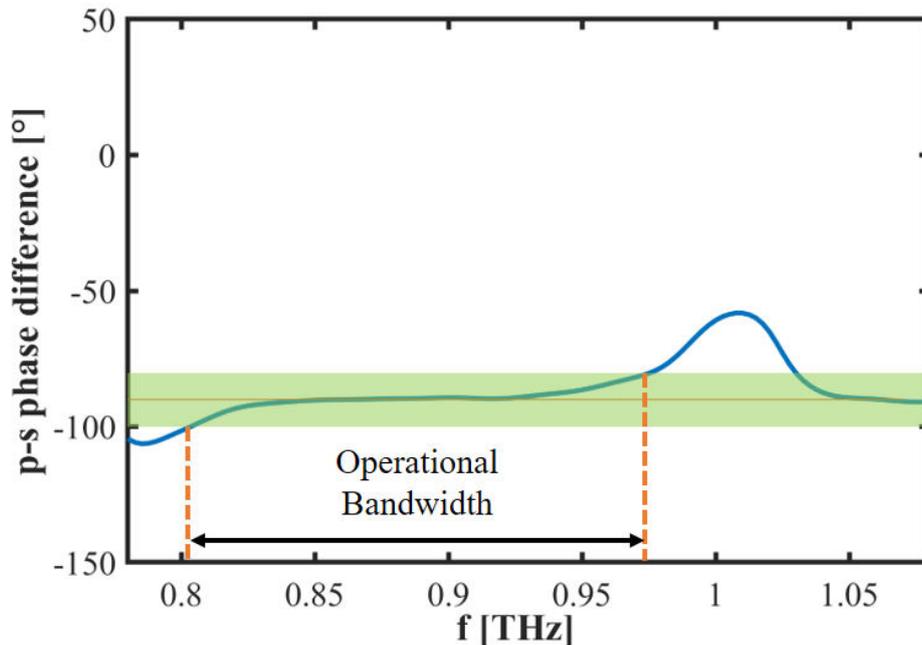


Figure 3.18: FDTD simulation of a PTFE HCG with identical geoemtrical parameters to the stack shown in Figure 3.17 ($p = 400\,\mu$m, $d = 275\,\mu$m, $t = 3000\,\mu$m). The operational bandwidth of approximately 150 GHz of the simulated structure matches with the measurements of the HCG stack.

ations to produce feature sizes that are required for components with operational frequencies around 1 THz, at least with the available equipment. There are multiple possibilities to increase the operational bandwidth further. For the 3D printed

samples, the obvious approach is to find a method to remove the resin or a printer that does not face this issue. For the laser-cut wave plates, the period and bar width have to be reduced. This would be possible with a better laser cutter that allows better control over the laser power and duty cycle. However, even then, simulations show that the operational bandwidth will be limited to less than 300 GHz. This is mostly due to the low refractive index contrast to air of the used plastic materials. To increase the material contrast, a material such as HRFZ could be used. Simulations for such a component are shown in Figure 3.19, where the operational bandwidth exceeds 0.5 THz. Alternatively, using machinable ceramics might also be a way to increase bandwidth while still having robust components at a low price point.
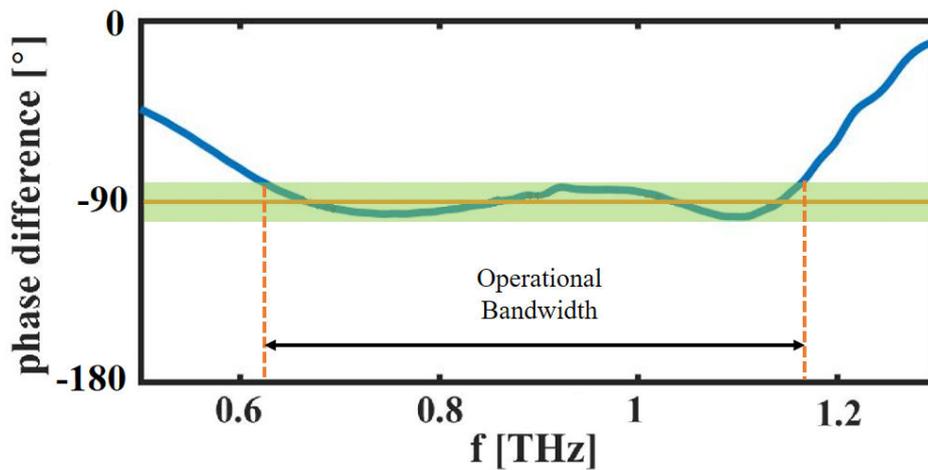


Figure 3.19: FDTD simulation of a silicon HCG with a thickness $h = 100\,\mu\text{m}$ and grating spacing of $p = 100\,\mu\text{m}$ and gap of $d = 50\,\mu\text{m}$ Due to the higher refractive index contrast, the operational bandwidth exceeds 0.5 THz.

## 3.3 Conclusion

Various novel materials and fabrication methods for THz optical components were studied. First, multiple low-cost ceramics were tested for their use as optical materials at THz frequencies. Shapal, an AlN and BN based ceramic, exhibits the lowest losses of the tested materials with $\alpha_{1\,THz}$=0.4 cm$^{-1}$, which is even lower than pure AlN and BN that have been reported with values of $\alpha_{1\,THz}$=1-3 cm$^{-1}$, but adds vast shaping capabilities for optical components as it is a machinable ceramic. The silicon based ceramics, Macor, a $SiO_2$ based mixture, and SiC on the other hand exhibited high attenuation coefficients ($\alpha_{1\,THz}$>20 cm$^{-1}$), which is a magnitude of order higher than their crystalline counterparts and renders them unsuitable for optical components. But Shapal has the potential to fill the gap between low-performance plastics with refractive indices n<2 and the high-performance, but very expensive, HRFZ-Si (n~3.42), as a material of choice for THz optics. Shapal's refractive index lays in between these materials with n=2.65 and has superior mechanical properties, like being more resiliant than plastics and better machinable than silicon. It's Abbe number is determined to be approx. 41, which means it has a low dispersion for its high refractive index, when compared with materials in the optical region. The micro-machining of a Fresnel lens with minimum feature sizes in the order of the smallest available milling head of $30\,\mu m$ is demonstrated and the drilling of holes down to a diameter of $100\mu m$ for photonic components in the ceramic is discussed. A ceramic prism, as an example for a bulk optical component, has been presented, which showed that the material's absorption is low enough for cm sized components. The results indicate that ceramic optical components are likely to be used in future industrial THz applications, as they are resilient, compact and cheap.

Following this, THz wave plates based on high-contrast gratings (HCGs) fabricated with low-cost additive and subtractive techniques, 3D printing and laser cutting respectively, were discussed. The limitations of the different fabrication techniques

to reach the required feature size of $<300\,\mu$m for frequencies of around $1\,$THz is discussed. Polymer based components with a broad operational bandwidth of up to $300\,$GHz centred at $0.925\,$THz are simulated. However, it can be seen that the target frequency band around $1\,$THz requires too small feature sizes to produce wave plates with 3D printing and laser cutting comfortably, pushing the techniques to their limits for their individual reasons. The 3D printed wave plates had an reduced operational bandwidth of $50\,$GHz due to excess resin which cannot be removed between the structure's bars. This residual deteriorated the waveguide modes in the structure in an unpredictable manner as the resin was unevenly distributed within the HCG and hence the design could not be adjusted for the residuals to improve performance.

The laser-cut wave plates could not reach the required feature size, despite the theoretical minimum line width of $125\,\mu m$, due to melting of the polymers. Hence, the dual-mode region which is desired for HCGs, could not be achieved but performance still improved compared to 3D printed structures and an operational bandwidth of almost $150\,$GHz was achieved with components that operate in the multi-mode region. Nevertheless, the results show potential for components for the lower frequency THz communication band around $300\,$GHz produced with currently available techniques. The minimum feature size of most commonly available 3D printer and laser cutters should allow the fabrication for the communication frequency band, while a further improvement in these fabrication techniques over time might enable components for higher frequency bands as well. For higher frequencies, clean room based manufacturing methods could produce components suitable for the spectrum at $1\,$THz and beyond. Simulations for such components show that the operational bandwidth would increase to $500\,$GHz centred around $0.9\,$THz due to the higher material contrast of the high refractive index silicon to air.

# Photonic Crystals Cavities for Enhancement of THz spectroscopy

This chapter will discuss the design process for THz photonic crystal cavities. After introducing the physical background, the influence of realistic geometric and material constraints on the quality factor is discussed. Following this, an application for the cavities to enhance the sensitivity of chemical sensing in liquids is explored, and this concept is subsequently extended to a concept for lab-on-a-chip spectroscopy systems by integrating it into a waveguide.

## 4.1   Introduction

Photonic crystals are periodic structures which affect photons in a similar to the manner in which the ionic lattices of crystalline materials affect electrons [51]. They are commonly made out of dielectric materials, but the concept has been extended to metallic structures in recent years [88–90]. While there are naturally occurring examples of photonic crystals, for example in the form of opals [91], or even biology [92], they have been undiscovered until the $20^{th}$ century due to their nanoscopic

nature. The first description of simple structures that could be regarded as prototypes of photonic crystals was made at the end of the $19^{th}$ Century by Lord Rayleigh [93] who reported on a stack of materials that could exhibit a bandgap – a frequency region where light is not permitted to propagate in the material. This is the simplest example of a photonic crystal, as it will only exhibit the bandgap behaviour along the axis in which the material is stacked and is therefore called one dimensional. It took another century to describe this behaviour in full with electromagnetic field theory [94] and even longer for an experimental realisation [95, 96].

Long before this, one-dimensional versions, so-called Bragg reflectors have been known and widely used in technology, for example for distributed-Bragg-reflector lasers [97, 98]. With the rise of nanophotonics, interest in two-dimensional photonic crystals has increased [99–101]. Both, the one and two-dimensional variants are still of more significance for applications than the three-dimensional version, as their simpler manufacturing process is more compatible with cuyrrent technology. An illustration of all three varieties is shown in Figure 4.1.

The mathematical description of photonic crystals usually involves Maxwell's
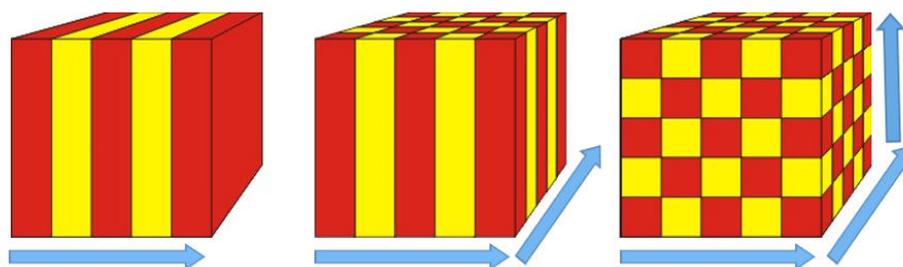


Figure 4.1: Illustrations of 1, 2 and 3 dimensional photonic crystals . The photonic band structure exists in the direction of the periodicity, indicated by the arrows. Based on [102].

Equations to take into account the (discrete) translational symmetry that the photonic crystals exhibit so that they can be treated as Bloch waves and eigenvalue problems. As the photonic crystals to be presented in this chapter have been designed solely using FDTD simulations, a complete derivation of the underlying

mathematical theory will not be presented, but it can be found in Joannopoulos et al. [51]. However, here some of the fundamental behaviours that arise from the mathematical part, especially regarding the symmetry, are considered as it is necessary to understand some of the behaviour observed during the simulations, for example the influence of the finite height and the vertical modes.

## 4.2 Physical Background

### 4.2.1 Distributed Bragg Reflectors – An example of 1D photonic crystals

The concept of photonic crystals is easiest to comprehend when looking at the one-dimensional case, such as distributed Bragg reflector (DBR). In this simple case, it is possible to understand photonic crystals in terms of interference and geometry rather than relying on the more complicated Maxwell equations and eigenvalues required for a general and complete description. DBRs are one-dimensional photonic crystals which serve as mirror structures. Hence, they are also known as Bragg mirrors and consist of a sequence of layers with alternating refractive indices, exhibiting symmetry along one axis. The thickness of each layer is chosen in a way that the multiple reflections from each layer combine with constructive interference for certain wavelengths. Therefore, a stack of multiple layers can act as a high-quality reflector. To achieve this, the thickness has to be chosen in a way that the optical path length (OPL) fulfils Bragg's law for constructive interference, which is designed for scattering at crystal lattices [103].

$$2a \sin \Theta = m\lambda, \tag{4.1}$$

where $a$ is the spacing between the planes of the atomic lattice, $\Theta$ is the angle of incidence, $m$ is an integer and $\lambda$ is the wavelength of the incident radiation. To apply this formula to a system consisting of layers of materials, the spacing between the planes needs to be replaced with with the OPL, which is defined for a medium

with a constant refractive index as

$$OPL = nd := a, \tag{4.2}$$

where $d$ is the thickness of the layer. Furthermore, only half a wavelength is required for a standing wave with constructive interference and, assuming normal incidence and $m = 1$, Equation (4.1) simplifies to

$$n = \frac{\lambda}{4d}, \tag{4.3}$$

as the equation for the thinnest possible layer required to achieve constructive interference. So, every single layer has to be a quarter-wavelength in (optical) thickness. For a mirror structure, one of the most important properties is its reflectivity, $R$, which specifies the fraction of the incident electromagnetic wave that is reflected, with a perfect mirror having a value of $R = 1$ , which means that no energy is transmitted or dissipated. However, for most of the materials used to produce Bragg Mirrors, the reflectivity of a single layer is not unity and this is why several layers of two different materials are stacked to achieve a higher reflectivity. For this reason, a Bragg mirror is also called a quarter-wave stack. While the reflectivity for a stratified medium can be expressed by a complicated formula [15], it can be simplified for normal incidence, at a given frequency, to

$$R = \left[ \frac{n_0 n_h^{2N} - n_t n_l^{2N}}{n_0 n_h^{2N} + n_t n_l^{2N}} \right]^2, \tag{4.4}$$

where $n_0$, $n_l$, $n_h$ and $n_t$ are, respective, the effective refractive indices at the centre wavelengths of the frequency in originating medium; the low, and, high refractive index materials the stack is made of and that of the terminating medium. $N$ is the integer number of pairs of layers in the stack.

The bandwidth $\Delta \omega_0$ of the DBR is dependent on the refractive indices differences and is

$$\Delta \omega_0 = \frac{4 \omega_m}{\pi} \arcsin \frac{n_h - n_l}{n_h + n_l}, \tag{4.5}$$

where $\omega_m$ is the centre frequency of the stop band [104]. In photonic crystal terms, the stop band is a result of the photonic band gap, the region of the energy diagram

where no states are allowed, as shown in Figure 4.2.

From a fabrication perspective, one dimensional photonic crystals are often produced by stacking multiple coatings on top of each other (e.g. anti-reflective coatings or dielectric mirrors) or by growing alternating layers of semiconductors, e.g. in semiconductor lasers. For optical components large-area coating techniques like Chemical Vapour phase Deposition or sputter coating are used while the semiconductor structures are grown in the same process as the active, optical components with Molecular Beam Epitaxy or Metal Organic Vapour Phase Epitaxy.
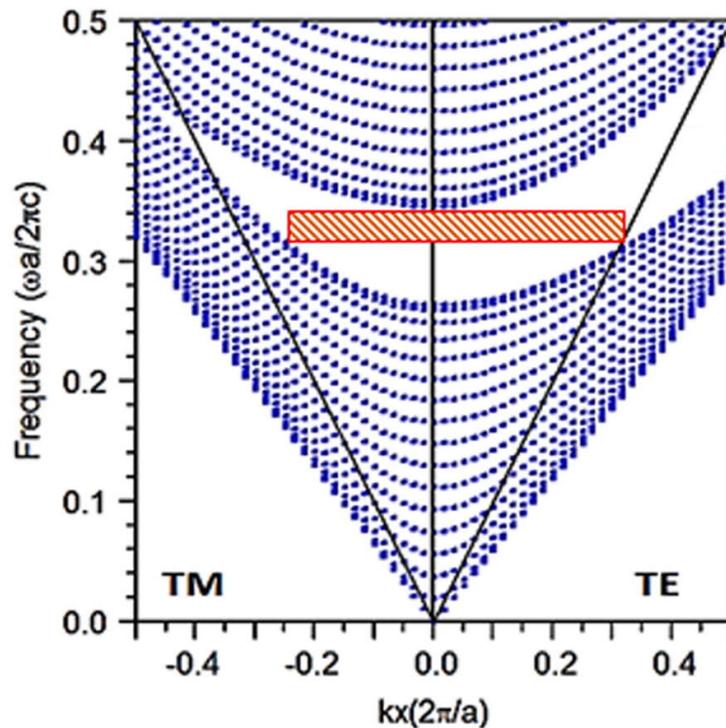


Figure 4.2: Photonic band structure of a distributed Bragg reflector with 7 periods simulated using the plane wave method. The red area marks the band gap. From [105].

### 4.2.1.1  2D Photonic Crystals

A two-dimensional photonic crystal comprises a periodic pattern made out of two or more different dielectric materials in two dimensions and is quasi-infinite in the dimension without periodicity. For certain combinations of periodicity and dielec-

tric material constants, the crystal can exhibit a photonic band gap within the plane of the periodicity, which prevents light from propagating in any direction within the plane. In contrast to the 1D case, it is possible to define transversal electric (TE) and transversal magnetic (TM) modes in a two-dimensional structure. Both will be influenced differently by the lattice, which means that there are structures which will exhibit band gaps for only one polarization, such as cubic lattices, while some structures have a complete band gap for all polarizations, such as certain hexagonal lattices. Two-dimensional photonic crystals can be produced with photolithography, as it is commonly done for nanophotonic components, but drilling of lattices of holes is also known for longer wavelengths [106].

### 4.2.1.2 Defect states

Just like crystals, especially semiconductors, photonic crystals can have different forms of defects as well; and, just like semiconductors, photonic crystals can have defect states in their bandgap. The defect state arises from the break in symmetry and, subsequently, the formation of a mode which allows light of a certain frequency to propagate through the crystal. This can be used. For example to emit or select frequencies for spectrometry or in a laser. The defect state is usually designed to be in the region of the stopband and has a reflectivity of $R < 1$, as shown in Figure 4.3. In a 1D structure, this defect is often a single layer with different thickness. In a 2D lattice, such a point defect can serve as a cavity when sized correctly.

Different defects can serve different functions. For example, a line defect in a 2D photonic crystal can serve as a waveguide, allowing light to propagate along the defect while being confined by the periodicity that surrounds the defect.

### 4.2.1.3 Photonic Crystal Slabs

While the quasi-infinite nature usually employed in the theoretical description significantly simplifies the mathematics involved, such structures are often not realistic.
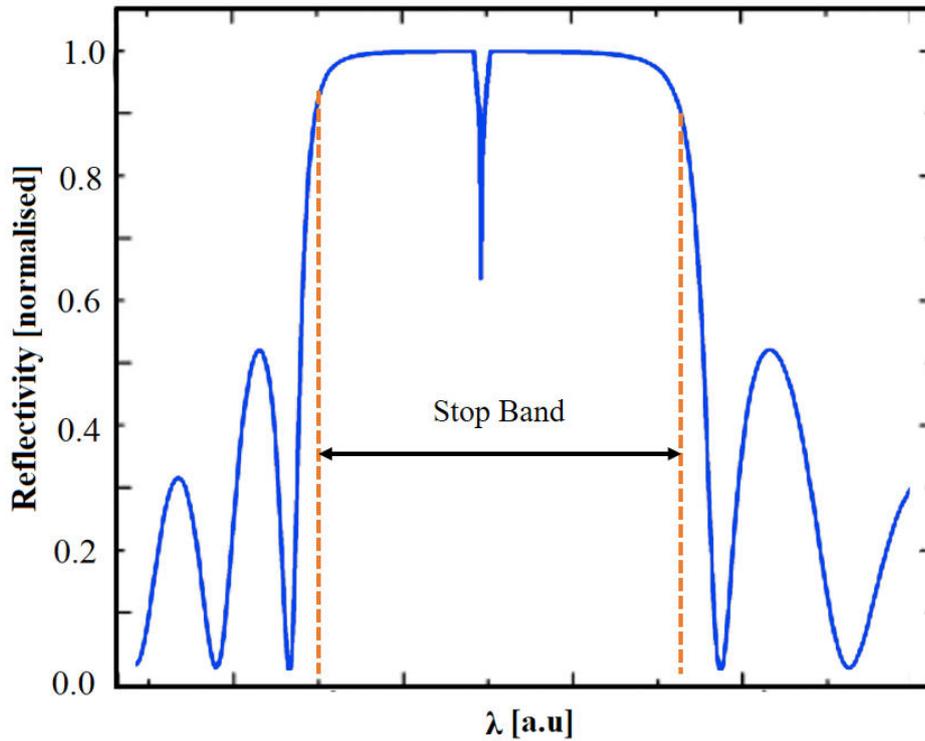
Figure 4.3: Schematic of a reflectivity spectrum of a Bragg Mirror with a defect state in the middle of the stop band.

A simple example of this would be a photonic crystal fabricated on a substrate which has a thickness which cannot be considered infinite. These changes from the ideal case introduce another break in symmetry and can significantly deteriorate the bandgap, which means that energy states are available in the previously forbidden range which reduces the width of the bandgap and possibly couples to intentional defect or guiding modes, resulting in losses. For THz wavelengths, a quasi-infinite structure would result in many-millimetre thick photonic components which would not only be counterproductive to any attempts at miniaturization but may also pose problems in the sourcing of materials, such as silicon wafers. This means any photonic crystal has to be carefully designed and optimized for a given thickness to minimize losses.

The ideal slab thickness is highly polarization-dependent. If a slab is too thin, the electric field extends outside of the slab. Hence, modes are weakly guided or not at all. In this case, the wave propagates mostly in the uniform surroundings, and

the periodicity becomes irrelevant. For very thick slabs, band gaps form (as for the infinite case) but additionally higher-order modes with a vertical orientation can also form and populate the bandgap, again resulting in a reduction or deterioration of it. Under these considerations, it becomes apparent that the ideal slab thickness is somewhere in the order of below a wavelength and up to a few wavelengths, depending on the refractive indices of the materials the crystal consists of. This would make the slab thick enough for the fundamental mode to be well confined and to experience the periodic nature of the slab, while also being thin enough to prevent higher-order modes from forming. The ideal thickness, therefore, is highly dependent on the dielectric constants involved, as the effective wavelength depends on the material that the wave propagates in.

A significant difference, however, is the influence on the polarization. For TE-like modes, the thickness is determined mostly by the higher permittivity dielectric material, while the lower permittivity dielectric material dominates the TM-like modes. Therefore, TE hole structures ideally have a smaller thickness than TM rod structures. To illustrate the influence of the slab thickness on the functionality of a photonic crystal, one can look at the width of the photonic bandgap. The bandgap reduces by up to 72% of the quasi-infinite case even for the ideal values of the slab thickness [51].

While it is possible to imagine a self-supporting array of holes, this becomes more difficult for rod-based photonic crystals, where a substrate becomes a necessity. A substrate breaks the reflection symmetry of a free-floating slab, and previously isolated modes will couple, resulting in leaky band gaps. This results in a loss during propagation, ultimately limiting the use of the structure.

## 4.3 Cavity Design of Photonic Crystal Slabs for the integration of active THz Components

### 4.3.1 Introduction

Cavities are some of the most fundamental and essential components for many optical applications. They are a basic requirement for key technologies such as lasers or current scientific frontier topics such as exciton-polaritons [107]. The quality factors of optical photonic crystal cavities exceed $10^7$ [108] and are orders of magnitude higher than at THz frequencies, which often do not exceed $10^4$ [109, 110]. While the THz values are still relatively high, another aspect has to be addressed: the integration of active components into a cavity. At optical frequencies, it is often possible to integrate Bragg reflectors with the same technologies, for example semiconductor Bragg reflectors [111]. The fabrication constraints caused by the length scales involved for THz operation means that these concepts often cannot be adapted. Therefore, cavities formed by photonic crystal slabs are discussed which allow for later integration with different devices under realistic manufacturing constraints. The design process first involves a maximisation of the Q factor and addressing different material losses and the influence of geometric factors, such as the finite structure size. Later on, this knowledge on how to adjust the quality factor is used to address highly absorbing cavity fillings, as the high absorption has to be balanced with a lower quality factor. The structures to be discussed here are one dimensional Bragg stacks and two-dimensional rod or hole crystals consisting of either HRFZ-Si, which is one of the preferred materials for THz applications due to its low losses and high refractive index, or low-loss polymers, such as HDPE or PTFE. The polymers have considerably higher absorption and lower refractive index than Si, but offer more flexibility in fabrication at a significantly lower cost point.

## 4.3.2  Method of Quality Factor Extraction

The quality factor can easily be extracted from experimental results using the Full-Width Half Maximum, $\Delta f$, and the resonant frequency, $f_R$, with

$$Q = f_R/\Delta f. \tag{4.6}$$

Lumerical offers two different methods to extract the quality factor. For a low Q resonator (up to values of hundreds), when extracting this value from FDTD results, it is possible to simply wait until the electric fields are fully decayed and the energy has dissipated, as seen in Figure 4.4, so the extraction is similar to that of experimental results. For high Q resonators, this becomes more difficult, as the
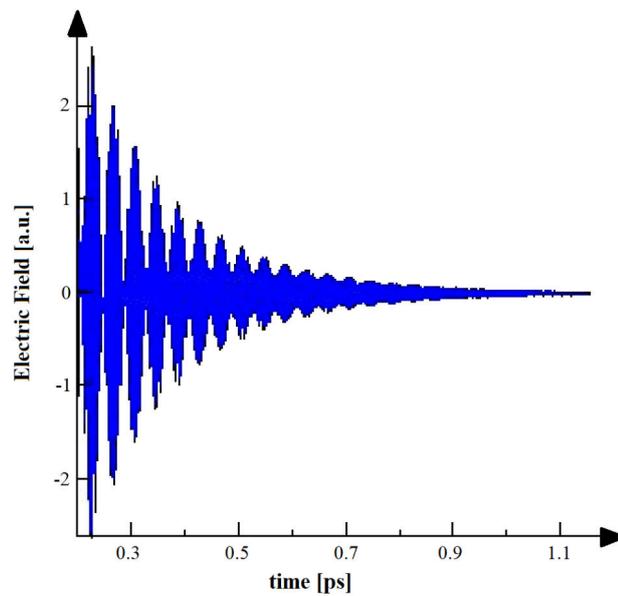


Figure 4.4: Exponential decay of the electric field of an optical photonic crystal resonator. With a full, time-resolved decay, one can extract the quality factor from the spectrum with confidence. From [112].

complete decay cannot be simulated using a reasonable amount of resources. This leads to an error in the Q factor extraction, as the FWHM is inversely proportional to the simulation time as long as the resonator is ringing

$$FWHM \sim \frac{q}{T_{simulation}}. \tag{4.7}$$

. A convenient way around this is by extracting the quality factor from the slope
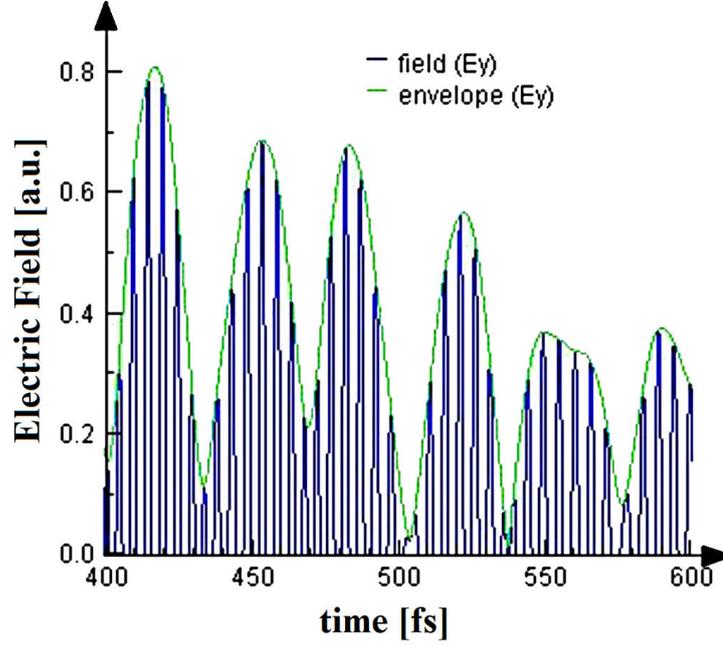


Figure 4.5: The envelope function of an electric field signal in the time domain. From [113]

of the envelope function of the decaying electric field, as seen in Figure 4.5, as this requires a significantly shorter simulation time. For this, the frequency in the equation of the quality factor has to be expressed with a quantity related to the electric field:

$$Q = \frac{\omega_r}{FWHM}. \tag{4.8}$$

Where $\omega_r$ is the resonant angular frequency ($\omega_r = 2\pi f_R$). The decay of the electric field in the time domain is described by

$$E(t) = e^{-t(\alpha - i\omega_r)}u(t), \tag{4.9}$$

with $\alpha$ as the decay constant. The Fourier transform is

$$|E(\omega)|^2 = \frac{1}{\alpha^2 + (-\omega - \omega_r)^2}. \tag{4.10}$$

The maximum value appears when the term in the parentheses disappears at $\omega = \omega_r$. The value of the half maximum occurs at $\omega = \omega_r + \alpha$ and $\omega = \omega_r - \alpha$. Therefore,

the FWHM can be expressed in terms of $\alpha$ as

$$FWHM = 2\alpha. \tag{4.11}$$

Substituting Equation (4.11) in equation Equation (4.8) gives

$$\alpha = \frac{\omega_r}{2Q}. \tag{4.12}$$

. As the decay is now directly related to $Q$, only the slope from the decaying electric field needs to be determined. Due to the exponential nature, this is most easily done when a logarithm is applied to the function:

$$log_{10}(|E(t)|) = \frac{-\omega_r t}{2Q}log_{10}(e) = mt, \tag{4.13}$$

where $m$ is the slope. Solving for $Q$ results in

$$Q = \frac{-\omega_r t log_{10}(e)}{2m}. \tag{4.14}$$

In many applications, it can be challenging to separate the decay of the envelope from other functions, especially in a multimode system where filtering and other techniques are required. However, when single mode systems are investigated in the following sections, the extraction is found to be straightforward using the tools available in Lumerical.

### 4.3.3 Simulating Band Structures

FDTD simulation can also be used to simulate band structures. Commonly, these simulations are performed on a single unit cell to find its band structure [114] and further functionalities, such as cavities, are designed with transmission curves only. However, analysing, for example defect modes in 2D photonic crystals with FDTD is also known [115]. The main reason for this is that with the deviation from the ideal case, for example non-infinite structures or defects, the simulation becomes increasingly difficult and uncertain. Because FDTD relies on finding peaks in a

discrete k-space for the band structures, the peaks of weaker or very narrow defect modes, especially with high Q-factors can be challenging to simulate. However, the tracking of the stronger bands, e.g. the highest dielectric band which forms the lower boundary of the bandgap, are easier to track.

The simulation of band structes is based on Bloch's theorem that states that modes in a periodic structure can be written for the one dimensional case as

$$E_k(x) = e^{ik_x} u_k(x), \tag{4.15}$$

where $u_k(x)$ is a periodic function of $x$ with a period of $a$. This means that $u(x + a) = u(x)$ and therefore, the Bloch's theorem can also be written as

$$E_k(x + a) = e^{ika} E_k(x). \tag{4.16}$$

The generalisation to more dimensions happens straightforwardly.

Bloch boundary conditions are used to calculate infinite periodic structures by simulating a single unit cell or the smallest multiple that fits in the rectangular simulation domain for a hexagonal lattice. To calculate the band structure, the angular frequencies $\omega_k(k)$ are determined as a function of the wave vector $\vec{k}$ for all Bloch modes in a given frequency range. The sources used are not particularly important in band structure simulations as long as all modes of interest are excited. The standard procedure for Lumerical is a randomly distributed dipole cloud. For structures with non-rectangular lattice, these calculations are slightly more complicated. To avoid issues with artificial zone folding caused by the rectangular simulation domain and the non-rectangular lattice, matching dipole sources are used in each unit cell. The matching dipoles must be in the same positions in each unit cell, and the phase must be adjusted according to

$$\Delta\Theta = \vec{k} \cdot \Delta\vec{r}, \tag{4.17}$$

where $\Delta\Theta$ is the phase offset from the reference dipole, $\vec{k}$ is the simulation wave vector and $\Delta\vec{r}$ is the position offset from the reference dipole.

The band structure is calculated in the following way: As a first step, the data from

the electric field monitors are Fourier transformed with appropriate windowing. The FFTs are summed up to include all resonant frequencies and therefore, modes. This step is repeated for each value of k until the data set is completed. For each k the different peaks are found and then extracted as points of the band structure. The minimum peak strength and the number of peaks are selected in this step as well.

## 4.3.4 Photonic Crystal Cavity Design with Finite Extension

In this section, some basic cavity designs are introduced and how their finite extension influences the quality factor. The aim is to explore different geometries to design cavities for later integration with other components.

All photonic crystal cavities consist of two stacks of layers flanking each side of a defect. The defect is designed to have a cavity mode at $\sim 1\,\text{THz}$. All of the proposed structures are designed within the limits of realistic sample fabrication, such as material dimensions and fabrication method-dependent feature sizes. Considerations of finite thicknesses are taking into account, for example extension in the z-direction as indicated in Figure 4.6, and number of layers to guarantee a close match with experiments. The length in the x-direction is many wavelengths and can, therefore, be considered infinite, whilst the height, i.e. the length in the z-direction, and the length of the sample, the y-direction, are limited. The maximum possible height for the different photonic crystals varies due to their different fabrication methods, e.g. the drilling of holes in polymers is limited by the length of the drill, which is as much as $\sim 1.78\,\text{mm}$ for $\varnothing : a = 100\,\mu\text{m}$. Common fabrication techniques for silicon photonic crystals, like deep reactive ion etching, are not dependant on any tool size. Therefore the thickness of commercially available wafers $500\,\mu\text{m}$ is used in the simulation. The milling of the polymer rods has a stronger limitation, since the commercial available milling heads have a limited aspect ratio, e.g. 1:6 for the tools used in our lab, which significantly limits the maximum height. This leads to a maximum feature height of several $100s\ \mu m$, depending on the unit cell size.

Photonic crystals with band gaps for different polarisations were chosen in order to investigate the feasibility of the concepts within the constraint of the limited height. There are two different cases for when the electric field oscillates in the direction of the finite thickness, therefore being TM polarised, with the magnetic field in the xy plane, rods structures offer a complete band gap as in Figure 4.6a. When the electric field oscillates in the direction of the quasi-infinite axis and therefore is TE polarised with the electric field in the xy plane, hole structures offer a com-
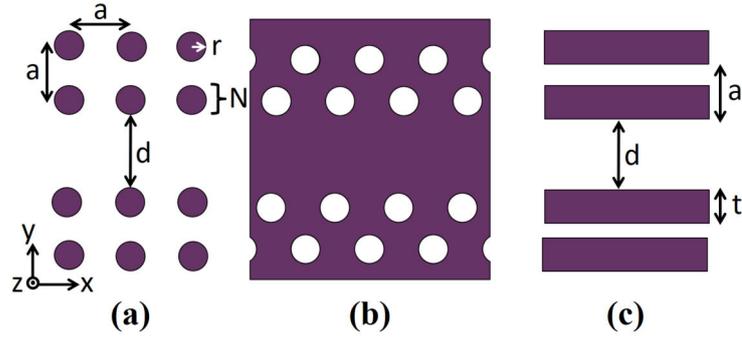
Figure 4.6: a) Schematic of a rod photonic crystal with the geometric parameters unit cell (a), rod diameter (r), defect length (d) and number of periods on each side of the defect (N). b) Schematic of a hole photonic crystal which has the same geometric properties as the rod structure of a) respectively. c) Photonic crystal based on Bragg mirrors with a layer thickness t.

Table 4.1: Geometric parameters as indicated in Figure 4.6 and the height of the structures (z) for photonic crystals operating at 1 THz.

| Type | Material | $a$ $[\mu m]$ | $r/t$ $[\mu m]$ | $d$ $[\mu m]$ | $z$ $[\mu m]$ | $n$ @1 $THz$ |
|------|----------|-----|------|-----|-----|-----|
| Rod | HDPE | 270 | 60 | 200 | 600 | 1.536 |
| Rod | PTFE | 270 | 60 | 200 | 600 | 1.446 |
| Bragg | Si | 104 | 24 | 320 | 500 | 3.418 |
| Holes | Si | 64 | 20 | 60 | 500 | 3.418 |
| Holes | HDPE | 120 | 50 | 80 | 1700 | 1.536 |

plete band gap as seen in Figure 4.6b. Additionally, a structure which in theory possesses no polarisation dependence was investigated (Bragg, Figure 4.6c). Due to their nature, the rods are considered standing on a substrate made out of the same material while the other structures are considered to be self-supported. All geometric parameters for the different samples are summarised in Table 4.1. The Q-factors are extracted from the simulation as described in the previous section.

## 4.3.5 Discussion

The different types of photonic crystals need different approaches in their design. It is known that the thickness of a photonic crystal slab can affect the band gap size severely [51]. The effect on the band gap is due to shifting of higher order modes in a non-infinite extended crystal. When these modes shift into the region

of the band gap, they offer energy states which allow propagation within the gap which results not only in a narrowing of the band gap but also in deterioration, or even complete suppression, of the cavity modes. This observation is particularly relevant for the rod type photonic crystals with their TM polarisation, since the electric field oscillates along the length of the rods and their height limitation is on the same order of magnitude as the wavelength. In addition, the finite extension of only a few wave-lengths in y and z directions allows the formation of parasitic modes for a certain number of layers which also corrupts the cavity mode. Due to the large difference in the dielectric constant between silicon and air, compared to polymer and air, the splitting between the energy bands is larger, resulting in a wider band gap for Si photonic crystals. Yet the high dielectric constant also results in a stronger influence on the critical slab thickness which leads to a narrow range of slab thicknesses where a band gap can be maintained. This problem is less apparent for the TE polarised hole structures.

The largest band gap for TE structures can be obtained by choosing the maximum possible thickness which results in close agreement with the infinite extended model. The more common design would be to choose a thickness of around half the effective wavelength for a TE hole slab, but this would result in a very thin samples of less than $100\,\mu m$ for the polymers and less than $50\,\mu m$ for silicon. As these samples would be very fragile and potentially could not even support their own weight, the maximum possible thickness was chosen, as this would be more feasible for experiments and results in the highest quality factors.

For the results, only stronger cavity modes with a quality factor above 10 are considered , as low quality factors are harder to observe, since the error for lower quality factors is on the same order of magnitude as the quality factor itself. The quality factors for all structures can be seen in Figure 4.7, where multiple different behaviours can be seen that are discussed one by one.

The Bragg design suffers from an apparent deterioration of the cavity mode as it is completely suppressed for more than 4 layers. For the TM polarisation, where the
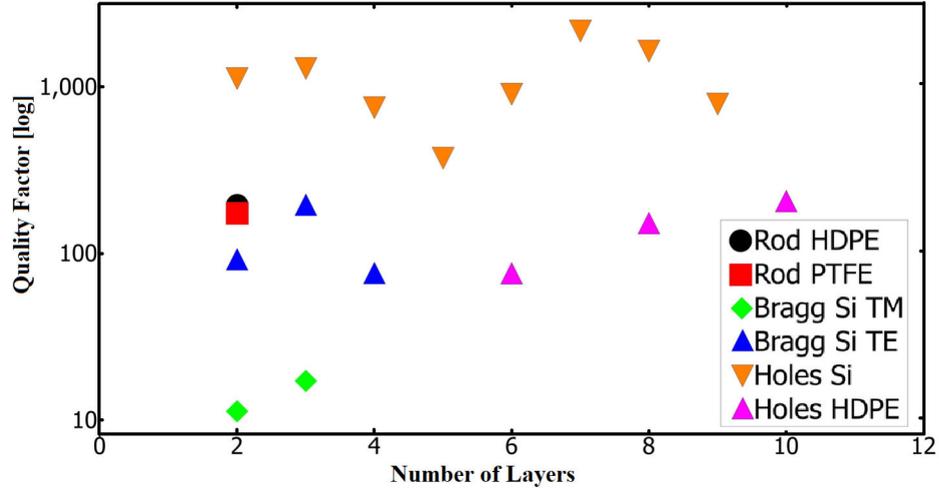
Figure 4.7: The simulated reduction of the quality factor due to parasitic modes in the band gap can be seen in the periodic dips for the PC formed from holes in silicon (orange). For the TE PCs, i.e. the rod designs, the finite size leads to a degradation of the performance and results in a complete suppression for a number of layers above 3. That this is a consequence of the design and not of the low refractive index material is apparent, as the TM based hole structure of HDPE is behaving the opposite way around. The parasitic modes are being suppressed with an increased number of layers, enabling a high-Q mode to form (pink).

electric field oscillates in the dimension of the infinite extension, the quality factors is five times lower with Q<20 than for the TE. As this is the structure type with the weakest confinement within the photonic crystal slab (as the mode propagates for large parts in pure air), the leakage is substantial with increased structure size. Therefore, Bragg mirrors are not suitable for slab-like structures with thicknesses on the order of wavelengths.

For the polymer photonic crystals, the rod designs outperform the hole designs with considerably higher quality factors with a maximum of $Q \sim 370$ for even a low numbers of layers ($n \leqslant 3$). However, at the same time, they only show noticeable resonances for up to 3 layers indicating again weak confinement due to internal reflection which increases due to the leakage into a substrate with the same refractive index. The HDPE holes show a reversed picture to their rod equivalent. They do not show a cavity mode for fewer than six layers. Above this value, the quality factor monotonically increases up to a value of $Q \sim 200$, but only for even numbers of layers. Odd numbers exhibited considerable losses resulting in almost

complete suppression of the cavity mode. This effect is based on the shifting of the dielectric band in which the cavity mode then radiates into and will be explained for the silicon samples, where it gives rise to the sinusoidal shape. The effect appears to be directly related to the substrate thickness, as it does not appear when the thickness is halved.

The effect on the band structure, in dependence on the finite dimensions, can best be observed with the silicon hole photonic crystal results. The silicon slab offers good confinement and the high material contrast results in high reflectivities even for a low number of layers. Figure 4.8 shows the simulated transmission with the cavity mode for a structure with 2 layers.

It exhibits the highest quality factors with $Q_{max} \sim 2200$, comparable to the values
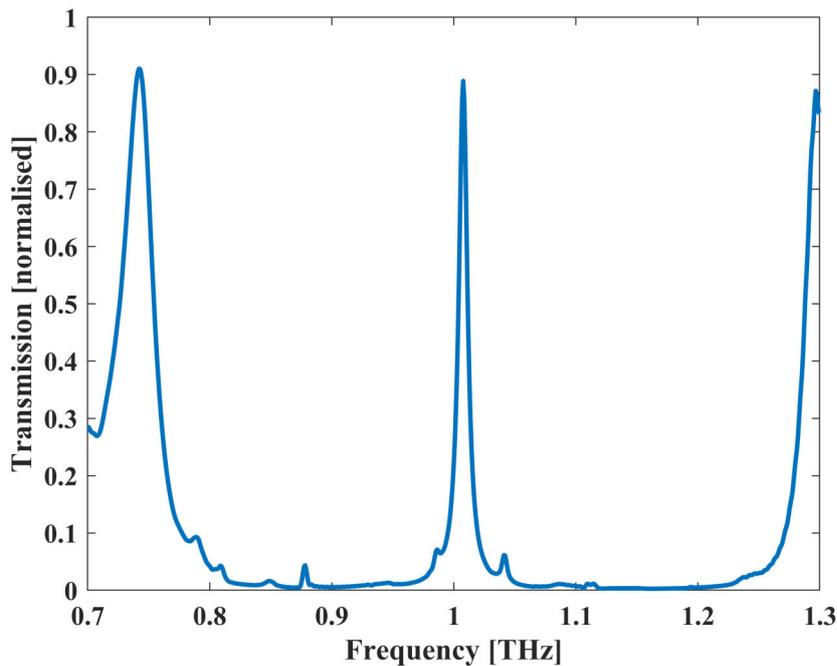


Figure 4.8: Simulated transmission spectrum of a silicon photonic crystal (hole type) with two layers. The transmission of the cavity mode can be seen at $\sim 1\,THz$.

found in literature. The fact that the quality factor is not simply monotonically increasing with the number of layers can again be explained with the parasitic modes that leak energy from the resonant mode. As an example, the shift in the highest dielectric and lowest air band of a silicon photonic crystal between a

structure with 4 and 5 layers can be seen in Figure 4.9. The bands for the 5 layer structures are shifted, offering energy states close to the cavity mode at ∼1 THz, in which energy is leaking into away from the cavity mode, which reduces the quality factor. At 4 layers, the dielectric and air bands have a sufficient spacing to the cavity mode and therefore the quality factor is higher. This explains the sinusoidal shape in Figure 4.7 as every added layer slightly shifts the bands and offers different coupling situations for the cavity mode, depending on the overall size of the slab. Simultaneously, the overall quality factor increases because of the increased reflectivity with number of layers.

This shows the importance of the consideration of all dimensions for a non-quasi infinite photonic crystal. The different geometric parameters cannot be regarded independently, for a photonic crystal with limited extension of few wavelength in more than one dimension, as the modes are dependant in a nonlinear way on all dimensions.
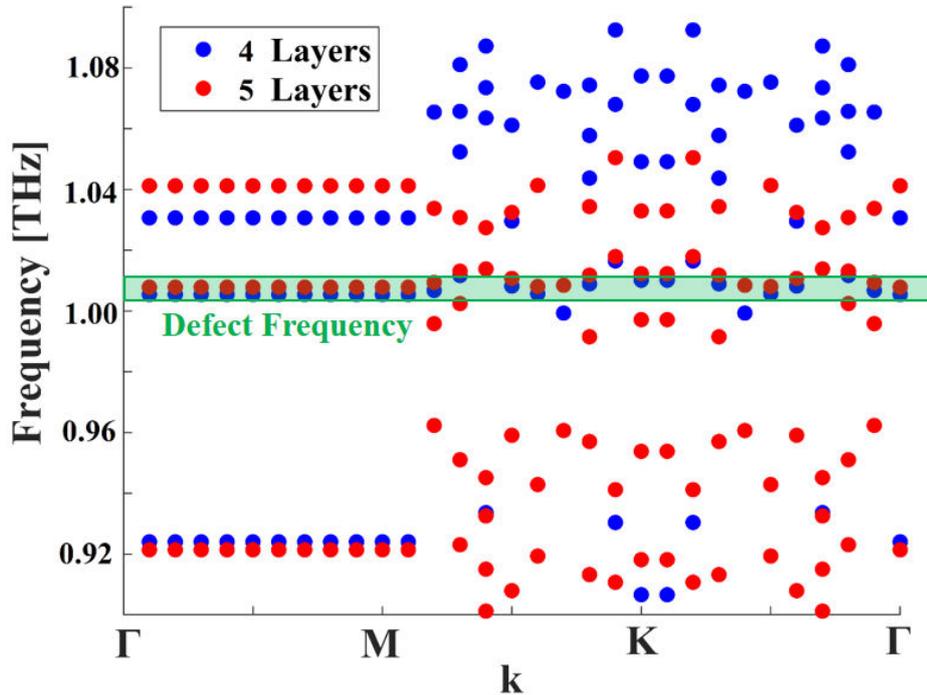


Figure 4.9: Comparison between the band structures of silicon photonic crystals (hole type) with 4 (blue) and 5 (red) layers. The 5 layer structure has shifted energy bands close to the defect mode (green) and therefore a considerably lower quality factor as a structure with 4 layers, as shown in Figure 4.7.

## 4.4 Photonic-Crystal based Enhancement of Terahertz Spectroscopy on Microfluidic Channels

### 4.4.1 Introduction

As mentioned in the introduction, THz technology promises many applications in the field of chemical and biochemical analysis due to the excitation of intermolecular vibrational modes in large molecules. The vibrational resonances, and their associated absorption, in the THz region, can serve as a material fingerprint – leading to a clear identification. However, in a realistic scenario, many of the chemicals of interest are found in aqueous solutions. This is true for many biological or biomedical applications as it is for possible quality control applications, e.g. in agriculture, where concentrations of pesticides or insecticides, such as methomyl, have to be monitored. Liquids, in general, represent a significant challenge for THz measurement systems due to high absorption losses across the frequency range. This reduces the signal to noise ratio of the instrument and can have a detrimental impact on measurement sensitivity and detection limits.

In this section, it is proposed to address these issues by placing a microfluidic channel in a photonic crystal cavity. While the combination of a microfluidic channel within a photonic cavity has been used in the optical region [116], a similar concept has yet to be exploited for the THz regime. Cavity-enhanced spectroscopy not only increases the sensitivity of the measurement, but also leads to the concept of a low-cost THz fingerprint spectrometer which not only identifies substances but also can quantify the amount of different substances in a mixture. To study the enhancement effect of the cavity, the model of a simple photonic crystal was chosen in the first instance consisting of two identical quasi-infinite HDPE Bragg mirrors with a one wavelength long defect in the centre. The microfluidic channel runs through the centre of the defect and carries the chemical under investigation. A series of such devices could deliver a finger print of a material, each individual

device being designed to have a transmission line at a different, specific frequency. In combination with THz diodes, this would constitute a low-cost room temperature THz lab-on-a-chip device which is compact and robust enough for real-world applications. Here, the simulation results from a single photonic-crystal-enhanced microfluidic device are discussed to demonstrate the potential for increased sensitivity. Due to the high absorption of the liquid-filled cavity, it is important to balance the enhancement and the transmission, which can be achieved through tuning the Q factor with the methods from the previous section.

A schematic of the proposed device concept can be seen in Figure 4.10. The microfluidic cells are connected via tubes to an automatised syringe on one side and a collecting vessel on the other side, allowing measurements of a continuous flow. The design here is optimised to the frequency range of the Terahertz network analyser with a frequency range from 0.75 to 1.1 THz as used in Durham.
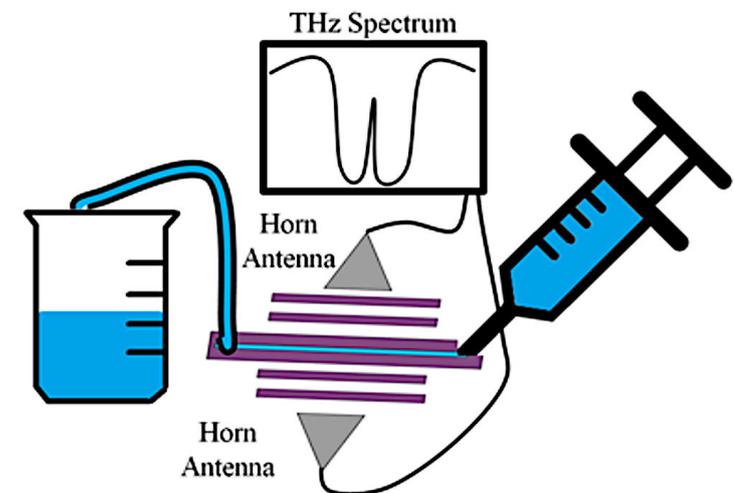


Figure 4.10: Illustration of the experimental setup. A syringe pumps the aqueous solution (blue) into the microfluidic channel in the photonic crystal (purple). After passing through the channel the liquid gets disposed of in a beaker. The horn antennas of the network analyzer (grey) measure the photonic crystal in transmission recording the spectrum.

## 4.4.2 Design and Simulation of a Simple Bragg Cavity with Embedded Microfluidic Channel

The Bragg mirrors which flank the microfluidic channel are formed from stacked pairs of HDPE and air layers; each layer with a thickness of $\lambda/4$. The $\lambda$-sized defect in the centre is also formed from HDPE and contains the microfluidic channel. The $20\,\mu$m wide microfluidic channel is located in the centre of the defect which is the point of maximum electric field strength. The result is a photonic crystal, schematically illustrated in Figure 4.11a, with a propagating defect mode at $0.85\,$THz, in the centre of the band gap (Figure 4.11b). As an interesting example of a test chemical, water and a 5% aqueous solution of the insecticide methomyl are used in the simulations; methomyl has already been characterized in the THz region [117]. The permittivities used in the simulations can be found in Chapter 7. The simulation results from the cavity are optimized with respect to the sensitivity of the transmitted signal and power of the defect mode by maximising the change in signal between pure water and the aqueous methomyl solution while simultaneously keeping the transmission above -30 dB, as otherwise noise becomes a significant factor during the readout.

To demonstrate the enhancement, the simulated change in transmission of a mi-
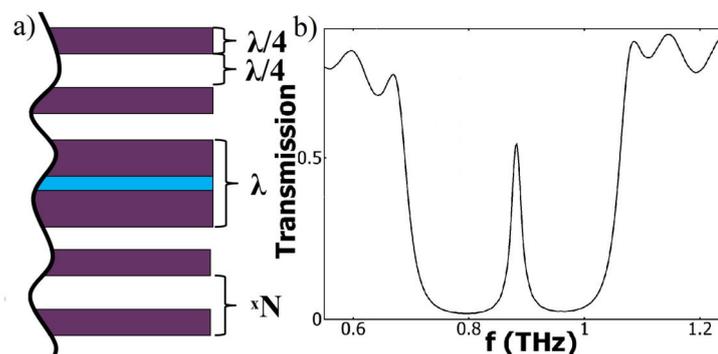


Figure 4.11: a) Schematic of the photonic crystal with two identical Bragg Mirrors at the top and bottom with N layer pairs flanking a defect with the microfluidic channel in its centre. b) Transmission spectrum of the photonic crystal with 3 pairs of layers in each Bragg mirror without a fluid present.

crofluidic channel filled with pure water is compared to the same channel filled with a 5% aqueous solution of methomyl. It can be seen in Figure 4.12 that the simulated change in transmission for a plain microfluidic cell without any photonic crystal is around 1% and therefore even lower than the amount of added material. When the microfluidic channel is placed in a photonic crystal, the simulated change in transmission increases with the number of layers of the Bragg mirrors, just as two layers of photonic crystal on each side of the microfluidic channel increase the change in transmission from ∼1.3% to 4%; three layers have a maximum change of 7%. But, simultaneously, due to the overall reduction in transmission with an increasing number of Bragg mirror layers, the change in power reaches a turning point for more than 5 layers (Figure 4.12 inset), meaning that other material losses become dominant and the point of optimum balance between enhancement and losses has been exceeded. Considering a realistic scenario where the signal has to be kept at measurable levels, a cell with more than 4 layers is of limited interest anyway, since the transmission drops to less than 1% posing a challenge to discriminating any changes of signal in a realistic measurement scenario. This leads to an optimal design of 3 to 4 layers in each Bragg mirror. But this still equals an enhancement of the factor of above 6 for the targeted measurement equipment and higher for more sensitive equipment.
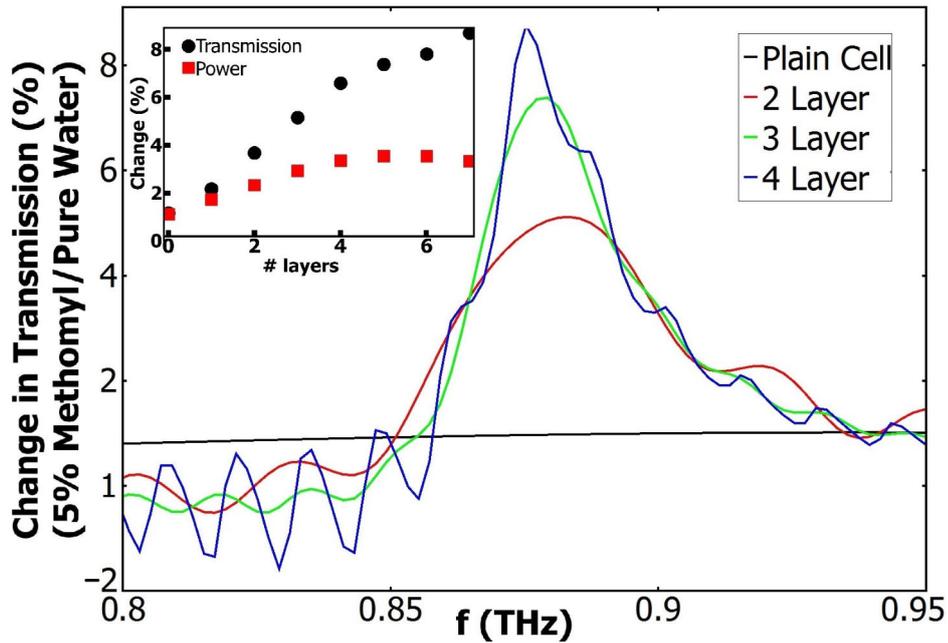
Figure 4.12: The simulated change in transmission through a microfluidic channel filled with pure water is compared to the transmission through a channel with the analyte, a 5% aqueous solution of methomyl. The change in transmission through a channel located in a photonic crystal is larger than the change in a plain cell (black line) and an increased number of layers leads to an increased change in transmission. The power decreases if more than 5 layer pairs are used for each Bragg mirror stack (inset).

## 4.4.3 Integrating cavity-enhanced microfluidic channels in photonic crystal waveguides

While the enhanced sensitivity of spectroscopic measurements on microfluidic channels placed in a photonic crystal cavity has been shown in the previous section, the quasi-infinite structure employed is lacking convenience for a real-world application. It would be more convenient for an application to integrate the microfluidic channel and its cavity with a photonic crystal waveguide which can be directly connected to sources and detectors in a lab-on-a-chip device. As photonic crystal waveguides that use resonant tunneling diode (RTD) have been already demonstrated around 300 GHz, and RTDs are more commonly available at these frequencies, it is the logical step to adapt the design from the previous subchapter to these frequencies for a demonstrator. The photonic crystal waveguide described by Tsuruda et al. in

[52] has $72\,\mu$m holes in a hexagonal lattice with a lattice constant of $a = 240\,\mu$m on a $200\,\mu$m thick substrate. The waveguide itself comprises a line-defect so that the photonic crystals on both sides of the defect provide the confinement within the substrate. The thickness of the slab and the contrast in refractive index provides confinement in the plane of the substrate. While the waveguide can guide radiation over a broader frequency range, only the range from 0.318 to 0.336 THz is supported by a fundamental mode, and the higher frequencies are carried by higher-order modes, resulting in higher losses [52]. There will be three different designs simulated to integrate the cavity with the photonic crystal waveguides. The first one being a cavity defect directly placed in-waveguide, as this is the most straightforward implementation of the concept from the previous subsection. As this first design does not address the low-loss frequency domain, the second design uses a larger cavity, which does, albeit with the trade-off of losing the single-mode property of the first design. The third design is a circular cavity that is next to the waveguide, which is coupling the evanescent field of the waveguide; this design has proven to exhibit high Q-factors of 1600[118]. As a higher Q-factor also results in higher losses when an absorptive medium is present in the cavity, the Q-factor actually can be too high as will be discussed later.

## 4.4.4 Methodology for Data Extraction

Due to the multimode nature of some of the cavities investigated here, the previously described high-Q extraction method cannot be applied. Additionally, as the introduction of the high absorbance liquid dampens the Q factor considerably, a different method to evaluate the performance is required for the filled microfluidic channels. Therefore, a variant of the low-Q extraction method is employed with some limitations due to the high-Q nature of the simulations with empty microfluidic channels. The transmission curves are obtained with FDTD simulation, and the resonant nature of the cavities means that there is a trade-off to be made between simulation time and the precision of the simulation, as described in Sec-

tion 4.3.2. Hence, the simulations are ended before all the energy is dissipated due to limited computational resources, which results in lower Q-factors.

Therefore, the Q-factors can be seen as minimum values, but the centre frequency would not change with longer simulation times and it was ensured that the intensity of the original electric field strength of the resonance falls under 10%, so that a majority of the intensity is captured and the results are consistent. This coarser value is necessary as the simulation domain size is significantly increased to account for the photonic crystal waveguide. The simulation of the whole device, waveguide and cavity, is necessary as the fundamental mode of the waveguide has to couple to the cavity mode and this is the only way to account for this in simulation. Consequently, an empty waveguide and cavity combination is first designed as the simulations are significantly shorter with no fluid present, and the geometry parameters are swept over a wider range. Cavity size and defect position are changed during those geometry parameter sweeps to find the maximum Q-factor in the low-loss guiding-region of the waveguide. When an optimal design candidate is found, the structure is simulated with a fluid present. The change in the transmission is recorded as in the previous subsection. For the simulations with a fluid present, the simulations are long enough so that the original electric field decays to less than 1%. This increases the accuracy of the results significantly which is necessary as the quantity of the transmission is required to measure the enhancement.

### 4.4.5 Compact in-waveguide Cavity Design

The cavity of the compact in-waveguide design (Figure 4.13) consists of 3 holes using the smae lattice and hole-size as for the photonic crystal waveguide, except for the central hole which has a different size to generate the defect mode within the stopband, and therefore hereafter is referred to as "the defect". This particular design has a connection between the microfluidic channel and defect, which is also filled with liquid.

With this defect, it is possible to tune the resonant frequency of the cavity by
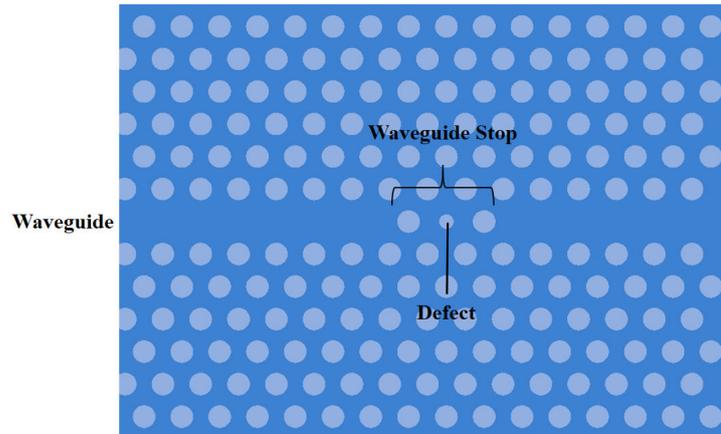
Figure 4.13: Schematic of the in-waveguide cavity design. The microfluidic channel (not shown) is placed in the centre and therefore connected to the defect hole.

changing the size of the defect hole. As Figure 4.14 shows, this works as expected for defect sizes smaller than $72\,\mu$m hole size of the photonic crystal, where the positioning of the defect mode (pulled down into the band gap from the airband), directly correlates to the defect size. In theory, a larger defect should provide a "push up" from a lower band mode, which would allow coverage of the rest of the waveguide range. However, this is not the case, and none of the larger defect sizes investigated of up to $112\,\mu$m showed a transmission within the defect region, which might be explainable due to the more complex mode coupling structure mentioned earlier, as the simple models with "push up" and "pull-down" come from idealised (quasi-infinite) systems with single modes.

As Figure 4.14 also shows, the resonant frequencies of the cavities do not lie in the ideal region of $0.318 - 0.336\,$THz. Usually, one would try to increase the lattice constant between the individual defect holes to reduce the frequency, but in this case, this leads to a multimode system. Even removing the defect hole completely, which would represent the extreme case of the smallest defect size with a radius of $0\,\mu$m, does not lower the frequency enough to reach the desired frequency range.
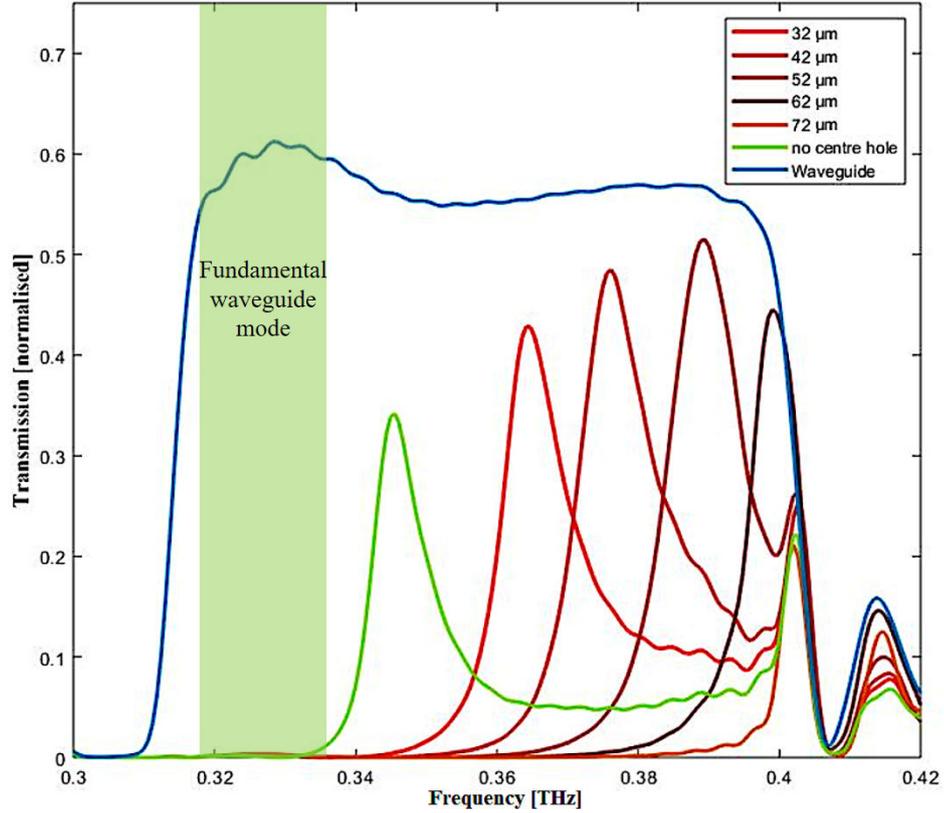
Figure 4.14: Simulated spectra for the compact in-waveguide design. The dependency between defect size and resonant frequency is as expected: the smaller the defect, the more the defect mode is "pulled down" (red curves). But even for the smallest size of the defect of $0\,\mu$ m (green), which corresponds to the centre hole missing entirely, the defect mode does not reach the desired region with the highest transmission on the left of the waveguide (blue).

## 4.4.6 Large Cavity in-waveguides design

The cavity consists of two sets of holes, with the inner holes on both sides being offset from the lattice and reduced in size, as seen in Figure 4.15. The cavity can be tuned over its lattice constant $a$, hole offset $dx$ and hole size reduction $dr$.

As the design space becomes more complex with three variables only two examples for the influence of the factors of $dx$ and $dr$ are shown in Figure 4.16 besides the design with the parameters used. Due to the more complex variable space, a design with a high transmission defect mode in the desired region was chosen, for which the geometric parameters were optimised using the built-in particle swarm method
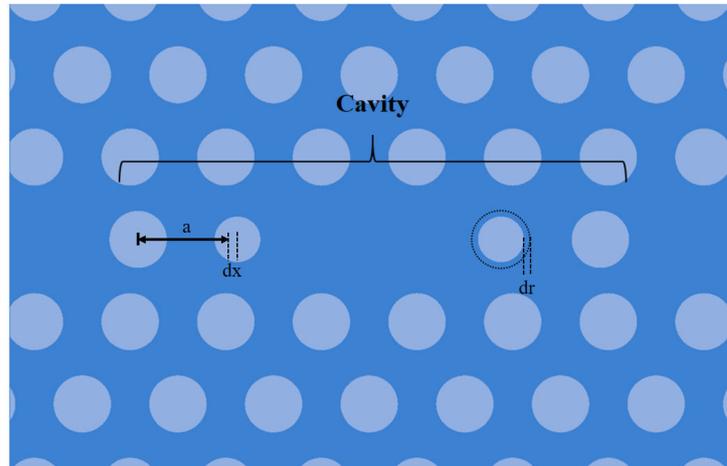
Figure 4.15: Schematic of the large cavity in-waveguide design. The geometric parameters to tune the resonant frequency are indicated. a: lattice constant, dx: offset of the smaller holes, dr: size reduction of the smaller holes.

of Lumerical on all three variables to maximise the Q-factor.

### 4.4.7 Cavity-Coupled-waveguides design

Instead of integrating the cavity directly into the waveguide, it can also be placed next to and is coupled through the evanescent field reaching into the photonic crystal. As the isolation is large compared to the in-waveguide cavities, less radiation leaks out of the cavity and Q-factors above 1000 can be achieved [118]. The cavity-coupled-waveguide design consists of two parallel waveguides coupled over a circular cavity, as seen in Figure 4.17. The cavity is comprised of seven holes, with the outer holes of the circle completely missing and the centre hole being variable in size to tune the resonant frequency of the cavity. The radiation is transmitted from the injection waveguide through the cavity to the measurement waveguide. The cavity is separated by only one row of holes from the waveguides, which represents the strongest coupling. A stronger separation would increase the quality factor by leaking less energy, but would also reduce the overall transmission.

Both waveguides, called injection and measurement waveguides according to their
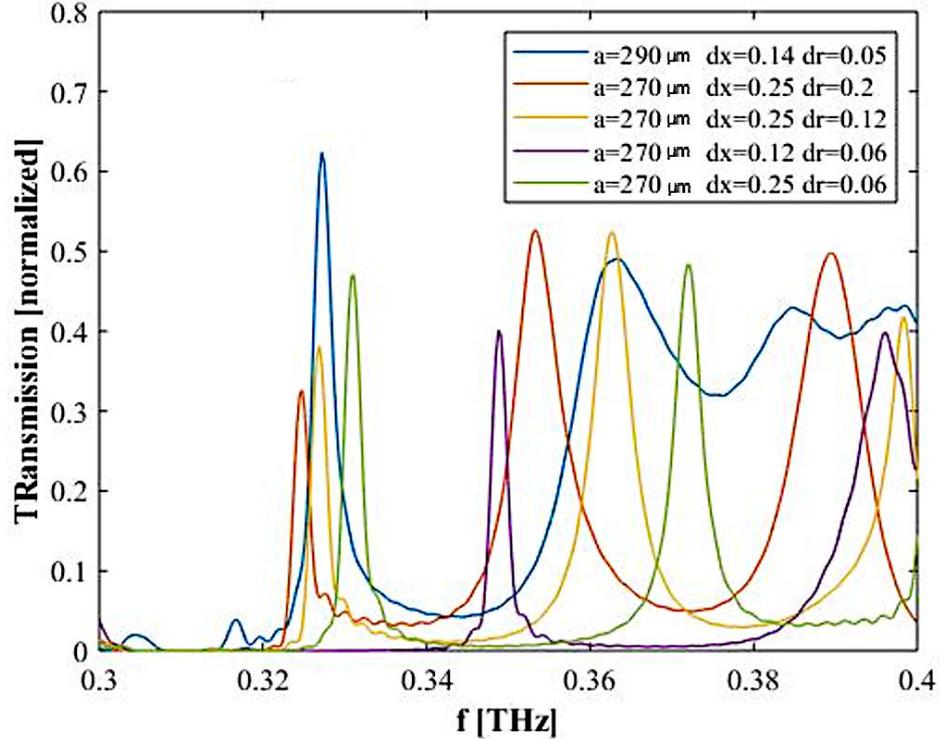
Figure 4.16: Simulated spectra for the cavity in-waveguide design. The resonant frequency can be tuned over three parameters: a: lattice constant, $dx$: offset of the smaller holes, $dr$: size reduction of the smaller holes. Beside the starting design used for the optimisation (blue), there are two pairs of graph shown; one shows the effect of the change in $dr$ (orange, yellow) and one shows the effect of the change in $dx$ (purple, green).

function, have a waveguide stop integrated to maximise the amount of radiation transmitted from the injection to the measurement port. The inset in Figure 4.18 shows that results from the simulations for all the investigated defect modes for centre defect sizes ranging from $32\,\mu$m to $112\,\mu$m lay within the preferred low-loss fundamental mode frequency range and the tunable range is also visible in Figure 4.18. The cavity-coupled-waveguides provide higher Q-factors than the in-waveguide designs when comparing the spectra of both, with the former exhibiting Q-factors in excess of 100 and the later having Q-factors below 50.
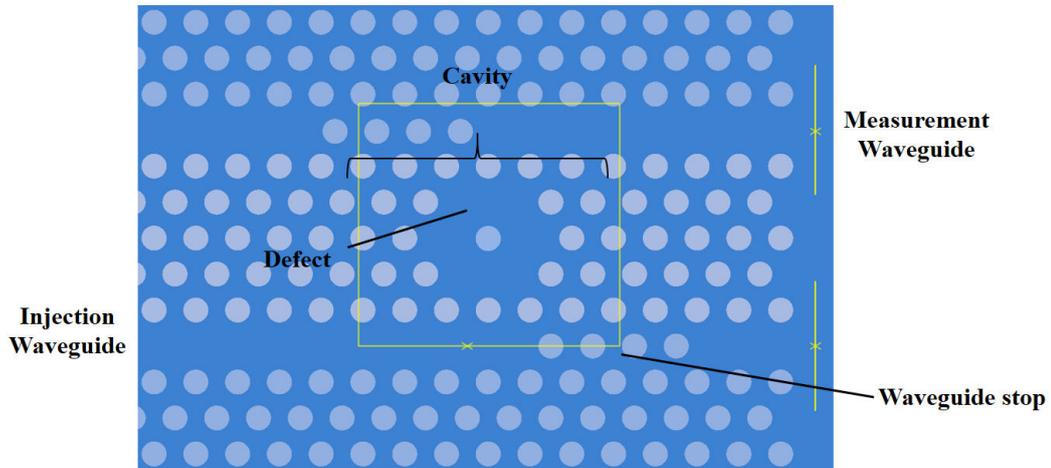
Figure 4.17: Two waveguides are coupled over a cavity. The resonant frequency can be tweaked through the size of the central defect.
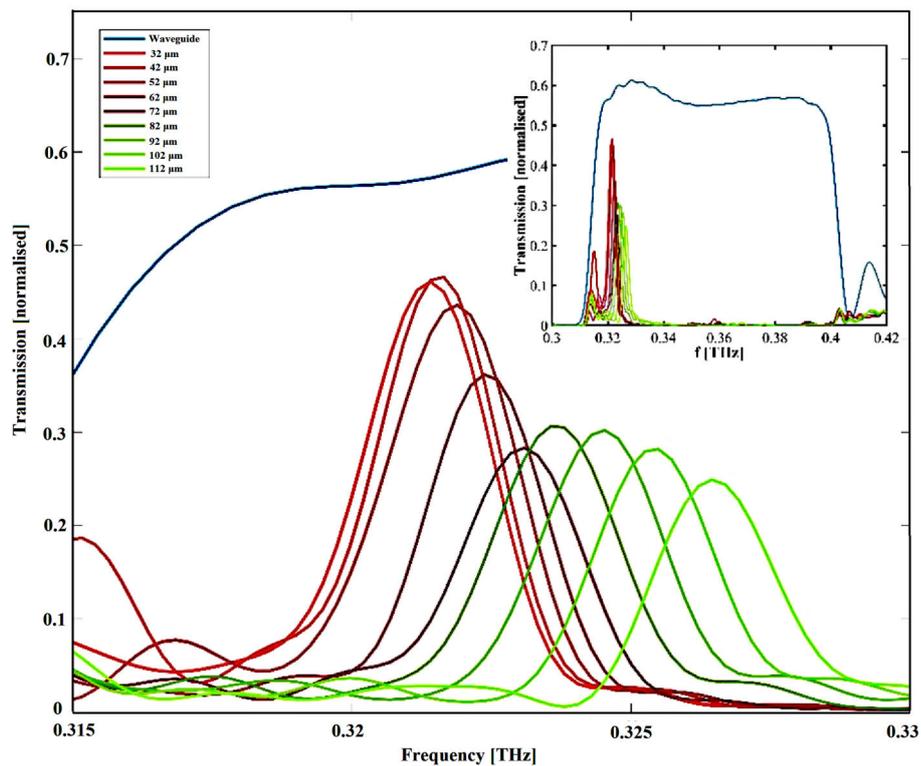


Figure 4.18: Simulated spectra of the cavity-coupled-waveguides. All cavity modes lay within the low-loss region of the waveguide (inset). Changing the radius of the centre hole of the defect cavity allows tuning of the cavity range over the whole low-loss frequency span supported by the waveguide.

## 4.4.8 Enhancement Effect on Microfluidic Channels

To evaluate the enhancement a reference has to be used to show the increased change in signal when a liquid is present.A bare microfluidic channel is used, without any additional structures but with identical geometry, which is placed across a straight waveguide as reference. As an exemplar chemicals, pure water and an aqueous solution of 5% insecticide methomyl are again used. Using a different aqueous solution for experiments might be beneficial as methomyl does not exhibit any specific features in the absorption spectrum at these frequencies and other material combinations might be less toxic and allow for a higher solubility. As Figure 4.19 shows, the transmission for the two fluids is almost identical, with an average change of approx. 1% and up to 3% as maximum change at the edge of the guiding frequency range. Therefore, the change in transmission is actually smaller than the amount of material added, which makes it challenging to detect smaller changes in the composition of the liquid.
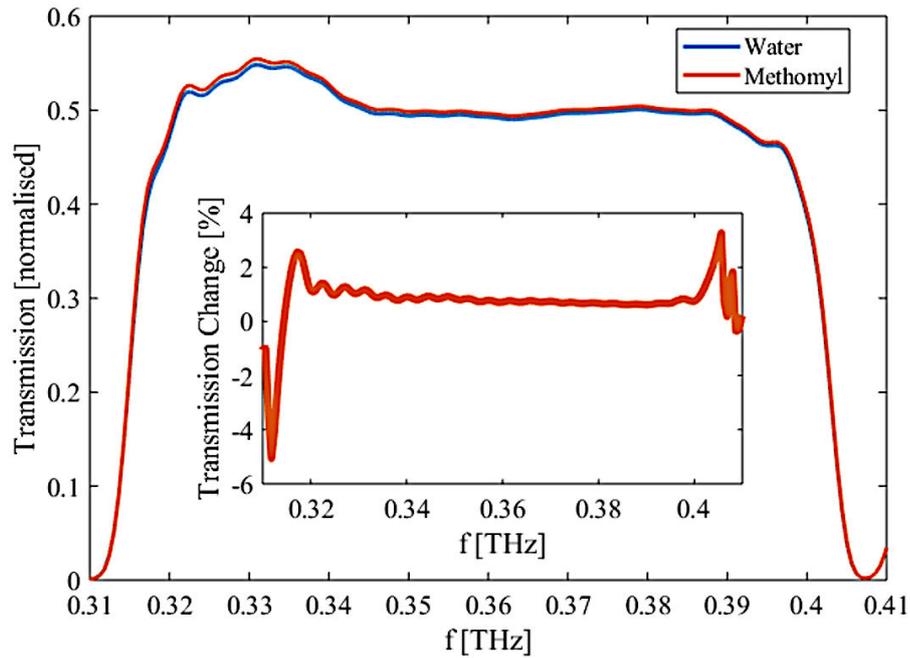
Figure 4.19: Simulated spectra showing the transmission through the microfluidic channel for pure water and an aqueous solution of 5% methomyl. The change in transmission (inset) is smaller than the added amount of chemical with an average of $\sim 1\%$.

For the compact cavity design shown in Figure 4.20, the original transmission peak is flattened completely (compare Figure 4.14) and the transmission is greatly reduced so that the transmission at the edge of the waveguideing frequency band now looks like a peak. The change in transmission (Figure 4.20b) reaches its maximum at the same frequency that previously exhibited the peaks without a liquid present. The maximum change in transmission is around 7%, which is a significant increase over the bare channel.

For the larger cavity in-waveguide design the peak shape is maintained and the largest change also is observed at the peak frequencies, as seen in Figure 4.21. With almost 10% change, the change is even larger than for the previous design while maintaining reasonably high transmission.

It is worth mentioning that the microfluidic channel for this design is not placed in the centre due to the electric field distribution but rather on the edge of the cavity. This is already known from the design of the Bragg cavities and can be
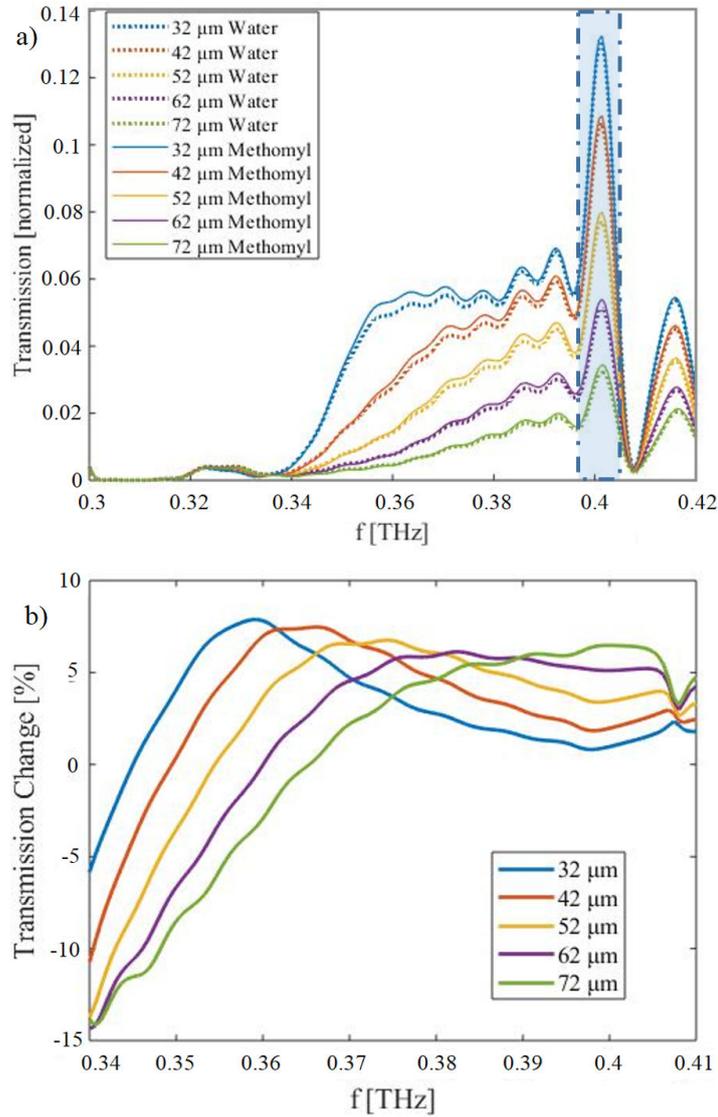
Figure 4.20: a) Simulated spectra for the compact in-waveguide cavity design filled with fluid. The previous transmission peaks of the empty structures are flattened by the absorption in the microfluidic channel, but the maximum change in transmission corresponds to the previous peak frequencies (b). While the peaks on the edge of the waveguide in the highlighted area look like resonances, they are not the the defect modes and therefore less affected by the change in transmission.

easily addressed by placing the microfluidic channel at the edge, as displayed in Figure 4.22.

The previously mentioned swarm optimisation was set to maximise the transmission at the centre frequency of the guiding mode when water is present. This optimised structure exhibits an increased change in signal of ~11%, as seen in
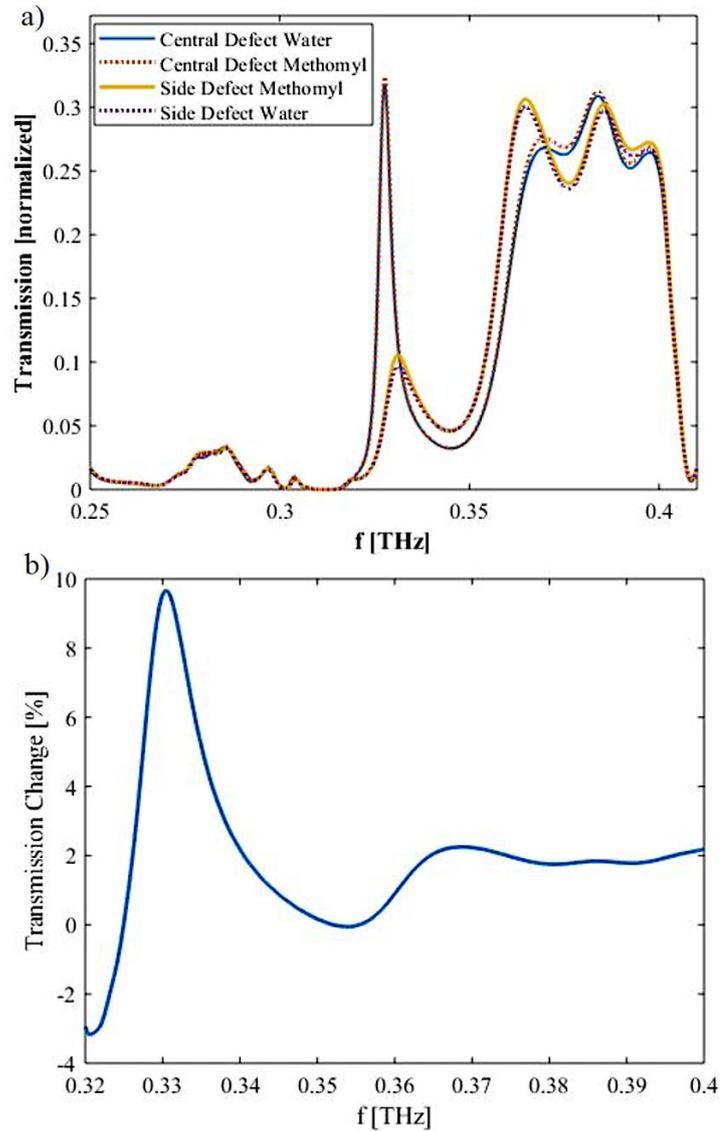
Figure 4.21: Transmission (a) and change in transmission (b) for the larger cavity in-waveguide (a=290 $\mu$m, dx=0.14, dr=0.05). While there is hardly any change in transmission when the microfluidic channel is placed in the centre of the cavity, the change in transmission is large when the defect is placed on the side of the cavity (right), as seen in Figure 4.22.

Figure 4.23, showing that the second optimisation has successfully increased the sensitivity.

Despite its larger quality factor, the observed change in transmission for the coupled waveguide design is smaller with a maximum of ~3.5% (Figure 4.24). This might be partly explainable due to the more complicated electric field distribu-
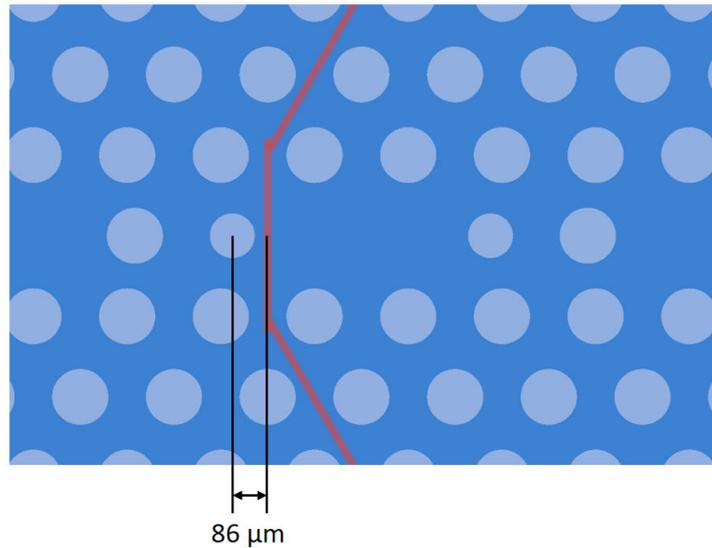
Figure 4.22: Due to the electric field symmetry there is no change in transmission when the microfluidic channel (red line) is placed in the centre of the cavity, but the change is large when the channel is placed the edge as depicted here.
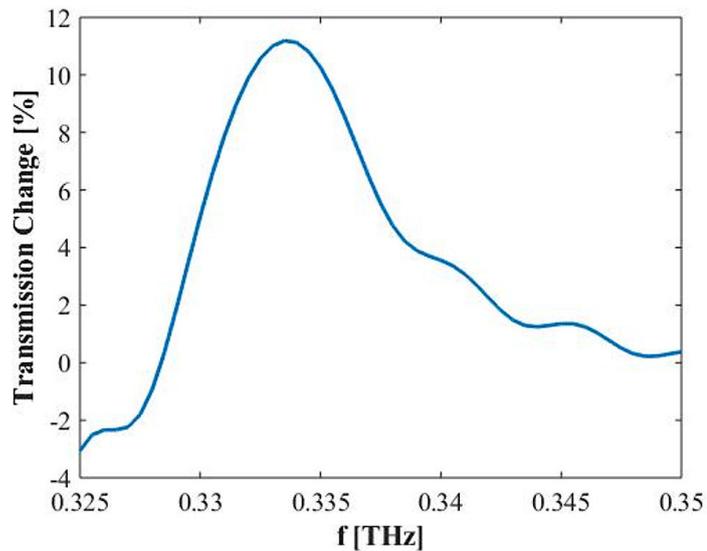


Figure 4.23: The transmission of the particle swarm optimised cavity exhibits a larger change in transmission than the original structure (Figure 4.21).

tion in the cavity itself and the difficulty in placing a microfluidic channel without drastically reducing the transmission. The results shown here are a compromise between change in transmission and transmitted signal so that they are more comparable to the other two designs. This demonstrates that for a maximum enhancement of the sensitivity, it is not sufficient to simply maximise the quality

factor when an absorptive medium is present in the cavity.

In summary, it can be stated that the most significant factor to maximise the
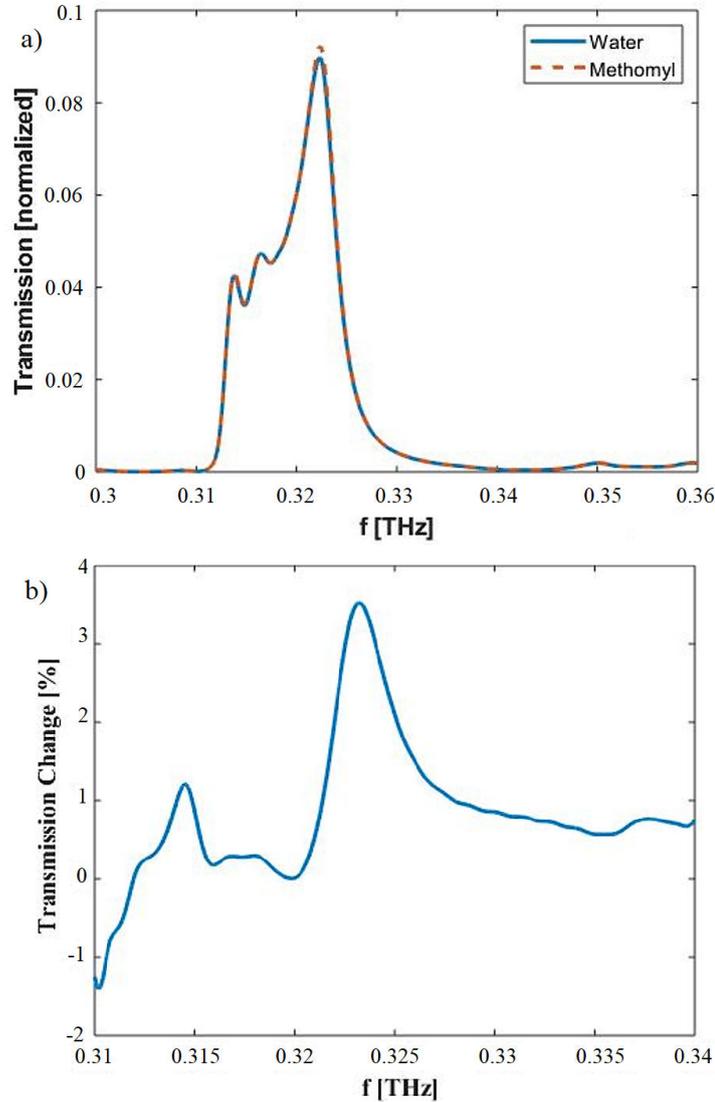


Figure 4.24: Simulated transmission spectra for the coupled waveguide design (a). Due to the complex mode distribution and the need to place only small parts of the microfluidic channel in the cavity due to the high absorption caused by the high Q factor, the change in transmission (b) is lower for the coupled waveguide design than for the previously shown designs.

enhancement effect of the cavity for sensing is to balance the transmission to the absorption of the material. While the cavity does not have to be single mode to achieve the maximum change in transmission in the 1D cavity, as shown with the swarm optimised design, the more complex electric field distribution in the larger

2D cavity is negatively influenced by the introduction of the liquid medium, resulting in a lower enhancement of the sensitivity despite a higher Q-factor of the cavity.

## 4.5 Conclusion

The design of photonic crystals cavities for the enhancement of THz spectroscopy has been discussed. First, simple cavities out of different common and ready available THz materials have been designed. Maximum quality factors of $Q_{max,polymers} \sim 200$ and $Q_{max,silicon} \sim 2200$ have been achieved for the low-refractive index polymers and high-refractive index silicon, respectively. The influence on the cavities of strong geometric constrains with extension in the order of the waveglength for more than one dimension has been discussed. These geometrical constraints deviate from the infinite-extended case of the ideal photonic crystal and introduce parasitic modes. These parasitic modes can couple to the cavity defect mode and leak energy from it, therefore reducing or completely suppressing the cavity defect modes. This effect could be observed as complete suppression for the polymer photonic crystals, which showed no cavity modes for certain number of layers. For the silicon based photonic crystals, the parasitic modes lead to a reduced quality factor for certain number of layers. This was proven with changes in the band diagrams depending on the number of layers in the cavity, which showed energy states shifting closer to the defect mode for number of layers with reduced quality factors.

The concepts of photonic crystal cavities have then been utilised to demonstrate their functionality in an application – the spectroscopy on fluids. It was demonstrated that cavities can be used to increase the sensitivity when sensing chemicals in solutions. To evaluate the performance, the change in transmission between pure water and a chemical in aqueous solution has been simulated. The trade-off between high transmission and high quality factors when using highly absorptive

fluids, such as water, was discussed. In a final step, the cavity is integrated with a waveguide for a lab-on-a-chip application. Multiple designs have been investigated and a swarm optimised cavity integrated into a waveguide showed the largest change in signal (>10%), as compared to a microfluidic device without a cavity which shows a change in transmission of ∼1%. The transmission through to the water is significantly reduced (approx. -25 dB), but this is still in a realistic range for an experimental setup.

# Frequency-domain THz Ellipsometry for In Situ-Measurements

## 5.1 Introduction

In this chapter, the development of an angular resolved measurement setup, based on the VNA as measurement instrument, and the subsequent extension to enable the implementation of a THz ellipsometer is discussed. The performance of the ellipsometry setup was tested with material characterisation and in-situ measurements.

The angular measurement setup was designed for Brewster angle and antenna characterisation, measuring in either p- or s-polarization, and will be discussed first. The addition of polarisation filters and the possibility to rotate the receiver over $200°$ around the optical axis enabled the system to be used as an ellipsometer which allows for material characterisation and thickness measurements. As a VNA is used for the measurements, there is direct access to the complex amplitude. Hence, the usual analysis with wave plates is not necessary and, therefore, the typical notation with Jones or Mueller matrices is also not necessary, as the p- and s-polarisation

can be measured directly. The measurement data can be directly fitted to the Fresnel equations, modified to account for reflections.

First the technical development of the measurement system is discussed. Subsequently, the testing of the performance of key properties for ellipsometry, i.e. polarisation sensitivity and the reliability of complex amplitude recordings is conducted. This is followed by the physical background of ellipsometry, continuing with the characterisation of different classes of materials and concluding with a demonstration of an in-situ measurement.

## 5.2   Physical Background

Ellipsometry is an optical technique which traditionally is used to obtain the dielectric properties of materials or the material thickness of materials with known optical properties, but other characteristics, such as the roughness, crystallinity and electrical conductivity can also be investigated in variations of the technique [119–121]. The technique is based on recording the change in polarisation of an electromagnetic wave undergoes when it interacts with materials. The name "ellipsometry" origins from the fact that light typically has an elliptic polarisation state after the interaction with matter but, in general, it is only necessary to have a known initial state of polarisation and record the change after the interaction. The typical ellipsometry setup operates in reflection, as shown in Figure 5.1. This configuration has some advantages for THz measurements, especially in the characterisation of highly absorptive materials which can be challenging to measure in transmission. The traditional quantity recorded is the complex reflectance ratio $\rho$, which is parametrised by the amplitude component $\Psi$ and the phase difference $\Delta$ and has the following relation

$$\rho = \frac{r_p}{r_s} = tan\Psi e^{i\Delta}. \tag{5.1}$$

These quantities are traditionally used, as they can be measured with only amplitude sensitive instruments in combination with phase retardation plates (wave

plates). However, with a VNA, it can record complex amplitudes, therefore it can record $r_p$ and $r_s$ directly without the need to consider $\Psi$ and $\Delta$.

However, even with direct measurement of the complex reflection, ellipsometry
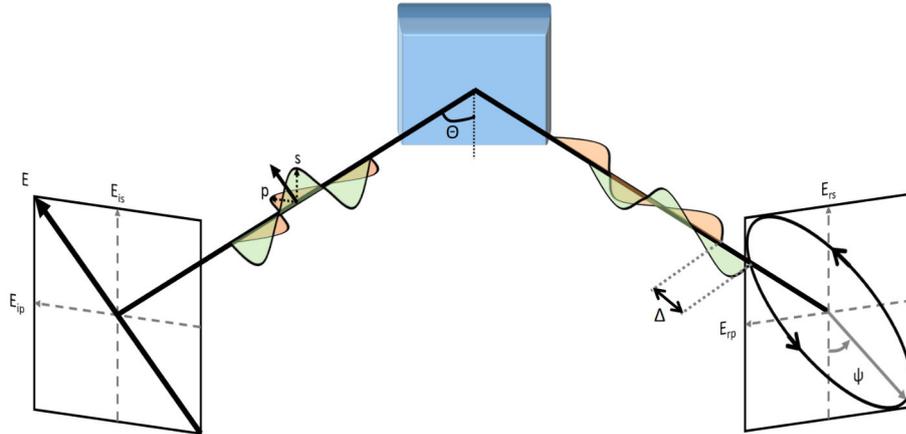


Figure 5.1: Schematic of an ellipsometry setup. An electromagnetic wave E with linear polarisation at $45°$ can be regarded as two in-phase waves with p- and s-polarisation with equal initial electric field vectors $E_{ip}$ and $E_i s$. After being reflected from the sample the amplitude and phase of both electric field vectors change, resulting in an elliptic polarisation, which is expressed in the amplitude ratio $\Psi$ and the phase difference $\Delta$ in traditional ellipsometry.

remains an indirect method. For indirect methods, the measurement results cannot be directly converted into optical constants, but have to be fitted to a model. This process can be seen in Figure 5.2 The model employed greatly depends on the sample under investigation, which means correct values can only be obtained when the structure of the sample is known. In the simplest case, sometimes referred to as "standard ellipsometry", the samples are optically isotropic, as it is the case for crystalline materials with cubic crystal structures or amorphous samples. In anisotropic materials, e.g. non-centrosymmetric crystals, "generalized ellipsometry" models are required as light can be converted from p- to s-polarisation (and vice versa). Different models also have to be applied to multi-layered samples and structured samples [122–124]. There also is a difference between single-wavelength and spectroscopy ellipsometry, the latter one being used here. While single frequency sources, such as lasers, often have higher output power and therefore better signal,

they only provide a single data set of reflection coefficient per measurement and this sparser dataset does not allow the application of some of the previously mentioned more complex models, which rely on spectroscopy data.

From a phenomenological point of view, there are two characteristics one expects
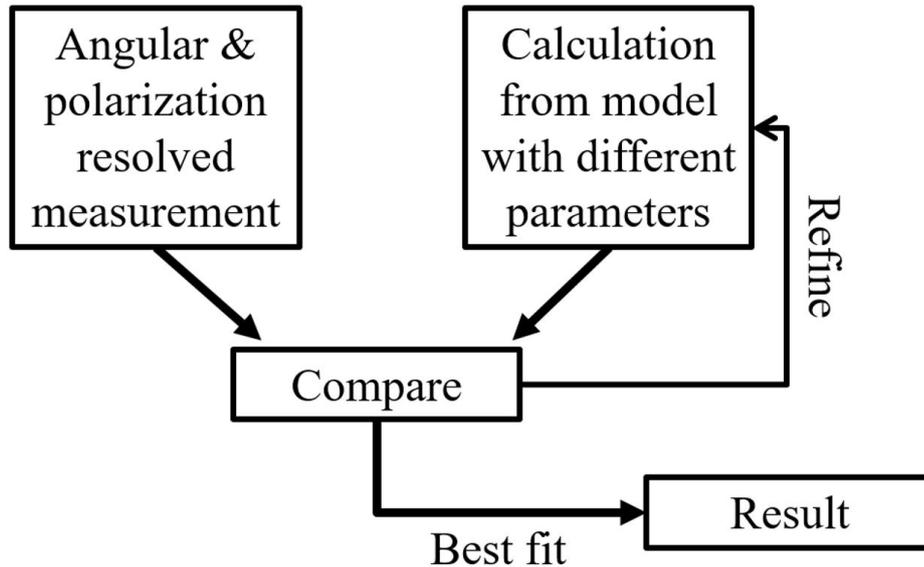


Figure 5.2: Generalised data extraction process for ellipsometry. The measurement results are compared to the results from a model. The parameters inputted into the model are varied and compared again, either until a best result within the defined parameter space is found or until a certain degree of similarity is reached.

to see in a frequency, and angle-resolved measurement – Fabry-Pérot resonances and the Brewster angle. Both can be seen in the exemplary result of an ellipsometry measurement in Figure 5.3. The former are periodic resonances appearing due to reflections in a medium with plane-parallel facets, and their periodicity is dependent on the optical path length between these facets [125]. The shape of the Fabry-Pérot resonances is a function of the refractive index and sample thickness, as seen in Figure 5.4.

The Fabry-Pérot resonances appear as horizontal lines in the plots shown in Figure 5.3. The sharpness of the resonances depends on the refractive index contrast between the material in which the reflections occur and its surroundings. The resonances are also subject to intrinsic material losses. Brewster's angle is the incident angle depending phenomena for dielectric materials at which the p-polarisation is
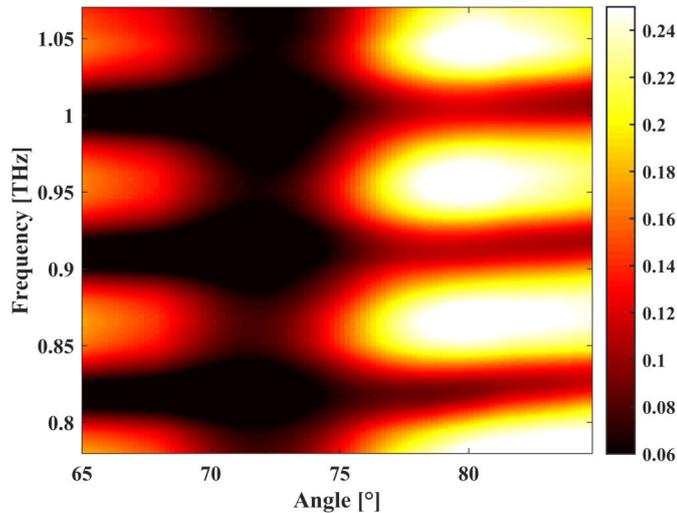
Figure 5.3: Exemplary result of an ellipsometry scan of a silicon wafer. The horizontal lines are Fabry-Pérot resonances, the vertical line is Brewster's angle.

perfectly transmitted with no reflection, and all of the reflected light will be s-polarised, as shown in Figure 5.5.

Brewster's angle occurs at

$$\Theta_B = \arctan \frac{n_2}{n_1}, \tag{5.2}$$

where $n_1$ is the initial medium and $n_2$ the other medium. Therefore, it is a very good indicator for the refractive index, especially when the initial medium is air ($n_1 = 1$). Brewster's angle will be visible as a vertical line in the plots, as seen in Figure 5.3.

## 5.2.1 Data Post Processing

As the measurement method returns 3D data, i.e. intensity over angle and frequency, a different data fitting algorithm had to be developed, as most freely available ellipsometry software, such as refit[126], only fit data at a single fixed angle. As 3D fitting of complex data is not a trivial task and not covered by the built-in fitting tools of Matlab, a different approach was chosen. The data can be visualised as a picture when the angle and frequency give a position of a pixel and the intensity the 'colour' of the pixel and, therefore, it is possible to apply comparison
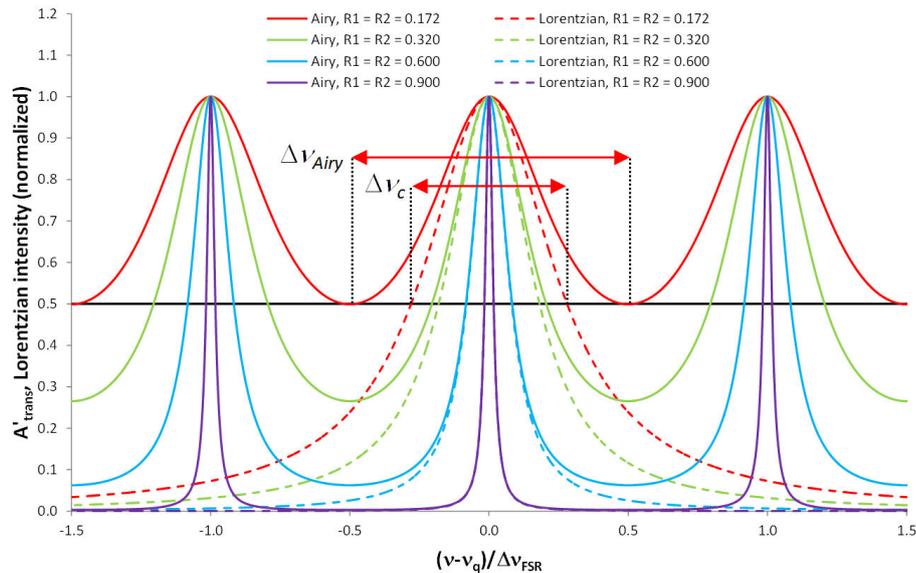
Figure 5.4: Airy distribution (solid lines), corresponding to light transmitted through a Fabry-Pérot resonator, calculated for different values of the reflectivities, and comparison with a single Lorentzian line (dashed lines) calculated for the same. The Lorentzian lines show that the higher the refractive index and thus the reflectivity, the narrower the resonances are. At the same time, the material thickness determines the spacing between resonances and therefore also changes the linewidth of the resonances, as seen in the difference between the FWHM of the Lorenzian $\Delta\nu_C$ and the FWHM of the Airy distribution $\Delta\nu_{Airy}$. From [125].

algorithms from the image processing community to obtain a metric for the similarity between the measured data and the data obtained from the model. A significant advantage of this approach lays within the different comparison method that the chosen structural similarity index (SSIM) employs [127]. The SSIM method is a technique for the prediction of perceived quality of an image which has been widely adopted since its first publication in 2004 and is one of the highest cited methods in the fields of image processing and video engineering. As it measures structural information, it accounts that pixels have strong inter-dependencies to the pixels surrounding them, which means it recognises similar structures which are, for example offset by a line or distorted, which standard mean squared errors of line by line comparison would not identify. Another advantage is that the SSIM can be easily modified to be locally and quasi-convex, which makes it a suitable target for an optimisation function as convexity is required for convergence [128]. These
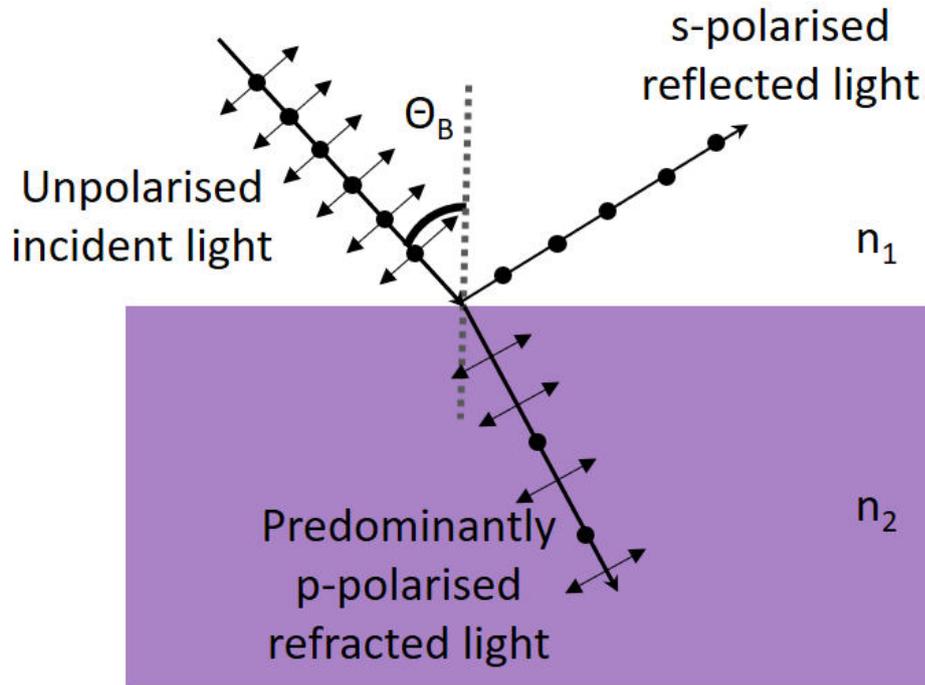
Figure 5.5: Illustration of Brewster's angle. The reflection of the incident unpolarised light is completely s-polarised.

properties make the algorithm employed here significantly faster than line by line fitting, as the total image is compared at once.

The general fitting process is conducted according to the schematic in Figure 5.2, where an initial guess is used to create the image from the model data, which is subsequently compared to the image generated from the measurement data. For the comparison process, the magnitude and phase are plotted for s- and p-polarisation individually. The intensity is normalised so that it always lies between 0 and 1. The normalisation is necessary, as otherwise, the images calculated with the model would be on different brightness scales. The image so processed is compared to the image calculated with the model with the SSIM method. In an iterative process, the constants in the model are adjusted and the comparison process is repeated for magnitude and phase for each polarisation until the SSIM reaches a local maximum.

To give an impression of what values are to be expected for the SSIM for a good fit, an example is given here, but there are more examples in the literature [127]. The

SSIM has a minimum value of 0 and a maximum value of 1. To get an impression of how much it changes, the example shown in Figure 5.6 has an index value of 0.9407 while adding only a small amount of noise to the photo. Therefore, similarly high values for the THz measurements are not to be expected due to the noise occurring at the low intensities available from THz instruments, especially in the reflection configuration used. To account for the better quality of a fit with higher SSIM the results of the different fits from p- and s-polarisation are weighted with the SSIM by averaging with

$$n = \frac{SSIM_p \; n_p + SSIM_s \; n_s}{SSIM_p + SSIM_s}.$$

(5.3)



Figure 5.6: The example photos can give an impression on which values of the SSIM can be expected. Despite only little noise being added, the two pictures have a SSIM of 0.9407. From [129].

## 5.3 Technical Development

### 5.3.1 Angular measurement setup

To allow for a change in angle, the VNA extender heads are placed on movable plates. The technical drawing of the components of the setup without the VNA

extender heads and optics can be seen in Figure 5.7. The plates are connected with movable links to an optical stage which pushes them. As they are fixed to the optical table in the red marked location, they pivot around this point. This configuration allows for a simultaneous change in the angle of both extender heads with a single stage. It is possible to disconnect one plate to vary a single angle, as it has been done in the angular resolved measurements in Section 6.4.2.4.

To reduce friction while being pushed, the plated have bearings on each side. Mul-
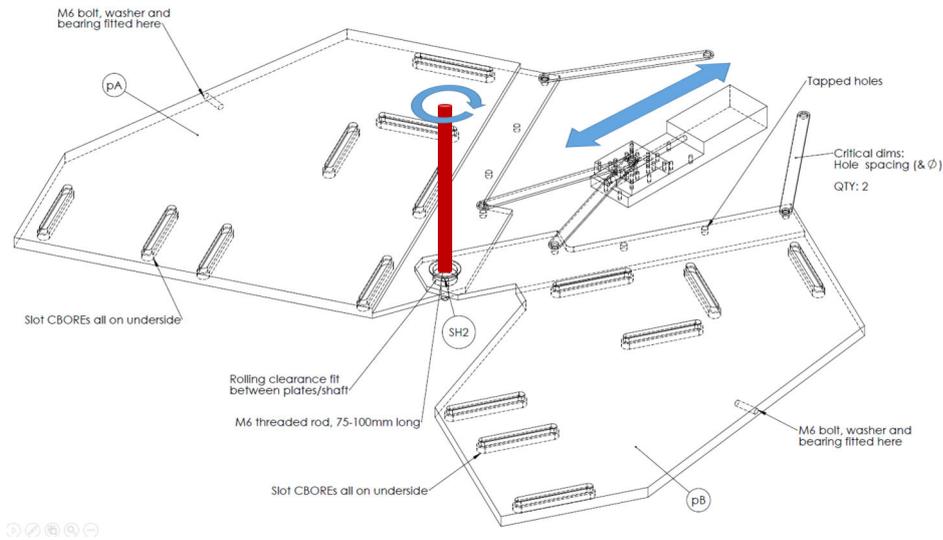


Figure 5.7: Technical drawings of the mechanical components of the angular measurement setup. The plates are pushed by the linear optical stage and pivot around the point marked in red.

tiple slots are available to allow for different configurations of optical components. It is possible to measure using a collimated and a focused beam, or by directly placing the extender heads without any beam path optics. The VNA extender heads are either mounted on standard optical posts for measurements at p-polarisation or on L-brackets for measurements in s-polarisation. Hence, for a change in polarisation, the system has to be realigned. The realignment is a significant downside of the system that was overcome with the extension to the ellipsometry setup, to be discussed in the next section. For measurements with changing incident and exit angle, the sample is placed at the pivot point.

The plates can be screwed together in the parallel position. This allows for easy

alignment by placing an iris at the pivot point as the system can be treated as a conventional two-mirror transmission setup.

As the available linear stage that pushes the plates has a limited travel distance of 15 cm, there are multiple places to attach the links on the rotational plates and the adapter plate on the linear stage which allow to address different angle ranges, as illustrated in Figure 5.8. While some of the angle ranges could be larger from a purely geometrical point of view, the stage has proven too weak to push the plates when the angle between links and direction of travel is too high.

The angular setup is controlled over a Matlab Graphical User Interface (GUI)
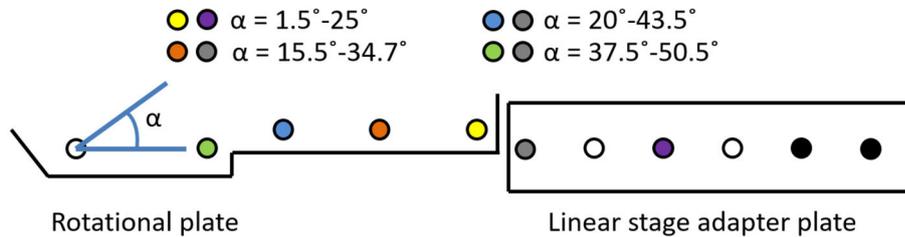


Figure 5.8: Schematics of the different link connection points on the rotational plates and the adapter plate for the linear stage. The colour coding shows which combination of two linking points results in which angle range.

which the relevant measurement parameters, such as the angular range, angular resolution, frequency range, number of frequency points, IF bandwidth and number of averages to be set. The GUI also displays a 2D map of the measurements, where the angle and frequency are displayed on the x- and y-axis respectively, while the colour indicates the signal strength. The live monitoring is a convenient feature for longer measurements enabling any measurement issues to be identified early on.

## 5.3.2   Ellipsometry Setup

To upgrade the angular system to the ellipsometry setup shown in Figure 5.9, a few additional components had to be constructed. First, the transmitting head is mounted on a $45°$ stand. Therefore, the p- and s- polarisations have equal intensities, without remounting and realigning the extender heads. The receiver is

mounted on a rotational stage that rotates around the axis of propagation, allowing the measure p- and s-polarisation by rotating the head from a horizontal to a vertical orientation. The development of a THz polariser was necessary as direct transmission measurements have shown that the difference between both extender heads in the same orientation vs one of them rotated by 90° was only around 3 dB, indicating that they exhibit a low polarisation selectivity, which is not surprising as the horn antenna radiates about 10% of the power into the cross-polarised component Chapter 7.
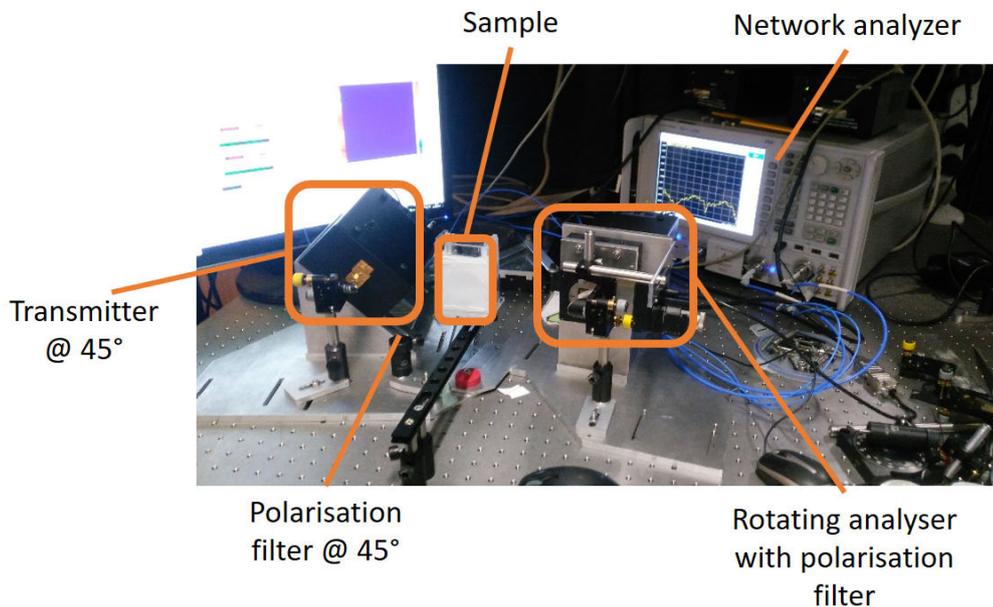


Figure 5.9: Photo of the ellipsometry setup with the key components indicated.

### 5.3.2.1 Polarisation Sensitivity

As a high polarisation selectivity is necessary to minimise cross-talk between the p- and s-polarisation, the polarisation sensitivity has to be improved. Therefore, a wire grid polariser is introduced [68]. The polariser comprises of a metal wire grid. When the electric field is oriented perpendicular to the wires, they are nearly invisible to THz radiation, as long as their width is considerably smaller than the wavelength of the incident radiation. If the electric field is oscillating parallel to the

wires, the electrons in the wire can oscillate as well and therefore act as a metallic surface which blocks the incident radiation from passing through the grid. The wire grid is on a $10\,\mu$m thick polyimide film and the device was fabricated in the Durham cleanroom. For the fabrication, polyimide is spun on the wafer, followed by photolithography and selective wet etching of the metal. FDTD simulations were used for the design to maximise transmission for one polarisation while minimising it for the other. The isolation between the TE and TM polarisation for different geometries can be seen in Figure 5.10. Due to the low-cost acetate film mask that was used in the photolithography based fabrication, with a minimum resolution of the mask is $10\,\mu$m, a periodicity of $30\,\mu$m is used.

The polariser was characterised by placing it in the collimated beam of a trans-
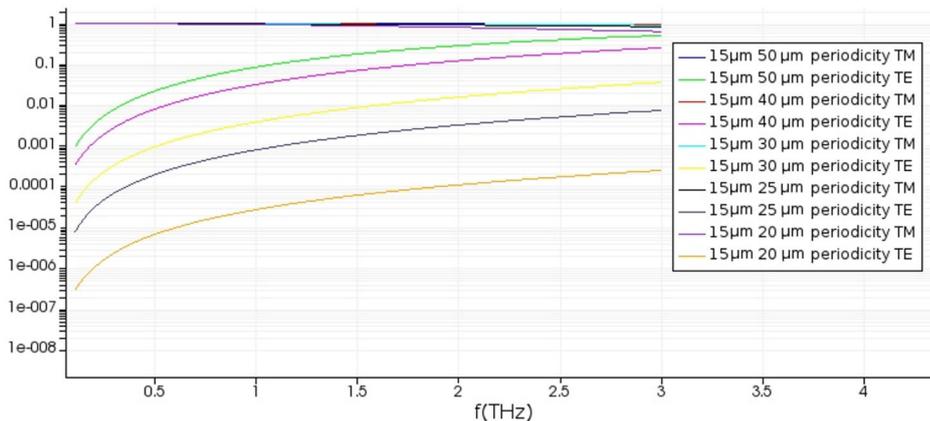


Figure 5.10: Comparison of the isolation of TE and TM polarisation for a polarizer grid with different geometric parameters (from simulation). While all the TM modes have virtually identical transmission, the transmission of the TE polarisation is heavily influenced by the geometry.

mission measurement and rotating it in $1°$ steps. Figure 5.11 shows that the transmission for the perpendicular alignment of the wires is above 90% and that the difference between p- and s-polarisation is near 0%, the exact value corresponds to around -33 dB. The polarisation sensitivity of the setup was then verified in the ellipsometry setup, where the transmitter is mounted on a $45°$ angle and the receiver rotates. A first measurement is conducted without any polarisation filter (Figure 5.12b), then the polarisation filter in front of the rotating analyser is ad-
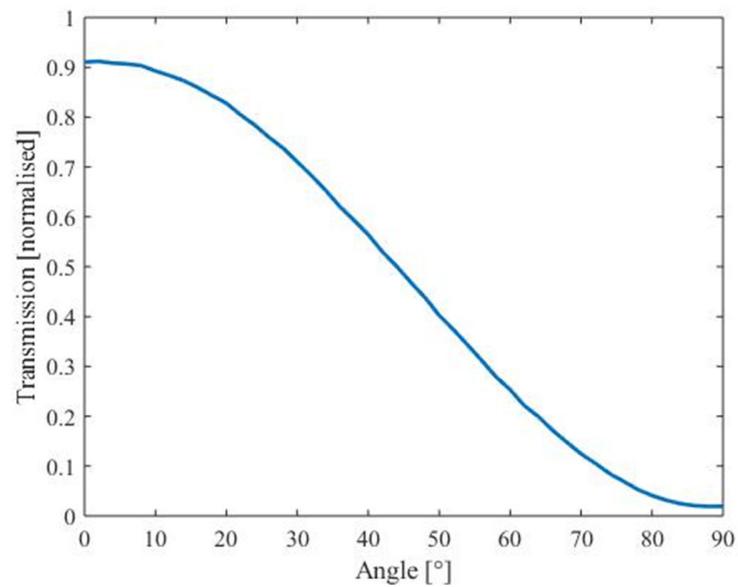
Figure 5.11: The characterisation of the polarisation filter shows that there is a high transmission in excess of 90% and a relative attenuation of 33 dB between p- and s-polarisation.

ded (Figure 5.12c) and in a third and final measurement a second filter is added in front of the transmitter (Figure 5.12d) for the final configuration, as shown in the schematic in Figure 5.12a. The improvement in polarisation selectivity with every added polarisation filter is clearly visible in Figure 5.12b-d and is in close agreement with the ideal factor of $1/\sqrt{2}$ (Pythagoras' theorem) for the p-and s-polarisation that is expected for a transmitter mounted at $45°$ and the intensity is split into equal parts into both polarisations. The two filters combined provide an extinction ratio of <30 dB across the frequency range of the instrument. This means there is sufficient polarisation selectivity of the instrument to measure p- and s- polarisation independently when polarisation filters are used.
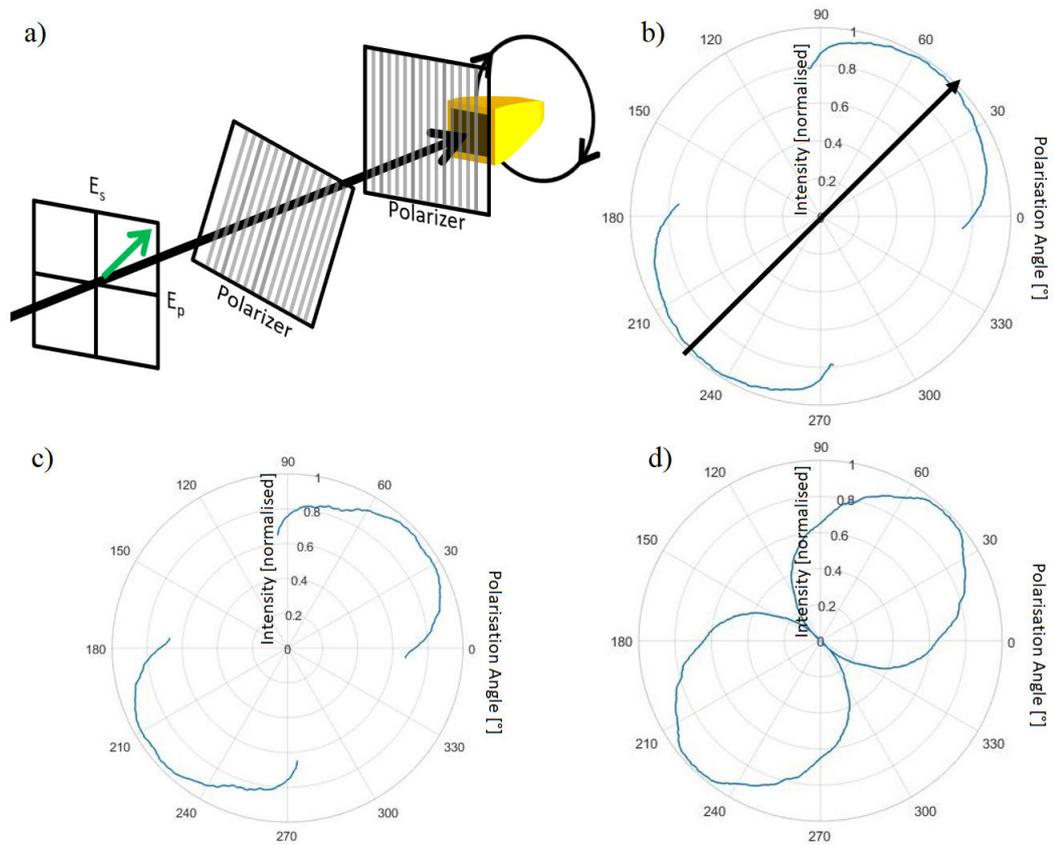
Figure 5.12: (a) Schematic of the polarisation characterisation of the ellipsometry setup. The measurement without polarisation filters shows a transmission of close to 90% for p- and s- polarisation (b), indicating that the polarisation selectivity is low. This considerably improves when adding a polarisation filter in front of the analyser (c) and is very close to the ideal factor of $1/\sqrt{2}$ when a second filter is added at $45°$ in front of the transmitter (d). The measured angle range is higher in the (d) as the rotational stage holder was modified to have an increased measurement range above $180°$ and this measurement has been retaken.

## 5.3.2.2 On phase information

There are some differences between the VNA used here and other ellipsometry systems. While THz-TDS systems have been used in the past for ellipsometry [130, 131], the complexity of the measurements and constantly changing pulse shape depending on the incident angle gives them a disadvantage over frequency-domain systems and therefore THz-TDS based ellipsometry is usually conducted at a fixed angle. The most advanced THz ellipsometry systems rely on sources like backward wave oscillators [132] but, as these have poor phase stability, the read-out is realised

without phase-sensitive detectors and the traditional use of wave plates [131–134]. The network analyser used in this thesis has the advantage that it can obtain highly reliable phase information, which potentially can reduce the measurement time and increase precision, compared to BWO (Backward Wave Oscillator) based setups. Usually, phase information is not used in traditional ellipsometry, as ellipsometry originates from the visible and infrared regions and obtaining phase information would require additional equipment, such as an auto-correlator, and, more importantly, a rather elaborate calibration procedure to obtain a reference, due to the significantly shorter wavelengths. At optical and IR frequencies, a reference sample, such as a metallic mirror, would have to be placed with nm precision, which is generally considered unfeasible, especially since the measurement of all Stokes' polarisation parameters can be achieved with wave plates which are readily available at these frequencies and give access to the polarisation states.

However, at THz frequencies, the longer wavelength drastically reduces the necessary precision of sample and reference placement to the order of (tens of) micrometres, which can be readily achieved in an ordinary lab setup. To demonstrate the reliability of the phase data, a mirror was repeatedly placed in the sample holder. The sample holder itself is a simple 2" threaded optical component holder with a fixed ring on the side of the incident beam. The sample is pressed against this ring by a second ring screwed into the holder behind the sample. For each measurement, the mirror is removed from the holder, rotated by $\sim 90°$ and replaced in the sample holder. Figure 5.13 shows that all measurements are within a $10°$ confidence interval, which corresponds to a deviation of $\pm 3\%$ of the phase. Overall, the phase varies in the order of $40°$ over an angle range of $15°$, which corresponds to a beam drift of around $40\,\mu$m which, in general, shows the good alignment of the system. Compared to other measurement methods at THz frequencies, no further calibration has to be applied to achieve stable phase results [135]. Provided the sample and reference can be placed in the same holder, reliable phase information can be obtained.
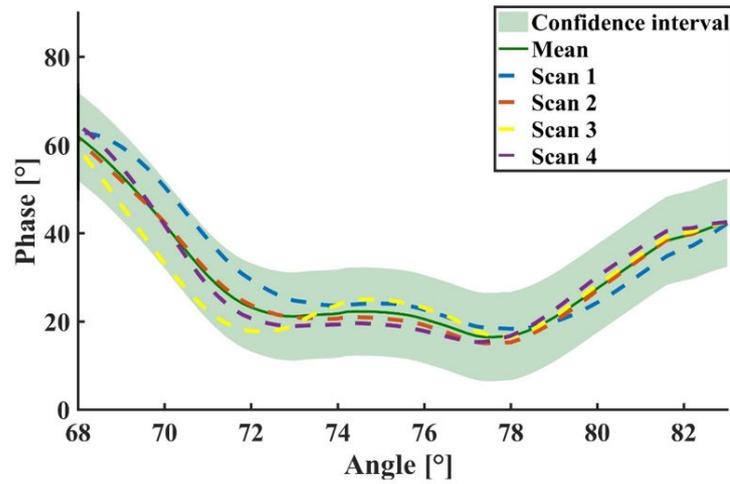
Figure 5.13: Repeatability test to gain confidence in the phase data obtained. Repeatedly removing and replacing a metal mirror and rotating it by 90°every during every replacement shows that the phase deviation is acceptably low. All measurements fall within a confidence interval of $\pm10°$which corresponds to a deviation of less than 3%.

## Results

To validate the measurement method, some common and well-studied materials in the THz frequency range are characterised and the optical parameters extracted. This is followed by characterisation of thin films and in-situ measurement of a silicon wafer during chemical wet-etching.

## 5.4  Ellipsometry for the extraction of optical constants at THz frequencies

### 5.4.1  Ellipsometry on a High Refractive Index Material: HRFZ Silicon

The first sample studied is the well-known HRFZ silicon, in form of a wafer. In Figure 5.14, the expected characteristic features are visible, such as the Fabry–Pérot resonances as horizontal lines and the Brewster angle in p-polarisation.

As HRFZ silicon has a relatively high refractive index and low absorption, these
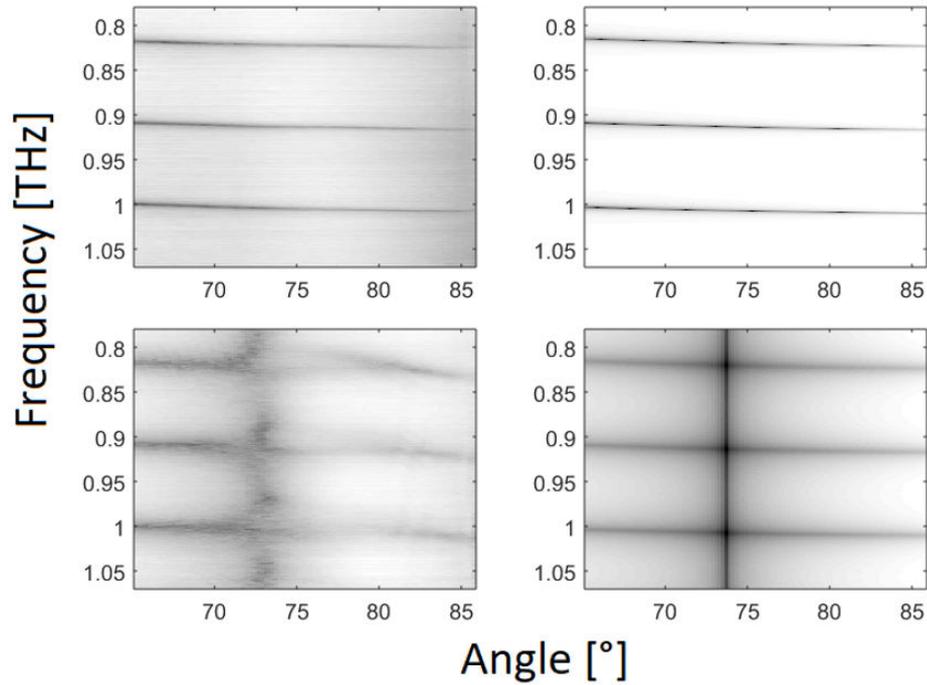


Figure 5.14: Comparison of the amplitude measurements (left) and a simulation with identical physical parameters (right) of the s- (top) and p-polarisation (bottom) of a HRFZ silicon wafer with a thickness of $500\,\mu$m. The similarity index ranges from 0.78-0.85.

resonances are very sharp and defined and, due to the high refractive index, the overall reflected intensity is higher than for the materials shown following. The confidence (SSIM) values are 0.85 and 0.78 respectively. The measurements are in excellent agreement with the literature values, as Table 5.1 shows. All refractive index values are in an interval of less than 0.5% of the refractive index, which is a very narrow window, especially since the low standard deviation of literature values of 0.006. Notably, the attenuation coefficient is often not measured in the literature, which is mostly because the absorption in HRFZ silicon is extremely low and therefore under the detection limit of most measurement systems.

Table 5.1: Comparison between the values for HRFZ silicon obtained by THz ellipsometry with literature values at 1 THz.

|  | Refractive index $\Re(n)$ | Attenuation coefficient $\alpha$ $(cm^{-1})$ |
|---|---|---|
| This work | $3.416 \pm 0.002$ | $0.018 \pm 0.017$ |
| [14] | 3.4175 | $\sim 0.01$ |
| [136] | 3.425 | NA |
| [137] | 3.42 | NA |
| [21] | 3.414 | NA |
|  | 3.414 |  |
|  | 3.412 |  |
|  | 3.411 |  |
|  | 3.406 |  |
|  | 3.405 |  |

## 5.4.2 Ellipsometry on a Low Refractive Index Material: HDPE

For the second material, high-density polyethylene (HDPE) is used. The lower signal quality in Figure 5.15 is apparent when comparing to the HRFZ silicon measurement, but this is expected as the refractive index is considerably lower. The difference in refractive index is also notable in the different angle range where Brewster's angle occurs and that the resonances are less well defined. Due to the lower signal quality, Brewster's angle is washed out in the measurement and appears to be considerably wider than in the simulation with identical parameters. However, the SSIM has a value of 0.63 showing that the algorithm can still identify similiarities between the simulated and measured data. The spacing between the Fabry–Pérot of the measurement and simulation is similar, but has a clear offset. This offset is not visible for the silicon and therefore might be caused by less well-defined interfaces and potential buckling of the less rigid HDPE when compared to the monocrystalline silicon.

Table 5.2 again shows that the values are in general in good agreement with literature. The deviation between measured refractive index and literature values is less than 4%, which is larger than the silicon, but standard deviation of the literature values is also significantly higher with 0.03. While the attenuation coefficient of HDPE is significantly higher than the coefficient for HRFZ silicon, the absorption

is still very low which is also evident in literature, where the noise often has the same magnitude as the measured value [21], and as such the measured value agrees with the majority of literature values, but there are some notable outliers and the standard deviation is twice the average value, which shows the wide spread in literature data.
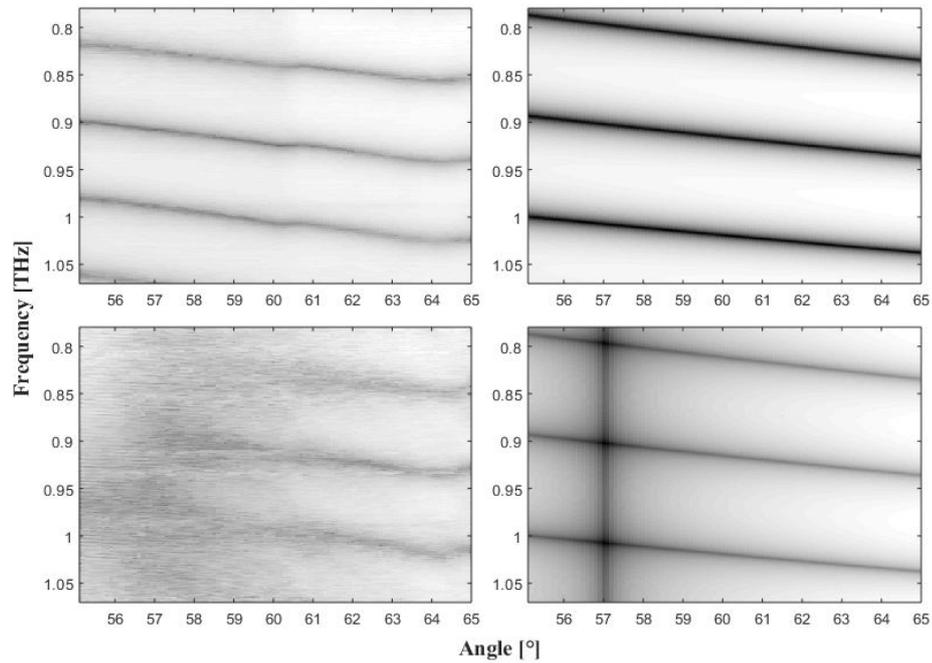


Figure 5.15: Comparison of measurements (left) and a simulation with identical physical parameters (right) of the s- (top) and p-polarisation (bottom) of a HDPE slab with a thickness of 1.5 mm. The similarity index ranges from 0.63-0.68.

Table 5.2: Comparison between the values for HDPE obtained by THz ellipsometry with literature values at 1 THz.

| | Refractive index $\Re(n)$ | Attenuation coefficient $\alpha$ $(cm^{-1})$ |
|---|---|---|
| This work | $1.538 \pm 0.004$ | $0.69 \pm 0.40$ |
| [138] @0.7 THz | 1.53 | 0.38 |
| [22] | 1.59 | 13 |
| [139] | 1.526 | 0.15 |
| [23] | 1.54 | 2.2 |
| [21] | 1.545 | ~0.1 |
| | 1.53 | ~0.1 |
| | 1.5 | ~0.1 |
| | 1.48 | $0.2 \pm 0.2$ |

## 5.4.3 Ellipsometry on High Absorption Material: Tufnol

As a third example an even more difficult to measure material, Tufnol 1P13, was chosen with an expected low refractive index and high absorption. Tufnol is a composite material of cotton fabric and a phenolic resin and signal layer transmission measurements [67] have shown that it has a refractive index of $1.6 \pm 0.3$, but as the reported method relies on fitting to the Fabry–Pérot resonances, it struggles with the high absorption of the material and the therefore weak resonances. The attenuation coefficient at 1 THz can be estimated as $12 \pm 2$ cm$^{-1}$ from a single layer measurement. The high absorption of the sample is also visible in the ellipsometry measurements in Figure 5.16. While the Brewster's angle is still visible, the Fabry–Pérot resonances are considerably harder to see than in the HDPE measurements, especially for the p-polarisation where they are only a light shadow. Despite these issues, the similarity indices are actually higher than for HDPE, indicating a good fit of the simulation to the measurement. This might be explainable as the measurement for Tufnol looks mostly like weak signal and is very noisy and this is something the SSIM algorithm can address as it is common in digital image processing. In contrast, the HDPE measurement is less noisy, but the features are more smeared out. The optical constants of Tufnol are determined as $n = 1.87 \pm 0.02$ and $\alpha = 14.7 \pm 0.8$ cm$^{-1}$. Therefore, the ellipsometry results

are in agreement with the single layer measurement, albeit only in the fairly large error margin of the transmission measurement. This shows one of the advantages of the reflection measurements over the transmission measurements, when it comes to high absorption materials.
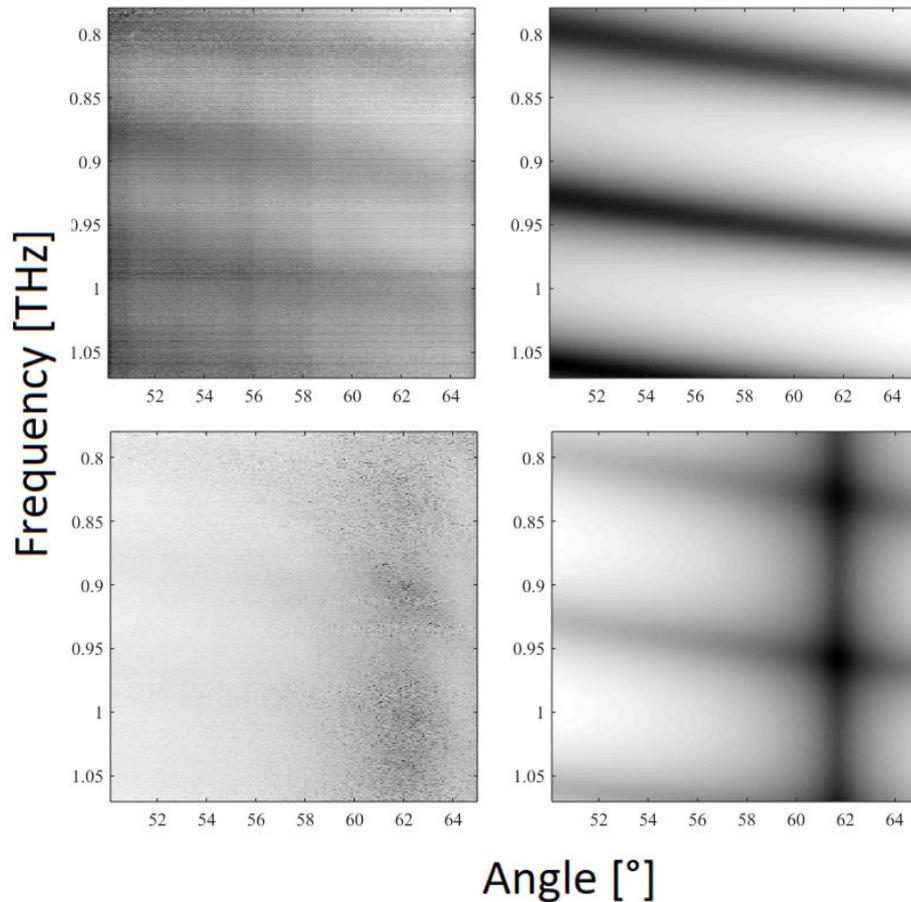


Figure 5.16: Comparison of measurements (left) and fitted model (right) of the s-(top) and p-polarisation (bottom) of a Tufnol slab with a thickness of 1 mm. The similarity index ranges from 0.64-0.77.

## 5.4.4 Ellipsometry on a Sample without Fabry–Pérot resonances: PDMS Loaded with TiO₂

This leads to the last sample, which again represent a different case, a sample which shows no Fabry–Pérot resonances, as seen in Figure 5.17. A PDMS (Polydimethyl-

siloxane) sample mixed with 3.2 wt% $TiO_2$ nanoparticles is used. The sample is cast with a thickness of $5\,\mathrm{mm}$ and the top is not very smooth ($RMS \gg 100\,\mu\mathrm{m}$, stylus profilometer measurement), but the bottom side is smooth and therefore the measurements were conducted on this side. The reference parameters are obtained with the same methods as for the previous Tufnol sample and the optical constants are $n \approx 1.57 \pm 0.09$ and $\alpha \approx 17 \pm 2\,cm^{-1}$. While the Brewster's angle is evident, the s-polarisation does not show any clear features and is expected to only show a continuous gradient of increasing intensity towards higher angles. The similarity indices are high, but this might be caused by the lack of visible features. The fit, however, is in good agreement with the single layer measurements with $n = 1.57 \pm 0.05$ and $\alpha = 16.9 \pm 1.9\,cm^{-1}$.
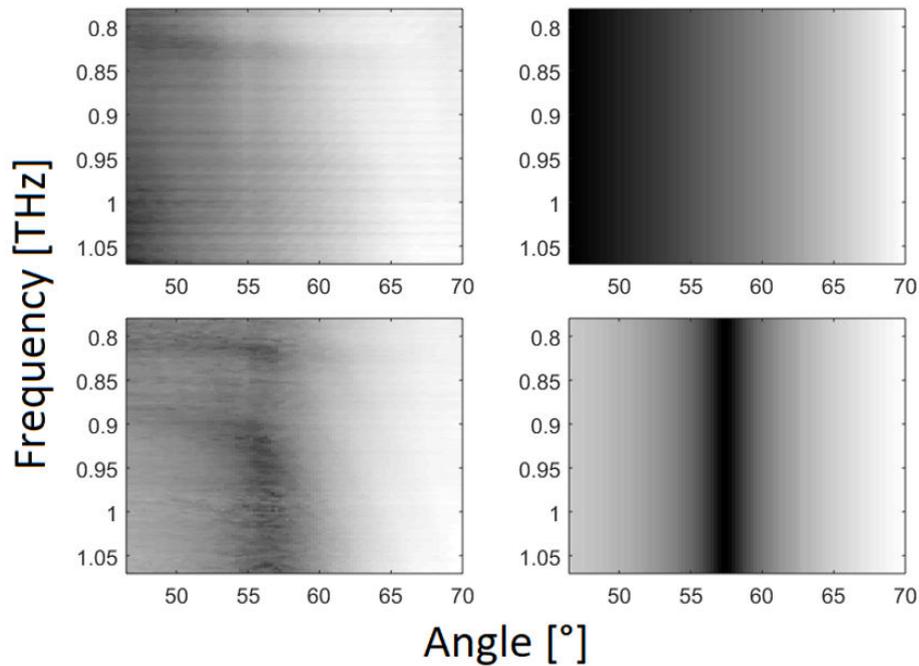


Figure 5.17: Comparison of measurements (left) and fitted model (right) of the s- (top) and p-polarisation (bottom) of a casted PDMS sample loaded with $TiO_2$ nanoparticles. The similarity index ranges from 0.69-0.73.

## 5.5 In-situ Ellipsometry

One of the largest advantages of reflection measurements is that they are often more suitable for in-situ measurements. This can be mostly be attributed to the property that reflection setups are easier to integrate in existing machines and processes, as they only need to have access to a single facet of the sample accessible to the beam. Therefore, reflective measurement methods are commonly used for in-situ observations, i.e. Reflection high-energy electron diffraction (RHEED) is commonly used during the growth of semiconductors [140].

As there are no growth facilities accessible, the etching of a silicon wafer in potassium hydroxide (35% solution) is chosen as a sample with changing thickness. A box which contains the base and the wafer has been constructed. It has a PTFE window through which the wafer can be accessed with the THz radiation, as seen in the schematic in Figure 5.18.The wafer is etched only from the backside, allowing the THz radiation to not pass through the aqueous solution. The photo in Figure 5.9 shows the ellipsometry setup with the box for the in-situ measurements as a sample. As a reference, the thickness of the wafer is measured before and after etching. Additionally, there is an indirect in-situ estimation from the temperature of the etching solution, which is observed during the process.

The major challenge in this experiment is the scan speed. Even if the etch rate is only in the order of $\sim 5\,\mu$m/hr, the previously shown measurements take 40 minutes to 2 hours, depending on the averaging and IF bandwidth required for the signal level. The intended thickness resolution is in the order of micrometres. Hence, scan time has to be in the order of minutes at such etch rates. Therefore, the resolution in frequency and angle has to be drastically reduced. As can be seen in Figure 5.19, the measurement time was adjusted during the in-situ observation as the first scans started to increase in noise, and therefore, the uncertainty increased during the thickness extraction. Therefore, the time between measurements was increased to $\sim$8 minutes, allowing for the necessary reduction in noise.
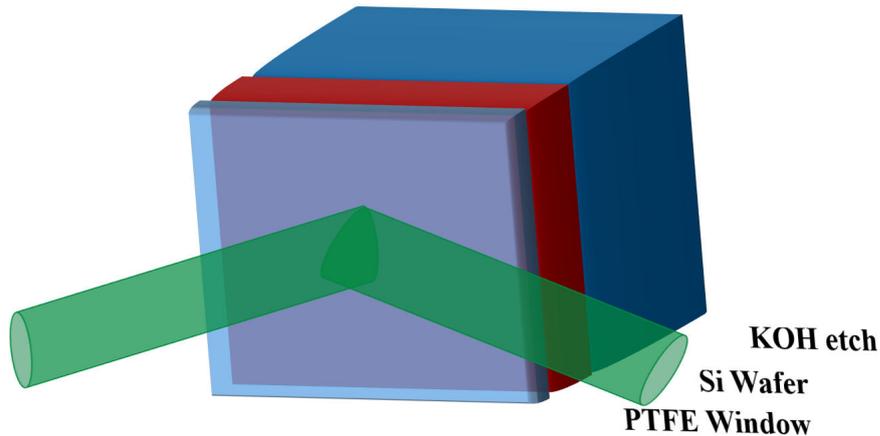
Figure 5.18: Schematic of the in-situ setup. The terahertz beam enters through a PTFE window and reflects off the silicon wafer (red). The silicon wafer is etched from the backside while measuring.

The KOH solution was changed at ∼150 minutes with a higher temperature solu-
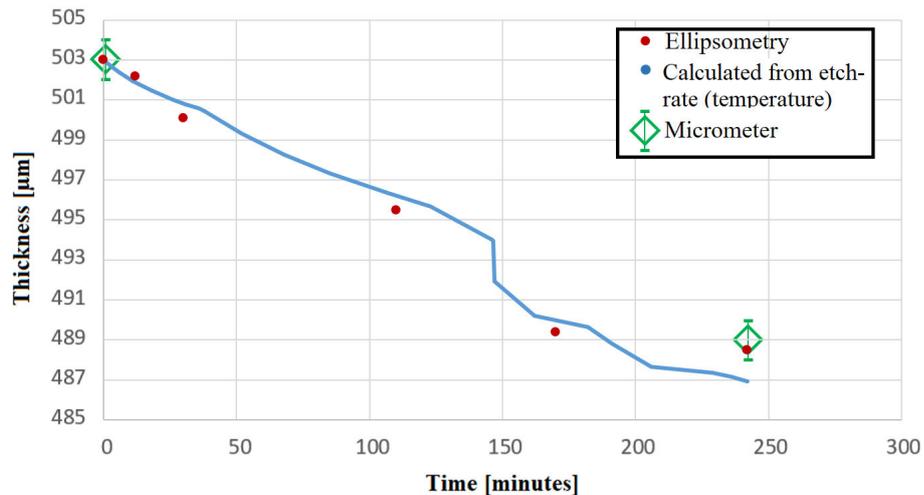


Figure 5.19: In-situ thickness measurement of a silicon wafer during etching with the ellipsometry setup. The step where the gradient of the curve quickly changes is caused by a change of the base with a fresh, higher-temperature solution.

tion to increase the etch rate, causing the discontinuity for the thickness calculated from the temperature dependant etch-rate. The wafer thickness measured with ellipsometry follows the trend of the thickness calculated from the etch-rate. The largest discrepancy between the two methods is at the last measurement point at ∼240 minutes. However, the ellipsometry measurement agrees with the ex-situ

micrometer measurements while the calculated thickness from the etch-rate does not.

## 5.6 Conclusion

The design and construction of an angular resolved THz ellipsometer has been discussed. The feasibility of the instrument to conduct polarisation sensitive complex amplitude measurements has been confirmed, the polarisation filter employed provide an extinction ratio of <30 dB across the frequency range of the instrument. The phase stability has been evaluated and has shown a deviation of less than 3% in the phase for repeated measurements.

To validate the performance of the instrument different common materials have been characterised and the results are compared to literature and single layer transmission measurements. Four different materials with different properties have been used: silicon as a material with a high refractive index and low absorption; HDPE as a low refractive index material; TUfnol as a material with absorption; and PDMS loaded with $TiO_2$ as a nonuniform material without Fabry-Pérot resonances. The results of the first two materials are in good agreement with literature, with the deviation between measured and literature values being within an interval of less than 0.5% of the refractive index and a standard deviation of less than 0.006 for silicon. The HDPE shows a deviation of less than 4% between measured and literature values with a standard deviation of less than 0.03 for the refractive index. While the absorption of silicon is too low to have reliable data in literature for a meaningful comparison, there is sufficient data for HDPE available and 6 out of 8 literature references agreeing with the measured values, which is a good agreement as literature values have a wide spread with a standard deviation of twice the average value. As there are no literature values for the last two materials they are compared to a different, transmission based, measurement method. The results of the ellipsometry and the transmission method agree as well, albeit in the larger error of the transmission based method which are in the order of 10-20% of the refractive index and attenuation coefficient. The errors of the transmission measurements are at least twice as large as the errors of the ellipsometry measurement,

showing the advantages of the reflection based measurement method. Finally, in-situ mesurements have been performed to test the method in a realistic scenario with a strong time-constraint on the measurements. For this, the thickness of a silicon wafer was measured during etching and the results are compared with the thickness calculated from the temperature dependent etch-rate and ex-situ micro-meter measurements at the beginning and the end of the experiment. The overall thickness change of the wafer during testing was around 3% of the total thickness. The in-situ ellipsometry measurements follow the trend of the calculated thickness within 0.2% of the total thickness and agreed with the micrometer measurements within the error of 1 micrometre, showing that THz ellipsometry is a suitable tool for in-situ characterisations and can reach micrometre precission for thickness measurements.

# Spoof plasmonics for integrated photonic circuits with novel fabrication methods

This chapter introduces plasmonics, the scientific field at the boundary of physical optics and condensed matter physics, for THz applications. First, integrated photonic circuits and components constructed with spoof plasmonic waveguides are discussed. These components are produced with photolithography to minimise defects and allow for longer propagation length required for more complex components. Following this, experimental results for 3D printed spoof plasmonic waveguides are presented. While being poor waveguides ,due to a high defect density, the 3D printed structures have interesting physical properties, such as unassisted coupling to free-space. First, the physical background is explained with the concept of classical plasmonics at optical and near-infrared frequencies; the frequency range is consequently extended to THz frequencies with the introduction of the concept of 'spoof' plasmonics. This is followed by the experimental characterisation techniques and a comparison between different technologies which shows why plasmonics is so attractive for waveguiding at THz frequencies.

## 6.1 Physical Background

Originally, plasmonics is the field of research on the interaction between the electromagnetic field of a photon and the free electrons of a material. Free electrons can be described as plasma, and a quasiparticle, the plasmon describes their fluctuation in density. While plasmonics, as a term, is also used for localised plasmonic modes, this thesis focuses on propagating plasmonic modes. The electric field of the photon excites the electrons to have a collective oscillation, which can travel along the surface of the material the electrons are in. This phenomenon is therefore called a surface plasmon. Under certain conditions, the photon can couple to the oscillation of the electron to form a surface plasmon polariton (SPP) as both, photon and surface plasmon, travel alongside each other. As these conditions require certain permittivities of the material, as the normal components of the wave vector need to be purely imaginary, which can only be found near the resonance in permittivity around the plasma frequency, every material naturally supports SPPs in a specific frequency region. As it will be later shown, the resonance at the plasma frequency can be emulated by structuring the material, leading to an extension of plasmonics to virtually any frequency. This emulation is called spoof plasmonics.

The large interest in plasmonics arises from the possibilities of the subwavelength manipulation of light. Subwavelength optics could lead to the integration of optical communication into electronic circuits, merging the fields of electronics and photonics [141]. The increased field strength, which can be multiple orders of magnitudes, at the plasmonic structures, also called plasmonic enhancement [142], enables many advances in the field of light generation [143], solar cells, microscopy or bio-sensing [144] and has already introduced innovations, such as the tip-enhanced Raman spectroscopy [145]. To choose an example more closely related to this thesis, the increased emission of THz radiation [146].

To couple to the surface plasmon and form the SPP, the free-space photon has to match the bound state in frequency and momentum. The momentum mismatch

that has to be bridged, as seen in the dispersion curve in Figure 6.1, is described
by

$$k_{SPP} = k_0 \sqrt{\frac{\epsilon_d \epsilon_m}{\epsilon_d + \epsilon_m}} \tag{6.1}$$

with $k_{SPP}$ and $k_0$ being the wave vectors of the bound SPP and in free space, $\epsilon_d$
and $\epsilon_m$ being the permittivity of the dielectric and metal respectively, and will be
derived in the following section.

In the Drude model [45], the dielectric function of metal in the free electron model
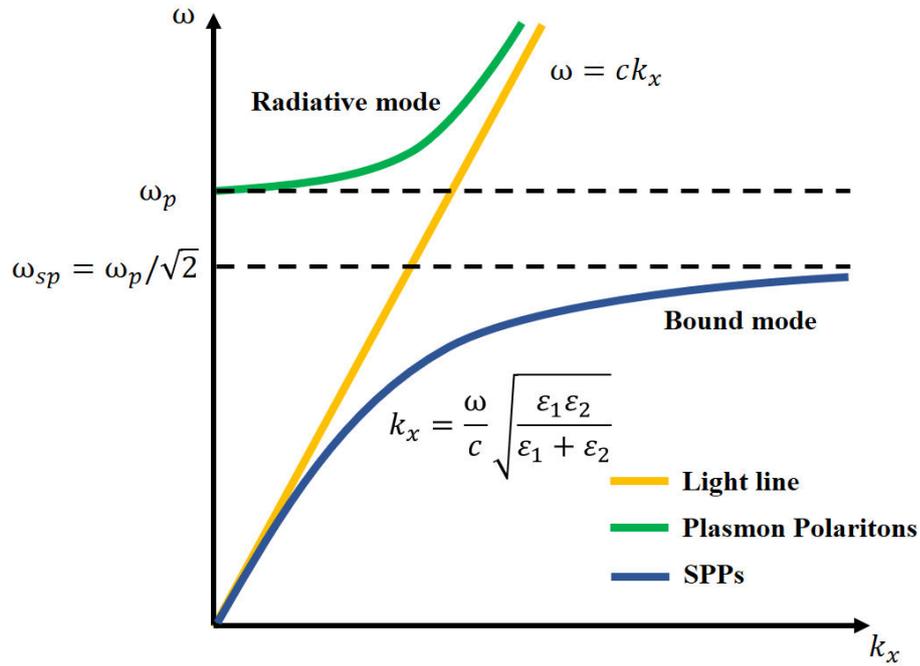


Figure 6.1: Dispersion curve for a surface plasmon. At lower frequency, the curve
of the SPP (blue) is very close to the light line of the free photon (yellow). As
the plasmon curve approaches the surface plasma frequency $\omega_{sp}$, the difference in
wavevector and therefore momentum is increasing and the plasmon polariton is
bound to the surface. Above the plasma frequency $\omega_p$ the plasmon polariton is not
bound and radiates off into free space.

of an electron gas is described by

$$\epsilon(\omega) = 1 - \frac{\omega_p^2}{\omega^2}. \tag{6.2}$$

Since $k_{SPP}$ has to be larger than $k_0$, only materials with a negative value for $\epsilon_m$
can support SPPs. This condition is true for metals below the plasma frequency.
As a further limitation, since the photon has to couple to the surface plasmon,

Table 6.1: Different metals with their plasma frequency and SPP propagation lengths for different wavelengths. From [147–149].

| Material | Plasma Frequency Drude Model (eV) | $\lambda$ (nm) | Propagation length ($\mu$m) |
|---|---|---|---|
| Silver(Ag) | 8.6-9.6 | 650 | 84 |
| | | 1000 | 340 |
| | | 1550 | 1200 |
| Aluminium (Al) | 14.75-15.3 | 280 | 2.5 |
| Gold (Au) | 8.55-9.03 | 650 | 20 |
| | | 1000 | 190 |
| | | 1550 | 730 |
| Copper (Cu) | 7.39-8.76 | 650 | 24 |
| | | 1000 | 190 |
| | | 1550 | 820 |

the difference in momentum cannot be arbitrarily high as it cannot be bridged. Therefore every material only supports a limited part of the frequency spectrum, as shown in Table 6.1.

As seen in Table 6.1, naturally occurring materials only support SPPs in the visible or near IR spectrum of light. To overcome these limitations, material scientists design artificial material combinations with plasma frequencies suitable to support SPPs in the infrared, hence compatible with communication technology wavelengths [150] or developed concepts like the spoof SPPs, which work at even longer wavelengths, such as THz frequencies.

## 6.1.1 Surface Plasmon Polaritons

Many properties of SPPs can be derived from the more general case of electromagnetic surface waves. A full derivation of all properties can be found in textbooks [151]. Here the focus is on the necessary properties used in this thesis. Surface electromagnetic waves (SEW) have been described first by Zenneck, who showed that the solution of Maxwell's equation with the corresponding boundary conditions of a flat conductor result in surface waves [151]. Accordingly, SEWs are also called Zenneck waves. The conditions for a propagating wave can be derived
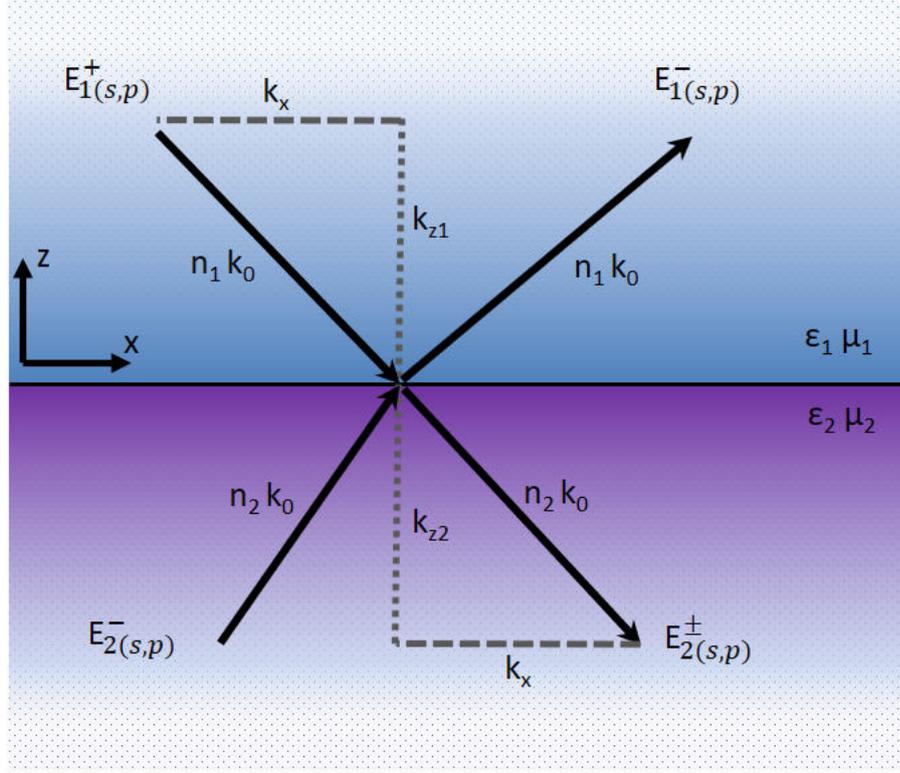
Figure 6.2: Schematic of the forward and backward going field amplitudes used in the scattering matrix with the according wavevector components.

from the scattering matrix of the well-known Fresnel coefficients for reflection and transmission:

$$
\begin{pmatrix} E^-_{1(s,p)} \\ E^+_{2(s,p)} \end{pmatrix} = S \begin{pmatrix} E^+_{1(s,p)} \\ E^-_{2(s,p)} \end{pmatrix} = \begin{pmatrix} r_{s,p} & t_{s,p} \\ t_{s,p} & r_{s,p} \end{pmatrix} \begin{pmatrix} E^-_{1(s,p)} \\ E^+_{2(s,p)} \end{pmatrix} \tag{6.3}
$$

where $E^+$ and $E^-$ are the forward and backward propagating field amplitudes for the s- or p- polarisation respectively, as defined in Figure 6.2.

The Fresnel coefficient expressed by the normal components of the wave vectors can be expressed as:

$$
r_p = \frac{\dfrac{k_{z2}}{\epsilon_2} - \dfrac{k_{z1}}{\epsilon_1}}{\dfrac{k_{z2}}{\epsilon_2} + \dfrac{k_{z1}}{\epsilon_1}} \quad t_p = \frac{2\dfrac{k_{z2}}{\epsilon_2}}{\dfrac{k_{z2}}{\epsilon_2} + \dfrac{k_{z1}}{\epsilon_1}} \quad (p-polaristion), \tag{6.4}
$$

$$
r_s = \frac{\dfrac{\mu_2}{k_{z2}} - \dfrac{\mu_1}{k_{z1}}}{\dfrac{\mu_2}{k_{z2}} + \dfrac{\mu_1}{k_{z1}}} \quad t_s = \frac{2\dfrac{\mu_2}{k_{z2}}}{\dfrac{\mu_2}{k_{z2}} + \dfrac{\mu_1}{k_{z1}}} \quad (s-polaristion), \tag{6.5}
$$

where

$$k_{zi} = \sqrt{n_i^2 k_o^2 - k_x^2},$$ (6.6)

where $k_0$ is the free space wavevector, $k_z$ is the in-plane wavevector and $n_i = \sqrt{\epsilon_i \mu_i}$. As the excitation of bound modes will occur near the poles [152, 153], the denominator of the reflection and transmission coefficient has to be zero. Therefore

$$\frac{k_{z2}}{\epsilon_2} = -\frac{k_{z1}}{\epsilon_1}$$ (6.7)

and

$$\frac{\mu_2}{k_{z2}} = -\frac{\mu_1}{k_{z1}}.$$ (6.8)

By substituting equation Equation (6.7) and Equation (6.8) into Equation (6.6) these equations can be rewritten as the dispersion relations for p- and s-polarisation:

$$k_x = k_0 \sqrt{\frac{\epsilon_1 \epsilon_2 (\epsilon_1 \mu_2 - \epsilon_2 \mu_1)}{\epsilon_1^2 - \epsilon_2^2}}$$ (6.9)

and

$$k_x = k_0 \sqrt{\frac{\mu_1 \mu_2 (\epsilon_2 \mu_1 - \epsilon_1 \mu_2)}{\mu_1^2 - \mu_2^2}}.$$ (6.10)

For non-magnetic media ($_i = 1$) this simplifies to the previously shown relation in Equation (6.1) for p-polarised surface waves, which is restated here for convenience:

$$k_x = k_0 \frac{\epsilon_1 \epsilon_2}{\epsilon_1 + \epsilon_2}$$ (6.11)

As there is no equivalent solution for Equation (6.10) for the s-polarisation, this indicates that only p-polarised surface waves can exist on non-magnetic surfaces. Additionally, in order for the mode to be bound to the surface, $k_{zi}$ needs to be imaginary as otherwise, the wave would be propagating away from the surface. Therefore, $k_x > n_i k_0$, which means bound surface waves can only exist on certain material combinations which satisfy these conditions. With the wavevectors defined, Maxwell's equations can be written as:

$$E_1 = E_x \left[ 1, 0, -\frac{k_x}{k_{z1}} \right] e^{i(k_x x + k_{z1} z - \omega t)},$$ (6.12)

$$E_2 = E_x \left[ 1, 0, \frac{k_x}{k_{z2}} \right] e^{i(k_x x + k_{z2} z - \omega t)}, \tag{6.13}$$

$$H_1 = E_x \left[ 1, \frac{\omega \epsilon_1}{k_{z1}}, 0 \right] e^{i(k_x x + k_{z1} z - \omega t)}, \tag{6.14}$$

$$H_2 = E_x \left[ 1, -\frac{\omega \epsilon_2}{k_{z2}}, 0 \right] e^{i(k_x x + k_{z2} z - \omega t)}, \tag{6.15}$$

where $E_i$ and $H_i$ are the electric and magnetic fields in the $i$th medium, $\omega$ is the angular frequency and $E_x$ the tangential electric field strength at the interface. There are some characteristic lengths defined for surface plasmons, namely the propagation length $L_x$ and the confinement, $L_z$. The field strength of a surface wave in its direction of propagation is described by

$$E(x) = E_0 e^{ik_x x} = E_0 e^{ik_x' x} e^{ik_x'' x}, \tag{6.16}$$

where $k$ is the wave vector with its real and imaginary components, $x$ denotes the direction of propagation and $E_0$ the initial field strength. Both characteristic lengths are defined as the distance when the initial field intensity decays to $1/e$, therefore propagation length is defined as

$$L_x = \frac{1}{2k_x''}. \tag{6.17}$$

In a similar fashion for the extension of the electric field of the SPP in the direction $z$, perpendicular to the surface without a propagating component, the electric field is described as an evanescent wave by

$$E(z) = E_0 e^{-k_z'' z}. \tag{6.18}$$

And the characteristic length of the extension of the electric field, the confinement, is defined as

$$L_z = \frac{1}{|k_{zi}''|}. \tag{6.19}$$

So far, all the above stated is true for surface waves but are also true for surface plasmon polaritons. The SPP is, therefore, a special case caused by the asymptotic behaviour of the dispersion relation near the plasma frequency, i.e. when

$\epsilon_1(\omega) = -\epsilon_2(\omega)$. This asymptotic limit occurs at the surface plasma frequency $\omega_{sp} = \omega_p/\sqrt{2}$), as indicated in Figure 6.1, and below this frequency, the surface wave becomes a mixed-mode consisting of a photon combined with a surface plasmon to form the SPP. How close the frequency of the SPP is to the limit is also important for its properties. When the frequency is considerably lower than $\omega_{sp}$, the SPP is very close to the light-line, which allows easy coupling but also easy decoupling into free space and therefore the SPP is only weakly bound to the surface. Conversely, the closer the SPP mode is to the cut-off frequency, the stronger it is confined to the surface.

### 6.1.2 Spoof Surface Plasmon Polaritons

As discussed earlier, SPPs are only supported near the plasma frequency and therefore, the frequency range at which a material supports SPPs is particular to the individual material. This limits the frequency at which plasmonics can be used and even the development of artificial plasmonic materials focuses on the near-infrared region because it is more reasonable to tune the plasma frequency in the same order of magnitude, which is in the order of hundreds of THz for optical and near-infrared, rather than to try to reduce the plasma frequency by three orders of magnitude or more for THz and microwave frequencies. If it is not feasible to tune the plasma frequency, it is worth considering from a more general perspective what causes the material only to support SPPs at particular frequencies. The deciding property is the change in the dielectric constant of the material, which has a discontinuity at the plasma frequency and therefore provides negative values. Physically, the reason for the change is that the electrons are resonating at this frequency. In 2005 Pendry et al. published the concept of a periodic perforated metal film which exhibits a resonance depending on the size of the perforating holes [154]. They have shown analytically that for an array of closely spaced holes in a perfect conductor the effective plasma frequency is given by the cut-off frequency of the waveguide mode, which leads to a dispersion relationship which is typical for

SPPs. This allows mimicking the effect of the resonating electrons at the plasma frequency. From this arises the research field of spoof SPPs, which concerns itself with tuning the properties of SPPs through the geometric structure of the material they propagate on. Beside the major advantage of overcoming the frequency limitations of plasmonics and making it possible to apply the concept to virtually every frequency, the tailoring over the surface morphology gives more degrees of freedom and is easier to realise than the development of complex multi-layered material stacks which are represented in the many different geometries that have been developed in the following years, including holes, grooves and cones to name a few [155–158].

The spoof plasmonic structure mostly used in this chapter is a metallic groove structure, as shown in Figure 6.3. The structure is well explored theoretically in the case of a one-dimensional groove array [159]. The dispersion relation for such
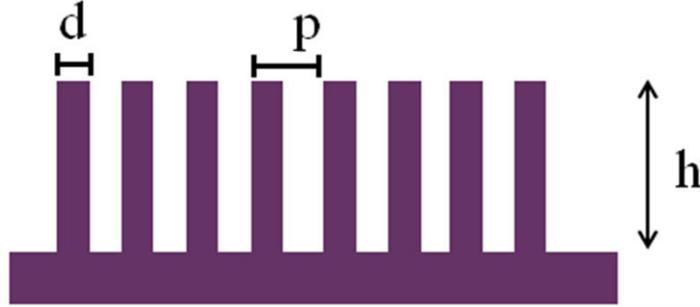


Figure 6.3: Schematic of the metallic spoof plasmonic grove structure used in this thesis. The unit cell size $p$, groove width $d$ and height of the groove $h$ are indicated.

a structure is known as a first-order approximation

$$k_x = \frac{\omega}{c}\sqrt{\frac{(p-d)^2}{p^2}\tan^2\left(\frac{\omega}{c}h\right) + 1},$$

(6.20)

with $d$, $p$ and $h$ as geometric parameters as indicated in figure Figure 6.3. It is shown later that this equation predicts the position of cut-offs correctly for waveguides of a width$\gg \lambda$ where the 1D assumption is true.

## 6.1.3   Coupling

As for every bound particle, SPPs have a non-trivial dispersion relation which therefore differs from the linear dispersion relation of light. Additionally, from Equation (6.1) it can be seen, that the momentum of propagating SPPs is, in fact, larger than the momentum of a free propagating photon. Therefore, a free space photon needs additional momentum to couple to the surface and form the SPP. There are two common ways to bridge this momentum gap: Prism coupling and knife-edge scattering.

### 6.1.3.1   Prism coupling

While the dispersion relation of free propagating light is linear, the slope does vary with a dependence of the refractive index of the material, i.e. the photons have more momentum. If a prism of a high refractive index material is placed on top of a sample with a small gap or a lower refractive index spacer layer above the sample, the two lines outline an area (Figure 6.4) in the dispersion relation corresponding to a band of frequencies and momentums that can be accessed depending on the coupling angle of the incoming radiation. This setup is called the Otto configuration, and is the only configuration discussed as the other configuration (called Kretschmann) is not applicable for the samples investigated in this thesis, as this configuration is used to excite SPPs on the rear side of the metallic structure which is not possible with the closed surfaces of the groove structures used in this thesis.

### 6.1.3.2   Coupling with knife-edge scattering

Every scattering event causes a change in momentum. In the direct vicinity of the scattering point, a whole range of momenta are available, in contrast to the prism method that offers a single momentum per angle, but only within a few wavelengths of the scatting point (the near-field). Experimentally, this effect can be utilised by
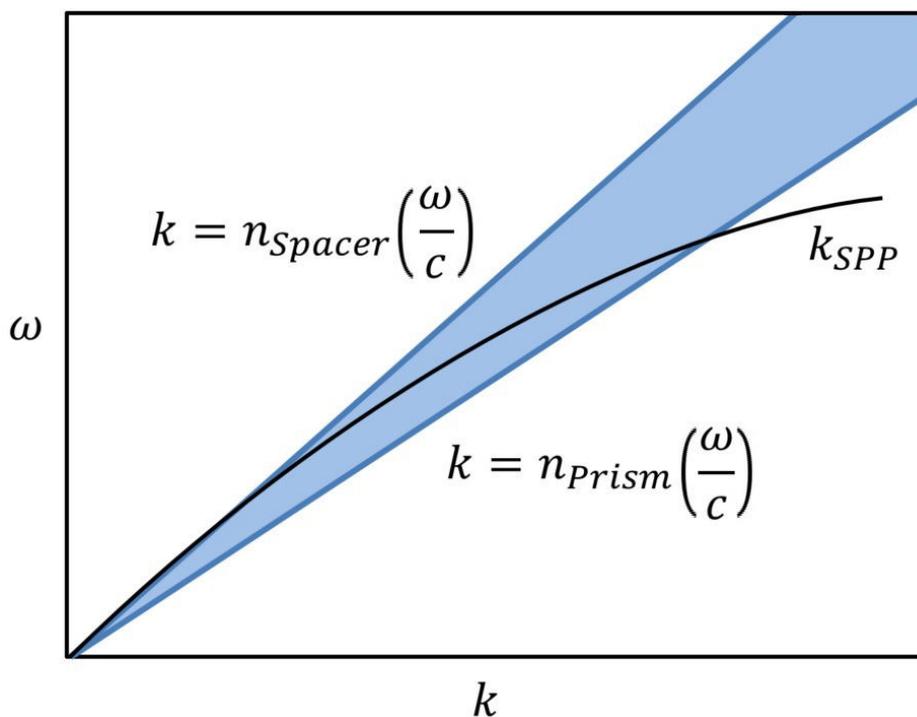
Figure 6.4: Schematic of a dispersion relation of an SPP at a metal-dielectric interface during prism coupling. The upper and lower blue lines illustrate the dispersion of an electromagnetic wave propagating in the spacer dielectric and the high refractive index prism respectively. Only photons with momenta lying between the two lines can couple to the SPP.

placing an object in the direct proximity of the surface to scatter and therefore excite SPPs.

In a lab environment, this is realised with a knife whose edge is placed parallel to the sample surface. By stepwise reduction of the distance between knife-edge and sample, the ideal distance can be found which excites the SPPs and has the maximum transmission and therefore the highest coupling efficiency. Knife-edge scattering can also be used to determine some of the characteristic lengths of a plasmonic structure, such as the propagation length $L_x$ and the confinement $L_z$. Typically, three parallel knives are used to determine these two characteristic lengths, as shown in Figure 6.5. Knife-edge scattering experiments were carried out in the laboratory at Durham University by placing the transmitting and receiving horn antennas at a $60°$ angle to the sample surface normal, aiming at the gap between the sample and in-coupling (or respectively outcoupling) knife from a

distance of less than 5 cm. For the propagation length measurements, one knife is placed near the sample and kept in a fixed position to couple the radiation in while a second knife is placed parallel to the first one to couple out. The distance between the two knives is incrementally increased, and the spectra for each increment are recorded. A third knife was placed between the two knives to reduce transmission through the direct line of sight to ensure that only the contribution of the SPPs is measured. The configuration for confinement measurements was similar, but the outer two knives used for coupling in and out are kept at a fixed position, and only the middle knife was moved perpendicular to the surface. Both measurements show transmission over distance and the characteristic lengths are obtained by fitting to the exponential decay.

Standing waves can be an issue occurring during knife-edge scattering exper-
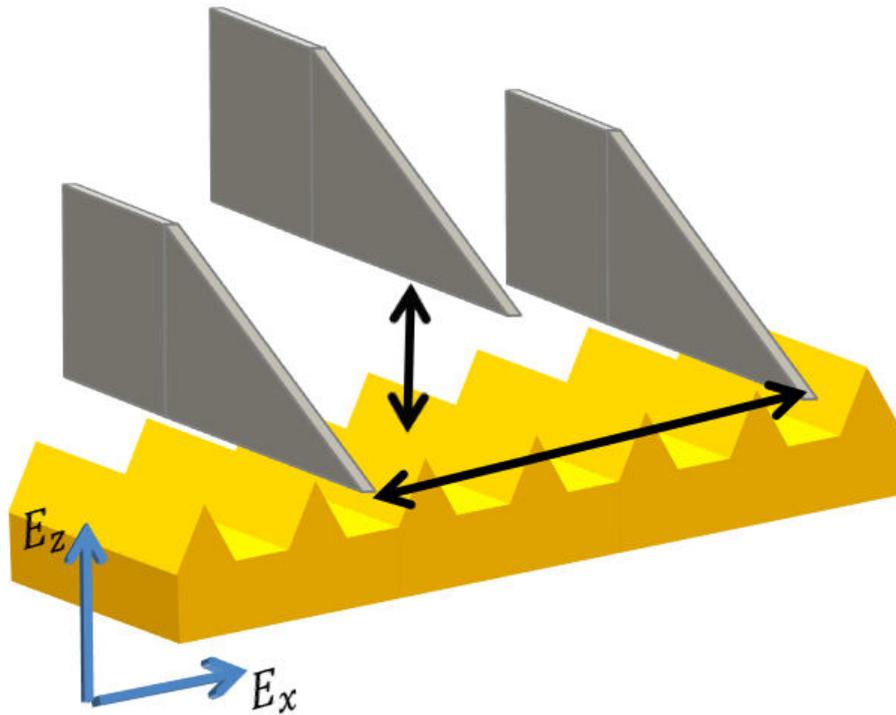


Figure 6.5: Schematic of the placement of knives in a knife-edge-scattering experiment. The two outer knives are used to couple in and out, the middle one is used to measure confinement.

iments. They can appear as resonances in a recorded spectrum and arise from standing waves between any two plane-parallel surfaces. As the spacing in fre-

quency and magnitude of the resonance depend on the relative position of the plane-parallel surfaces, the spacing between knives, the angle of a single knife and the positioning relative to the sample should be changed multiple times per measurement. The third knife in between the outer two knives also helps to prevent the occurrence of standing waves.

Therefore, for every measurement, the knives were repositioned a minimum of three times, and the spectrum was only considered valid if no considerable change in position and shape of the resonances was observed (resonant frequency within $\sim 5\,\mathrm{GHz}$).

## 6.2 Spoof SPPs for THz applications

One of the interests in spoof SPPs at THz frequencies is for waveguiding. At telecom and optical frequencies, there are usually three methods for waveguiding available: Optical fibres for long-distance guiding; photonic crystals for compact, integrated optical circuits; and plasmonics for compact, subwavelength guides, such as interconnects. To date plasmonics so far has not made it into commercial applications yet as the need for such ultra-compact waveguides is not great enough to justify the complex implementation and poorer performance in comparison with photonic crystals. The situation is quite different at THz frequencies, as Table 6.2 shows.

Traditional fibre waveguides suffer from comparably large losses with typical propagation lengths in the order of cm rather than km as is the case for telecom frequencies. Photonic crystals in materials with very low losses, such as HRFZ silicon do have long propagation lengths in the order of tens of cm. However, photonic crystals scale directly with the wavelengths and, given that a few periods of photonic crystal are necessary on each side of a waveguide to prevent leakage of the wave, are not as compact as they are at higher frequencies. At the same time, the self-supporting photonic crystal slabs currently demonstrated in literature for lower

frequencies [52] are less practical for frequencies above 1 THz, where the substrate thickness is decreasing below $100\,\mu$m. parallel-plate waveguides (PPWG) have been shown to have the lowest absorption at 1 THz, within the order of dB/km, but are impractical for integration into circuits. The lower performance and reduced convenience accompanying THz wavelengths make plasmonics based approaches a potential route forward, where their performance in terms of losses is comparable to the other technologies, and the advantage of the compactness pays off. It is worth mentioning that most SPP studies focus on the confinement to the surface and the width of the components if kept intentionally large, to make the alignment easier. Typical characteristic values for all three technologies are summarised in Table 6.2.

An additional advantage of spoof plasmonic technology is the possibility to com-

Table 6.2: Comparison between the losses and dimensions of different waveguide technologies at THz frequencies.

| Technology | Frequency (THz) | Losses (1/cm) | Size absolute in largest dimension | Size relative (d/$\lambda$) |
|---|---|---|---|---|
| Fibre [160] | 0.6 | <0.1 dB/cm | Diameter 6mm | 12 |
| [161] | 1 | <0.1 dB/cm | Diameter $\sim$3mm | 10 |
| Silicon Photonic Crystal [52] | 0.3 | <0.1 dB/cm | Diameter 1.5 mm (estimated) | 3 |
| SPP [162] | 1.3 | $\sim$1.74 dB/cm | Not investigated Estimate <0.5 mm | 2 |
| [163] | 0.28 | $\sim$1.09 db/cm | 0.2mm | $\sim$0.4 |
| [164] | 0.27 | $\sim$0.72 dB/cm | 0.55 mm | |
| 3D printed WM-250 [165] | 1 | $\sim$2 dB/cm | Diamerter >>1mm | >>10 |
| PPWG [166] | 1 | 2.6 db/km | Diameter= 10mm | >>10 |

bine multiple frequencies on a single chip. While photonic crystals only support a narrow frequency band which depends on the thickness of the substrate, multiple spoof plasmonic waveguides can be integrated on the same chip with different geometries which support a wide range of frequencies.

## 6.2.1 Spoof SPP waveguides produced with photolithography for THz applications

While the 3D printed waveguides have some interesting properties, as shown in the next section, the high losses do render these structures useless as waveguides, especially for components which require several centimetres of propagation distance. Therefore, waveguides produced with classic photolithography with SU-8 have been used for structures shown in the following sections. These structures have high transmission over centimetre distances and exhibit well-defined resonances at their cut-off with sharp roll-offs, as shown in Figure 6.6.

A comparisons between the transmission curves in Figure 6.6a and the dispersion curves in Figure 6.6b, calculated with Equation (6.20), shows a good agreement between experiment and theory. The propagation losses are in the order of $0.5 - 2\,dB/cm$, which is in good agreement with the values in literature, as seen Table 6.2. The uncertainty is too large for the propagation losses, as the wavveguides are to short to observe the exponential decay reliably. The waveguides are produced on 2" wafers and through the high viscosity of SU-8, beads occur at the edges, rendering these areas useless for measurements. This leaves an effective waveguide length of ∼2-3 cm which results in an uncertainty of $\pm 1.5\,dB/cm$.
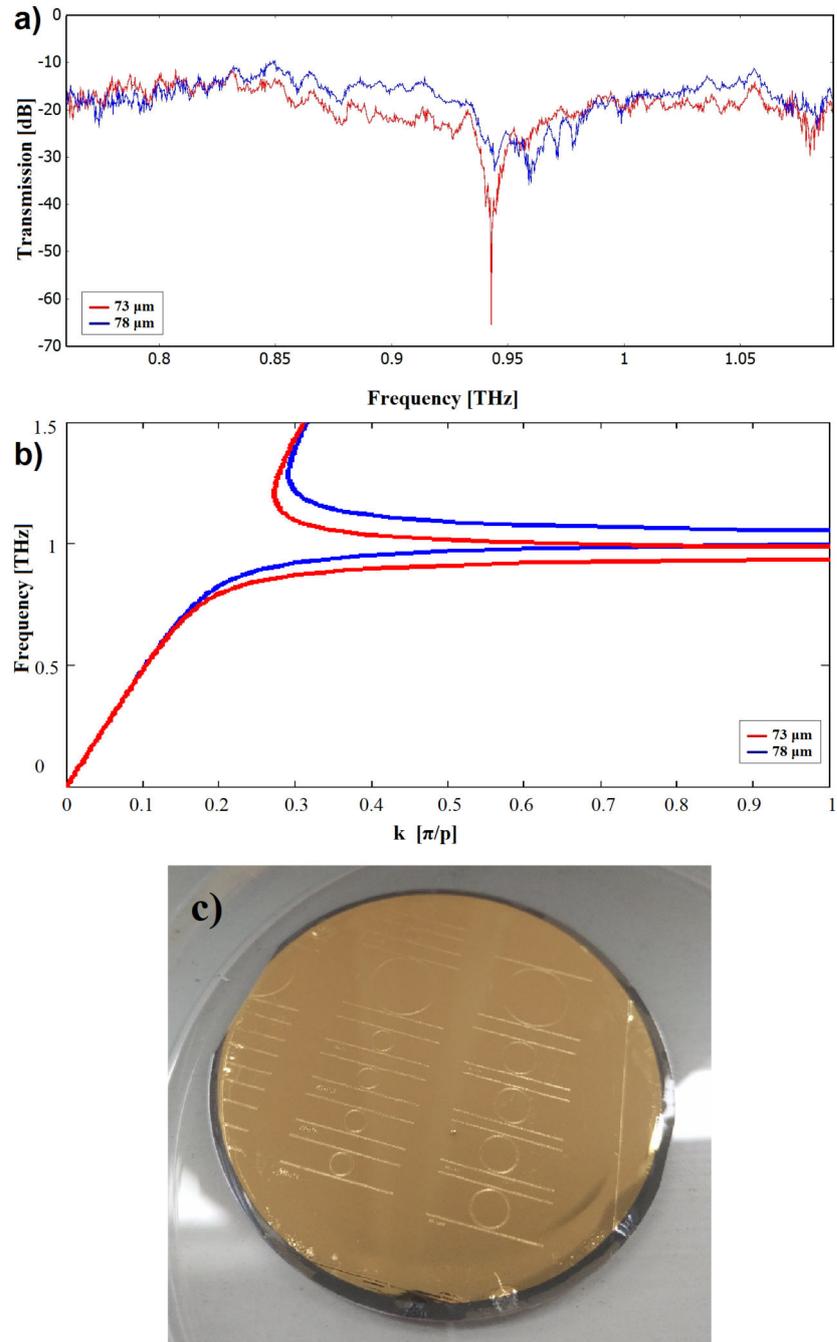
Figure 6.6: a) Measured transmission spectrum of two 1D groove structures over a distance of ~1 cm. The two structures only vary in height and are otherwise identical. A large drop in transmission can be seen around 0.95 THz for both structures, shifted by less than 100 GHz between them. This matches well with the theoretically predicted band gap as visible in the dispersion curves in b). The dimensions of the structures are: $p = 61.5\,\mu m$, $d = 12.3\,\mu m$ and $h = 73\,\mu m$ and $h = 78\,\mu m$ respectively. c) Photo of a wafer with spoof SPP waveguides fabricated with photolithography on top.

## 6.3 Highly integrated THz SPP waveguide circuits

In this section, several components based on spoof SPP waveguides are discussed. Coupling between waveguides is discussed, which leads to components such as a demultiplexer. Afterwards, switching on SPP waveguides is demonstrated and used for components. The subsection concludes with the presentation of SPP whispering gallery resonators.

As mentioned before, one possible application for SPPs are highly integrated waveguide circuits. As interconnects play an important role in communication systems, SPPs can be used in future THz based communications. The term "sub-wavelength optics" is used regarding plasmonics, but this often refers to the confinement on the surface, and for an integrated circuit, the lateral dimension is of more significance. Literature shows that spoof SPP structures can exhibit lateral dimensions of much less than the wavelength [167], but for an integrated circuit, however, the overall packing density of interconnects is the significant parameter. Therefore, not only the lateral extension of the SPP structure is relevant, but also how close a waveguide can be placed next to another without a negative influence on its performance, such as cross-talk or coupling between two waveguides.

Cross-talk usually is not investigated for many THz structures, except when it is utilised for additional functions, e.g. for a plasmonic Y-splitter where a signal is transferred to another waveguide in close proximity. Splitters and switches are important components for communication systems. Similar devices also exist in different technologies at THz frequencies. One example would be a photonic crystal diplexer where the wave leaks over to a waveguide in close proximity with different specifications and therefore separating the frequencies [168]. In the following subsections, the limits of the packing density of THz SPP waveguides for use in highly integrated photonic circuits will be investigated.

## 6.3.1 Waveguide width

The influence of the waveguide width on the guiding properties is investigated with FDTD simulation. A dipole is used to inject THz radiation at the beginning of the waveguide. The intensity is measured at the other end of the waveguide. All geometric parameters are kept constant, except for the width of the waveguide.

It can be seen in Figure 6.7 how the resonant frequency and therefore the guiding mode shifts to lower frequencies with increasing waveguide width and converges to a value just below $1\,\text{THz}$. The intensity varies with width as well, and therefore a minimum width of $150\,\mu\text{m}$ is recommendable to have a small dependency on deviations in the width of the structure. The drop in intensity with increasing width after $\sim 350\,\mu\text{m}$ is notable but could be caused by the use of a dipole source in the simulation, as it is significantly less pronounced when a Gaussian source is used, but normalisation is not straight forward for Gaussian sources in this scenario, making their results less useful. Additionally, from a pure design perspective, choosing a width closer to the converging value makes experimental results more predictable as simulation always have slightly deviating results, and when using a narrow band system for characterization, such as the THz-VNA, this range can be quickly missed by such a slight deviation.
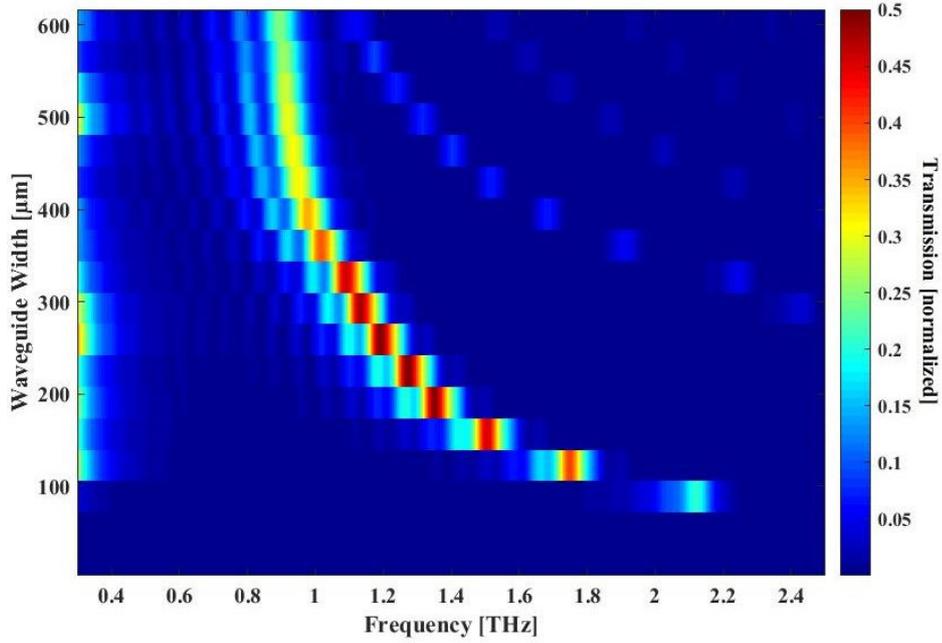
Figure 6.7: Simulated transmission of identical SPP waveguides with different widths. While there is no transmission for structures below $80\,\mu\text{m}$ width, the transmission converges with increasing width. The parameters of the SPP waveguide are $p = 80\,\mu\text{m}$, $d = 30\,\mu\text{m}$ and $h = 40\,\mu\text{m}$ and 20 periods.

## 6.3.2 Coupling

To investigate the coupling between waveguides, two identical SPP waveguides (width $w = 200\,\mu\text{m}$, $p = 55\,\mu\text{m}$, $d = 25\,\mu\text{m}$ and $h = 45\,\mu\text{m}$) are placed in a staggered position next to each other as depicted in Figure 6.8. The wave is launched in the longer waveguide and propagates for 20 periods without interference to ensure that the launching mechanism does not cause the crosstalk, then the second waveguide starts and runs in parallel with a fixed distance to the original SPP waveguide for 30 periods. At the end of both waveguides, transmission spectra are recorded over the complete width of the waveguide.

Interestingly, for very close proximity of 10-20 $\mu$m, there is no crosstalk between the two waveguides, as seen in Figure 6.9. Only when the distance exceeds a certain threshold, there is transmission to the second waveguide. This could be explained by resonant coupling between the two waveguides. While the SPP wave is closely confined to the waveguide, it extends over the physical edges of the waveguide. For
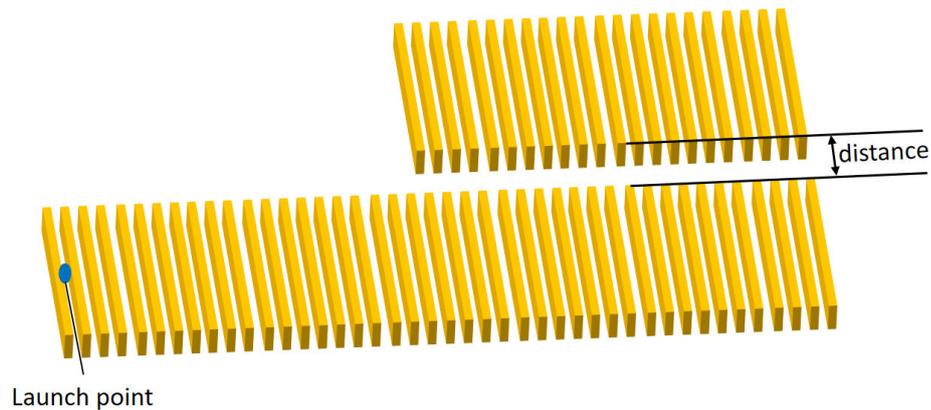
Figure 6.8: Schematic of the simulation setup to investigate coupling between two waveguides. The electromagnetic radiation is injected at the launch point and propagates along the lower waveguide. After 20 periods the second waveguide starts. The distance between the two waveguides is varied and the transmission recorded at the end of both waveguides.

resonant coupling, a standing wave has to form, and if the distance between the waveguides is too short, this cannot happen. At a spacing of $40\,\mu$m the coupling is ideal, and most energy is almost entirely transferred to the second waveguide.

This means that splitting intensity in different ratios can be achieved by changing the separation between waveguides. This can be used to produce Y-splitters which split a signal from a single input into two outputs. Additionally, it is an advantage for the packaging density of integrated plasmonic circuits that there is no transmission when the waveguides are too close, meaning that waveguides carrying different signals can be placed in close proximity to each other without crosstalk, which is in stark contrast to to other waveguides, such as photonic crystals, where a minimum distance is required to isolate waveguides from each other.
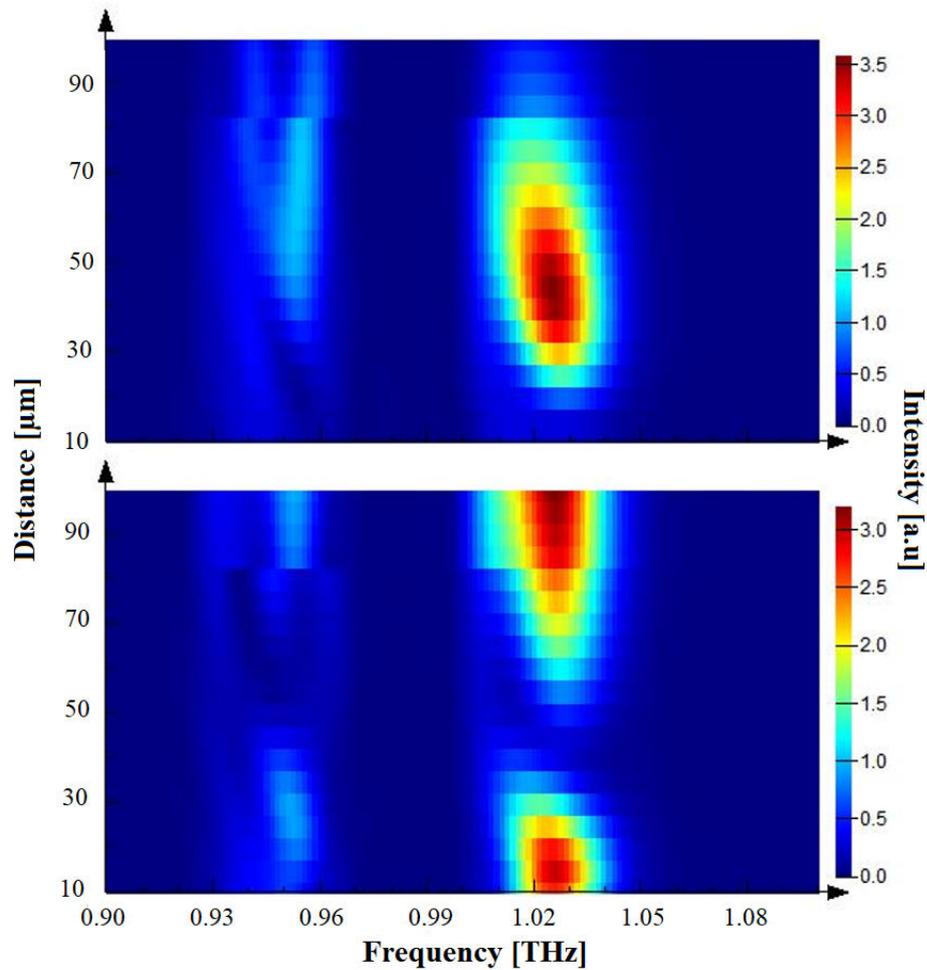
Figure 6.9: Simulated transmission in dependence of waveguide distance of the launch waveguide (bottom) and coupling waveguide (top).

### 6.3.3   Spoof plasmonic (De-)multiplexer

A multiplexer is a device that takes multiple inputs and combines them in one output. A demultiplexer does the inverse, having a single input and multiple outputs. An example for analogue demultiplexing is Frequency-Division multiplexing (FDM). In FDM several signals are transmitted through the same medium, but different frequencies are separate data channels. This means a device is required which separates the different frequency channels for individual processing. Such devices do exist for THz communication applications but are large compared to spoof SPP devices [169–171].

Here a spoof plasmonic demultiplexer is presented based on a modification of the coupling device presented in the previous subchapter, as shown in Figure 6.10. The device is modified by the introduction of a stop band – a waveguide with different geometric properties that leads to a lower cut-off frequency. The recorded trans-
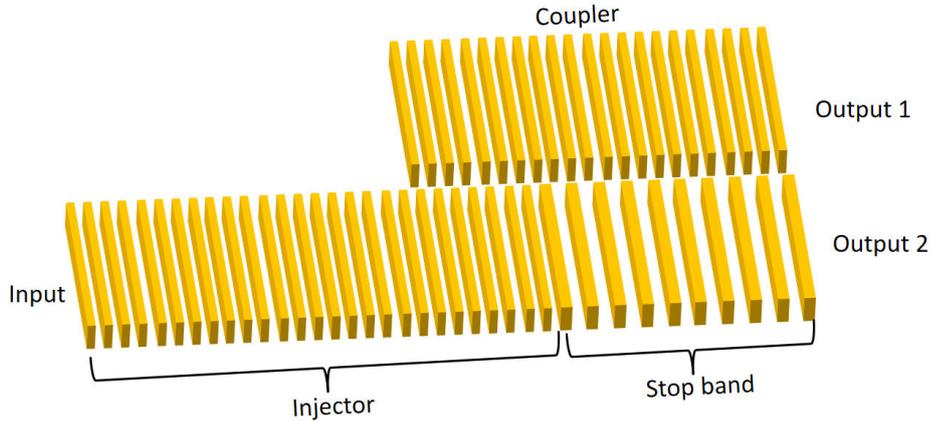


Figure 6.10: Illustration of a plasmonic demultiplexer. The input is coupled through the injector to the identical coupler, which carries the higher frequency channels. After several periods of injector and coupler running in parallel, a waveguide with different geometric properties with a lower cut-off frequency commences, indicated as 'stop band'. The stop band rejects the higher frequencies so that they can only couple to the coupler waveguide that leads to output 1, while simultaneously offering no coupling for the lower frequencies so that they are guided to output 2.

mission spectra of the original waveguide, and an example of a stopband waveguide, can be seen in Figure 6.11. The injector waveguide and the coupler will have a higher cut-off frequency than the stopband. How narrow the separation between frequency channels is can be controlled by the proximity of cut-off frequencies.

As the stopband rejects the higher frequencies they will couple to the parallel running waveguide leading to output 1. The spacing between waveguides is kept at a distance favourable to couple to the stopband waveguide. Therefore, the lower frequencies are guided to output 2. The result can be seen in Figure 6.12 which shows that it is possible to isolate a $\sim 20\,GHz$ narrow frequency channel at $\sim 0.95\,THz$ for output 2 with isolation in excess of $30\,\mathrm{dB}$ to output 1 which carries the higher frequencies. A cascade of such devices can be used to separate multiple channels. As the process is invertible, the same device can be used as a multiplexer.
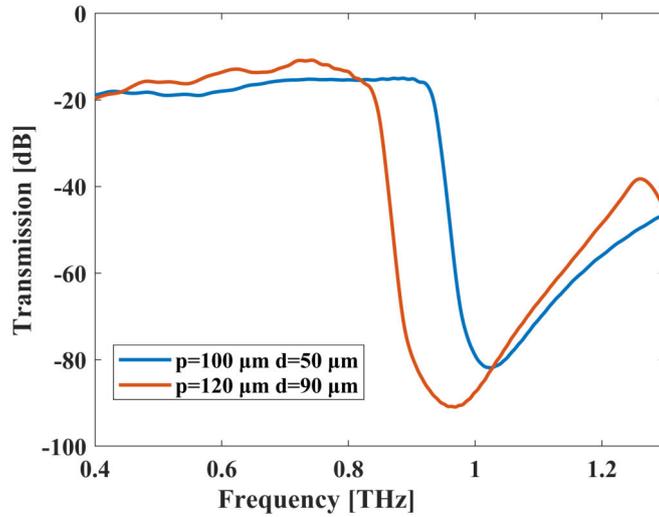
Figure 6.11: Cut-off frequencies depending on the geometrical properties of the spoof plasmonic waveguides. The height of the waveguides is kept constant ($h = 40\,\mu m$) to enable a single layer manufacturing process. The shown stop band waveguide has a lower cut-off frequency to the one used for the simulation in Figure 6.12 to clearly show the influence of the geometrical parameters.
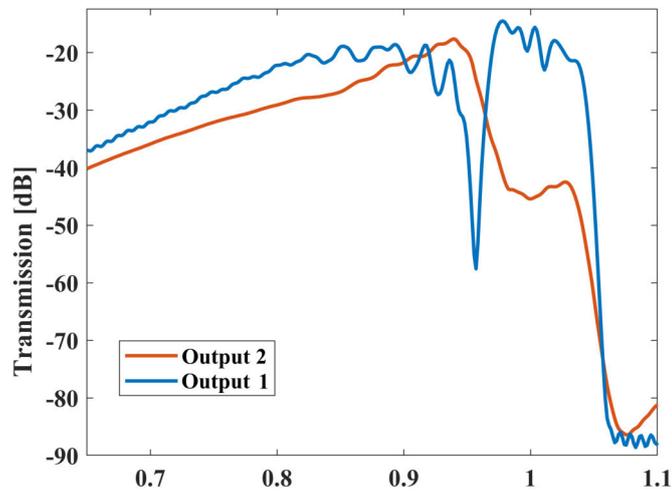


Figure 6.12: Simulated transmission of output 1 and 2 shows that there is a frequency channel at $0.95\,\mathrm{THz}$ outputting at output 2 which is isolated from output 1 by more than $30\,\mathrm{dB}$. Geometrical parameters of the injector and the coupler: $p = 100\,\mu m$, $d = 50\,\mu m$ and $h = 40\,\mu m$; and the stop band: $p = 120\,\mu m$, $d = 60\,\mu m$ and $h = 40\,\mu m$.

## 6.3.4 Switchable Spoof Surface Plasmon Polariton Terahertz Structures for Reconfigurable Photonic Circuits

In this subsection, an active spoof plasmonic device is discussed. At THz frequencies, where the frequency is so high that switching with diodes or transistors used at microwave frequencies reaches its limitations, alternatives for switches are required. Active plasmonic devices are of great interest for applications and have been demonstrated at microwave frequencies [172], whereas active devices such as diodes are readily available but have only been theoretically studied at THz frequencies [173, 174]. The switching is experimentally realized by introducing a liquid crystal (LC) to a spoof SPP structure. A temperature-induced phase transition results in a refractive index change that shifts the resonance frequencies of the structure. It is experimentally demonstrated how this can be used to switch between an off and on state. A design for a switchable Y-junction is presented.

The temperature-induced phase transition in the liquid crystal results in a small change in refractive index $n$. The change in $n$ based on the thermal phase transition ($\Delta n_{0.7THz} \approx 0.02$) is smaller than the optical or electrically controlled change between the ordinary and extraordinary orientation ($\Delta n \approx 0.2$) [175], but is easier to implement experimentally. The SPP waveguides have the geometric properties $p = 200\,\mu\text{m}$, $d = 40\,\mu\text{m}$ and $h = 80\,\mu\text{m}$. Knife-edge scattering is used with the knives immersed in the liquid crystal, as shown in Figure 6.13. The complete area between the blades is covered in LC (Merck E7), and the blades are immersed as well. This ensures that all SPP propagation takes place at the metal/liquid-crystal interface only. The horn antennas of the VNA extenders are aimed at the gap between knives and sample from a distance of $\leqslant 5\,\text{cm}$ on both sides of the sample, so that transmission spectra are recorded. The bottom side of the substrate is heated to induce the change in $n$ of the LC. Temperature probes are used to record the temperature at the bottom of the sample.

The behaviour of the 1D groove structures with no LC present has been discussed

earlier and the agreement between theoretical and the experimental results are shown in Section 6.2.1. However, the simple analytical model developed in [159] does not account for a dielectric other than air. Nevertheless, in analogy to the analytical model, the phase transition and the concomitant change in refractive index can be interpreted as a change in optical path length which changes the band structure accordingly.

At room temperature, the LC is in the nematic phase and the transmission, as
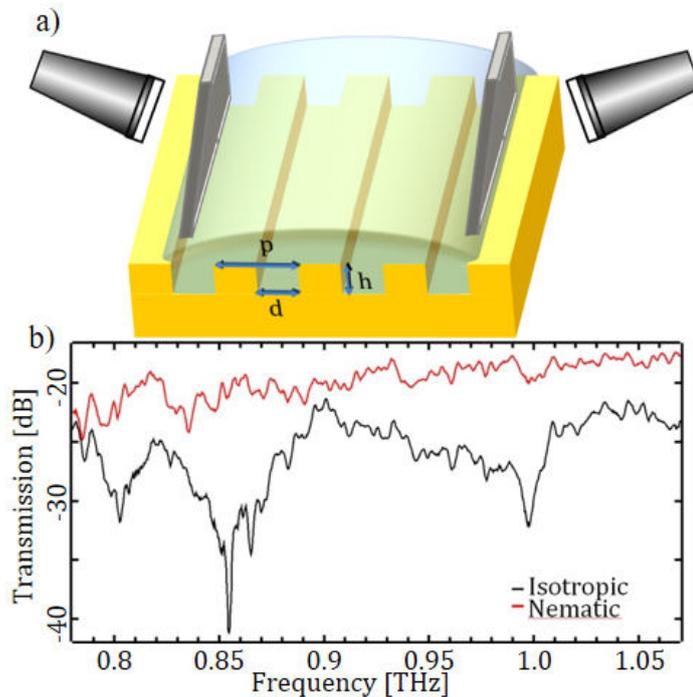


Figure 6.13: a) Illustration of the measured switchable spoof SPP liquid crystal samples. The knives, which are used to couple the THz radiation in and out of the horn antennas, are immersed in the liquid crystal. The relevant geometric properties are indicated. b) Transmission spectrum of the spoof SPP structure in its "on" state at room temperature (red) and "off" state above the phase transition temperature above 61°C (black). The difference between the two states switchable states at 0.86 and 1.1 THz is approximately 10 dB.

seen in Figure 6.13b, resembles a flat line without any striking features, meaning that SPP propagation takes place in a frequency region where no band gaps are present. The temperature is increased in 5°increments. With the used heating method from underneath the sample, which is also the point where the temperat-

ure is measured, the phase transition temperature cannot be resolved with a higher temperature resolution. The transmission remains flat when the temperature is increased, and there are no changes to be observed up to $60°$. If the temperature is raised above ∼$61°$C, the LC makes a transition to the isotropic phase which leads to two significant dips in the transmission spectrum at 0.86 THz and 1 THz. The modulation depth, the difference between the on and off state, is 10 dB for both frequencies.

Similiar structures, as shown at the beginning of Section 6.2.1, show a sharper cut-off with a steeper roll-off and a drop off of approximately 20-30 dB. This can be explained by the fact that the cut-off is sharpest at the first resonance of a structure, i.e. at the frequency of the fundamental mode. The approximation of the dispersion relation is restated here for convenience:

$$k_x = \frac{\omega}{c}\sqrt{\frac{(p-d)^2}{p^2}\tan^2\left(\frac{2\pi fh}{c}h\right) + 1}. \qquad (6.20)$$

Therefore the fundamental resonances are spaced by multiples of the first fundamental resonance $f_0$ or every time the $tan^2$ reaches an asymptote. Since the first fundamental resonance of a structure with similar geometry without LC is in the order of 1 THz, even the introduction of the LC, which will decrease the spacing between fundamental resonances proportional to the increase in the optical path length of $h$ ∼1.6 cannot explain the small spacing of ∼0.1 THz between the two resonances. The small spacing between the resonances, and their disappearance rather than shift, indicates that the observed dips in transmission are due to secondary resonances after the cut-off as they are also observed in the simulations (Figure 6.14 black and red lines).

FDTD simulations are used to explore the maximum modulation depth between two states and possible applications based on the change in $n$, using literature values for the E7 LC at THz frequencies [175–177]. Figure 6.14 shows that the thermally-induced phase transition results in a much smaller shift in the 3 dB cut-off frequency of 0.02 THz than the shift induced by electrical/optical control of 0.1 THz which reflects the difference in $\Delta n$ between the two switching methods.

The smaller shift makes it more difficult to exploit the effect for technical applications and reduces the modulation depths, demonstrating that for real applications an electrical control is desirable, which additionally also allows fast switching in the order of kHz rather than Hz for the thermal switching. While the simulation results show a qualitative fit with the experimental results, the quantitative difference is larger than observed with the SPP structures without LC. This can have several reasons, the primary probably being that the surface tension of the LC prevents a completely uniform coverage, especially within the grooves, since the LC is dispensed on top of the sample. Additionally, the simulations do not account for the anisotropy of the LC's Nevertheless, the switching enables new applications at THz
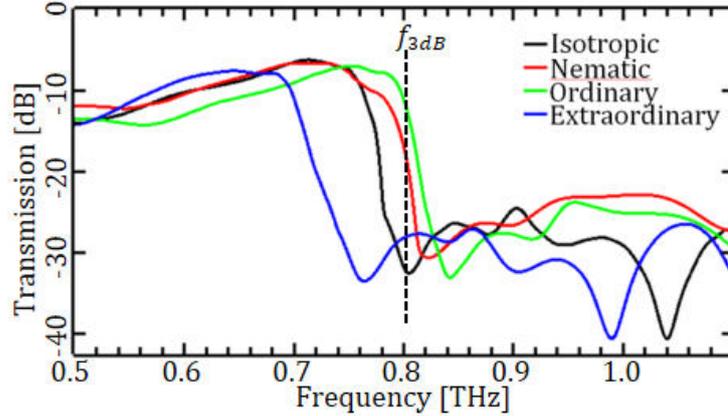


Figure 6.14: FDTD simulations to compare the different switching mechanisms of liquid crystal spoof SPP structures: While all curves show approx. the same drop in transmission at their cut-off frequency ($f_3dB$, indicated for green curve) the temperature-induced phase transition (black and red curve) only shows a small change in cut-off frequency of 0.02 THz, while the optical or electrical induced change in cut-off frequency is 0.1 THz.

frequencies, such as reconfigurable photonic circuits, e.g. by extending the functionality of Y-splitters [178] or the previously shown demuxer to include switchable branches. By using two different spoof plasmonic geometries in the branches, the change in $n$ can be used to shift the transmission curves in a way that one branch is transmitting when the LC is in its high $n$ state while the other branch is blocked and vice versa when the LC is in the low $n$ state. Such a concept is shown in Figure 6.15. The lower branch of the switch is transmitting when the LC is in the

extraordinary orientation ($n = 1.74$). The right arm is switched "off" with strongly reduced transmission. When the LC is in the ordinary orientation with an $n$ of 1.59, the right arm is switched "on" and the left is switched "off" (refractive indices from [177]). The design of the concept is kept as simple as possible with the minimum number of geometric changes between the different SPP structures. It comprises an injector that guides the THz radiation to the Y-junction which is not immersed in the LC with the geometric parameters $p = 50\,\mu$m, $d = 20\,\mu$m and $h = 50\,\mu$m. Minimising the exposure of the waveguide to the liquid crystal is necessary to reduce losses because the LC has a higher attenuation coefficient than air, being highest in the ordinary orientation with $14.3\,$cm$^{-1}$ [177]. Both branches are immersed in LC and are mirrored with the same lateral geometry ($p = 110\,\mu$m, $d = 40\,\mu$m) and only differ in height (left branch: $h = 120\,\mu$m, right branch: $h = 125\,\mu$m). At a simulated operational frequency of $0.7\,$THz the modulation depths are $14.7\,$dB for the left branch and $17.9\,$dB for the right branch.

The efficiency of the device is high with up to $\sim54\%$ of the power entering the Y-junction measured at the end of the transmitting arm, given that a Y-junction usually splits the incoming power equally. The efficiency could be further increased by matching the dispersion curves of the structures to reduce coupling losses at the transition between two waveguide geometries, but this would require more complex geometry changes which might become feasible with the recent developments in 3D manufacturing for THz structures, as demonstrated with 3D printed waveguides [165]. This newly gained freedom in structure design also enables the use of much smaller microcavity filters [179] as the active switching zone, which could be used as a junction which would reduce size and losses even further.

In summary, switching of spoof SPP waveguides has been experimentally demonstrated and a switchable Y-junction proposed as an application for integrated photonic circuits has been presented. Both the measured switchable waveguide and the Y-junction have a high modulation depth of above $10\,$dB which makes this first concept feasible for applications.
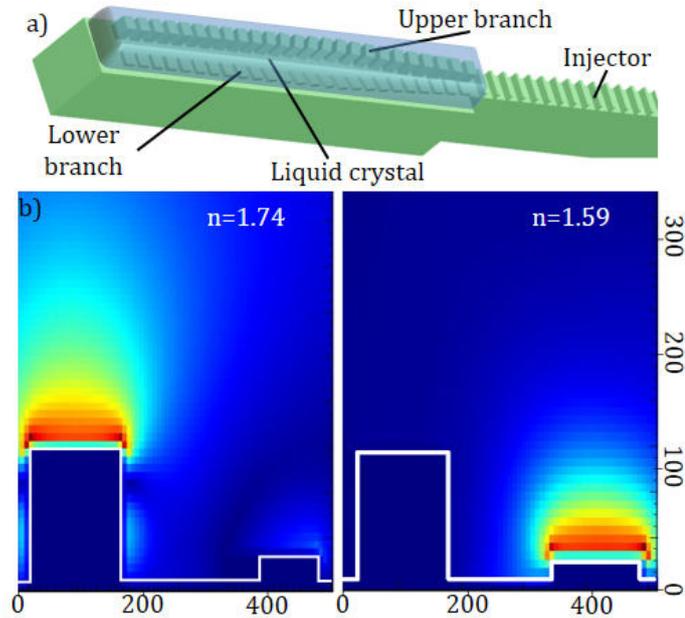
Figure 6.15: a) Illustration of the investigated reconfigurable waveguide. The injector guides the THz radiation to the Y-junction and is not immersed in the liquid crystal, to reduce losses. The geometry of the waveguides changes at the junction so that the waveguides operate at the same frequency as the injector while being in the higher n environment of the liquid crystal. They differ in height so that they are resonant with the operational frequency of 0.7 THz when the n is in different states. b) The electric field distribution at the two waveguides in the Y-junction. When in the higher n extraordinary orientation the left arm is switched on, while the right arm is switched on when the liquid crystal is ordinary orientation. The modulation depths are 14.7 dB and 17.9 dB respectively.

## 6.3.5  Spoof plasmonic whispering-gallery resonators

Whispering gallery (WG) modes are resonances occurring inside a large resonator (any dimension $\gg \lambda$) with smooth edges. The electromagnetic waves of WG modes travel around the resonator and interfere, therefore the resonance condition is that any given point has to have the same phase (modulo $2\pi$) after a roundtrip. The term 'whispering gallery' stems from the description of the phenomenon in St.Paul's Cathedral in London by Lord Rayleigh. The simplest form of such a resonator is a ring, as seen in Figure 6.16.

There are some common characteristics to a WG resonator. As for every resonator, there is the quality factor which gives the relation between the total energy stored
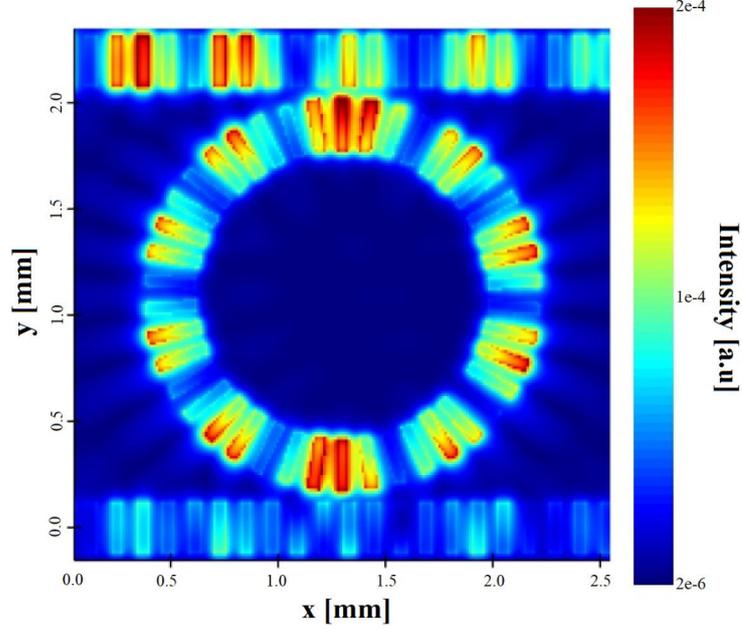
Figure 6.16: Electric fields in a whispering-gallery spoof SPP resonator. The resonant mode is visible with a standing wave pattern with regular spacing around the ring.

and energy lost per cycle.

$$Q = \omega_0 \frac{stored\ energy}{power\ loss} = \omega_0 \tau = \frac{\omega_0}{\Delta\omega_{FWHM}} \qquad (6.21)$$

Additionally, the losses of a WG resonator are typically expressed in terms of the individual loss mechanism [180]. The intrinsic quality factor $Q_{int}$ is the sum of the inverse losses

$$Q_{int}^{-1} = Q_{mat}^{-1} + Q_{surf}^{-1} + Q_{scatt}^{-1} + Q_{bend}^{-1}, \qquad (6.22)$$

where $Q_{mat}^{-1}$ descirbes the intrinsic material absorption, $Q_{surf}^{-1}$ the surface losses, e.g. through coatings or contaminants, $Q_{scatt}^{-1}$ describes scattering losses, e.g. on defects, and $Q_{bend}^{-1}$ describes bending losses.

As this is a general description of losses for WG resonators, not all specified loss mechanisms are applicable for this structure. For an SPP resonator, which only guides waves on the surface, there is no difference between the material losses and the surface losses, making $Q_{surf}$ redundant. Furthermore, as an SPP always suffers from radiative losses even when propagating straight, these losses can be included

in $Q_{mat}$, as they are fundamentally a property of the materials used.

The WG resonators are coupled to two straight waveguides. While the through measurement from port 1 to port 3, as indicated in Figure 6.17, is straightforward, for the return measurement, the experimental set up has to be changed, due to spatial constraints, and a collimated beam is used to couple in at port 2 and the return signal is measured at an angle from the side at port 1, resulting in overall lower intensity of these measurements and less pronounced peaks.

Figure 6.18 shows the frequency response of a ring resonator. The measured
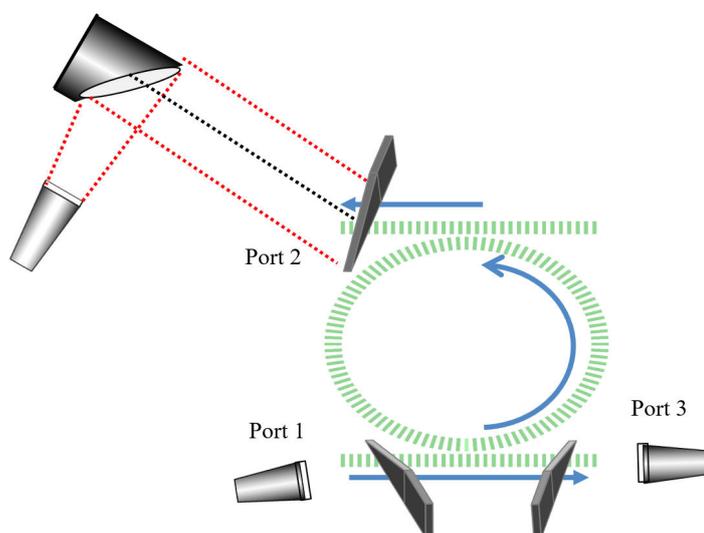


Figure 6.17: Schematic of the measurement configurations needed to characterize a whispering-gallery resonator. While the transmission measurement is straight forward from port 1 to port 3, the measurement of the return signal requires the use of mirrors due to spatial constraint, as the device diameters and therefore the spacing between waveguides is on the order of millimetres.

quality factors for these resonant features are in excess of 300. As the electric field is more strongly confined towards the band edge, there is little transmission at lower frequencies and no resonances are visible. Closer to the cut-off at higher frequencies, the resonances are more pronounced and have a higher Q factor, as seen in Table 6.3. This indicates that the radiative losses in the bendings are reduced due to the stronger confinement with increasing frequency. This increase of Q factor is visible for both the notches of the through and the peaks of the return measurements. The effect of the spoof plasmonic waveguide is also visible in the

spacing of the resonances. Common whispering-gallery resonators have equally spaced resonances, as positive interference will only occur when the circumference of the ring is equal to a multiple of the resonating wavelength $\lambda_R$

$$2\pi n_{mode} R_{mode} \approx M\lambda_R. \tag{6.23}$$

The "slow light" effect of the plasmonic structures acts as a highly dispersive medium on the resonances, decreasing the spacing between resonances from $\sim 9.5\,\mu$m to $\sim 4\,\mu$m with increasing frequency for the through measurement, and from $\sim 14\,\mu$m to $\sim 6\,\mu$m for the return measurement. In Figure 6.18a no resonances are visible for frequencies below $0.95$ THz. For higher frequencies it is visible that the notches and peaks of the through and return ports align well for lower frequencies, showing that these are indeed the frequencies transmitted through the whispering-gallery resonator. But with increasing frequency and non-linear spacing between resonances, there is an increased mismatch between notches and peaks, as shown in Figure 6.18b.

As the size of a ring resonator cannot be further reduced without losing the

Table 6.3: Frequencies and Q factors for the resonances of through and return ports, designated as notch and peak respectively, of the ring resonator shown in Figure 6.18

| Resonance [#] | $f_{notch}$ [THz] | $Q_{notch}$ | $f_{peak,return}$ [THz] | $Q_{peak}$ |
|---|---|---|---|---|
| 1 | 1.0363 | 104 | 1.0311 | 16 |
| 2 | 1.0554 | 139 | 1.0657 | 57 |
| 3 | 1.0713 | 235 | 1.0906 | 69 |
| 4 | 1.0895 | 304 | | |

coupling efficiency to the straight waveguides, an oval-shaped race track design, as shown in Figure 6.19a, is employed. This design allows for further reduction in size while simultaneously increasing the coupling region, where waveguide and ring resonator run approximately parallel to each other.

The spectra in Figure 6.19b also show agreement between peaks and valleys of the through and return port, but the quality factor of the resonances are lower than for the ring resonator a with maximum value of 260. The tendency of the

Q-factor to increase appears to be the same, as seen in Table 6.4, despite the lower value for the third notch of the through port, as this is caused by an additional feature which is clearly visible in the linear scale during data extraction (not shown). Overall, the spectra look like there is another resonance interfering, adding additional structure to the spectra, which partially reduces the measured Q factors. But it is notable, that the Q factors of the return port are significantly higher for the race track design than for the ring resonator. This indicates that the coupling between the ring resonator and the waveguide is more efficient which is expected due to both running longer in parallel to each other. That the Q factors of the race track design do not exceed those for the ring resonator might indicate that radiative losses caused by the smaller bend radius might counteract the increase in quality factor that would be expected with the shrinkage to a smaller size.

Overall, the spoof plasmonic WG resonators offer extremely high Q-factors at a

Table 6.4: Frequencies and Q factors for the resonances of through and return ports of the race track resonator shown in Figure 6.19. The $Q_{notch}$ for the fourth resonance is reduced as it coincides with another resonant feature.

| Resonance [#] | $f_{notch}$ [THz] | $Q_{notch}$ | $f_{peak,return}$ [THz] | $Q_{peak}$ |
|---|---|---|---|---|
| 1 | 1.0234 | 81 | 1.0234 | 144 |
| 2 | 1.0479 | 121 | 1.0519 | 234 |
| 3 | 1.0619 | 232 | 1.0659 | 244 |
| 4 | 1.0786 | (112) | 1.0790 | 260 |

small form factor, which makes them very attractive for integrated photonic circuits. The Q-factors are in the same magnitude of order as those for plastic and quartz disks at lower THz frequencies [181]. There is additional work necessary to find the ideal coupling for the structures [182], but the nonlinear spacing can be useful to extend the tunable range of a device which would be interesting for spectroscopy applications [183].
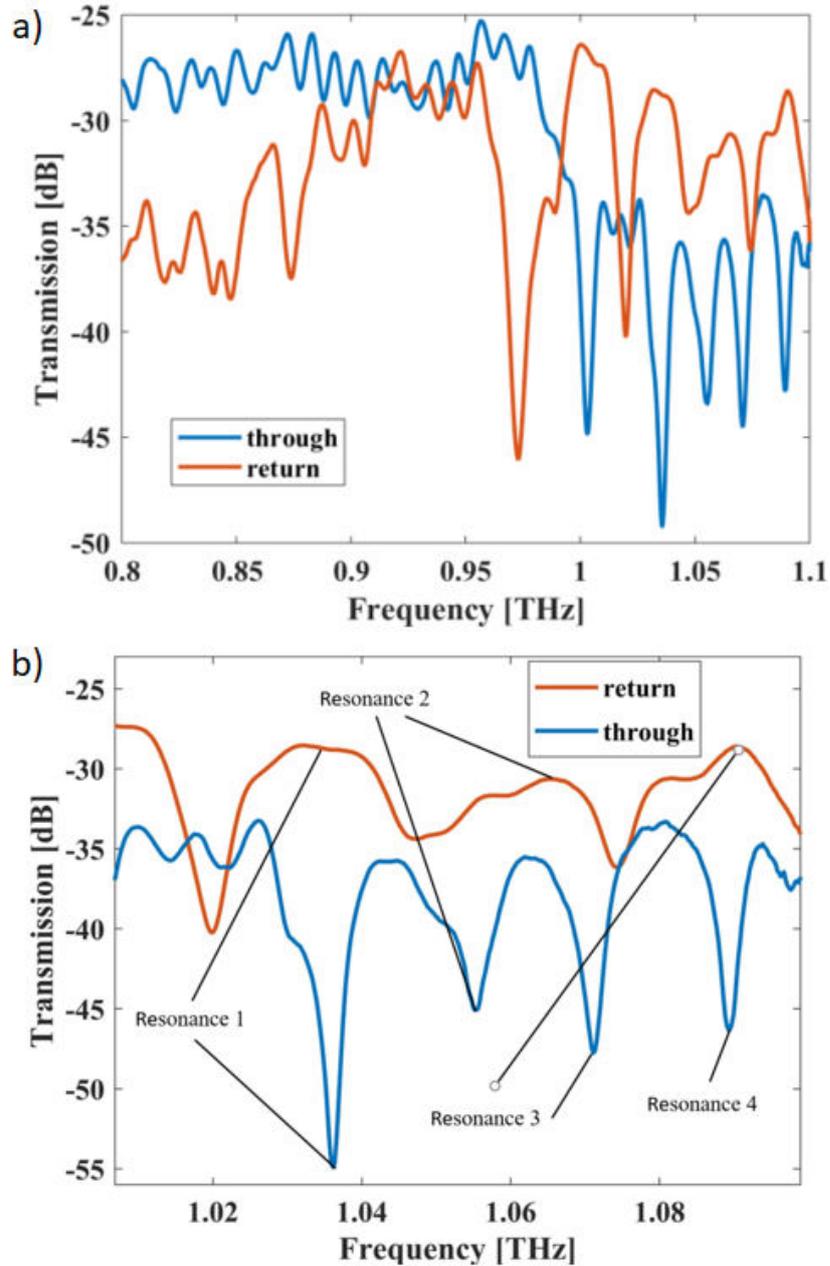
Figure 6.18: Frequency spectra of a whispering-gallery ring resonator with a $\sim 2\,\mathrm{mm}$ diameter which corresponds to 62 periods at a pitch of $120\,\mu\mathrm{m}$. a) The transmission spectrum shows that at lower frequencies there are no resonances and low transmission at the return port, indicating high losses and bad coupling. This changes at higher frequencies where the coupling is increasing and as the SPP is more strongly confined, the resonances are more pronounced. b) Zoom into the resonances at higher frequencies which show that there is an increasing miss alignment between resonant peaks at the return port and resonant notches at the through port.
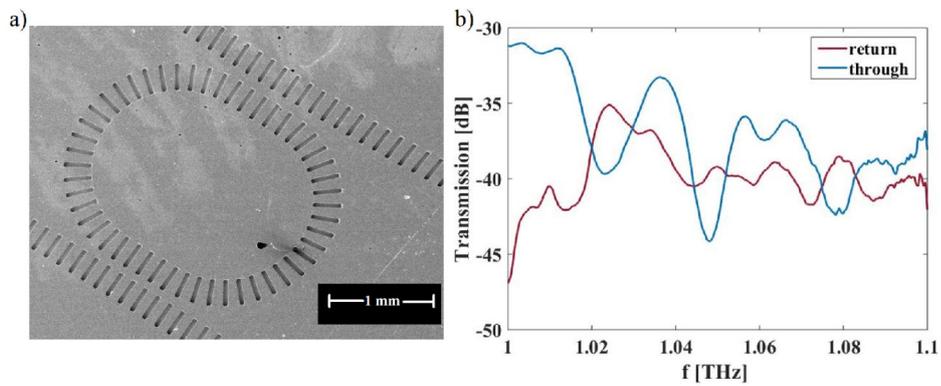
Figure 6.19: a) Micrograph of the race track resonator. b): Frequency response of the race track design showing that the notches of the through and the peaks of the return port of this structure align as well. It is noticeable that the resonances are less pronounced than for the ring resonator.

# 6.4 Scattering of spoof surface plasmon polaritons in defect-rich THz waveguides

## 6.4.1 Introduction

In this section,the first observation of SPP scattering from surface defects on metal-coated 3D printed, corrugated THz waveguiding surfaces is discussed. Surface defects, a result of the printing process, are shown to assist the direct coupling of the incident free-space radiation into a spoof SPP wave; removing the need to bridge the photon momentum gap using knife-edge or prism coupling. This effect is known for classic, optical SPPs [184], but has not been reported for spoof SPP structures. This is reasonable because, for operation in the microwave region, spoof SPP structures which possess feature sizes of the order of centimetres, are unlikely to include defects on the same scale. At higher (THz) frequencies, where wavelengths are of the order of tens of microns, semiconductor fabrication techniques are commonly used to produce the spoof SPP structures and are thus also usually free from defects comparable in scale to the used wavelengths. But 3D printing, which has been reported for millimetre waves [164] but not for spoof plasmonic THz structures before, does exhibit a high defect density as the feature sizes are pushing the limits of the fabrication technique. 3D printing has high commercial potential where it competes with other serial techniques, such as milling, and can produce low-cost and lightweight objects. One example is in the production of waveguides for high-frequency applications. Metalised, low-density 3D printed parts can replace commonly used materials such as brass. For example, 3D printed, metal-pipe rectangular waveguides capable of operating up to 1.1 THz have recently been reported [165].

The free space characteristics, propagation losses and confinement of the spoof SPPs to the surface are measured, and the results are compared to finite-difference time-domain simulations. Angularly resolved THz spectroscopy measurements re-

veal the scattering patterns from surfaces and are compared with Mie theory [185], taking into account the shortened wavelength of the photons in their bound SPP state compared to their free-space wavelength. These results confirm yet another similarity between the properties of THz spoof SPPs and their natural, non-spoof, counterparts at optical and infrared frequencies which also, unexpectedly, adds functionality to the structures.

## 6.4.2 Results

Four 3D printed spoof SPP structures with different geometric properties and defect densities are investigated. The geometrical and plasmonic properties, such as the propagation length and confinement, are summarised in Table 6.5 and compared with other spoof plasmonic structures from the literature. The structures were first characterised to obtain their plasmonic properties, such as the transmission spectrum, which shows the geometry dependent cut-off and knife-edge scattering experiments to determine the propagation length and confinement of the spoof plasmons to the surface. This was followed by the determination of the defect density with scanning electron microscopy and an optical surface profilometer. Finally, the scattering of the THz spoof plasmons at the defects was measured with angular resolved THz spectroscopy.

### 6.4.2.1 Sample design and dispersion engineering

The 3D-printed SPP structures have a triangular cross-section as shown in Figure 6.20. This is an unconventional shape as most 2D SPP structures have a rectangular cross-section, as shown in Figure 6.20c, with vertical sidewalls that are compatible with semiconductor manufacturing processes. Other shapes have been reported in the literature and can result in stronger confinement and longer propagation lengths [178, 186]. The rectangular geometry also results in a simplification of the equations which describe the dispersion curve, since all edges of the

Table 6.5: Geometric parameters and characteristic lengths of the 3D printed SPP structures in comparison with literature values. It is apparent that while the SPPs are highly confined, the propagation length of the 3D printed structures is strongly reduced compared to the literature values from structures with good surface quality. p: pitch, d: grove thickness, h: height as indicated in Figure 6.20. Defect Power Spectral Density (PSD) signal ratio: Ratio between defect peak and corrugation peak.

| Sample | Geometrical Parameters $[\mu m]$ | | | Propagation Length $L_x$ | | Confinement $L_z$ | | Defect PSD signal ratio | Unassisted free space coupling |
|---|---|---|---|---|---|---|---|---|---|
| | p | d | h | $\mu m$ | $\lambda$ | $\mu m$ | $\lambda$ | | |
| 1 | 150 | 50 | 30 | 706±181 | ∼2.4 | 75±4 | 0.25 | 2.1 | Yes |
| 2 | 150 | 50 | 35 | 384±23 | ∼1.3 | 119±5 | 0.4 | 6.8 | Yes |
| 3 | 165 | 50 | 30 | 478±32 | ∼1.5 | 75±4 | 0.23 | 7.3 | Yes |
| 4 | 75 | 30 | 15 | 590±36 | ∼2 | 69±2 | 0.23 | NA | Yes |
| [163] | slots in metal film @028 THz | | | 80000 | 75 | 1690 | 1.6 | | No |
| [162] | metamaterial array at ∼1 THz | | | 50000 | 176 | 600 | 2 | | No |

structure are parallel to the electric field components. Nevertheless, a comparison to the well-explored rectangular design which was used for the structures fabricated with photolitography in Section 6.3 is worthwhile for understanding how the different geometric parameters influence the frequency behaviour and the dispersion curve.
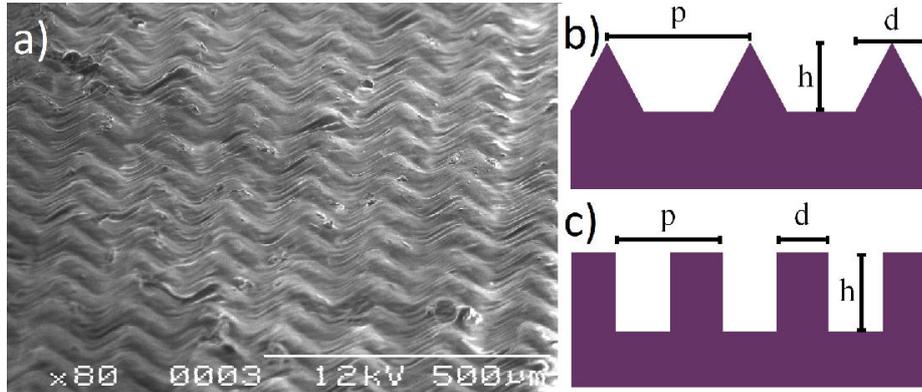


Figure 6.20: The micrograph (a) shows the typical triangular cross-section of the 3D printed samples and the relevant geometrical parameters are indicated in the schematic in b. c) shows the crosscut of the rectangular structures with all relevant geometric parameters laying on the axes of a Cartesian coordinate system allowing a simpler description of the dispersion curve with equation Equation (6.20).

Again, Equation (6.1) for the disperision relation of a spoof SPP structure with

rectangular crosssection is restated for convenience

$$k_x = \frac{\omega}{c}\sqrt{\frac{(p-d)^2}{p^2}\tan^2\left(\frac{2\pi f h}{c}h\right) + 1}. \tag{6.20}$$

The curvature of the dispersion relation is predominantly determined by the depth of the grooves, $h$. Since the velocity of the SPP is proportional to the slope, this variable has the largest influence on the SPP propagation properties. The fraction of pitch $p$ and groove thickness $d$ allows one to fine tune the cut-off frequency, so a change in ratio results in a shifted curve with similar shape. To understand how these changes in geometry and the concomitant changes in the dispersion curves influence the transmission properties of the actual samples the different dispersion curves are compared with transmission spectra obtained from Finite-difference time-domain (FDTD) simulations in Figure 6.21. Similar changes in dispersion curves and transmission spectra can be seen for a relative change of 15% in pitch $p$, which has only little influence other than on the cut-off frequency while the shape remains comparable, but an equal relative change in depth of the grooves $h$ has a large influence on the slope with a smaller change in the cut-off frequency. The shapes of the transmission curves can be compared in a quantitative way using the usual metrics of the $3\,\text{dB}$ cut-off frequency and the roll-off, the linear part of the slope after the cut-off. When the pitch is changed the roll-offs change from 560 to $562\,\text{dB/THz}$ with a shift in the $3\,\text{dB}$ cut-off frequency of $\Delta f \approx 0.08\,\text{THz}$ (blue/green lines); but the slope changes significantly to 263 dB/THz with an equal change in height (blue/red lines). This indicates the transmission data can indeed be used to deduce the shape of the dispersion curve. Following on from this, the effects of the same relative geometrical changes on the transmission properties of the triangular SPP structures in Figure 6.21b is compared. The cut-off frequency of the triangular SPP structures is also most sensitive to the change in pitch ($\Delta f \approx 0.1\,\text{THz}$, green/blue lines), but in contrast to the rectangular structures, the slope also shows a significant change from 1000 to 1739 dB/THz. This indicates that not only the cut-off frequency changes with the pitch but also does the overall shape of the dispersion curve. On the other hand, the change in height results in a

transmission curve shape which is comparable with the original curve, with a roll-off of 706 dB/THz and a smaller shift of $\Delta f \approx 0.03$ THz. This suggests that the design rules are not as straightforward for the triangular SPP structures as they are for the rectangular structures, where a change in a single parameter mostly changes only one characteristic of the transmission curve, but they do potentially add greater flexibility in design.
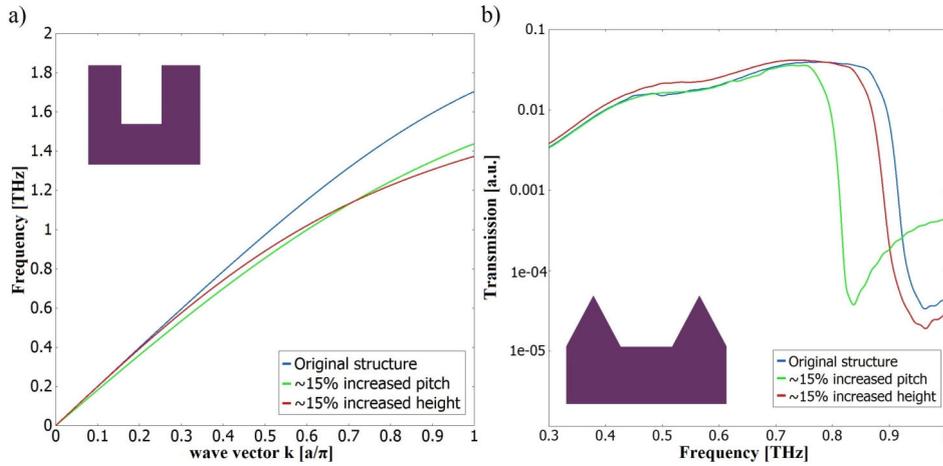


Figure 6.21: The comparison of the calculated dispersion curves of rectangular SPP structures (a, 6.20) with the transmission spectra (inset a, from FDTD) of the rectangular structures shows how the changes in the dispersion curve influence the transmission properties. With this, the influence that the changes in the geometry of the triangular SPP structure have on the dispersion curve from its transmission spectra can be deduced (b) by comparing the changes in transmission characteristic (cut-off frequency, roll-off). Original structures: $p = 150\,\mu m$, $d = 50\,\mu m$, and $h = 30\,\mu m$, with $p = 175\,\mu m$ for the increased pitch and $p = 35\,\mu m$ for the increased height.

## 6.4.2.2   THz characterization

The non-linear dispersion relation of SPP results in an increased momentum of the quasi-particle, in comparison to a free space photon, near the cut-off frequency. There are two common ways to bridge the momentum gap: high refractive index prisms, and scattering [184]. The latter technique, called knife-edge scattering in experimental setups, is favourable for broadband SPP structures because a wider

range of frequencies can be addressed simultaneously as the scattering offers a wide range of momenta. The 3D printed structures investigated here, however, do not require any such coupling techniques in contrast to previously reported THz spoof SPP structures. Here it is assumed that this property arises from the defect-rich surface. The Fourier decomposition of a rough surface contains many different wave vector components, enabling the excitation of many different SPPs over a wide range of angles simultaneously. The wide range of momenta available directly after the scattering at wavelength-sized defects results in the potential launch of SPPs at every defect. Although surface roughness as a means to launch SPPs is well known for optical frequencies, it has not previously been reported for spoof SPPs [187–190].
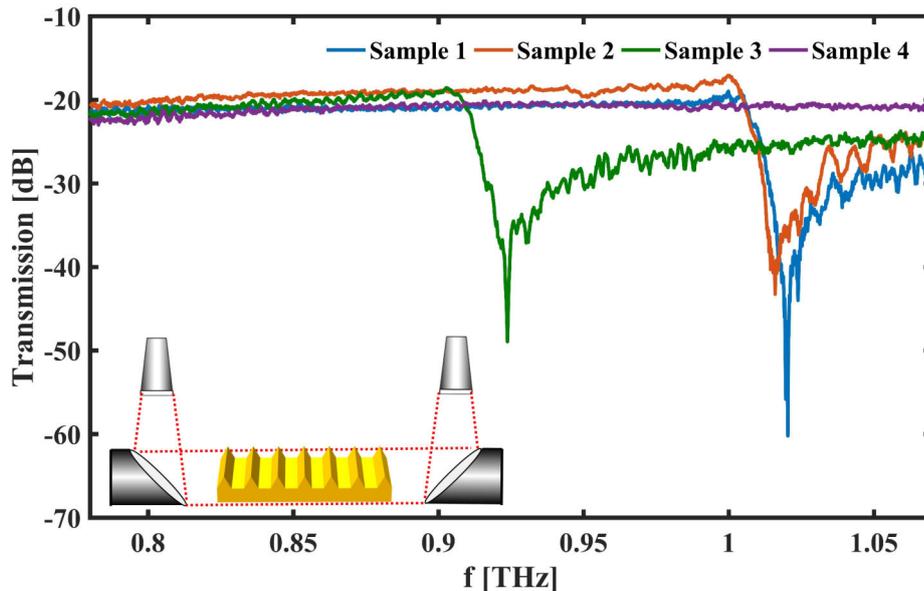


Figure 6.22: Transmission spectra of 3D printed spoof SPP structures with a triangular cross-section measured without additional means of coupling. A schematic of the measurement setup is shown in the inset. The THz beam originating at the horn antennas is collimated by a parabolic mirror, propagates across the surfaces and is then focused at the receiving horn antenna by a second parabolic mirror. The spectra agree very well with the results of the FDTD simulations in Figure 6.21. FDTD simulation of sample 4 shown in has simulated a cut-off frequency around 1.5 THz and, therefore the sample exhibits a flat spectrum in the measured range.

The transmission spectra in Figure 6.22 are measured by placing the 3D printed

devices in the collimated part of the beam between two parabolic mirrors without any additional means to couple from free space. The same measurements were repeated with the antennas pointing at an angle of $60°$ to the surface normal, to exclude the possibility that the free-space coupling happens due to edge-firing [151, 184]. The key characteristics of SPPs are the propagation length and the confinement of the SPP to the surface [151]. Both characteristic lengths are obtained by variations of the knife-edge scattering arrangement, as described in Section 6.1.3. Typical results of these measurements are shown in Figure 6.23 alongside the well matching fit of the exponential decay (all $R^2 > 0.995$). The results of the fittings can be found in Table 6.5.
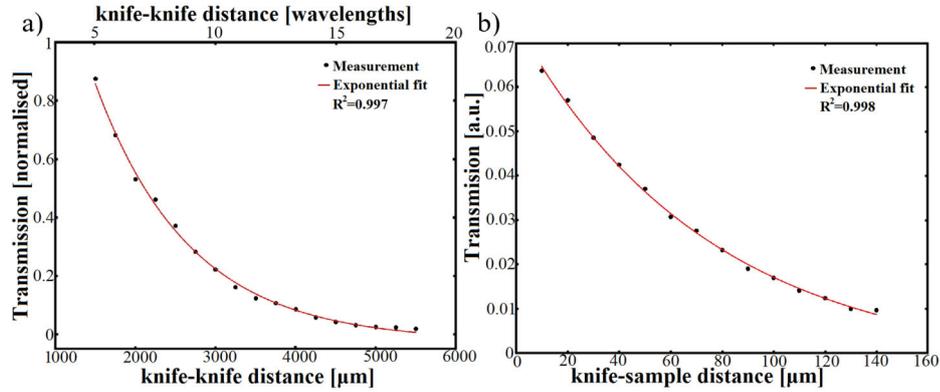


Figure 6.23: Measurement to extract the propagation length $L_x$ and the confinement $L_z$ for sample 2.

### 6.4.2.3 Defect density

The high defect density of the 3D printed samples is apparent when looking at the micrographs in Figure 6.24, where various types of defects are visible. For example, there are deformations to the surface along the ridges, probably originating from the stepwise printing process; defects where the grooves are damaged or incomplete; and debris, most likely originating from excess resin that forms irregularly shaped objects, on the surface.

The surface profiles allow the average power spectral density (PSD) to be calcu-
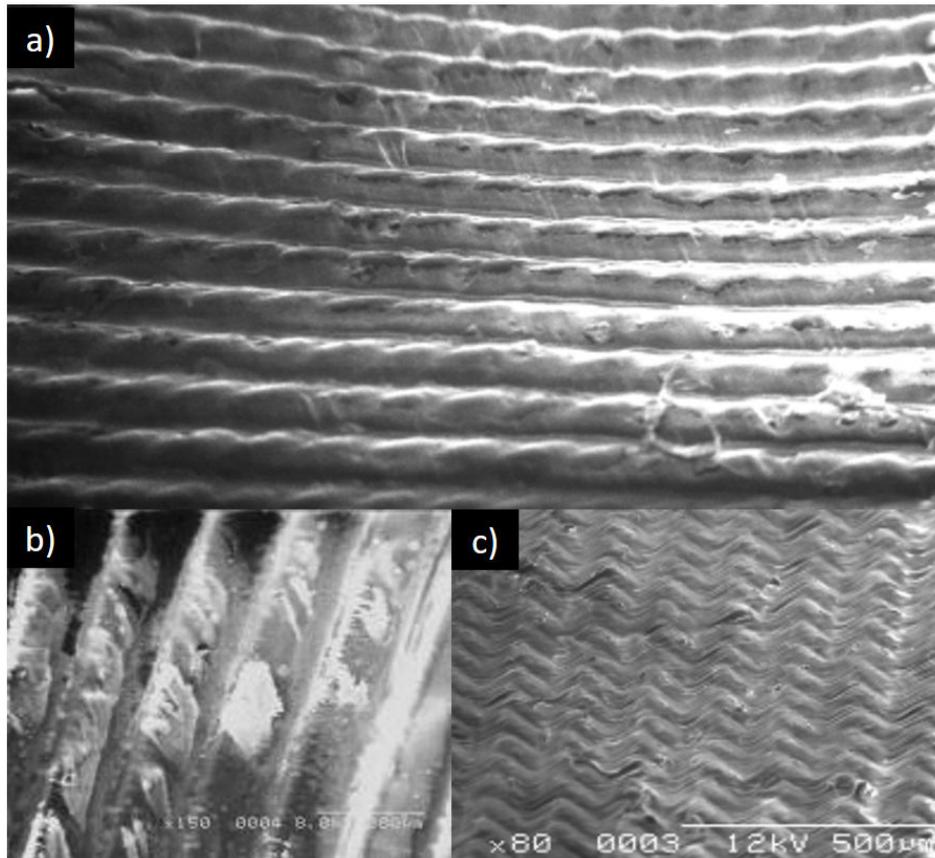
Figure 6.24: Micrographs from the sample surfaces. a) The ridges of the structures show a corrugation along the direction of printing, probably caused by the stepping of the printing process. b): Low surface quality like the incomplete printed groves are an indicator that the feature sizes push the limits of the technique used. c) Debris formed by excess resin.

lated which, in turn, gives access to the statistics of the surface roughness. As the term PSD is loosely defined and is displayed with different units on the x- and y-axes [191], the specific technique employed here are briefly elaborated. An averaged PSD is used, which has wavelength rather than the frequency on the x-axis, and is particularly useful for surface metrology applications as the wavelength correlates to the feature size. To evaluate the quality of the periodicity, an anisotropic PSD has been used which only includes horizontal spectral components, therfore cutting across the corrugations along the direction of propagation. To identify the relationship between the quality of the target feature (the period of the grooves) and all other features on the surface, an isotropic PSD is used which includes spectral

components from all directions. The parameters typically extracted from the PSD, such as surface roughness, are of limited use for a corrugated film, as the periodicity itself is the main contributor to it, and the defects would only be a deviation of the ideal value. However, the histograms of the PSD do show the distribution of features by their size and the intensity. A PSD of an ideal structure, for example, would only exhibit one infinitely sharp peak at the frequency of the chosen periodicity. A broadened peak at the wavelength of the periodicity indicates deviation from the periodicity, amplitude at any other wavelengths are indicative of defects.
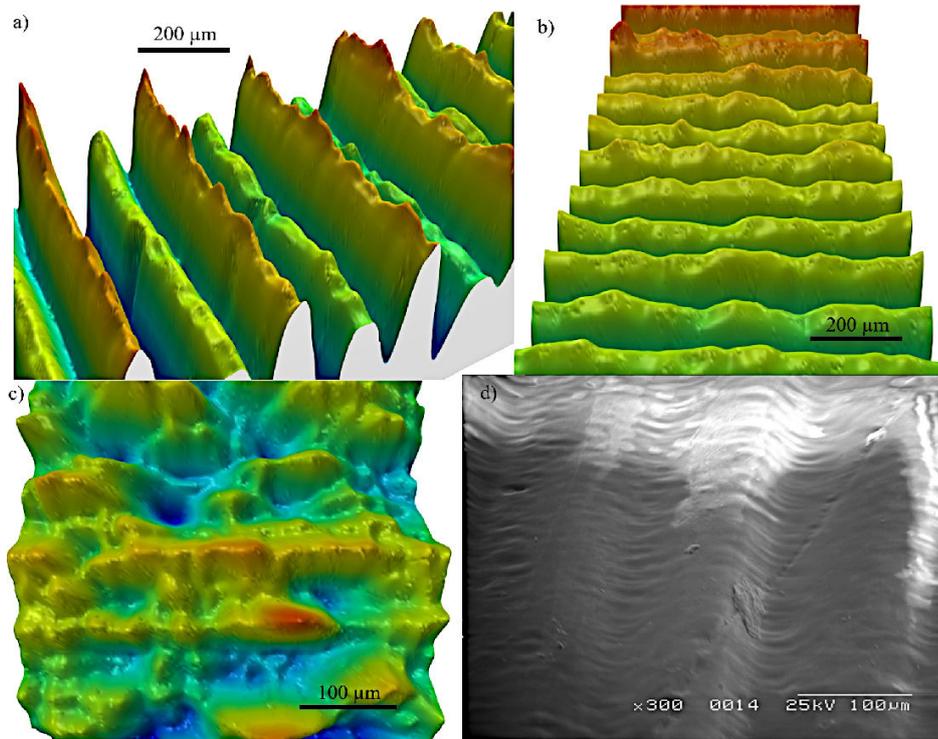


Figure 6.25: 3D maps from the optical profilometer measurements. a) shows the alternating height on sample 3. b) shows the surface roughness on the top of the ridges. c) while the presence of grooves on sample 4 is visible, the defects are in the same size order as the periodicity. d) The micrograph of sample 4 on the other hand, gives the impression that there is a periodicity that could support the measured spoof THz SPPs.

The high defect density shown in the 3D visualisation of the profilometer measurements in Figure 6.25 is visible in the micrographs taken with an SEM in Figure 6.24 as well. A chromatic lens profilometer has been used to provide a more quantitative

analysis of the defect density. The surface profiles allow the average (PSD) to be calculated which, in turn, gives access to the statistics of the surface roughness.

Figure 6.26 shows that the periodicities of samples 1-3 are in good agreement
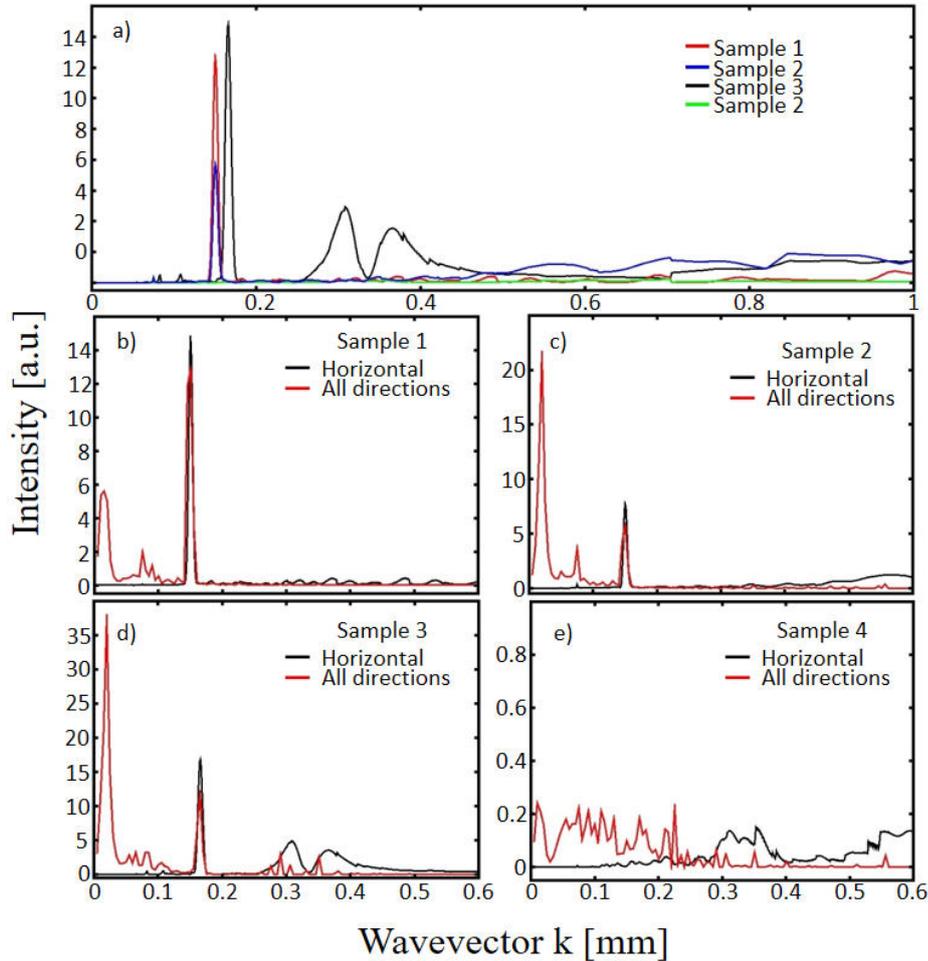


Figure 6.26: a) Averaged Power Spectral Density (PSD) including only horizontal wave vectors that go across the corrugation of the SPP structure. The first three samples are in good agreement with the target values listed in Table 6.5; the fourth sample does not have any prominent features. b-e) PSD only including the horizontal wave vectors in comparison with the PSD including wave vectors of all directions. While the periodicity of the structure dominates along the horizontal axis, the high amount of roughness and defects becomes apparent when considering all directions.

with the target parameters listed in Table 6.5, with $150\,\mu$m for samples 1 and 2 and $166\,\mu$m for sample 3. Additionally, two additional broad peaks can be seen for structure 3 at roughly double the wavelength of the desired periodicity. The 3D

visualisation of the surface in Figure 6.25a indicates that this might be caused by the variation in the height of every second groove. Furthermore, Figure 6.26 also shows that all structures have an above zero amplitude at most other wavelengths, indicating a broad range of defects. This is affirmed when comparing the horizontal component PSD with the PSD that includes all directions for each structure (Figure 6.26b-e).

Here it is shown that besides the prominent peak at the wavelength of the periodicity, there is a very well defined feature at shorter wavelengths and some small peaks scattered over the spectrum. The 3D maps and SEM micrographs show that this part of the PSD is indeed caused by the roughness or defects on the surface. The larger peak at the shortest wavelengths is most likely due to the general surface quality whereas the other smaller peaks in the spectrum are caused by other defects, for example debris or incomplete structures as seen in the micrographs in Figure 6.24.

The PSD spectra can be used to quantify both the quality of the periodic SPP structure and the defect density. The periodicities of sample 1-3 are in good agreement with the target parameters listed in Table 6.5, with $150\,\mu$m for sample 1 and 2 and $166\,\mu$m for sample 3 but structure 4 shows no periodicity. The Full Width Half Maximum values for the first three samples are 8, 7.4 and $9.4\,\mu$m respectively, meaning that the periodicity has a deviation of $\pm 3\%$. Besides the prominent peak at the wavelength of the periodicity, there is a very well defined feature at shorter wavelengths and some small peaks scattered over the spectrum. The 3D maps show that this part of the PSD is indeed caused by the defects on the surface. The maximum of the defect peaks is between 15 and $20\,\mu$m and they all have a FWHM of $\sim 8\,\mu$m. While the PSD can provide information on a surface, e.g. the surface roughness, it is not possible to extract a defect density. It is, however, possible to obtain a quantity that gives a good estimate on the number of defects on the surface by comparing the ratio between the contribution of the defect signal and the corrugation signal of the PSD. This ratio varies from 2.1 for sample 1, which

therefore is the defect poorest, up to 7.3 for sample 3, which is the defect richest. Sample 4 could not be evaluated this way; the PSD as a method of evaluation struggles with the smaller sizes and becomes meaningless when the surface roughness is of the same length scale as the feature height. Even the autocorrelation function in the PSD process cannot discriminate between the periodic signal and the noise when the defects are dominant.

### 6.4.2.4 Angularly resolved THz measurements

The scattering at defects on surfaces or rough surfaces are well-studied for nanometre-scaled defects and roughness at optical frequencies [185]. The properties of defect rich spoof plasmonic surfaces, however, have not been previously studied, as many spoof plasmonic experiments are conducted at microwave frequencies where no unintended defects due to manufacturing tolerances occur and defects are usually well defined and intended [192, 193]. As a first approximation, the defects can be regarded as metallic spheres and as the THz radiation propagates in the plane of the sample surface only, the well-known case of Mie scattering on a metal cylinder applies [194]. The measurements focus on the forward scattering properties, as these are the ones that can be determined experimentally, due to the geometrical constrains caused by the size of the THz transceivers. Section 6.4.2.4 shows the Mie scattering at a perfect electrically conducting sphere with a radius $r = 20\,\mu$m for different wavelengths (from FDTD simulations). When the sphere is significantly smaller than the wavelengths ($r < 1/5\lambda$) the scattering becomes less omnidirectional than at longer wavelengths where there are no striking features in the curve. For wavelengths of the order of the radius, forward scattering dominates, but with pronounced side lobes. These side lobes are known to increase in intensity and scatter more towards the forwards direction when the particle is placed on a substrate [195]. If these insights are applied to the present situation of scattering from defects on spoof plasmonic surfaces at THz frequencies, it can be expected that a first scattering event of a free-space photon will result in a nearly omnidirectional scat-

tering, as the free space wavelength is much larger than the measured defects. The spoof plasmonic surface, however, has a preferred direction of propagation across its corrugation where it is able to support SPPs. Therefore, the omnidirectional scattering only excites an SPP in the direction across the corrugation. The SPP waves have smaller wavelengths than their corresponding frequency in free-space and, therefore, will exhibit a different scattering pattern than the free-space wave for the same defects. As the samples have a high defect density, the effect of multiple scattering events needs to be taken into account along with the polydispersity of the defects. An increasing defect density leads to a reduction in the lobe pattern which is replaced by an increasingly uniform field pattern [185]. Furthermore, the polydispersity also decreases the visibility of the lobed pattern, as similar but not identically sized scatterers will have coinciding minima and maxima, as seen in Section 6.4.2.4a for wavelengths $10 - 15\,\mu$m. The results from FDTD simulations of a defect-rich SPP waveguide in Section 6.4.2.4b show that while the scattering intensity strongly increases with the number of defects from a sparse to a defect rich surface, the scattering intensity saturates quickly and the weak lobe pattern that is visible for lower defect densities disappears into wide, uniform lobes. Additionally, the scattering lobes move towards the centre with increased defect density. All this is in agreement with the previously described behaviour at optical frequencies of multiple scattering [185].

For the FDTD simulation, a workaround was used to address the issues accompanied by the attempt of simulating a realistic defect-rich SPP sample. It is challenging to generate a realistic model as it requires a significant level of computational resource for multiple reasons: To simulate Mie scattering a single defect has to be mapped with multiple mesh points; the simulated domain has to have a certain minimum size to allow multiple scattering; and the area has to be large enough to be of statistical significance, so that the positioning of individual defects does not significantly change the results. A simulation fulfilling all these requirements would require terabytes of RAM. To realise a simulation on the available work-

station with 128 GB RAM a smaller area of the SPP waveguide with randomly distributed defects is simulated. This step is repeated multiple times with different random distributions of the defects until the results converge and do not show significant change with the next iteration.

There are some considerable differences between the FDTD simulations and the experimental measurements: In the FDTD simulation a wave is launched at one end of the structure and then a far field projection of the electric fields at the other end of the structure results in the plots in Section 6.4.2.4 ; in the experiment, the source rotates around the sample and the receiver is stationary, i.e. the THz wave propagates in the opposite direction. Whilst Maxwell's equations are time reversible, the order in which the scattering events take place might matter. Unfortunately, neither an angularly-resolved FDTD simulation nor swapping receiver and transmitter in the measurements is feasible because of the vast computational resources required or the increased loss of signal, respectively.

Angular measurements were obtained over a range of $\pm 45°$; a schematic of the experimental setup is shown in Figure 6.28. For these angular measurements, the sample was placed at the pivot point, and the collimated beam is rotated around it at a fixed distance, as the receiving antenna remains stationary. The collimated beam has a diameter of 10 mm. The plotted intensity is the averaged intensity at this angle for all frequencies below the cut-off of the SPP-structure. All angular measurements are normalised to the $0°$ transmission of the same sample to avoid alignment dependent intensity differences. The frequency-resolved angular plots are normalised with the bare antenna in the pivot point instead of the SPP waveguide, to adjust for eventual antenna characteristics.

The polar plot in Figure 6.28 shows that all four samples have an increased acceptance angle compared to the bare horn antenna used as a reference. Additionally, multiple side lobes are visible, which resemble the shape of the previously shown Mie scattering plots. The side lobes are most pronounced for samples with the

a)



b)



.

.
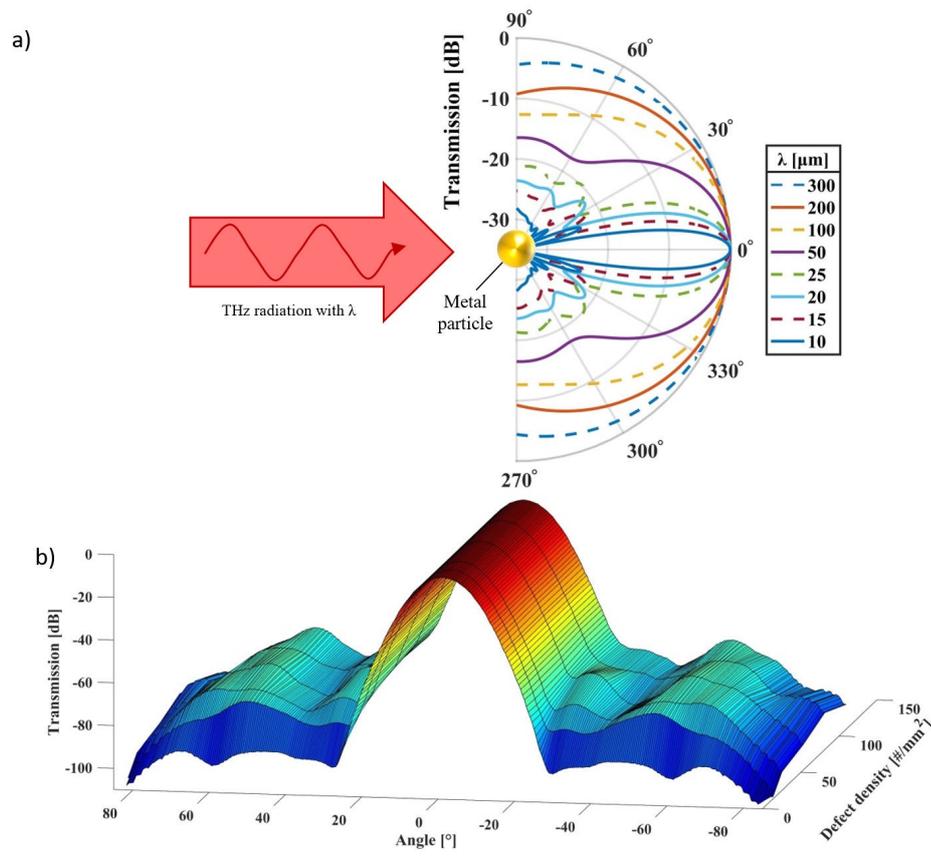
Figure 6.27: a) The forward scattering of THz radiation with different wavelengths incident on a metallic sphere with a radius of $20\,\mu$m as predicted by the Mie theory (from FDTD simulation). b) Simulation of the angular scattering pattern of a defect rich sample with different defect densities.

.

highest defect concentration, with samples 2 and 3 showing the first side lobes just below the $-10\,$dB mark, which is in good agreement with the simulations that quickly saturate in their side lobe intensity, which explains why the intensities are very similar despite having different defect densities. Additionally, the side lobes of samples 1 and 3 are nearly identical in shape and only vary in intensity, which again agrees with simulations where the side lobe shape is preserved for lower de-

fect concentrations. While sample 3 has an even higher defect concentration which is expected to result into a broadening of the side lobes, the broadening could be also attributed to the larger defects found in the PSD for this sample, especially since some additional side lobes at higher angles are visible as well.
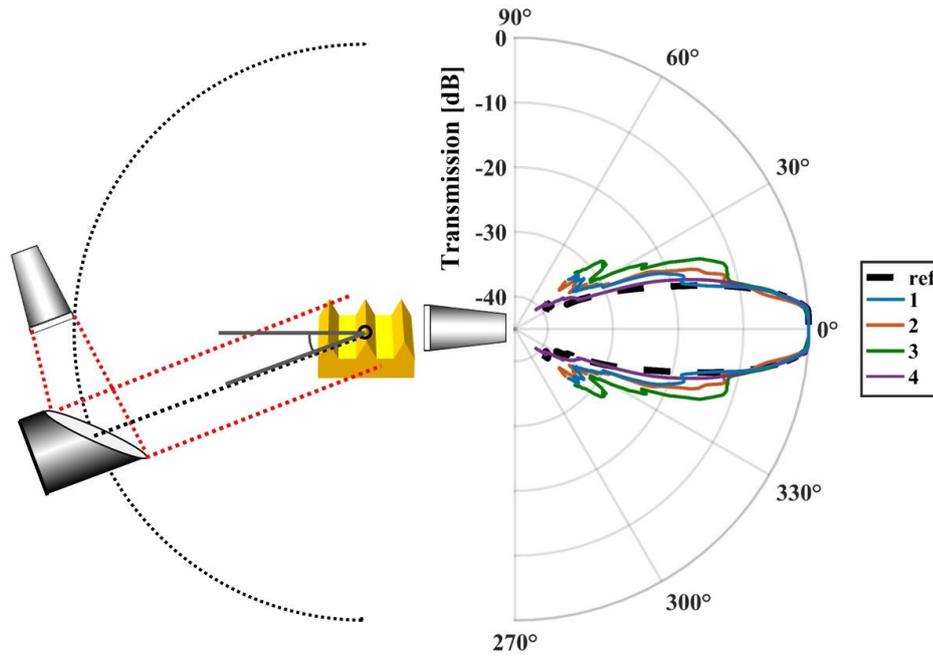


Figure 6.28: Schematic of the angular measurement setup (left) and the polar plot of the results (right). The angular plot shows the averaged intensity below the cut-off frequency of the individual samples. All SPP samples show an increased acceptance angle. Additionally, side lobes as they are known from Mie scattering are visible.

The frequency-resolved plots of the angularly-resolved measurements in Figure 6.29a reveal Mie like scattering characteristics similar to the theoretical case in Section 6.4.2.4a: When varying the frequency within the narrow band below the cut-off frequency of the SPP waveguide, it can be seen that the scattering side lobes change their angle increasingly towards the forward direction. Despite the narrow frequency range, the scattering angles of the forward scattering lobes changes from $\sim 6°$ for the highest frequency (0.9 THz) to $\sim 12.5°$ for the lowest frequency (0.8 THz), while according to the Mie theory, there would be hardly any change expected for a free wave scattering from particles of this size.

This is an indicator that the wavelength of the scattering wave has to be significantly shorter than the free-space wavelength, as otherwise the scattering pattern would be omnidirectional and would hardly vary with such small wavelength changes of less than 10% of the wavelength.
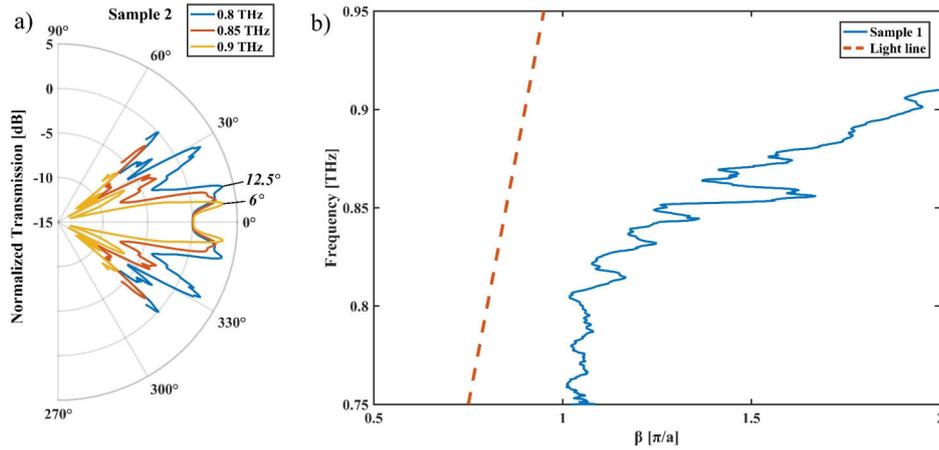


Figure 6.29: a) Frequency resolved angular plots show that the scattering lobes move toward the forward direction with increasing frequency. Due to normalization with the bare horn antenna, the forward scattering lobe is removed. b) The nonlinear dispersion curve shows the bound nature of the wave and the increasingly shortened wavelengths compared to free-space towards the cut-off of the sample.

It is challenging to directly measure the bound SPP wavelength as it is impossible to directly measure the wave vector $k \equiv 2\pi/\lambda$. It is, however, possible to extract the phase constant $\beta$ from S-parameters, which is proportional to $|k|$ where $\beta$ is the real part. As expected, the dispersion curve in Figure 6.29b, shows an increasing $\beta$ as the frequency approaches the cut-off frequency. Due the narrow frequency band (0.75 to 1.1 THz) of the THz vector network analyzer the convergence of the SPPs dispersion curve and the light line at lower frequencies cannot be observed. However, the dispersion curve does indicate that the SPP wavelength is around half the length of the wavelength of a freely-propagating wave at the same frequency.

### 6.4.3 Discussion

The most general approach to interpret the results of the angular measurements is to compare them to Mie theory. Whilst this comparison has to be of a qualitative nature, as Mie theory usually accounts for spherical (or cylindrical) uniform particles, which is not the experimental reality as the micrographs show, the shape of the measured polar plots still closely resemble Mie scattering. The similarities are even larger when taking multiple scattering events into account. The observation of the side lobes at these defect sizes is interesting in itself, as the majority of the defects are in the order of 5-10% of the free space wavelength and one would usually expect a uniform scattering pattern without lobes and with equal contributions to the backward and forward scattering. However, the observed scattering pattern shows more similarities to the scattering typically found with wavelength-sized defects. The most likely explanation is that the scattering of the bound SPPs is observed, which have a much shorter wavelength than their free space equivalent, but the THz radiation still has to couple to the surface first. The observed pattern, therefore, would be a convolution of the scattering of the more omnidirectional scattering of the free-space wave on particles much smaller than the wavelength and the scattering of the bound SPP wave on the same defects, but this time the wavelength is in the same order as the defect size. This fits with the observed changes in the different defect densities and distributions. It is worth noting that the two samples with similar defect size distributions (1 and 2) have the same shape of side lobes, and the two samples with the same defect concentration have the same amount of scattering/similar intensity of their side lobes (2 and 3), but different shapes of the scattering pattern.

Table 6.5 shows that while the SPPs are strongly confined to the surface of the 3D printed structures, the propagation lengths are only of the order of the wavelength itself. The confinement is between $69\,\mu$m and $119\,\mu$m, which is a third to a quarter of the free-space wavelength and to which the FDTD simulations agree which show an extension of $\sim 70-110\,\mu$m. The map of the electric field strength in Figure 6.30

gives a good impression on how localised the fields are due to the triangular shape of the plasmonic structures.
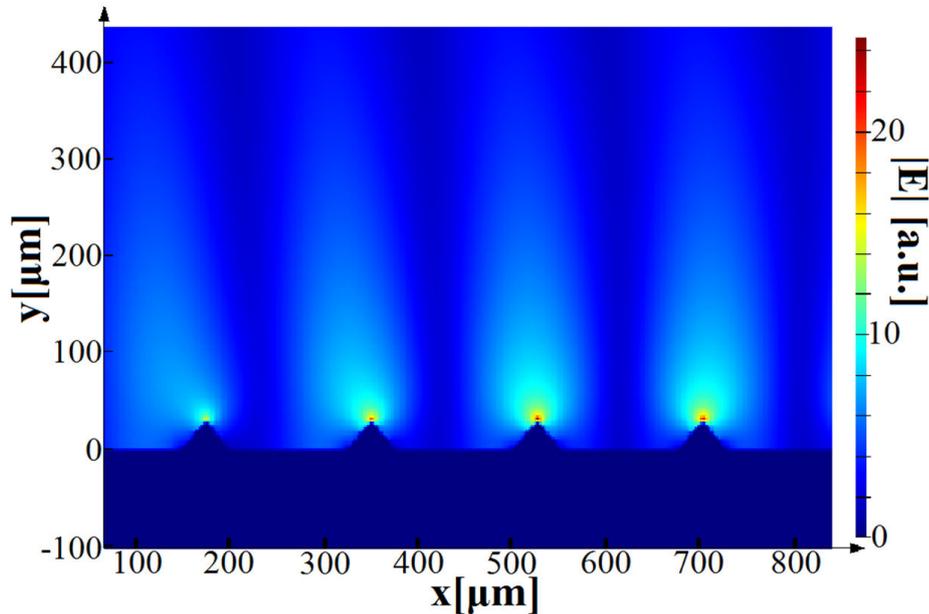


Figure 6.30: The crosscut of the triangular SPP structures from FDTD simulation shows the strong confinement of the electric field strength on top of the structures.

This confinement is approximately four times higher than that for previously reported THz SPP structures [162, 163], but the propagation length is just greater than two free-space wavelengths, which is extremely short in comparison to the order of tens [163] or hundreds [162] times the wavelength in literature. The sample with the lowest defect concentration has the longest propagation length, indicating that the short propagation length is caused by the defects.

Whilst enabling unassisted free space coupling, the defects also cause constant decoupling of the SPPs, resulting in high radiative losses, and hence very short propagation lengths. Even if the unassisted coupling is very useful for interconnect applications, the attenuation is of the order of $10\,\mathrm{dB/mm}$ and so is too high for waveguides. Better control of the printing quality, or potentially some postprocessing, would circumvent this issue by having a defect-free waveguide with only small sections with defects to couple in and out. Better control of the print quality also opens up the possibility of tailoring the receiver characteristics, for

example, by making forward scattering dominant or tailoring the acceptance angle of the structures to minimise cross-talk in highly integrated photonic circuits.

## 6.5 Conclusion

In this chapter, high-quality, nearly defect-free, SPP structures fabricated with traditional photolithography are discussed, which allows for the construction of integrated photonic components and defect-rich SPP waveguides fabricated with 3D printing, which exhibit new physical effects.

The optimum width for spoof SPP structures for integrated circuits have been evaluated to be around $200\,\mu m$ to make the waveguides as compact as possible while simultaneously having a well predictably resonant frequency, as a further reduction in width increases the resonant frequency exponentially.

The coupling between THz spoof SPP waveguides has been discussed to optimise the coupling distance for energy transfer between waveguides and to evaluate the maximum packing density. Ideal coupling to transfer almost all energy from one waveguide to another has been determined to be $40\,\mu m$. To suppress energy being transferred from one waveguide to another the distance can be reduced to $20-30\,\mu m$, which means SPP waveguides can be densely packed without crosstalk instead of increasing the distance between two waveguides until no power is transmitted. How these coupling properties can be used to design devices such as a Y-splitter and demultiplexer has been shown, with isolation in excess of $30\,\mathrm{dB}$ for 20 GHz wide channels at $0.95\,\mathrm{THz}$ for the demultiplexer, showing that the concept of SPP multiplexer is feasible for communication applications. On- and off-switching of spoof plasmonic waveguides with liquid crystals has been experimental demonstrated with a minimum modulation depth of $10\,\mathrm{dB}$. It has been explored how this effect can be combined with the waveguide coupling to produce switches. Whispering-gallery resonators have been used to show that the losses of the waveguides produced with photolithography are low enough to produce high-

quality resonators with Q-factors above 300.

The free-space coupling of THz radiation to 3D printed defect-rich spoof SPP surfaces was demonstrated. While the SPPs are strongly confined to the surface with an extension of less than a third of the free space wavelength, the propagation lengths however are only in the order of a few free-space wavelengths due to the scattering on the many defects, which is significantly lower than the expected values of hundreds of free-space lengths for defect free structures. The scattering patterns of the structures have been investigated by comparing them to Mie theory, which revealed that the scattering is dominated by the bound SPPs rather than the free-space waves, as the forward scattering lobes vary too strongly with frequency. Samples with similar defect size distribution show the same scattering in their side lobes, while samples with similar amount of defects show similar amount of scattering intensity, which matches the prediction from FDTD simulations. To the best of my knowledge, this is the first study on scattering of spoof SPPs.

The resulting observed unassisted free-space coupling of radiation has great potential for highly integrated photonic circuits, as no other components to couple are necessary and the radiation patterns can be tailored to the needs of the application, e.g. to minimising cross-talk between interconnects or for frequency selectivity. For this, improvements in the printing quality are necessary for better control over the surface quality and intended "doping" with specific defect concentration and distributions.

CHAPTER **7**

# Conclusions

The field of THz technology has matured considerably over the past two decades. It developed from a purely scientific driven subject, with only the astronomy community having actual activities outside a lab, to an application-driven field with a wide range of activities in different fields of industry. While the main attention used to be on the development of sources and detectors, considerable strides have been made in the field of auxiliary components as well. In this thesis, a novel fabrication methods and materials for THz components were presented that will help the ongoing maturing process of THz technology towards a developed industry. Additionally, some of the more recently developed instruments are used to develop measurement techniques that make THz measurements more useful for applications.

Chapter 3 presented a new material for THz optical components and wave plates. The new material, Shapal, has a high refractive index while having acceptable losses and being considerably easier to machine than the popular HRFZ-silicon. As a ceramic, this material is also resilient to scratches and temperature influences, and comparably cheaper than the aforementioned silicon, making it a viable candidate for industrial applications. The need for such materials will increase if THz instruments are used for in-line testing or for medical applications, where shatter-resistant optics are required.

The high-contrast gratings used as wave plates are a young class of components

on their own. Due to the long wavelength and therefore large feature sizes, as compared to infrared and optical components, this type of component could for the first time be produced with 3D printing and laser-cutting. Many components, such as waveplates and filters, are currently not readily available and expensive at THz frequencies. The increasing availability of in-house fabrication techniques allows printing such optical components for the lab use. Additionally, due to the small form factor, high-contrast gratings are also attractive for the integration into THz systems. They might offer an alternative as frequency selective reflectors to other techniques, such as grown Bragg reflectors, for active THz components.

In chapter 4, the use of photonic crystal cavities for the Enhancement of THz spectroscopy is discussed. First, how the constraints of a finite extension, a consequence of the longer wavelength of THz components, influenced the resonant behaviour of the cavities is considered. This was followed by the design of microfluidic channels integrated into cavities. It was shown the cavity increases the sensitivity during spectroscopy of liquids at THz frequencies. By transporting this design to an existing photonic crystal platform the basis for a THz lab-on-a-chip was created. The lab-on-a-chip approach is desirable for THz applications, as it addresses issues like intensity losses in free-space measurements and, in particular, a more controlled measurement environment for the spectroscopy of liquids. The lab-on-a-chip, therefore, might be a viable candidate for THz in-line sampling of liquid processes, which otherwise have to be tested ex-situ in a lab.

Chapter 5 presented the development of a THz ellipsometer for in situ measurements. The development of the instrument and additional components were discussed, and the polarisation sensitivity was verified. The performance of the system and the necessary post-processing of the data is shown with the characterisation of different materials and a comparison of the results to literature and other techniques. The advantages of the reflective measurement configuration of the ellipsometry setup was demonstrated with an in situ thickness observation of a wafer during etching.

Chapter 6 presented spoof plasmonic components and the influence of the fabrication method on their properties. Multiple components, such as switches and high-quality filter, are shown which shows the potential of spoof plasmonics for integrated THz circuits. Future development will focus on active components, as these are still rare at THz frequencies, especially with high-switching frequencies and small form factors. The demonstrated combination of liquid crystals and spoof plasmonic waveguides is an exciting candidate for such active THz devices. Liquid crystals offer high switching speeds, and the spoof plasmonic waveguides can be adjusted for any frequency region. These two advantages are especially relevant for frequencies beyond 1 THz, where there are currently no other technology candidates for active components.

Additionally, 3D printed spoof plasmonic waveguides are shown, which demonstrate a previously unreported effect: the unassisted coupling of free-space radiation to the waveguide. While the high defect density makes 3D printing currently unsuitable for waveguides at frequencies around 1 THz, the potential of the technology is shown as a better control of the print quality can lead to compact interconnects based on the scattering effects reported here.

# Further Work

The ceramic material shows that it is still worthwhile to test new materials at THz frequencies to extend the range of available materials for different applications.

The development of 3D printers with better resolution and using different low-loss polymers will motivate future work on 3D printed optical components and gratings. The realisation of the proposed photonic crystal based lab-on-a-chip is currently taking place at Osaka University. The photonic crystal used for the design in this thesis was developed there and has been used for different communication devices. Proof of principle measurements will show the sensitivity of the concept and the influence of the refractive index and absorption coefficient on the measurements. Transporting the concept of enhanced sensitivity for the spectroscopic investigation of microfluidic channels to a spoof plasmonic platform would be desirable. While the losses of photonic crystals are still lower, radiation in a lab-on-a-chip does not need to travel longer distances, but the frequency agility of the plasmonic technology would allow covering a large frequency span on a single chip.

Additionally, using a controlled 'doping' with defects, as presented with the 3D printed structure, could serve as an interconnect technology for such a lab-on-a-chip.

# Bibliography

[1] Carlo Sitori. Applied physics: Bridge for the terahertz gap. *Nature*, 2002.

[2] Masayoshi Tonouchi. Cutting-edge terahertz technology. *nature photonics*, 2007.

[3] Bradley Ferguson and Xi-Cheng Zhang. Materials for terahertz science and technology. *Nature Materials*, 2002.

[4] Reinhold Kleiner. Filling the terahertz gap. *Applied Physics*, 2007.

[5] Jerome Faist and Federico Capasso. Quantum cascade laser. *Science*, 1994.

[6] S. Koenig, D. Lopez-Diaz, J. Antes, F. Boes, R. Henneberger, A. Leuther, A. Tessmann, R. Schmogrow, D. Hillerkuss, R. Palmer, T. Zwick, C. Koos, W. Freude, O. Ambacher, J. Leuthold, and I. Kallfass. Wireless sub-thz communication system with high data rate. *Nature Photonics*, 7:977, October 2013. URL `https://doi.org/10.1038/nphoton.2013.275`.

[7] Thomas Kürner and Sebastian Priebe. Towards thz communications - status in research, standardization and regulation. *Journal of Infrared, Millimeter, and Terahertz Waves*, 35(1):53–62, Jan 2014. ISSN 1866-6906. doi: 10.1007/s10762-013-0014-3. URL `https://doi.org/10.1007/s10762-013-0014-3`.

[8] Louise Ho, Michael Pepper, and Philip Taday. Signatures and fingerprints. *Nature Photonics*, 2:541, September 2008. URL `https://doi.org/10.1038/nphoton.2008.174`.

[9] Kodo Kawase, Yuichi Ogawa, Yuuki Watanabe, and Hiroyuki Inoue. Non-destructive terahertz imaging of illicit drugs using spectral fingerprints. *Opt. Express*, 11(20):2549–2554, Oct 2003. doi: 10.1364/OE.11.002549. URL `http://www.opticsexpress.org/abstract.cfm?URI=oe-11-20-2549`.

[10] E Pickwell and VP Wallace. Biomedical applications of terahertz technology. *Journal of Physics D: Applied Physics*, 39(17):R301, 2006.

[11] Zhaoxin Geng, Xiong Zhang, Zhiyuan Fan, Xiaoqing Lv, and Hongda Chen. A route to terahertz metamaterial biosensor integrated with microfluidics for liver cancer biomarker testing in early stage. *Scientific Reports*, 7(1): 16378, November 2017. ISSN 2045-2322. URL `https://doi.org/10.1038/s41598-017-16762-y`.

[12] R. D. Dupuis and P. D. Dapkus. Room -temperature operation of distributed bragg confinement ga1 xalxas1-x xgaas lasers grown by metalorganic chemical vapor deposition. *Applied Physics Letters*, 33(1):68–69, 1978. doi: http://dx.doi.org/10.1063/1.90147. URL `http://scitation.aip.org/content/aip/journal/apl/33/1/10.1063/1.90147`.

[13] S. F. Busch, M. Weidenbach, M. Fey, F. Schäfer, T. Probst, and M. Koch. Optical properties of 3d printable plastics in the thz regime and their application for 3d printed thz optics. *Journal of Infrared, Millimeter, and Terahertz Waves*, 35(12):993–997, Dec 2014. ISSN 1866-6906. doi: 10.1007/s10762-014-0113-9. URL `https://doi.org/10.1007/s10762-014-0113-9`.

[14] Jianming Dai, Jiangquan Zhang, Weili Zhang, and D. Grischkowsky. Terahertz time-domain spectroscopy characterization of the far-infrared absorption and index of refraction of high-resistivity, float-zone silicon. *J. Opt. Soc.*

*Am. B*, 21(7):1379–1386, Jul 2004. doi: 10.1364/JOSAB.21.001379. URL `http://josab.osa.org/abstract.cfm?URI=josab-21-7-1379`.

[15] Mohamed Nurul Afsar and Hua Chi. Millimeter wave complex refractive index, complex dielectric permittivity and loss tangent of extra high purity and compensated silicon. *International Journal of Infrared and Millimeter Waves*, 15(7):1181–1188, Jul 1994. ISSN 1572-9559. doi: 10.1007/BF02096073. URL `https://doi.org/10.1007/BF02096073`.

[16] W.R. Runyan. *Silicon Semiconductor Technology*. McGraw-Hill Book Company, 1966.

[17] S.M. Sze. *Physics of Semiconductor Devices*. Wiley, 1981.

[18] Turgut Ozturk, Osamu Morikawa, İlhami Ünal, and İhsan Uluer. Comparison of free space measurement using a vector network analyzer and low-cost-type thz-tds measurement methods between 75 and 325 ghz. *Journal of Infrared, Millimeter, and Terahertz Waves*, 38(10):1241–1251, Oct 2017. ISSN 1866-6906. doi: 10.1007/s10762-017-0410-1. URL `https://doi.org/10.1007/s10762-017-0410-1`.

[19] Mira Naftaly, Nosherwan Shoaib, Daniel Stokes, and Nick M. Ridler. Intercomparison of terahertz dielectric measurements using vector network analyzer and time-domain spectrometer. *Journal of Infrared, Millimeter, and Terahertz Waves*, 37(7):691–702, Jul 2016. ISSN 1866-6906. doi: 10.1007/s10762-016-0256-y. URL `https://doi.org/10.1007/s10762-016-0256-y`.

[20] *SU8 2000 Permanent Epoxy Negative Photoresist. PROCESSING GUIDELINES FOR: SU-8 2025, SU-8 2035, SU-8 2050 and SU-8 2075*. MicroChem, 2019.

[21] M. Naftaly. An international intercomparison of thz time-domain spectrometers. In *2016 41st International Conference on Infrared, Millimeter,*

*and Terahertz waves (IRMMW-THz)*, pages 1–2, Sep. 2016. doi: 10.1109/ IRMMW-THz.2016.7758763.

[22] Paul D. Cunningham, Nestor N. Valdes, Felipe A. Vallejo, L. Michael Hayden, Brent Polishak, Xing-Hua Zhou, Jingdong Luo, Alex K.-Y. Jen, Jarrod C. Williams, and Robert J. Twieg. Broadband terahertz characterization of the refractive index and absorption of some important polymeric and organic electro-optic materials. *Journal of Applied Physics*, 109(4):043505–043505–5, 2011. doi: 10.1063/1.3549120. URL `https://doi.org/10.1063/1.3549120`.

[23] Yun-Sik Jin, Geun-Ju Kim, and Seok-Gy Jeon. Terahertz dielectric properties of polymers. *Journal of the Korean Physical Society*, 49(2):513–517, 2006. ISSN 0374-4884. URL `http://inis.iaea.org/search/search.aspx?orig_q=RN:43010908`.

[24] Mira Naftaly John F. Molloy. Metrology for terahertz time-domain spectrometers. 9810, 2015. doi: 10.1117/12.2225622. URL `https://doi.org/10.1117/12.2225622`.

[25] Jens Neu and Charles A. Schmuttenmaer. Tutorial: An introduction to terahertz time domain spectroscopy (thz-tds). *Journal of Applied Physics*, 124(23):231101, 2018. doi: 10.1063/1.5047659. URL `https://doi.org/10.1063/1.5047659`.

[26] Mira Naftaly and Richard Dudley. Linearity calibration of amplitude and power measurements in terahertz systems and detectors. *Opt. Lett.*, 34(5): 674–676, Mar 2009. doi: 10.1364/OL.34.000674. URL `http://ol.osa.org/abstract.cfm?URI=ol-34-5-674`.

[27] Mira Naftaly and Richard Dudley. Methodologies for determining the dynamic ranges and signal-to-noise ratios of terahertz time-domain spectrometers. *Opt. Lett.*, 34(8):1213–1215, Apr 2009. doi: 10.1364/OL.34.001213. URL `http://ol.osa.org/abstract.cfm?URI=ol-34-8-1213`.

[28] Withawat Withayachumnankul and Mira Naftaly. Fundamentals of measurement in terahertz time-domain spectroscopy. *Journal of Infrared, Millimeter, and Terahertz Waves*, 35(8):610–637, Aug 2014. ISSN 1866-6906. doi: 10.1007/s10762-013-0042-z. URL `https://doi.org/10.1007/s10762-013-0042-z`.

[29] Gaudencio Paz-Martínez, Jesus Garduño-Mejía, Oleg V. Kolokoltsev, Carlos G. Treviño-Palacios, and Naser Qureshi. Focus and alignment tolerance in a photoconductive terahertz source. *Journal of Infrared, Millimeter, and Terahertz Waves*, 36(9):830–837, Sep 2015. ISSN 1866-6906. doi: 10.1007/s10762-015-0185-1. URL `https://doi.org/10.1007/s10762-015-0185-1`.

[30] Inc. Virginia Diodes. Specifications and characteristics of a wr-1.0 vnax. with permission of vdi., 2019. URL `https://www.vadiodes.com`.

[31] Jingzhou Xu, Tao Yuan, Samuel Mickan, and X. C Zhang. Limit of spectral resolution in terahertz time-domain spectroscopy. *Chinese Physics Letters*, 20(8):1266–1268, jul 2003. doi: 10.1088/0256-307x/20/8/324.

[32] Erich Schlecht Frank Maiwald Alain Maestrini John J. Gill Suzanne C. Martin Dave Pukala J. Ward Jonathan Kawamura William R. McGrath William Hatch Dennis G. Harding Henry G. LeDuc Jeffry A. Stern Bruce Bumble Lorene A. Samoska Todd C. Gaier Robert Ferber David Miller Alexandre Karpov Jonas Zmuidzinas Thomas G. Phillips Neal R. Erickson Jerry Swift Yun Chung Richard Lai Huei Wang John C. Pearson, Imran Mehdi. Terahertz-frequency receiver instrumentation for herschel's heterodyne instrument for far infrared (hifi). *IR Space Telescopes and Instruments*, SPIE 4850, 2003. doi: 10.1117/12.461757. URL `https://doi.org/10.1117/12.461757`.

[33] T. W. Crowe, W. L. Bishop, D. W. Porterfield, J. L. Hesler, and R. M. Weikle. Opening the terahertz window with integrated diode circuits. *IEEE Journal*

*of Solid-State Circuits*, 40(10):2104–2110, Oct 2005. ISSN 0018-9200. doi: 10.1109/JSSC.2005.854599.

[34] Alain Maestrini, Bertrand Thomas, Hui Wang, Cécile Jung, Jeanne Treuttel, Yong Jin, Goutam Chattopadhyay, Imran Mehdi, and Gérard Beaudin. Schottky diode-based terahertz frequency multipliers and mixers. *Comptes Rendus Physique*, 11(7):480 – 495, 2010. ISSN 1631-0705. doi: https://doi.org/10.1016/j.crhy.2010.05.002. URL `http://www.sciencedirect.com/science/article/pii/S1631070510000447`. Terahertz electronic and optoelectronic components and systems.

[35] T. W. Crowe, B. Foley, S. Durant, K. Hui, Y. Duan, and J. L. Hesler. Vna frequency extenders to 1.1 thz. In *2011 International Conference on Infrared, Millimeter, and Terahertz Waves*, pages 1–1, Oct 2011. doi: 10.1109/irmmw-THz.2011.6105028.

[36] S. Rehnmark. On the calibration process of automatic network analyzer systems (short papers). *IEEE Transactions on Microwave Theory and Techniques*, 22(4):457–458, Apr 1974. ISSN 0018-9480. doi: 10.1109/TMTT.1974.1128250.

[37] G. F. Engen and C. A. Hoer. Thru-reflect-line: An improved technique for calibrating the dual six-port automatic network analyzer. *IEEE Transactions on Microwave Theory and Techniques*, 27(12):987–993, Dec 1979. ISSN 0018-9480. doi: 10.1109/TMTT.1979.1129778.

[38] I. Rolfes and B. Schiek. Calibration methods for microwave free space measurements. *Advances in Radio Science*, 2:19–25, 2004. doi: 10.5194/ars-2-19-2004. URL `https://www.adv-radio-sci.net/2/19/2004/`.

[39] Francesco D'Angelo, Zoltán Mics, Mischa Bonn, and Dmitry Turchinovich. Ultra-broadband thz time-domain spectroscopy of common polymers using thz air photonics. *Opt. Express*, 22(10):12475–12485, May 2014. doi: 10.1364/

OE.22.012475. URL `http://www.opticsexpress.org/abstract.cfm?URI=oe-22-10-12475`.

[40] SPat. Illustration for time-domain response of an optically gated photoconductive antenna, 2014. URL `wikipedia`.

[41] F. W. Smith, H. Q. Le, V. Diadiuk, M. A. Hollis, A. R. Calawa, S. Gupta, M. Frankel, D. R. Dykaar, G. A. Mourou, and T. Y. Hsiang. Picosecond gaas-based photoconductive optoelectronic detectors. *Applied Physics Letters*, 54 (10):890–892, 1989. doi: 10.1063/1.100800. URL `https://doi.org/10.1063/1.100800`.

[42] Magda O. El-Shenawee Nathan M. Burford. Review of terahertz photoconductive antenna technology. *Optical Engineering*, 56(1):1 – 20 – 20, 2017. doi: 10.1117/1.OE.56.1.010901. URL `https://doi.org/10.1117/1.OE.56.1.010901`.

[43] Y. Cai, I. Brener, J. Lopata, J. Wynn, L. Pfeiffer, and J. Federici. Design and performance of singular electric field terahertz photoconducting antennas. *Applied Physics Letters*, 71(15):2076–2078, 1997. doi: 10.1063/1.119346. URL `https://doi.org/10.1063/1.119346`.

[44] Zhisheng Piao, Masahiko Tani, and Kiyomi Sakai. Carrier dynamics and terahertz radiation in photoconductive antennas. *Japanese Journal of Applied Physics*, 39(1R):96, 2000.

[45] C. Kittel. *Introduction to Solid State Physics, 8th Edition*. Wiley, 2004.

[46] Bahaa E. A. Saleh and Malvin Carl Teich. *Fundamentals of Photonics*. Wiley, 1991.

[47] C Winnewisser, P Uhd Jepsen, M Schall, V Schyja, and H Helm. Electro-optic detection of thz radiation in litao 3, linbo 3 and znte. *Applied Physics Letters*, 70(23):3069–3071, 1997.

[48] Martin van Exter, Ch. Fattinger, and D. Grischkowsky. Terahertz time-domain spectroscopy of water vapor. *Opt. Lett.*, 14(20):1128–1130, Oct 1989. doi: 10.1364/OL.14.001128. URL `http://ol.osa.org/abstract.cfm?URI=ol-14-20-1128`.

[49] Kane Yee. Numerical solution of initial boundary value problems involving maxwell's equations in isotropic media. *IEEE Transactions on Antennas and Propagation*, 14(3):302–307, May 1966. ISSN 0018-926X. doi: 10.1109/TAP.1966.1138693.

[50] FDominec. Illustration of how the finite-difference time-domain method in computational electromagnetism discretizes the space, 2015. URL `wikipedia`.

[51] John D Joannopoulos, Steven G Johnson, Joshua N Winn, and Robert D Meade. Molding the flow of light. *Princeton Univ. Press, Princeton, NJ [ua]*, 2008.

[52] Kazuisao Tsuruda, Masayuki Fujita, and Tadao Nagatsuma. Extremely low-loss terahertz waveguide based on silicon photonic-crystal slab. *Opt. Express*, 23(25):31977–31990, Dec 2015. doi: 10.1364/OE.23.031977. URL `http://www.opticsexpress.org/abstract.cfm?URI=oe-23-25-31977`.

[53] D. Grischkowsky, Søren Keiding, Martin van Exter, and Ch. Fattinger. Far-infrared time-domain spectroscopy with terahertz beams of dielectrics and semiconductors. *J. Opt. Soc. Am. B*, 7(10):2006–2015, Oct 1990. doi: 10.1364/JOSAB.7.002006. URL `http://josab.osa.org/abstract.cfm?URI=josab-7-10-2006`.

[54] B. Morgan, C. M. Waits, J. Krizmanic, and R. Ghodssi. Development of a deep silicon phase fresnel lens using gray-scale lithography and deep reactive ion etching. *Journal of Microelectromechanical Systems*, 13(1):113–120, Feb 2004. ISSN 1057-7157. doi: 10.1109/JMEMS.2003.823220.

[55] D Seliuta, I Kasalynas, V Tamosiunas, S Balakauskas, Z Martunas, S As-
montas, G Valusis, A Lisauskas, HG Roskos, and K Kohler. Silicon lens-
coupled bow-tie ingaas-based broadband terahertz sensor operating at room
temperature. *Electronics Letters*, 42(14):825–827, 2006.

[56] Daniel F Filipovic, Steven S Gearhart, and Gabriel M Rebeiz. Double-slot
antennas on extended hemispherical and elliptical silicon dielectric lenses.
*IEEE Transactions on microwave theory and techniques*, 41(10):1738–1749,
1993.

[57] ED Walsby, SM Durbin, DRS Cumming, and RJ Blaikie. Analysis of silicon
terahertz diffractive optics. *Current Applied Physics*, 4(2-4):102–105, 2004.

[58] S Wietzke, C Jansen, M Reuter, T Jung, D Kraft, S Chatterjee, BM Fischer,
and M Koch. Terahertz spectroscopy on polymers: A review of morphological
studies. *Journal of Molecular Structure*, 1006(1-3):41–51, 2011.

[59] Binghao Ng, Jianfeng Wu, Stephen M Hanham, Antonio I Fernández-
Domínguez, Norbert Klein, Yun Fook Liew, Mark BH Breese, Minghui Hong,
and Stefan A Maier. Spoof plasmon surfaces: a novel platform for thz sensing.
*Advanced Optical Materials*, 1(8):543–548, 2013.

[60] Benedikt Scherger, Christian Jördens, and Martin Koch. Variable-focus tera-
hertz lens. *Optics express*, 19(5):4528–4535, 2011.

[61] M Naftaly, JF Molloy, B Magnusson, YM Andreev, and GV Lanskii. Silicon
carbide—a high-transparency nonlinear material for thz applications. *Optics
express*, 24(3):2590–2595, 2016.

[62] *Machinable ceramic - chemical composition and thermal conductivity of
shapal-m machinable ceramic from precision ceramics.* Precision Ceramics,
2008.

[63] *Macor - A Unique Materia.* Precision Ceramics, 2016.

[64] Khalid Z Rajab, Mira Naftaly, Edmund H Linfield, Juan C Nino, Daniel Arenas, David Tanner, Raj Mittra, and Michael Lanagan. Broadband dielectric characterization of aluminum oxide (al2o3). *Journal of Microelectronics and Electronic Packaging*, 5(1):2–7, 2008.

[65] M Naftaly, PJ Greenslade, RE Miles, and D Evans. Low loss nitride ceramics for terahertz windows. *Optical Materials*, 31(11):1575–1577, 2009.

[66] Alexander Podzorov and Guilhem Gallot. Low-loss polymers for terahertz applications. *Applied optics*, 47(18):3254–3257, 2008.

[67] Jonathan Hammler, Andrew J Gallant, and Claudio Balocco. Free-space permittivity measurement at terahertz frequencies with a vector network analyzer. *IEEE Transactions on Terahertz Science and Technology*, 6(6): 817–823, 2016.

[68] E. Hecht. *Optics, 2nd Edition*. Addison Wesley, 1987.

[69] Technical Committee : ISO/TC 172 Optics and photonics. Iso 7944 standard on "optics and optical instruments". *ISO*, 1998.

[70] Bob Mellish. A half-wave plate, 2006. URL `wikipedia`.

[71] Jean-Baptiste Masson and Guilhem Gallot. Terahertz achromatic quarter-wave plate. *Optics letters*, 31(2):265–267, 2006.

[72] Connie J Chang-Hasnain and Weijian Yang. High-contrast gratings for integrated optoelectronics. *Advances in Optics and Photonics*, 4(3):379–440, 2012.

[73] Ye Zhou, Michael CY Huang, and Connie J Chang-Hasnain. Large fabrication tolerance for vcsels using high-contrast grating. *IEEE Photonics Technology Letters*, 20(6):434–436, 2008.

[74] Ye Zhou, Michael Moewe, Johannes Kern, Michael CY Huang, and Connie J Chang-Hasnain. Surface-normal emission of a high-q resonator using

a subwavelength high-contrast grating. *Optics express*, 16(22):17282–17287, 2008.

[75] Mehmet Mutlu, Ahmet E Akosman, Gokhan Kurt, Mutlu Gokkavas, and Ekmel Ozbay. Experimental realization of a high-contrast grating based broadband quarter-wave plate. *Optics express*, 20(25):27966–27973, 2012.

[76] Anders Pors, Michael G Nielsen, Giuseppe Della Valle, Morten Willatzen, Ole Albrektsen, and Sergey I Bozhevolnyi. Plasmonic metamaterial wave retarders in reflection by orthogonally oriented detuned electrical dipoles. *Optics letters*, 36(9):1626–1628, 2011.

[77] Longqing Cong, Ningning Xu, Jianqiang Gu, Ranjan Singh, Jiaguang Han, and Weili Zhang. Highly flexible broadband terahertz metamaterial quarter-wave plate. *Laser & Photonics Reviews*, 8(4):626–632, 2014.

[78] Erwin G Loewen and Evgeny Popov. *Diffraction gratings and applications.* CRC Press, 2018.

[79] Max Born and Emil Wolf. *Principles of optics: electromagnetic theory of propagation, interference and diffraction of light.* Elsevier, 2013.

[80] Bernard C Kress and Patrick Meyrueis. *Applied Digital Optics: from micro-optics to nanophotonics.* John Wiley & Sons, 2009.

[81] MG Moharam and TK Gaylord. Rigorous coupled-wave analysis of planar-grating diffraction. *JOSA*, 71(7):811–818, 1981.

[82] ST Peng. Rigorous formulation of scattering and guidance by dielectric grating waveguides: general case of oblique incidence. *JOSA A*, 6(12):1869–1883, 1989.

[83] Lifeng Li. A modal analysis of lamellar diffraction gratings in conical mountings. *Journal of Modern Optics*, 40(4):553–573, 1993.

[84] Vadim Karagodsky, Forrest G Sedgwick, and Connie J Chang-Hasnain. Theoretical analysis of subwavelength high contrast grating reflectors. *Optics express*, 18(16):16973–16988, 2010.

[85] Vadim Karagodsky, Christopher Chase, and Connie J Chang-Hasnain. Matrix fabry–perot resonance mechanism in high-contrast gratings. *Optics letters*, 36(9):1704–1706, 2011.

[86] Vadim Karagodsky and Connie J Chang-Hasnain. Physics of near-wavelength high contrast gratings. *Optics express*, 20(10):10888–10895, 2012.

[87] Theodor Tamir, Giora Griffel, and Henry L Bertoni. *Guided-wave optoelectronics: device characterization, analysis, and design.* Springer Science & Business Media, 2013.

[88] Jean-Michel Lourtioz and André de Lustrac. Metallic photonic crystals. *Comptes Rendus Physique*, 3(1):79–88, 2002.

[89] Zihe Cai, Yang Yan, Lin Liu, Shengxuan Lin, and Xiaobin Hu. Controllable fabrication of metallic photonic crystals for ultra-sensitive sers and photodetectors. *RSC Advances*, 7(88):55851–55858, 2017.

[90] Benjamin Reinhard, Garik Torosyan, and René Beigang. Band structure of terahertz metallic photonic crystals with high metal filling factor. *Applied Physics Letters*, 92(20):201107, 2008.

[91] Frank Marlow, Parvin Sharifi, Rainer Brinkmann, and Cecilia Mendive. Opals: status and prospects. *Angewandte Chemie International Edition*, 48 (34):6212–6233, 2009.

[92] Pete Vukusic and J Roy Sambles. Photonic structures in biology. *Nature*, 424(6950):852, 2003.

[93] JW Strut. The propagation of waves through a medium endowed with a periodic structure. *Philosophical magazine*, pages 145–159, 1887.

[94] Eli Yablonovitch, TJ Gmitter, and Kok-Ming Leung. Photonic band structure: The face-centered-cubic case employing nonspherical atoms. *Physical review letters*, 67(17):2295, 1991.

[95] Shawn-yu Lin, JG Fleming, DL Hetherington, BK Smith, R Biswas, KM Ho, MM Sigalas, W Zubrzycki, SR Kurtz, and Jim Bur. A three-dimensional photonic crystal operating at infrared wavelengths. *Nature*, 394(6690):251, 1998.

[96] Susumu Noda, Katsuhiro Tomoda, Noritsugu Yamamoto, and Alongkarn Chutinan. Full three-dimensional photonic bandgap crystals at near-infrared wavelengths. *Science*, 289(5479):604–606, 2000.

[97] Shyh Wang. Principles of distributed feedback and distributed bragg-reflector lasers. *IEEE Journal of Quantum Electronics*, 10(4):413–427, 1974.

[98] CK Chong, DB McDermott, MM Razeghi, NC Luhmann, J Pretterebner, D Wagner, M Thumm, M Caplan, and B Kulke. Bragg reflectors. *IEEE Transactions on Plasma Science*, 20(3):393–402, 1992.

[99] Thomas F Krauss, M Richard, and Stuart Brand. Two-dimensional photonic-bandgap structures operating at near-infrared wavelengths. *Nature*, 383 (6602):699, 1996.

[100] Yoshihiro Akahane, Takashi Asano, Bong-Shik Song, and Susumu Noda. High-q photonic nanocavity in a two-dimensional photonic crystal. *nature*, 425(6961):944, 2003.

[101] Oskar Painter, RK Lee, Axel Scherer, A Yariv, JD O'brien, PD Dapkus, and I Kim. Two-dimensional photonic band-gap defect mode laser. *Science*, 284 (5421):1819–1821, 1999.

[102] DMB. Schematic diagrams illustrating the difference between one-, two- and three-dimensional photonic crystals, 2008. URL `wikipedia`.

[103] William Henry Bragg and William Lawrence Bragg. The reflection of x-rays by crystals. *Proceedings of the Royal Society of London. Series A, Containing Papers of a Mathematical and Physical Character*, 88(605):428–438, 1913.

[104] Crawford H Greenewalt, Werner Brandt, and Daniel D Friel. Iridescent colors of hummingbird feathers. *JOSA*, 50(10):1005–1013, 1960.

[105] R.S. Dubey and V. Ganesan. Fabrication and characterization of tio2/sio2 based bragg reflectors for light trapping applications. *Results in Physics*, 7:2271 – 2276, 2017. ISSN 2211-3797. doi: https://doi.org/10.1016/j.rinp.2017.06.041. URL `http://www.sciencedirect.com/science/article/pii/S2211379717304126`.

[106] E. Yablonovitch, T. J. Gmitter, and K. M. Leung. Photonic band structure: The face-centered-cubic case employing nonspherical atoms. *Phys. Rev. Lett.*, 67:2295–2298, Oct 1991. doi: 10.1103/PhysRevLett.67.2295. URL `https://link.aps.org/doi/10.1103/PhysRevLett.67.2295`.

[107] KV Kavokin, MA Kaliteevski, RA Abram, AV Kavokin, S Sharkova, and IA Shelykh. Stimulated emission of terahertz radiation by exciton-polariton lasers. *Applied Physics Letters*, 97(20):201111, 2010.

[108] Parag B Deotare, Murray W McCutcheon, Ian W Frank, Mughees Khan, and Marko Lončar. High quality factor photonic crystal nanobeam cavities. *Applied Physics Letters*, 94(12):121106, 2009.

[109] Tao Chen, Pingan Liu, Jianjun Liu, and Zhi Hong. A terahertz photonic crystal cavity with high q-factors. *Applied Physics B*, 115(1):105–109, 2014.

[110] Cristo M Yee and Mark S Sherwin. High-q terahertz microcavities in silicon photonic crystal slabs. *Applied Physics Letters*, 94(15):154104, 2009.

[111] P. B. Hansen, G. Raybon, U. Koren, B. I. Miller, M. G. Young, M. Chien, C. A. Burrus, and R. C. Alferness. 5.5-mm long ingaasp monolithic extended-cavity laser with an integrated bragg-reflector for active mode-locking. *IEEE*

*Photonics Technology Letters*, 4(3):215–217, March 1992. ISSN 1041-1135. doi: 10.1109/68.122370.

[112] lumerical knowledge base - simple high q cavity, 2015. URL `https://kb.lumerical.com`.

[113] lumerical knowledge base - quality factor calculations, 2015. URL `https://kb.lumerical.com`.

[114] Y. Zhang, S. Han, S. Zhang, P. Liu, and Y. Shi. High-q and high-sensitivity photonic crystal cavity sensor. *IEEE Photonics Journal*, 7(5):1–6, Oct 2015. ISSN 1943-0655. doi: 10.1109/JPHOT.2015.2469131.

[115] Yan Li, Ning-Feng Bai, Ming-De Zhang, and Xiao-Han Sun. Fdtd based analysis for electromagnetic band gap structure and defect mode of 2d metallic photonic crystals. In *2005 IEEE International Symposium on Microwave, Antenna, Propagation and EMC Technologies for Wireless Communications*, volume 2, pages 906–909 Vol. 2, Aug 2005. doi: 10.1109/MAPE.2005. 1618067.

[116] Demetri Psaltis, Stephen R. Quake, and Changhuei Yang. Developing optofluidic technology through the fusion of microfluidics and optics. *Nature*, 442(7101):381–386, July 2006. ISSN 1476-4687. URL `https://doi.org/10.1038/nature05060`.

[117] Joo-Hiuk Son Dong-Kyu Lee, Giyoung Kim. Optical characteristics of pesticides measured by terahertz time domain spectroscopy. 9655, 2015. doi: 10.1117/12.2184387. URL `https://doi.org/10.1117/12.2184387`.

[118] R. J. Coles, N. Prtljaga, B. Royall, I. J. Luxmoore, A. M. Fox, and M. S. Skolnick. Waveguide-coupled photonic crystal cavity for quantum dot spin readout. *Opt. Express*, 22(3):2376–2385, Feb 2014. doi: 10.1364/OE.22.002376. URL `http://www.opticsexpress.org/abstract.cfm?URI=oe-22-3-2376`.

[119] Hiroyuki Fujiwara. *Spectroscopic ellipsometry: principles and applications.* John Wiley & Sons, 2007.

[120] F Ferrieu. Infrared spectroscopic ellipsometry using a fourier transform infrared spectrometer: Some applications in thin-film characterization. *Review of Scientific Instruments*, 60(10):3212–3216, 1989.

[121] K Vedam. Spectroscopic ellipsometry: a historical overview. *Thin solid films*, 313:1–9, 1998.

[122] AR Forouhi and I Bloomer. Optical dispersion relations for amorphous semiconductors and amorphous dielectrics. *Physical review B*, 34(10):7018, 1986.

[123] AR Forouhi and I Bloomer. Optical properties of crystalline semiconductors and dielectrics. *Physical review B*, 38(3):1865, 1988.

[124] Edward D Palik. *Handbook of optical constants of solids - Chapter 7*, volume 3. Academic press, 1998.

[125] Nur Ismail, Cristine Calil Kores, Dimitri Geskus, and Markus Pollnau. Fabry-p&#x00e9;rot resonator: spectral line shapes, generic and related airy distributions, linewidths, finesses, and performance at low or frequency-dependent reflectivity. *Opt. Express*, 24(15):16366–16389, Jul 2016. doi: 10.1364/OE.24.016366. URL `http://www.opticsexpress.org/abstract.cfm?URI=oe-24-15-16366`.

[126] AB Kuzmenko. Kramers–kronig constrained variational analysis of optical spectra. *Review of scientific instruments*, 76(8):083108, 2005.

[127] Zhou Wang, A. C. Bovik, H. R. Sheikh, and E. P. Simoncelli. Image quality assessment: from error visibility to structural similarity. *IEEE Transactions on Image Processing*, 13(4):600–612, April 2004. ISSN 1057-7149. doi: 10.1109/TIP.2003.819861.

[128] D. Brunet, E. R. Vrscay, and Z. Wang. On the mathematical properties of the structural similarity index. *IEEE Transactions on Image Processing*, 21 (4):1488–1499, April 2012. ISSN 1057-7149. doi: 10.1109/TIP.2011.2173206.

[129] Matlab documentation - ssim, 2019. URL `https://uk.mathworks.com`.

[130] Takeshi Nagashima and Masanori Hangyo. Measurement of complex optical constants of a highly doped si wafer using terahertz ellipsometry. *Applied Physics Letters*, 79(24):3917–3919, 2001.

[131] M Hangyo, T Nagashima, and S Nashima. Spectroscopy by pulsed terahertz radiation. *Measurement Science and Technology*, 13(11):1727, 2002.

[132] Tino Hofmann, CM Herzinger, A Boosalis, TE Tiwald, John A Woollam, and Mathias Schubert. Variable-wavelength frequency-domain terahertz ellipsometry. *Review of Scientific Instruments*, 81(2):023101, 2010.

[133] T Hofmann, CM Herzinger, JL Tedesco, DK Gaskill, John A Woollam, and Mathias Schubert. Terahertz ellipsometry and terahertz optical-hall effect. *Thin Solid Films*, 519(9):2593–2600, 2011.

[134] Nicholas Karl, Martin S Heimbeck, Henry O Everitt, Hou-Tong Chen, Antoinette J Taylor, Igal Brener, Alexander Benz, John L Reno, Rajind Mendis, and Daniel M Mittleman. Characterization of an active metasurface using terahertz ellipsometry. *Applied Physics Letters*, 111(19):191101, 2017.

[135] Mohammad Neshat and NP Armitage. Terahertz time-domain spectroscopic ellipsometry: instrumentation and calibration. *Optics express*, 20(27):29063–29075, 2012.

[136] Cecilie Ro/nne, Lars Thrane, Per-Olof Åstrand, Anders Wallqvist, Kurt V. Mikkelsen, and So/ren R. Keiding. Investigation of the temperature dependence of dielectric relaxation in liquid water by thz reflection spectroscopy and molecular dynamics simulation. *The Journal of Chemical*

*Physics*, 107(14):5319–5331, 1997. doi: 10.1063/1.474242. URL `https://doi.org/10.1063/1.474242`.

[137] Sun Wen-Feng, Wang Xin-Ke, and Zhang Yan. Measurement of refractive index for high reflectance materials with terahertz time domain reflection spectroscopy. *Chinese Physics Letters*, 26(11):114210, oct 2009. doi: 10.1088/0256-307x/26/11/114210.

[138] R. Piesiewicz, C. Jansen, S. Wietzke, D. Mittleman, M. Koch, and T. Kürner. Properties of building and plastic materials in the thz range. *International Journal of Infrared and Millimeter Waves*, 28(5):363–371, May 2007. ISSN 1572-9559. doi: 10.1007/s10762-007-9217-9. URL `https://doi.org/10.1007/s10762-007-9217-9`.

[139] A. Sengupta, A. Bandyopadhyay, B. F. Bowden, J. A. Harrington, and J. F. Federici. Characterisation of olefin copolymers using terahertz spectroscopy. *Electronics Letters*, 42(25):1477–1479, December 2006. ISSN 0013-5194. doi: 10.1049/el:20063148.

[140] Wolfgang Braun. *Applied RHEED: reflection high-energy electron diffraction during crystal growth*, volume 154. Springer Science & Business Media, 1999.

[141] Ekmel Ozbay. Plasmonics: merging photonics and electronics at nanoscale dimensions. *science*, 311(5758):189–193, 2006.

[142] Alexandre Aubry, Dang Yuan Lei, Stefan A Maier, and JB Pendry. Interaction between plasmonic nanoparticles revisited with transformation optics. *Physical review letters*, 105(23):233901, 2010.

[143] Murat Sivis, M Duwe, B Abel, and C Ropers. Extreme-ultraviolet light generation in plasmonic nanostructures. *Nature Physics*, 9(5):304, 2013.

[144] C. L. Wu. Nanostructures for plasmonic solar cells and biosensing. In *The Ninth International Conference on Advanced Semiconductor Devices and Mircosystems*, pages 83–86, Nov 2012. doi: 10.1109/ASDAM.2012.6418550.

[145] Matthew D Sonntag, Eric A Pozzi, Nan Jiang, Mark C Hersam, and Richard P Van Duyne. Recent advances in tip-enhanced raman spectroscopy. *The journal of physical chemistry letters*, 5(18):3125–3130, 2014.

[146] Christopher W Berry, N Wang, Mohammad R Hashemi, M Unlu, and Mona Jarrahi. Significant performance enhancement in photoconductive terahertz optoelectronics by incorporating plasmonic contact electrodes. *Nature communications*, 4:1622, 2013.

[147] Kevin M McPeak, Sriharsha V Jayanti, Stephan JP Kress, Stefan Meyer, Stelio Iotti, Aurelio Rossinelli, and David J Norris. Plasmonic films can easily be better: rules and recipes. *ACS photonics*, 2(3):326–333, 2015.

[148] Jiří Homola. Present and future of surface plasmon resonance biosensors. *Analytical and bioanalytical chemistry*, 377(3):528–539, 2003.

[149] Pablo G Etchegoin, EC Le Ru, and M Meyer. An analytic model for the optical properties of gold. *The Journal of chemical physics*, 125(16):164705, 2006.

[150] Gururaj V Naik, Vladimir M Shalaev, and Alexandra Boltasseva. Alternative plasmonic materials: beyond gold and silver. *Advanced Materials*, 25(24): 3264–3294, 2013.

[151] Alexei A Maradudin, J Roy Sambles, and William L Barnes. *Modern plasmonics*, volume 4. Elsevier, 2014.

[152] M Nevière, E Popov, and R Reinisch. Electromagnetic resonances in linear and nonlinear optics: phenomenological study of grating behavior through the poles and zeros of the scattering operator. *JOSA A*, 12(3):513–523, 1995.

[153] D Yuk Kei Ko and JR Sambles. Scattering matrix method for propagation of radiation in stratified media: attenuated total reflection studies of liquid crystals. *JOSA A*, 5(11):1863–1866, 1988.

[154] JB Pendry, L Martin-Moreno, and FJ Garcia-Vidal. Mimicking surface plasmons with structured surfaces. *science*, 305(5685):847–848, 2004.

[155] Chongchong Chen. A new kind of spoof surface plasmon polaritons structure with periodic loading of t-shape grooves. *AIP Advances*, 6(10):105003, 2016.

[156] Haizi Yao and Shuncong Zhong. Plasmonic corrugated cylinder–cone terahertz probe. *JOSA A*, 31(8):1856–1860, 2014.

[157] Zhen Gao, Linfang Shen, Jin-Jei Wu, Tzong-Jer Yang, and Xiaodong Zheng. Terahertz surface plasmon polaritons in textured metal surfaces formed by square arrays of metallic pillars. *Optics Communications*, 285(8):2076–2080, 2012.

[158] Zhen Gao, Linfang Shen, Xiaodong Zheng, Jin-Jei Wu, Tzong-Jer Yang, and Dongxiao Yang. Terahertz plasmonic microcavity with high quality factor and ultrasmall mode volume. *Plasmonics*, 8(2):319–324, 2013.

[159] Qiaoqiang Gan, Zhan Fu, Yujie J Ding, and Filbert J Bartoli. Ultrawide-bandwidth slow-light system based on thz plasmonic graded metallic grating structures. *Physical review letters*, 100(25):256803, 2008.

[160] Kristian Nielsen, Henrik K Rasmussen, Aurèle JL Adam, Paul CM Planken, Ole Bang, and Peter Uhd Jepsen. Bendable, low-loss topas fibers for the terahertz frequency range. *Optics Express*, 17(10):8592–8601, 2009.

[161] Alireza Hassani, Alexandre Dupuis, and Maksim Skorobogatiy. Porous polymer fibers for low-loss terahertz guiding. *Optics express*, 16(9):6340–6351, 2008.

[162] Christopher R Williams, Steven R Andrews, SA Maier, AI Fernández-Domínguez, L Martín-Moreno, and FJ García-Vidal. Highly confined guiding of terahertz surface plasmon polaritons on structured metal surfaces. *Nature Photonics*, 2(3):175, 2008.

[163] Wenqi Zhu, Amit Agrawal, and Ajay Nahata. Planar plasmonic terahertz guided-wave devices. *Optics express*, 16(9):6216–6226, 2008.

[164] Shashank Pandey, Barun Gupta, and Ajay Nahata. Terahertz plasmonic waveguides created via 3d printing. *Optics express*, 21(21):24422–24430, 2013.

[165] WJ Otter, NM Ridler, H Yasukochi, K Soeda, K Konishi, J Yumoto, M Kuwata-Gonokami, and S Lucyszyn. 3d printed 1.1 thz waveguides. *Electronics Letters*, 53(7):471–473, 2017.

[166] Rajind Mendis and Daniel M. Mittleman. An investigation of the lowest-order transverse-electric (te1) mode of the parallel-plate waveguide for thz pulse propagation. *J. Opt. Soc. Am. B*, 26(9):A6–A13, Sep 2009. doi: 10.1364/JOSAB.26.0000A6. URL `http://josab.osa.org/abstract.cfm?URI=josab-26-9-A6`.

[167] Xiaopeng Shen, Tie Jun Cui, Diego Martin-Cano, and Francisco J Garcia-Vidal. Conformal surface plasmons propagating on ultrathin and flexible films. *Proceedings of the National Academy of Sciences*, 110(1):40–45, 2013.

[168] Masahiro Yata, Masayuki Fujita, and Tadao Nagatsuma. Photonic-crystal diplexers for terahertz-wave applications. *Optics express*, 24(7):7835–7849, 2016.

[169] Jianjun Ma, Nicholas J Karl, Sara Bretin, Guillaume Ducournau, and Daniel M Mittleman. Frequency-division multiplexer and demultiplexer for terahertz wireless links. *Nature communications*, 8(1):729, 2017.

[170] T. Ishigaki, M. Fujita, M. Nagai, M. Ashida, and T. Nagatsuma. Photonic-crystal slab for terahertz-wave integrated circuits. In *IEEE Photonics Conference 2012*, pages 774–775, Sep. 2012. doi: 10.1109/IPCon.2012.6358852.

[171] Masahiro Yata, Masayuki Fujita, and Tadao Nagatsuma. Photonic-crystal diplexers for terahertz-wave applications. *Opt. Express*, 24(7):7835–7849, Apr

2016. doi: 10.1364/OE.24.007835. URL `http://www.opticsexpress.org/abstract.cfm?URI=oe-24-7-7835`.

[172] Yong Jin Zhou, Chao Zhang, Liu Yang, and Qian Xun Xiao. Electronically switchable and tunable bandpass filters based on spoof localized surface plasmons. *JOSA B*, 34(7):D9–D12, 2017.

[173] Kyungjun Song and Pinaki Mazumder. Active terahertz spoof surface plasmon polariton switch comprising the perfect conductor metamaterial. *IEEE Transactions on Electron Devices*, 56(11):2792–2799, 2009.

[174] Kyungjun Song and Pinaki Mazumder. Dynamic terahertz spoof surface plasmon–polariton switch based on resonance and absorption. *IEEE Transactions on electron devices*, 58(7):2172–2176, 2011.

[175] Chan-Shan Yang, Chia-Jen Lin, Ru-Pin Pan, Christopher T Que, Kohji Yamamoto, Masahiko Tani, and Ci-Ling Pan. The complex refractive indices of the liquid crystal mixture e7 in the terahertz frequency range. *JOSA B*, 27(9):1866–1873, 2010.

[176] Xuefeng Li, Nicholas Tan, Mike Pivnenko, Juraj Sibik, J Axel Zeitler, and Daping Chu. High-birefringence nematic liquid crystal for broadband thz applications. *Liquid Crystals*, 43(7):955–962, 2016.

[177] Hongkyu Park, Edward P. J. Parrott, Fan Fan, Meehyun Lim, Haewook Han, Vladimir G. Chigrinov, and Emma Pickwell-MacPherson. Evaluating liquid crystal properties for use in terahertz devices. *Opt. Express*, 20(11):11899–11905, May 2012. doi: 10.1364/OE.20.011899. URL `http://www.opticsexpress.org/abstract.cfm?URI=oe-20-11-11899`.

[178] Xiaoyong Liu, Lei Zhu, Qiongsen Wu, and Yijun Feng. Highly-confined and low-loss spoof surface plasmon polaritons structure with periodic loading of trapezoidal grooves. *Aip Advances*, 5(7):077123, 2015.

[179] Zaihe Yu, Zhen Gao, Zhengyong Song, and Zhuoyuan Wang. Terahertz spoof plasmonic coaxial microcavity. *Applied optics*, 53(6):1118–1123, 2014.

[180] Mikhail L Gorodetsky, Anatoly A Savchenkov, and Vladimir S Ilchenko. Ultimate q of optical microsphere resonators. *Optics letters*, 21(7):453–455, 1996.

[181] S. Preu, H. G. L. Schwefel, S. Malzer, G. H. Döhler, L. J. Wang, M. Hanson, J. D. Zimmerman, and A. C. Gossard. Coupled whispering gallery mode resonators in the terahertz frequency range. *Opt. Express*, 16(10):7336–7343, May 2008. doi: 10.1364/OE.16.007336. URL `http://www.opticsexpress.org/abstract.cfm?URI=oe-16-10-7336`.

[182] M. L. Gorodetsky and V. S. Ilchenko. Optical microsphere resonators: optimal coupling to high-q whispering-gallery modes. *J. Opt. Soc. Am. B*, 16(1):147–154, Jan 1999. doi: 10.1364/JOSAB.16.000147. URL `http://josab.osa.org/abstract.cfm?URI=josab-16-1-147`.

[183] M. Pöllinger, D. O'Shea, F. Warken, and A. Rauschenbeutel. Ultrahigh-q tunable whispering-gallery-mode microresonator. *Phys. Rev. Lett.*, 103: 053901, Jul 2009. doi: 10.1103/PhysRevLett.103.053901. URL `https://link.aps.org/doi/10.1103/PhysRevLett.103.053901`.

[184] Dror Sarid and William A Challener. *Modern introduction to surface plasmons: theory, Mathematica modeling, and applications*. Cambridge University Press, 2010.

[185] Alexei A Maradudin. *Light scattering and nanoscale surface roughness*. Springer Science & Business Media, 2007.

[186] Xi Gao, Liang Zhou, and Tie Jun Cui. Odd-mode surface plasmon polaritons supported by complementary plasmonic metamaterial. *Scientific reports*, 5: 9250, 2015.

[187] Edward A Stern. Plasma radiation by rough surfaces. *Physical Review Letters*, 19(23):1321, 1967.

[188] E Kretschmann. The angular dependence and the polarisation of light emitted by surface plasmons on metals due to roughness. *Optics Communications*, 5(5):331–336, 1972.

[189] E Kretschmann. Die bestimmung der oberflächenrauhigkeit dünner schichten durch messung der winkelabhängigkeit der streustrahlung von oberflächenplasmaschwingungen. *Optics Communications*, 10(4):353–356, 1974.

[190] Heinz Reather. Surface plasmons on smooth and rough surfaces and on gratings. *Springer tracts in modern physics*, 111:1–3, 1988.

[191] Tevis DB Jacobs, Till Junge, and Lars Pastewka. Quantitative characterization of surface topography using spectral analysis. *Surface Topography: Metrology and Properties*, 5(1):013001, 2017.

[192] Abdelwaheb Ourir, Agnes Maurel, Simon Félix, J-F Mercier, and Mathias Fink. Manipulating light at subwavelength scale by exploiting defect-guided spoof plasmon modes. *Physical Review B*, 96(12):125133, 2017.

[193] Hong-Wei Wu, Hua-Jun Chen, Hui-Ying Fan, Yang Li, and Xian-Wen Fang. Trapped spoof surface plasmons with structured defects in textured closed surfaces. *Optics letters*, 42(4):791–794, 2017.

[194] Hendrik Christoffel Hulst and Hendrik C van de Hulst. *Light scattering by small particles*. Courier Corporation, 1981.

[195] Martina Schmid, Patrick Andrae, and Phillip Manley. Plasmonic and photonic scattering and near fields of nanoparticles. *Nanoscale research letters*, 9(1):50, 2014.

[196] D.M. Pozar. *Microwave Engineering, 4th Edition*. Wiley, 2011.

[197] Jeffrey L. Hesler, Yiwei Duan, Brian Foley, and Thomas W. Crowe. Thz vector network analyzer measurements and calibration. In *21st International Symposium on Space Terahertz Technology 2010, ISSTT 2010*, 21st International Symposium on Space Terahertz Technology 2010, ISSTT 2010, pages 273–275, 12 2010. ISBN 9781617823626.

[198] J. F. Johansson and N. D. Whyborn. The diagonal horn as a sub-millimeter wave antenna. *IEEE Transactions on Microwave Theory and Techniques*, 40 (5):795–800, May 1992. ISSN 0018-9480. doi: 10.1109/22.137380.

[199] *Nominal Horn Specifications. With permission of VDI.* Virginia Diodes, Inc., 4 2015.

[200] E. Brigham. *The Fast Fourier Transform,*. Prentice-Hall, Inc., 1974.

[201] R. Courant, K. Friedrichs, and H. Lewy. Über die partiellen differenzengleichungen der mathematischen physik. *Mathematische Annalen*, 100 (1):32–74, Dec 1928. ISSN 1432-1807. doi: 10.1007/BF01448839. URL https://doi.org/10.1007/BF01448839.

[202] Wenhua Yu and Raj Mittra. A conformal finite difference time domain technique for modeling curved dielectric surfaces. *IEEE Microwave and Wireless Components Letters*, 11(1):25–27, 2001.

[203] Allen Taflove and Susan C Hagness. Computational electromagnetics: the finite-difference time-domain method. *Artech House, Norwood*, 2005.

[204] Yan Zhao and Yang Hao. Finite-difference time-domain study of guided modes in nano-plasmonic waveguides. *IEEE Transactions on Antennas and Propagation*, 55(11):3070–3077, 2007.

[205] Ahmad Mohammadi, Hamid Nadgaran, and Mario Agio. Contour-path effective permittivities for the two-dimensional finite-difference time-domain method. *Optics Express*, 13(25):10367–10381, 2005.

[206] lumerical knowledge base - symmetric and anti-symmetric bcs, 2015. URL `https://kb.lumerical.com`.

[207] JT Kindt and CA Schmuttenmaer. Far-infrared dielectric properties of polar liquids probed by femtosecond terahertz pulse spectroscopy. *The Journal of Physical Chemistry*, 100(24):10373–10379, 1996.

[208] Yuefang Hua and Hongjian Zhang. Qualitative and quantitative detection of pesticides with terahertz time-domain spectroscopy. *IEEE Transactions on Microwave Theory and Techniques*, 58(7):2064–2070, 2010.

[209] Nanfang Yu, Qi Jie Wang, Mikhail A. Kats, Jonathan A. Fan, Suraj P. Khanna, Lianhe Li, A. Giles Davies, Edmund H. Linfield, and Federico Capasso. Designer spoof surface plasmon structures collimate terahertz laser beams. *Nature Materials*, 9:730, August 2010. URL `https://doi.org/10.1038/nmat2822`.

[210] David Keun Cheng et al. *Field and wave electromagnetics*. Pearson Education India, 1989.

# Appendix

## THz Vector Network Analyzer - Fundamentals

Here we explain some fundamentals about the THz VNA, starting with a general introduction to frequency multiplying and mixing, followed by the layout of the frequency range extenders and finishing with the beam shape of the instrument when used in free-space experiments.

### Frequency Multipliers and Mixers

Every circuit that generates or detects electromagnetic radiation requires a local oscillator which produces a periodic signal with high stability and low noise characteristics [196]. However, with increasing frequency, it becomes increasingly difficult to build a fundamental oscillator, so frequency multipliers are necessary for microwave frequencies and beyond. Frequency multipliers use nonlinear components to generate harmonics which can be utilised for the generation of higher frequencies. There are a variety of nonlinear components available to build frequency multipliers which have different advantages and disadvantages. Multipliers based on varactor diodes have very high power conversion efficiencies which in theory can reach up to 100% for low, single-digit multiplier factors but have a limited bandwidth rendering them less useful for a network analyser which aims to cover a broad

range of frequencies. In addition, the variable capacitance giving the varactor diode its functionality is based on a changing depletion region, and with increased frequency the charge carrier mobility is too low to follow these changes, reducing the change in capacitance, and the performance is severely degraded. Therefore the frequency multipliers used in the VNA use Schottky barrier diodes which provide a larger bandwidth than varactor diodes. The downside to Schottky barriers is the low conversion efficiency which reduces with the square of the harmonic number, therefore a series of integrated multipliers is used, e.g. the multiplier factor of 81 which occurs in the extenders is realised by a series of four frequency tripplers instead of one single multiplier with a multiplier factor of 81 (which would be a component of hypothetical nature in any case). Nevertheless, even this design results in low output powers in the $\mu$W region, compared to mW powers of the microwave region.

Since it is considerably easier to analyse a signal at lower frequencies than at THz frequencies and with higher precision, the THz signal is translated to lower frequencies through frequency mixing after passing the experimental setup. A frequency mixer is a three-port, nonlinear device which can mix two frequencies resulting in either a higher or a lower frequency, as shown in Figure 7.1. Hence the frequency mixer always generates several harmonics simultaneously, the lower and higher frequencies. Additional filters are required to select the desired product.
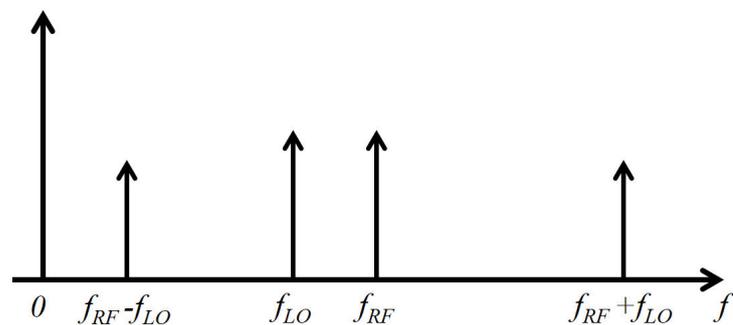


Figure 7.1: Down-conversion from a higher frequency (RF) with a different provided frequency ($f_{LO}$) to the lower target frequency ($f_{RF} - f_{LO}$). The simultaneously generated higher harmonic ($f_{RF} + f_{LO}$) will be filtered with a low pass filter.

**Frequency Extender Layout**

A schematic of the frequency extender can be seen in Figure 7.2. The incoming signal from the network analyser (RF Input) is fed into the signal generator which multiplies the frequency by a factor of 81, extending the incoming GHz frequencies to the THz regime. The generator is followed by a directional attenuator, called an isolator, which minimises the unwanted leakage of THz radiation into the signal generator from the test port. Afterwards, two back to back directional couplers are used; the first one to split up a fraction of the generated THz radiation to be used as a reference signal after it was mixed down to lower frequencies by a subharmonic mixer; the second directional coupler lets all THz radiation generation pass through unhindered since it couples in the opposite direction to pick up the incoming THz radiation from the test port. The THz radiation coming in from the test port is directed to another directional attenuator which is minimising the leakage of other frequencies into the test port. Afterwards, the THz radiation is mixed down, again by a subharmonic mixer, to bring it to frequencies which can be processed by the network analyser. Both subharmonic mixers are driven by the local oscillator signal provided via the network analyser. The local oscillator signal is multiplied by a factor of 36.

The different multiplication factors for generation and measurement are necessary for the simultaneous generation and detection to obtain a full set of S-parameters, i.e. reflection and transmission. The VNA uses frequencies from approx. 9.3 to 13.6 GHz to generate and approx. 20.8 to 30.6 GHz to analyse the THz signal.

**Beam Shape and Control**

As the frequency range extenders use standardised rectangular waveguides, as indicated by the WR-1.0 in the instruments name, which is identical to the metric waveguide standard WM-250, horn antennas have to be used to efficiently couple the radiation to free space. The relevant dimensions of the antennas are indicated
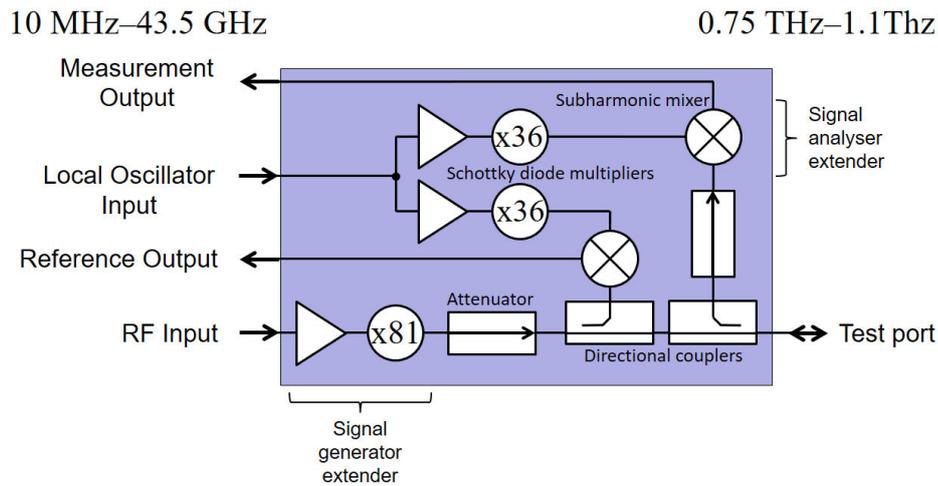
Figure 7.2: Diagram of the VDI frequency range extender. The different multiplication factors for the generation (x81) and measurement (x36) are shown. The assymetry is necessary for the simultaneous generation and measurement. After [197].

in the schematic of Figure 7.3. Diagonal horns are used as they can be produced

with split-block techniques, which are common in mm and sub-mm technology and

have a high fraction of about 84% of the power radiated into the fundamental mode

and about 10% radiated into the cross-polarised mode [198]. Additionally, diag-
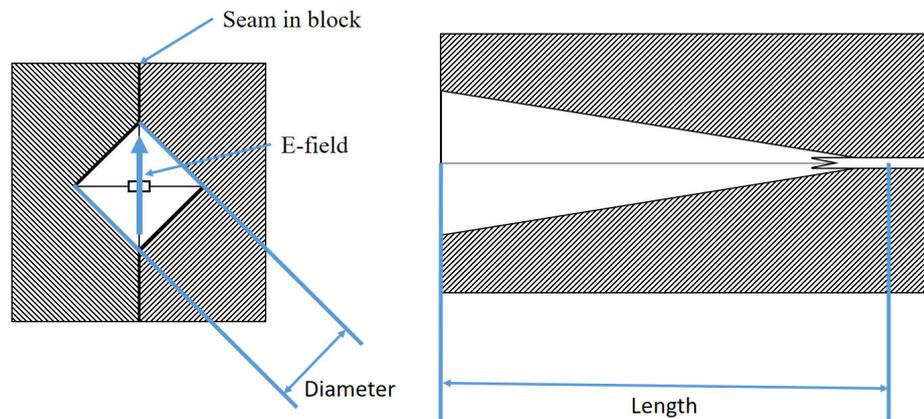


Figure 7.3: Schematic of the diagonal horn constructed out of split-blocks. The indicated aperture diameters is $1.6\,\text{mm}$ and the length is $16\,\text{mm}$ for the antennas used.

onal horns are linearly polarised and have low side-lobes. The antennas used here

have a taper half-angle of $2.9°$, which results in a full $3\,\text{dB}$ beamwidth of $10°$. The

mid-band gain of the antenna is $26\,\text{dB}$, as seen in Figure 7.4, but is not completely

flat.

Due to the divergent beam, the intensity quickly drops over distance and therefore
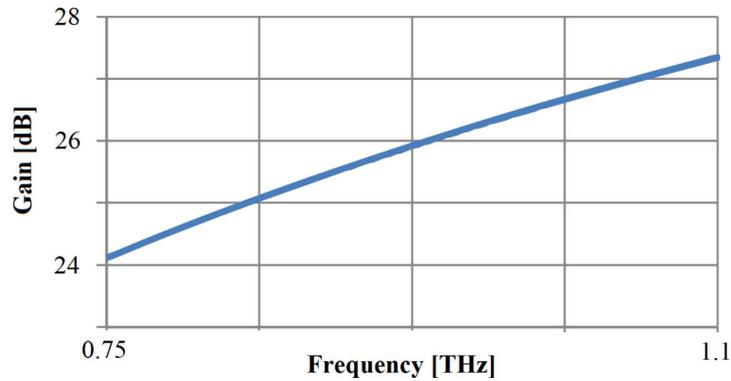


Figure 7.4: Typical gain of the used diagonal horn antenna. From [199].

off-axis parabolic mirrors, as seen in Figure 7.5, are used for many experiments to increase the intensity as more radiation is collected. Additionally, depending on the number of mirrors used, the mirrors allow the collimation (two mirrors) or focusing (4 mirrors) of the beam. At THz frequencies mirrors, as reflective optical elements, are often preferred over diffractive optical components, such as lenses, due to the losses which occur in the materials of such components.

Despite the mirrors and high gain antennas, even with ideal alignment, around 5 dB is lost in comparison to the ideal instrument performance that is shown in Figure 2.7 when the waveguides are directly connected.
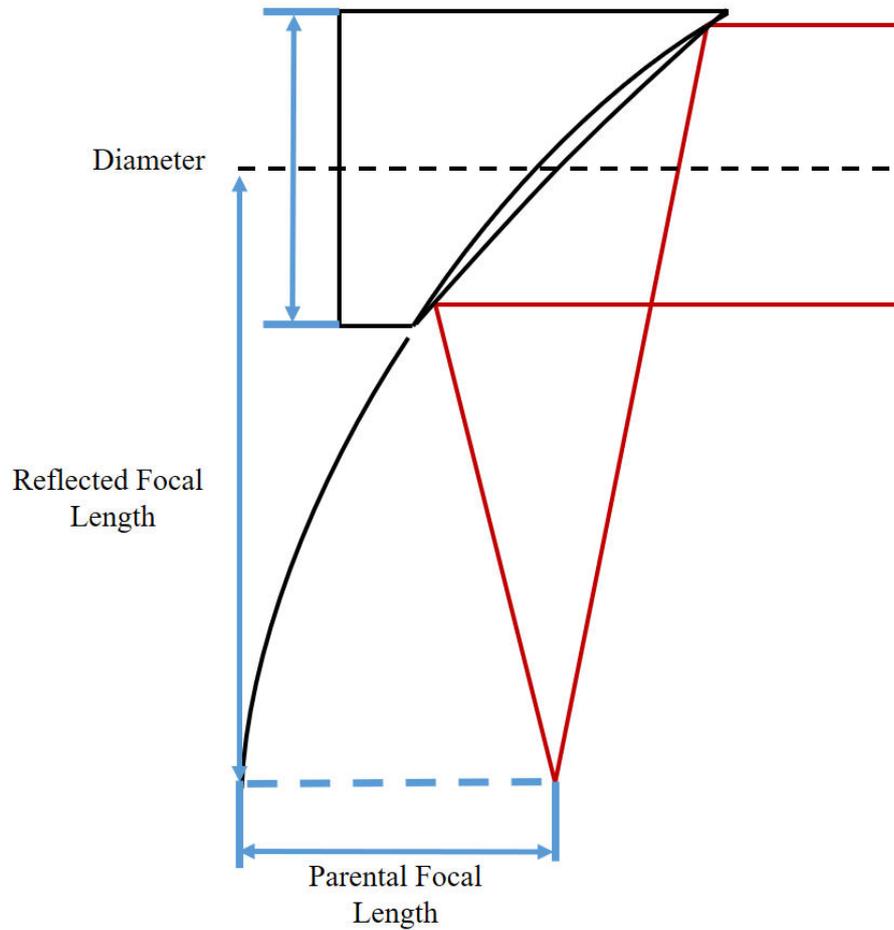
Figure 7.5: Schematic of a parabolic mirror with its relevant parameters.

## THz Time-Domain Spetroscopy - Data Postprocessing

As explained in Section 2.2.3, the TDS records data in the time-domain, but for most applications, a frequency spectrum is required. With a Fast Fourier Transformation fast Fourier transformation (FFT), the time domain data can be transferred into the frequency domain to analyse spectral features. An FFT is an algorithm which is used to transfer a signal from its original domain, most commonly time or space, to a representation in the frequency domain and vice versa. An FFT is an approximation of a continuous Fourier transform. The approximation is necessary for the sampled nature of an experimental data set. The accuracy of the approximation is dependent on the sample interval $T_N$ and the truncation length,

i.e. the number of points used [200]. Truncation is important to select the information in the relevant range and not the high-frequency components, which are essentially zero and the number of points is typically specified as a power of 2. For a continuous function containing no frequencies larger than the Nyquist frequency $f_{Nyquist}$, the Fourier transform can be determined uniquely by a given sample interval by

$$T_N = \frac{1}{2f_{Nyquist}} \tag{7.1}$$

When the sampling rate is at least twice as high as the largest frequency compon-
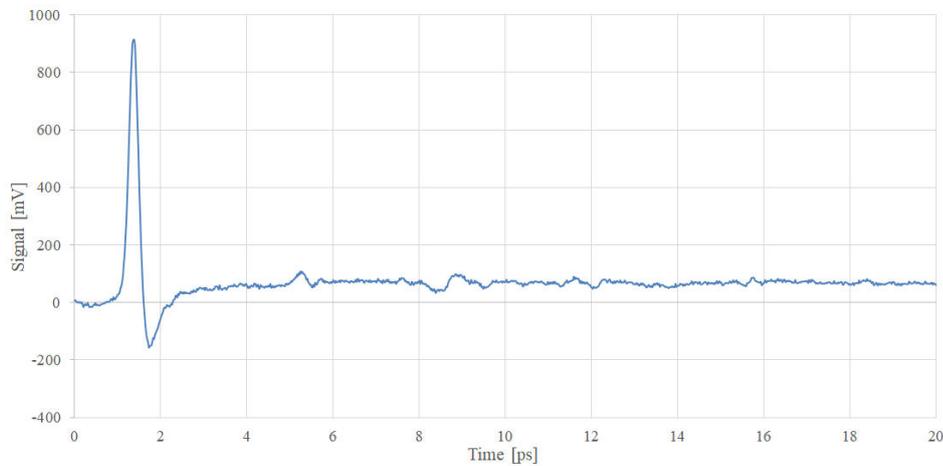


Figure 7.6: Typical THz pulse recorded with the Durham Engineering THz TDS.

ent, it fulfils the Nyquist-Shannon sampling theorem, and no information will be lost due to the sampling process. Truncation can introduce ripples in the frequency domain, but these can be avoided by windowing the data, i.e. multiplying the signal with other functions. Simple examples are rectangular or triangular functions, but usually, functions without discontinuities are preferred, such as the Hann or Hamming windows, which are raised cosines.

There are some additional ways to make the spectrum obtained by the FFT more useful. A typical THz pulse is seen in Figure 7.6. First of all, a correction for a DC offset of the signal is helpful. A DC offset is a non-zero base level of the signal in the time-domain and leads to value towards $0\,\mathrm{Hz}$ in the frequency spectrum and therefore influences the amplitude scale of the FFT, as seen in Figure 7.7. The

offset can be easily corrected by levelling the signal level before the start of the THz pulse to 0.

An additional commonly used method to improve the usability of the spectrum
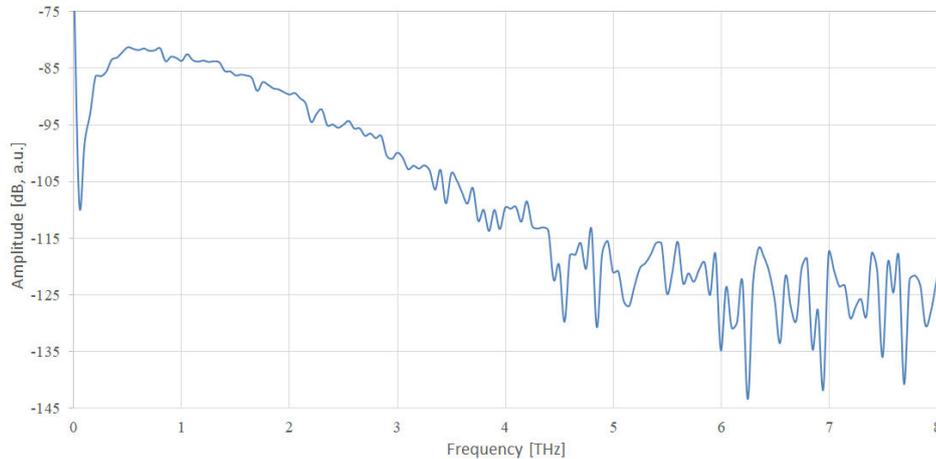


Figure 7.7: THz spectrum obtained from the FFT of Figure 7.6. The amplitude artefact towards 0 Hz caused by the DC offset in the time-domain signal is exaggerated due to the dB scale. The intensity drops considerably beyond 4 THz, but scans with longer lock-in time constants and averaging are able to resolve 5.2 THz LO phonon band of the ZnTe crystal.

is zero-padding. In those methods the data set size is increased by adding zeroes to it, which results in closer spacing between data points in the frequency domain. However, the actual frequency resolution of the FFT will not be increased and no additional data created, therefore the resulting effect is a smoothing of the frequency domain data.

# FDTD Simulation - Fundamentals and Background

This section discusses the fundamentals to set up simulation environment, such as the mesh and boundary conditions, correctly for FDTD simulation as discussed in Section 2.3. Afterwards, the simulation of dielectric and metallic materials at THz frequencies is discussed.

## Setting up FDTD Simulations

The first step is to design the structure and to define the simulation domain with the CAD interface that Lumerical offers. The definition of the simulation domain includes the spatial region in 2D or 3D, boundary conditions, the simulation time and the mesh size. As described before, the mesh defines the distance between every calculation step and therefore, the accuracy of the simulation but also the required time and resources. The conformal mesh does not employ a fixed mesh size but has a mesh accuracy parameter varying from 1-8 as integers. Many different factors influence the actual mesh size of a conformal mesh, but the accuracy parameter allows for an impression of the accuracy used as the integer values represent the target number of mesh points per wavelength (PPW). A value of 1 corresponds to a target of 6 PPW, and every additional step increases this number by 4, up to a maximum of 34 PPW for a mesh accuracy of 8. A reasonable approach is to simulate at low accuracy first and then increase the accuracy until results converge. The lowest accuracy values at which the results converged is the ideal meshing, as it delivers accurate results while using the least computational resources.

Accurate meshing is particularly relevant for structures which change their properties massively even by small deviations in size, due to the resonant behaviour in the underlying physics, such as spoof plasmonic structures.

The next step is the placement and specification of the EM-source. The source specifies not only the frequency region of the pulse, but also polarisation, angle of incidence and, depending on the chosen boundary conditions, the beam profile. The results are recorded with different monitors, offering features like recording the frequency spectrum, refractive index, electrical field and S-parameters. Lumerical offers a variety of data post-processing features, making results like the calculation of quality factors or far-field projections easy accessible.

Another parameter that has to be chosen carefully is the simulation time. The simulation time has to be long enough for the radiation to propagate through all of the simulation domain. As energy is commonly allowed to dissipate at the simu-

lation boundaries, a cut-off value is often used to which the energy dissipates. The value gives the fraction of the original injected energy that is still present in the system at the given time step; the standard value is $10^{-5}$. Choosing a lower value is often necessary for resonant structures, as the energy is calculated based on all the frequencies present in the ejected pulse and resonances might only represent a small fraction of the total energy.

To only account for the relevant electric fields, i.e. to cut out the original pulse, reflections, and to observe the relevant electric fields, it is recommendable to use apodization. Apodization is a filtering technique, similar to truncation in the TDS data processing, by gradually attenuating the undesired part of the results in the time domain. Lumerical offers three different apodizations: Start, end and full. The start apodization allows removing the initial pulse from the recorded data, which is especially useful to display electric fields of resonant structures, as shown in Figure 7.8. End apodization attenuates all signals after a given time, which can be used to remove reflections. The full apodization is a windowed function.
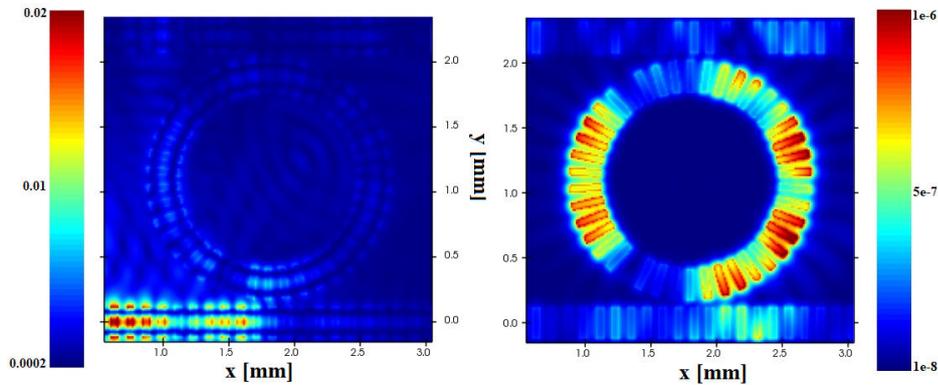


Figure 7.8: Example of the electric field distribution at a resonant frequency of a spoof plasmonic ring resonator without (left) and with (right) apodization. Without apodization, the resonances in the ring are not visible as the intensity of the initial pulse is too high.

## Numerical Constraints and Meshing

Any numerical method based on approximation of equations faces the trade-off between precision and computational effort. Therefore, one has to ensure that the precision of the simulation is chosen high enough that the approximation is reasonably well and no wrong solution is obtained. Fortunately, there are also mathematical conditions that ensure that the numerical solution converges to a solution. One of these conditions is the Courant-Friedrichs-Lewis (CFL) condition, which defines a maximum time step for the simulations [201]. The condition ensures that no energy can propagate further than one single spatial step, i.e. half a cell, as every mesh point is computed as a function of its nearest neighbours only. Mathematically, this condition can be expressed as

$$u\Delta t \leqslant \Delta x \tag{7.2}$$

for the one-dimensional case where $u$ is the magnitude of the velocity, $\Delta t$ the time step and $\Delta x$ the spatial step. This can be rewritten as

$$C = \frac{u\Delta t}{\Delta x} \leqslant C_{max} \tag{7.3}$$

where $C$ is the Courant number. By default, Lumerical uses a time step that is 0.99 of the Courant number. $C$ is calculated assuming propagation of light in a homogeneous vacuum. Once physical structures and interfaces are included in the simulation, particularly when dispersive materials are involved, a smaller time step is sometimes required. Reducing the time step might avoid instabilities, but increases the simulation time.

For the two-dimensional case, the CFL condition becomes

$$C = \frac{u_x\Delta t}{\Delta x} + \frac{u_y\Delta t}{\Delta y} \leqslant C_{max} \tag{7.4}$$

By analogy this can be extended to the general, n-dimensional case

$$C = \Delta t \left( \sum_{i=1}^{n} \frac{u_{x_i}}{\Delta x_i} \right) \leqslant C_{max}. \tag{7.5}$$

Table 7.1: Dependence of memory requirements and simulation time on the mesh step size $\Delta x$ for a cubic mesh for different volumes $V$ and areas $A$ for 3D and 2D simulation respectively.

|  | 3D | 2D |
|---|---|---|
| Memory requirements | $\sim V(\lambda/\Delta x)^3$ | $\sim A(\lambda/\Delta x)^2$ |
| Simulation time | $\sim V(\lambda/\Delta x)^4$ | $\sim A(\lambda/\Delta x)^3$ |

The expansion into multiple dimensions introduces another issue. Even with uniform spatial step sizes $\Delta x = \Delta y = ... = \Delta x_i$ energy can propagate not along the principal axes. For example for a cubic lattice, the distance between the diagonally opposite points of the cube is $\sqrt(3)\Delta x$, which reduces the courant number to $C_{max} \leqslant \frac{1}{\sqrt{3}}$.

The condition that any point is only meant to be a function of its nearest neighbours also becomes relevant when non-cubic spacing in different dimensions is used, which can naturally occur at interfaces with materials with large different refractive indices, especially for interfaces not parallel to the principal axes. Therefore, interfaces and materials with different refractive indices have to be meshed differently to avoid artefacts and a "staircase" effect on curvatures. Meshing describes the process of defining the spatial step sizes within the simulation domain. Lumerical employs conformal mesh technology, which is similar to methods described in the literature [202–205]. The concept of conformal meshing tries to account for subcell features by solving Maxwell's integral equations near structure boundaries. As a consequence, the mesh size changes dynamically and gradually near interfaces and uses more mesh points while relaxing the mesh size in bulk materials. As a result, the simulation accuracy is higher and complex objects are meshed correctly, while simultaneously keeping the required computational resources low. The big advantage of this technique over meshing the whole simulation region with the smallest required mesh can be seen in Table 7.1. Therefore, conformal meshing often reduces the simulation time to a fraction of a uniform meshed simulation.

**Boundary Conditions**

Boundary conditions define the properties of the outer boundaries of the simulation region. They are important to obtain correct results and can reduce the simulation time when solving certain types of problems. First of all, boundary conditions are a necessary requirement for every FDTD simulation for the following reason: A FDTD solver approximates Maxwell's curl equations by finite-difference equations in every point of the simulation mesh through the energy flowing into the point from its nearest neighbours. At the edge of the simulation domain, the nearest neighbours do not exist and are determined by the boundary conditions. Dirichlet boundary conditions set all those values to zero, effectively making the boundaries perfect electric and magnetic conductors. While this solves the computational problem, it also leads to reflections on the boundaries which influence the simulation results or prevent the simulation from converging. Therefore, the Dirichlet boundary conditions are hardly used as stand-alone solution nowadays but in combination with perfectly matched layers (PML). PMLs are a set of layers added outside the boundaries, typically ten or more layers, which are set up in a way that they do absorb the radiation while simultaneously minimizing reflections. Another possibility are periodic boundary conditions, which set the fields of one boundary equal to the fields in the boundary opposite of it. This is obviously useful if the simulated structure exhibits a periodic nature since the simulation region can be reduced to the size of a unit cell. The last possibility are symmetric boundaries. They can be used whenever the EM fields have a plane of symmetry in the middle of the simulation region in one or more dimensions. The electric or magnetic field components are mirrored as shown in Figure 7.9, reducing the simulation volume by a factor of 4 or 8, depending on the simulation being 2D or 3D.
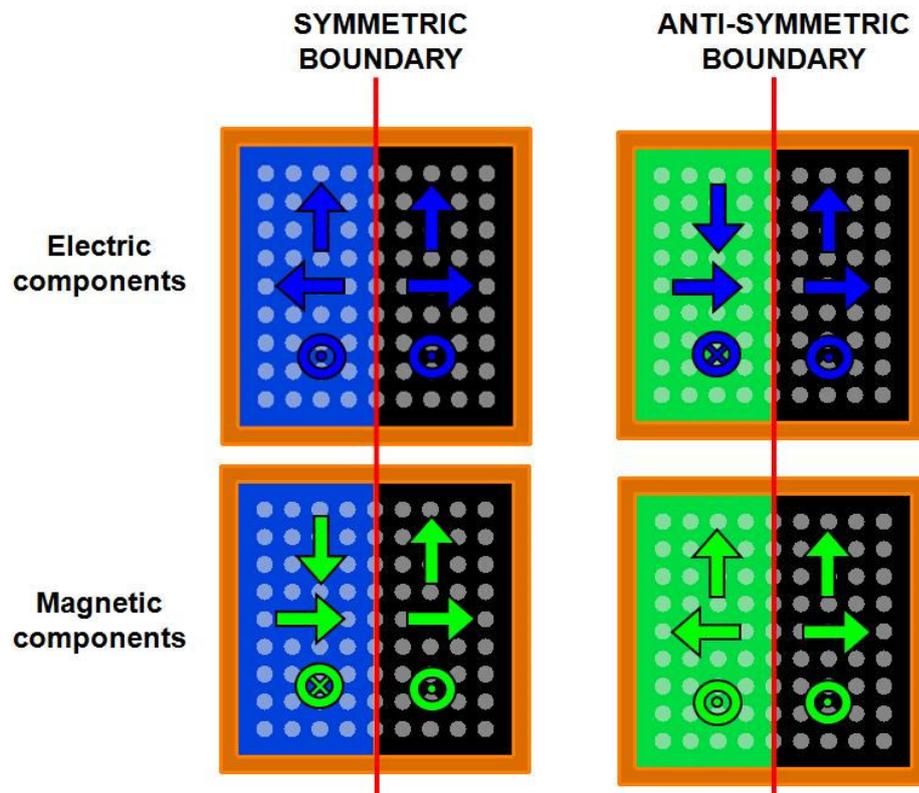
Figure 7.9: The mirroring of electric and magnetic fields for symmetric and anti-symmetric boundary conditions is illustrated for a two-dimensional simulation space . From [206].

## Simulating Materials

Most commercial photonic simulation tools come with a set of common materials already implemented. However, since material properties change over the electromagnetic spectrum, most of the pre-implemented materials cannot be used for simulations in the THz region because the database only provides values up to the near- or mid-infrared. Therefore, most materials have to be implemented by the user.

## Dielectric Materials

For dielectric materials, the simplest possibility to address this issue is to just use a single custom value for the refractive index which can be found for many

materials in the literature and usually remains constant over a broader range of frequency for most materials. But this method does not account for absorption (i.e. complex permittivity) which is substantial for many materials in the THz range. Hence, a purely real refractive index is only used for silicon in chapter Section 4.4.3 to reduce the simulation time. The material losses of silicons are so low that simulations show no difference when they are included. It is recommendable to use either self-obtained data from experiments or calculations or literature values for the complex permittivity to make the simulation as realistic as possible. For liquid mixtures, a simple weighted average of the optical constants can be used as a first approximation, even if this neglects eventual effects of non-ideal solutions. The values of the material parameters used during simulation are shown in Figure 7.10.
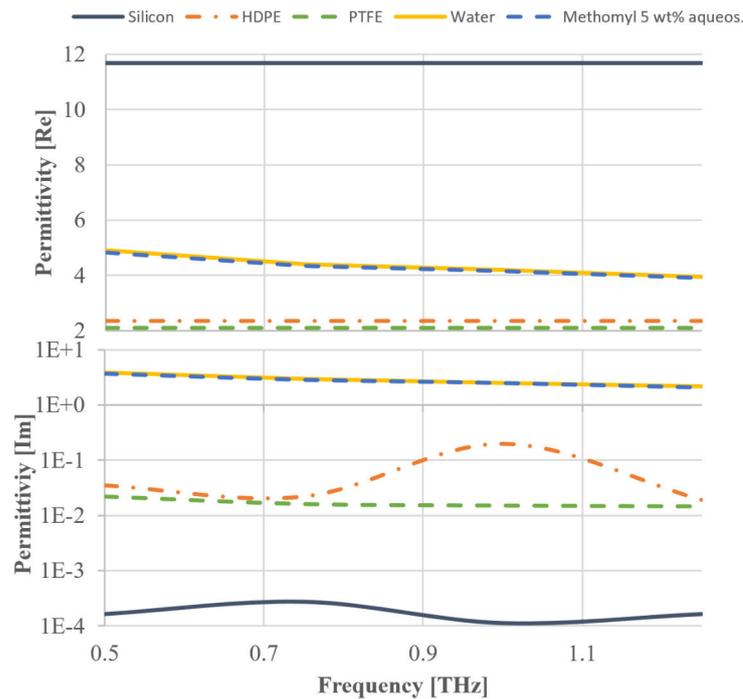


Figure 7.10: Real and imaginary parts of permittivity for the materials used in the thesis from literature [14, 23, 66, 207, 208]

**Perfect electronic conductor**

Perfect electric condutor (PEC) is an idealised material which possesses zero resistivity or, equivalently, infinite conductivity. Even if PECs do not exist in nature, they are a valid approximation for situations where the electrical resistance is negligible, which is the case for metals at the THz range and even highly doped semiconductors [209], as long as the thickness is larger than the skin depth. The advantage of PECs in simulation becomes apparent when considering that a  prevents the penetration of the electric field into the medium, therefore only the field at the interface of the PEC has to be computed.

# Ellipsometry Models - Fundamentals

Here the models used for the data extraction are discussed. All the measurements are conducted using optical isotropic samples. The first model described will be for a single layer, used for material characterisation. The second model is an extension for n-layers, to accommodate different sample structures and will be also used to extract layer thickness.

**Single layer model**

As the single-layer model of a sample with finite thickness has to account for the two materials at the sample's interfaces, the model employs the image of a finite layer with the thickness d and refractive index $n_2$ "sandwiched" between the two infinite media with the refractive indices $n_1$ and $n_3$ as indicated in Figure 7.11. As the outer media is assumed to be (dry) air, this simplifies to $n_1 = n_3 = 1$. The incident radiation is considered a collimated beam and is regarded as a linearly polarised plane wave with an angle of incident $\Theta_i$ and equal to the angle of reflection $\Theta_i = \Theta_r$. The angle of the transmitted wave into mediums 2 and 3 is denoted as $\Theta_t$, and $\Theta_{t,1}$

respectively. The angles for the transmission are subject to Snell's law:

$$n_1 \sin \Theta_i = n_2 \sin \Theta_t. \tag{7.6}$$

The following definitions, which are also shown in Figure 7.11, of the amplitude
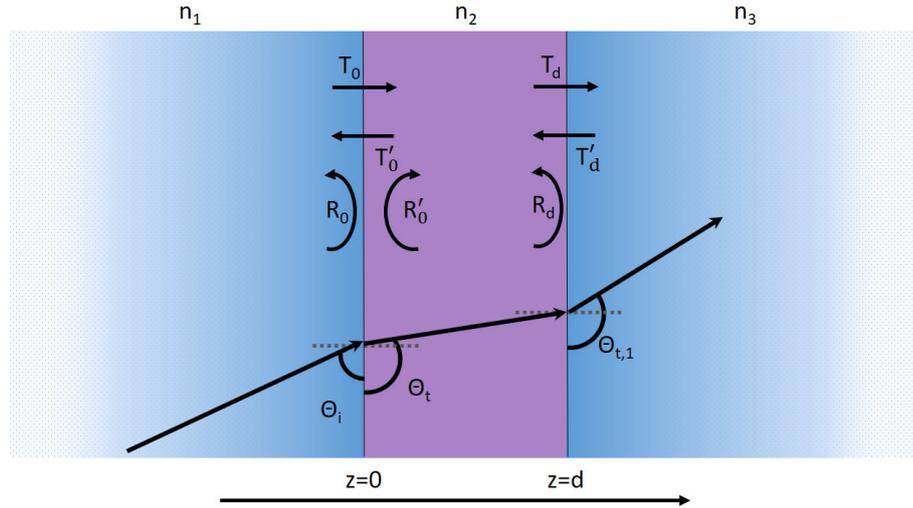


Figure 7.11: Schematic of the reflection and transmission processes that have to be accounted for in a single layer measurement.

transmission and reflection coefficients of the electric fields are used:

$T^0$ is the transmission coefficient at $z = 0$;

$T_0^{'}$ is the transmission coefficient of a return wave, coming from medium 2 into medium 1 at $z = 0$;

$R_0$ is the reflection coefficient at $z = 0$;

$R_0^{'}$ is the reflection coefficient of a wave coming from medium 2 and reflected at medium 1, $z = 0$; $T_d$ is the transmission coefficient at $z = d$;

$T_d^{'}$ is the transmission coefficient at $z = d$, for a wave traveling from medium 3 towards medium 2;

$R_d$ is the reflection coefficient of a wave traveling in medium 2 and reflected from medium 3, at $z = d$;

$R_d^{'}$ is the reflection coefficient of a wave traveling in medium 3 and reflected off medium 2, at $z = d$;

and the subscripts s and p denote the s and p polarisation respectively in the

following equations. The Fresnel equations for the amplitude coefficients at $z = 0$ can be expressed as:

$$R_{0s} = \frac{n_1 \cos \Theta_i - n_2 \cos \Theta_t}{n_1 \cos \Theta_i + n_2 \cos \Theta_t} \tag{7.7}$$

$$R_{0s'} = -R_{0s} \tag{7.8}$$

$$T_{0s} = \frac{2n_1 \cos \Theta_i}{n_1 \cos \Theta_i + n_2 \cos \Theta_t} \tag{7.9}$$

$$T_{0s'} = \frac{2n_2 \cos \Theta_t}{n_1 \cos \Theta_i + n_2 \cos \Theta_t} \tag{7.10}$$

$$R_{0p} = \frac{n_2 \cos \Theta_i - n_1 \cos \Theta_t}{n_2 \cos \Theta_i + n_1 \cos \Theta_t} \tag{7.11}$$

$$R_{0p'} = -R_{0p} \tag{7.12}$$

$$T_{0p} = \frac{2n_1 \cos \Theta_i}{n_2 \cos \Theta_i + n_1 \cos \Theta_t} \tag{7.13}$$

$$T_{0p'} = \frac{2n_2 \cos \Theta_t}{n_1 \cos \Theta_t + n_2 \cos \Theta_i} \tag{7.14}$$

These equations only account for the reflection on a single interface. Therefore, they have to be modified for the reflections on the second interface. Therefore, a modification which accommodates the change of phase at the point $z = d$ has to be introduced. To simplify this, we first regard normal incidence, which is later on modified for the incident angle. Due to the continuity required at the boundary between two media, we know that

$$E_2(d) = E_3(d) \tag{7.15}$$

and

$$H_2(d) = H_3(d). \tag{7.16}$$

From Maxwell's equations we know

$$E = \frac{-k \times \mu H}{n},$$ (7.17)

where $k$ is the vector of the propagating wave and $\mu$ is the permeability, which can be assumed to be 1 for non-magnetic materials. Furthermore, the electric field at the position $z$ will be the sum of the forward and backward, i.e. reflected, propagating waves. Ignoring multiple reflections we know that the electric field at $z = d$ are

$$E_2 = E_i e^{j\beta_2 z} + E_r e^{j\beta_2 z}$$ (7.18)

$$E_3 = E_t e^{j\beta_3 z}$$ (7.19)

With $\beta_2$ and $\beta_3$ being the propagation constants in medium 2 and 3 respectively. From Equation (7.17) we can obtain the magnetic fields

$$H_2 = n_2 E_i e^{j\beta_2 z} + n_2 E_r e^{j\beta_2 z}$$ (7.20)

and

$$H_3 = n_3 E_t e^{j\beta_3 z}.$$ (7.21)

With the boundary conditions from Equation (7.15) and Equation (7.16) we obtain:

$$E_i e^{j\beta_2 d} + E_r e^{j\beta_2 d} = E_t e^{j\beta_3 d}$$ (7.22)

and

$$n_2 E_i e^{j\beta_2 d} - n_2 E_r e^{j\beta_2 d} = n_3 E_t e^{j\beta_3 d}.$$ (7.23)

After rearrangement the expression for the amplitude transmission and reflection coefficients at $z = d$, defined by $T = E_t/E_i$ and $R = E_r/E_i$, are

$$T = \frac{2n_2 e^{-j(\beta_2 - \beta 3)d}}{n_2 + n_3}$$ (7.24)

and

$$R = \frac{(n_2 - n_3)e^{-2j\beta_2 d}}{n_2 + n_3}.$$ (7.25)

If now the change in path length due to the incident angle $\Theta_i$ is accounted for represented by modifying the propagation wave with

$$e^{-j\beta_1(x\sin\Theta_i + z\cos\Theta_i)}, \tag{7.26}$$

where the term containing x can be ignored as it is the part of the wave which propagates along the interface [210]. Then the Fresnel equations can be expressed as

$$R_{ds} = \frac{n_2 cos\Theta_t - n_3\cos\Theta_{t1}}{n_2\cos\Theta_t + n_3\cos\Theta_{t1}} e^{-2j\beta_2 d\cos\Theta_i}, \tag{7.27}$$

$$T_{ds} = \frac{2n_2 cos\Theta_t}{n_2\cos\Theta_t + n_3\cos\Theta_{t1}} e^{-j(\beta_2\cos\Theta_i - \beta_3\cos\Theta_t)d}, \tag{7.28}$$

$$R_{dp} = \frac{n_3 cos\Theta_t - n_2\cos\Theta_{t1}}{n_3\cos\Theta_t + n_1\cos\Theta_{t1}} e^{-2j\beta_2 d\cos\Theta_i} \tag{7.29}$$

and

$$T_{dp} = \frac{2n_2 cos\Theta_t}{n_3\cos\Theta_t + n_2\cos\Theta_{t1}} e^{-j(\beta_2\cos\Theta_i - \beta_3\cos\Theta_t)d}. \tag{7.30}$$

But these equations only take the very first reflection on the second interface into account. If now the equations are solved in the same way at the boundary $z = 0$ accounting for the reflected wave, it can be seen that the phase changes by $e^{-2j\beta_2 d\cos\Theta_i}$ for every round trip. The total transmission is therefore

$$T = T_0 T_d + T_0 R_d R_d' T_d e^{-j\beta_2 d\cos\Theta_i} + T_0 R_d^2 R_o'^2 T_d e^{-4j\beta_2 d\cos\Theta_i} +$$
$$T_{0s} R_d^3 R_0'^3 T_d e^{-8j\beta_2 d\cos\Theta_i} + ... = \frac{T_o T_d}{1 - R_d R_0' e^{-2j\beta_2 d\cos\Theta_i}}. \tag{7.31}$$

And the total reflection in the same way:

$$R = R_0 + T_0 R_d T_0' R_d R_0^i e^{-2j\beta_2 d\cos\Theta_i} + T_0 R_d T_0' R_d^2 R_o'^2 e^{-4j\beta_2 d\cos\Theta_i} +$$
$$T_0 R_d T_0' R_d^3 R_0'^3 e^{-8j\beta_2 d\cos\Theta_i} + ... = R_0 + \frac{T_o R_d T_0'}{1 - R_d R_0' e^{-2j\beta_2 d\cos\Theta_i}}. \tag{7.32}$$

**The n-layer model**

Now adding another layer to the previous "sandwich" to see how an increased number of layers changes the transmission and reflection coefficients. The newly

added layer has a thickness $d_0$, and a refractive index of $n_1$ has the thickness $d_1$ as shown in Figure 7.12. As the expressions for the coefficients for total reflection and transmission at the boundary of the media 1 and 2 have already been developed, given by Equation (7.32) and Equation (7.31), they can simply be used to describe the process that occur at $z = d_0$ and only have to modify them to account for the new layer.

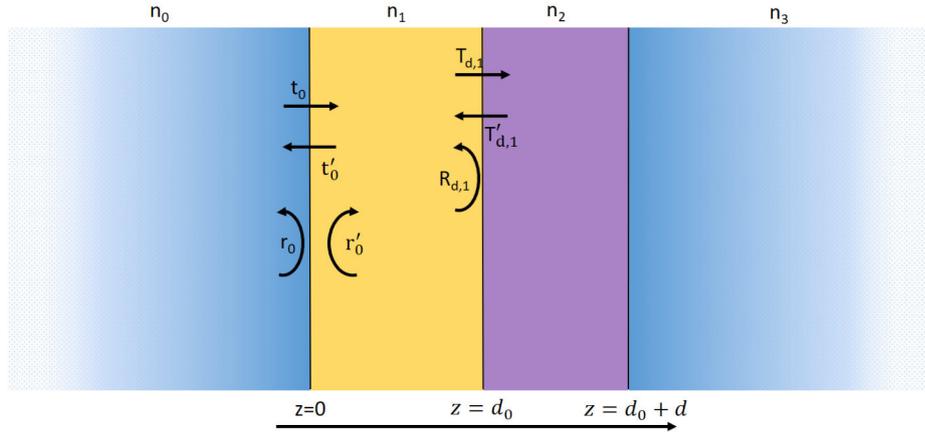The new boundary conditions are then as follows:



Figure 7.12: Schematic of the reflections in a 4 layer system. As the reflection and transmission on the right part of the system has been described in the previous section, these coefficients can be reused and are only modified to account for the new layer.

$t_0$ is the transmission coefficient at the new $z = 0$;

$t_0'$ is the transmission coefficient of a return wave, coming from medium 1 into medium 0 at $z = 0$;

$r_0$ is the reflection coefficient at $z = 0$;

$r_0'$ is the reflection coefficient of a wave coming from medium 1 and reflected at medium 0, $z = 0$;

$T_{d,1}$ is the transmission coefficient at $z = d_1$ through the effective medium.

$R_{d,1}$ is the reflection coefficient of a wave travelling in medium 1 and reflected from the effective medium, at $z = d_1$.

$$T_{d,1} = T e^{j(\beta_1 \cos \Theta_i - \beta_2 \cos \Theta_t)d_1} \tag{7.33}$$

and

$$R_{d,1} = Re^{j\beta_1 \cos \Theta_i d_1}. \tag{7.34}$$

The coefficients $t_0$, $t_0'$, $r_0$ and $r_0'$ are given by the Fresnel equations Equation (7.7)-Equation (7.14). The total transmission and reflection of the system is again expressed by Equation (7.32) and Equation (7.31), substituting with the new coefficients gives

$$T_n = \frac{t_0 T_{d,1}}{1 - r_0' R_{d,1} e^{-2j\beta_1 d_1 \cos \Theta_i}} \tag{7.35}$$

and

$$R_n = r_0 + \frac{t_0 t_0' R_{d,1}}{1 - r_0 R_{d,1} e^{-2j\beta_1 d_1 \cos \Theta_i}}. \tag{7.36}$$

We can therefore find an analytical expression recursively for any number of layers N in a system in a similar manner.